Synthesis, Structures and Properties of New 1111-type Rare-Earth Transition Metal Oxyarsenides

Andrea Marcinkova

Doctor of Philosophy

University of Edinburgh

2011

Declaration

I do hereby declare that I composed this thesis myself and that all research detailed within it, unless otherwise stated, is my own. This work has not been submitted for any other degree or professional qualification than this doctorate. Some of the research herein has already been published; these publications are included in the appendix.

Andrea Marcinkova
May, 2011

Acknowledgements

I have had doubts before I came to Edinburgh. I started my first PhD in the Czech Republic, but my Czech supervisor found another job and he could not keep his PhD students. I was devastated and I was not sure if I wanted to do another PhD. Thank God I changed my mind, because the last three years have been the best years in my life so far. I always wanted to study Materials Chemistry and I always wanted to live in Edinburgh, the most beautiful city in the world. There are no words that could ever describe how thankful I am to my supervisor Dr Jan-Willem G. Bos. He was the one who opened the "door" and introduced me to the fascinating world of Materials Chemistry. He is the one from whom I learnt everything I know. He gave me the chance to grow as an independent mind but he was always there when I needed a guide.

I thank my second supervisor Prof John Paul Attfield for very helpful discussions on any topic. Most importantly, I am indebted to Paul for his willingness to contribute towards the costs of the Summer School on Preparative Strategies in Solid State and Materials Chemistry held in California. I learnt a lot there.

I would like to acknowledge several other individuals who have greatly assisted me in conducting the research detailed within this thesis. I would like to thank Prof Andrew Huxley and Dr. Dmitry Sokolov for very fruitful discussions and the extensive PPMS measurements presented in chapter 6. All the neutron and synchrotron data presented in this thesis would have not been collected without the help and assistance of the local contacts, especially Andy Fitch (ESRF), Emmanuelle Suard, Thomas Hansen, Clemens Ritter (ILL) and Pascal Manuel (ISIS). Big thanks go to my colleagues and friends. Thank you; Javier, Gaetan, Kosmas, Artur, Miriam, Marta, Sandra, Wei-tin, Lindsay, Ale, Iris, Zlatko, Petra, Mark, George, Rob, Alex, Christina and Angel, for the lovely time I had and so many amazing and unforgettable memories. Dear Anya and Karolina, thank you for everything you two have done for me.

My biggest thanks go to my family, firstly to my parents who gave me everything that parents could possibly give to their child. They taught me to never give up my dreams, to always fight for everything I believe in. I wish my grandpa could be still here. He

was an amazing grandpa, artist, musician, and person that could build everything from nothing. It was him who fired my curiosity for everything. I will never forget the moment when he showed me a logarithmic ruler or explained the principle of electricity and how one can use it. Finally, I thank my sister who has always been here for me, supported me and always showed me that little light at the end of the tunnel called "life".

Abstract

The discovery of a second class of high-T_c superconductors based on tetrahedral iron arsenide layers has generated enormous interest. Currently four main groups are known: 1111-type *RE*FeAsO (*RE* = rare-earth) and *Ae*FeAsF (*Ae* = alkaline earth), 122-type $AeFe_2As_2$, 111-type *A*FeAs (A = Li, Na), and the 11-type $Fe_{1-d}Se$ compositions with selenium rather than arsenic. The highest superconducting transition temperatures (~ 55 K) are found among the 1111-type materials. NdFeAsO was chosen as representative of the 1111-type high-T_c superconductors, and the effect of chemical substitutions explored.

This thesis describes the synthesis, structures and properties of the Nd*TM*AsO (*TM* = Mn, Fe, Co, Ni) oxyarsenides. NdMnAsO is semiconducting and antiferromagnetic (AFM) with $T_{N,Mn} = 359(1)$ K. Neutron powder diffraction revealed that the Mn-spins are aligned along the *c*-axis with a magnetic moment $m_{Mn} = 2.26(1)\ \mu_B$ at 300 K. Upon ordering of the Nd sublattice ($T_{N,\,Nd} = 23$ K), a spin-reorientation of the Mn moments is observed.

NdFeAsO is a poor metal that shows a spin density wave (SDW) transition at 135 K. Hole doping via the substitution of Ca^{2+} on the Nd^{3+} site does not lead to superconductivity in the $Nd_{1-x}Ca_xFeAsO$ series. The maximum solubility of Ca^{2+} is limited to $x = 0.05$. Electron doping via replacement of Fe by Co does induce superconductivity for $0.05 < x < 0.20$ in $NdFe_{1-x}Co_xAsO$. A maximum critical temperature $T_c = 16.5$ K and upper critical field $H_{c2} = 26$ T are observed for optimally doped samples with $x = 0.12$. Underdoped samples show the structural P4/nmm to Cmma transition that is indicative of the SDW, suggesting that superconductivity may coexist with magnetic order.

NdCoAsO is a weak ferromagnetic (FM) metal with Curie temperature $T_c = 85$ K. The FM magnetic structure has two Co ions per unit cell with the moments constrained in the ab-plane. The ordered moment $m_{Co} = 0.30(1)\ \mu_B$ at 15 K. Below 9 K, ordering of the

neodymium moments results in the AFM coupling of the existing FM cobalt planes, and a transition to an AFM state.

NdNiAsO is found to be superconducting below 1.1 K from resistivity measurements. The normal state properties are consistent with those of a normal metal. Heat capacity and neutron powder diffraction reveal an incommensurate AFM ordering below 1.3 K, suggesting a possible coexistence of magnetic ordering and superconductivity.

The trends in the structural, magnetic and electronic properties of these new 1111-type rare-earth transition metal oxyarsenides are discussed.

Table of Contents

List of Tables

List of Figures

CHAPTER 1

Structure, Magnetic and Electronic properties of New 1111-type Rare-Earth Transition Metal Oxyarsenides

1.1 Introduction

The discovery[1] of high-temperature (high-T_c) superconductivity in $LaFeAsO_{1-x}F_x$ led to the rapid exploration of other iron based superconductors. Presently four main groups are known: 1111 type *RE*FeAsO and *Ae*FeAsF,[1-5] 122 type $AeFe_2As_2$,[6-9] 111 type A_xFeAs[10-12] and 11 type FeSe.[13] The Fe-based superconductors are, next to the copper oxide based materials (cuprates), the second class of the high-T_c superconductors.

Although Fe-based superconductors and cuprates share a lot of common features, they do have some differences which are also important for testing the theories of high-T_c superconductivity. The iron atom is surrounded by a tetrahedron of As sites, which is in contrast to the octahedral environment in the cuprates. Different crystal field symmetries lead to different crystal field splitting of the 3*d* orbitals. In the case of the cuprates, Cu^{2+} only has one unpaired electron in the $d_{x^2-y^2}$ orbital. For Fe^{2+} in the Fe-based superconductors, there have to be at least two unpaired electrons which lead to a moment much larger than in the cuprates.

Band structure calculations[14-16] suggest that all five 3d orbitals contribute to the density of states near the Femi surface in the Fe-based superconductors, resulting in a much more complicated band structure than for the cuprates, which is a single band material. In addition, the electron correlations in the parent compounds are weaker than in the strongly correlated cuprates. As a consequence, the parent compounds have a semimetallic ground state instead of an insulating one. The striking small moment

together with the metallic nature of the parent compounds suggest that the antiferromagnetism is due to itinerant electrons, rather than localised moments.

In this thesis new 1111-type rare-earth transition metal oxyarsenides are examined using neutron and X-ray scattering, together with complementary bulk measurements. In order to investigate the interplay between the magnetism and superconductivity in the 1111-type transition metal oxyarsenides, we have synthesised the Nd*TM*AsO (*TM* = Mn, Fe, Co and Ni), Ca-doped $Nd_{1-x}Ca_xFeAsO$ ($0 \leq x \leq 0.05$) and Co-doped $NdFe_{1-x}Co_xAsO$ ($0 \leq x \leq 1$) series and compared their properties with other analogues of the Fe-based superconductors.

In this chapter I will consider some of the interactions that are observed in solids. I will discuss the interactions of single ions, and will then move on to consider some of the plethora of ordered states that arise in multi-ion systems, such as different kinds of magnetic order and superconductivity. The background and general properties of the Fe-based superconductors will be given in the second part of this chapter.

1.2 Single-Ion Interactions

When electrons are placed in the potential well of a nucleus they cannot all have the same energy, but rather occupy 'shells' for which there is a well defined energy and angular momentum. Since each shell can accommodate a fixed number of electrons, then any added electrons to the system must to go into a shell with higher energy. In general, electrons in a filled shell do not interact with the atom's surroundings, thus the electrons in unfilled shells will be discussed within this chapter.

1.2.1 Crystal Fields

All samples prepared in this work were polycrystalline powders, thus the crystalline environment of the ion will determine some of its properties and has to be considered. Of particular importance is the effect of Coulomb repulsion between the electron wavefunctions of the ion and its nearest neighbour. For *d*-electrons, the crystal fields are

strong, because their wavefunctions extend a relatively long way from the nucleus towards the surrounding ions. On the other hand, *f*-electrons wavefunctions are smaller and are partly shielded from Coulomb interactions with the surroundings by the s- and p-electrons in filled levels.

The *d* orbitals can be classified into two classes, the t_{2g} orbitals that point between the x, y, and z axes (so-called d_{xy}, d_{xz}, d_{yz}) and the e_g orbitals that point along these axes. The e_g orbitals are the d_{z^2} orbital with lobes pointing along the z axis and the $d_{x^2-y^2}$, with lobes pointing along both the z-axes and y-axes. The effect of the environment on the *d*-orbitals is determined through the amount of overlap between the ligand orbitals and a given *d*-orbital. The *tetrahedral* environment, shown in Figure 1.1, is created by assuming that a magnetic ion (*M*) containing *d*-electrons is placed in the centre of the sphere of a radius *r* in which the charge on the sphere is collected into four discrete point charges. The total electronic energy of all the *d*-orbitals will not change, but the *d*-orbitals will no longer be degenerate. The *octahedral* environment, shown in Fig. 1.1, is analogous taking six discrete point charges, respectively.

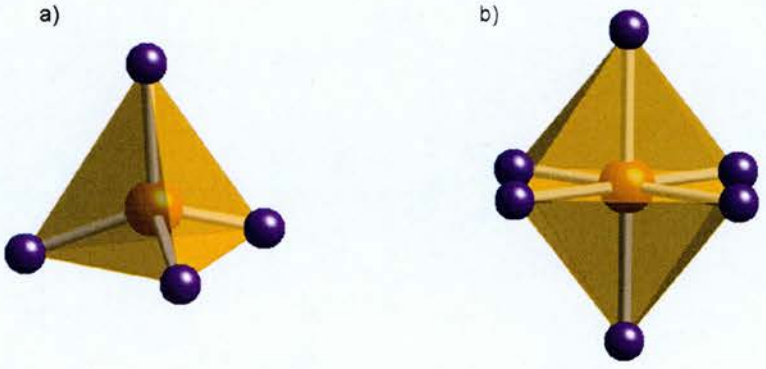

Figure 1.2: A magnetic ion (yellow sphere) in a) a tetrahedral and b) an octahedral crystalline environment of arsenic ions (purple spheres).

As an example, consider the tetrahedral environment MAs_4 in which the magnetic ion has four neighbour arsenic ions, with *p*-electron wavefunctions extending towards M along the bonds. The effect of the environment on the *d*-orbitals of the M ion is determined through the amount of overlap between the *p*-orbitals and a given *d*-orbital. This will result in an energy difference of the orbitals. In the *tetrahedral* environment, the $d_{x^2-y^2}$ and d_{z^2} orbitals will be lowered in energy, while the d_{xy}, d_{xz}, d_{yz} orbitals will be raised in energy, as depicted in Figure 1.2. In other words, the e_g will be maximally avoiding the charge density from the ligand ion, while the t_{2g} orbitals will be maximally overlapping the arsenic *p*-orbitals. In the case of the *octahedral* environment, the orbital splitting is exactly opposite (Fig. 1.2).

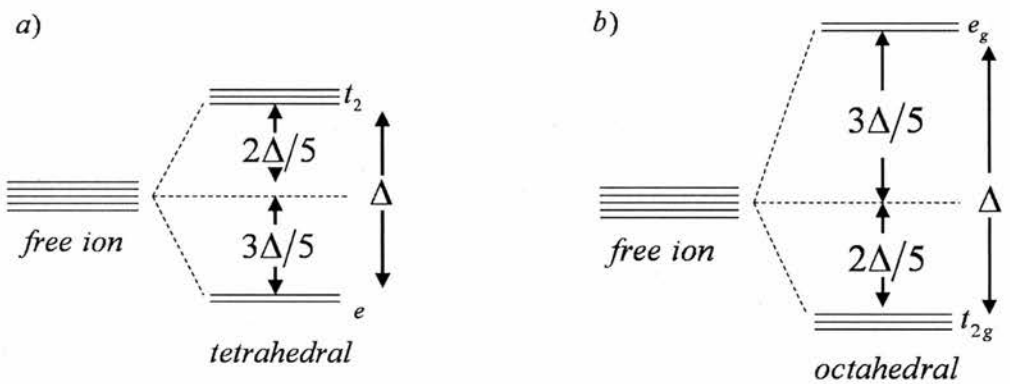

Figure 1.3: The 3d energy levels in the a) tetrahedral and b) octahedral environment

The crystal field in a material can be measured using several techniques. Neutron inelastic scattering can be used, whereby neutron energy is transferred to electrons in lower lying levels and excite them into the higher energy states. Such scattering is wavevector independent. Alternatively light can be used to excite electrons between levels, with, for example, peaks in the absorption (UV-Vis, IR) occurring at wavelength corresponding to energy gaps between levels.[17]

1.3 Collective Interactions

The magnetism in the rare-earth transition metal oxyarsenides is of interest because it is thought to be related to the superconductivity. Lots of questions have been raised based on theoretical and experimental work done on these materials. Are these systems made

up of localised spins that interact via short ranged, nearest neighbour exchange interactions or, are they better described in terms of itinerant magnetism? What are the main ingredients for an unconventional pairing mechanism? Is the superconductivity singlet or triplet (pairing symmetry) spin state? Is there any connection between the observed structural transition (T_S) and the magnetic transition (T_N)? In other words, is the magnetism essential for the distortion, or is the distortion essential for the magnetism?

The rare-earth transition metal oxyarsenides have been studied in much detail by band structure calculations. None of the proposed models can fully describe the magnetism, magnetic interactions and spin fluctuations in these materials. So far four pictures have been used: fully-itinerant, fully-localised, local-itinerant and orbital ordering picture. In the fully-itinerant picture, magnetism is driven by nesting; magnetic interactions, mainly Ruderman-Kittel-Kasuya-Yosida (RKKY), are of itinerant nature defined by the Fermi surface geometry and the superconductivity is described in terms of spin fluctuations that are modelled using random phase approximation.[18-22] The fully-localised model describes the magnetism by combination of the Hubbard U and Hund's rule coupling models. Magnetic interactions are local, of superexchange nature, and spin fluctuations are described using $J_1 + J_2$ model.[23, 24] In the third model, local-itinerant, magnetism is driven by Hund's rule coupling. Magnetic interactions are of itinerant nature, not always RKKY, defined by the Fermi surface geometry. The Fermi surface (FS) geometry cannot be explained in terms of superexchange mechanism.[25-27] The Orbital ordering model treats magnetism as a competition between the orbital ordering of the localised moments and the direct exchange of the itinerant electrons. The spin fluctuations are described by orbital-dependent superexchange and direct exchange mechanism.[28]

In the following, the theory of diamagnetism, paramagnetism, the origins of RKKY interactions, instabilities of the electron gas such as spin density wave (SDW) formation, and the theory of superconductivity will be discussed within this subchapter.

1.3.1 Theory of Magnetism

Atoms have a net magnetic moment when unpaired electrons are present. Therefore, the magnetic properties of materials are determined by the properties of the atoms within it, and in particular with behaviour of the electrons associated with these atoms. In general, atoms having all electrons in closed shells (paired) have no net magnetic moment and are diamagnetic. The presence of unpaired electron spins (*d* and *f* in transition metals; rare earths) gives rise to paramagnetism and possible magnetic order.

The main characteristics of an electron are the intrinsic spin given by $\mu_S = g\mu_B S$ and the associated orbital moment $\mu_L = g\mu_B L$ These properties, described by the quantum numbers S (spin) and L (orbital), give rise to the magnetic moment that can be given as:

$$\mu = -g\mu_B J \tag{1.1.}$$

where the total angular momentum J is characterized by the resultant of the vector sum of L and S. The magnetic moment due to the spin component of the unpaired electrons is intrinsic to the atom or ion in question. The orbital component is strongly influenced by the local environment of the ion. μ_B is the Bohr magneton and is equal to $eh/4\pi m$, and e, m are the mass and charge on the electron. g is the gyromagnetic ratio, and is itself defined by the Landé equation:

$$g_J = \frac{3}{2} - \frac{L(L+1) - S(S+1)}{2J(J+1)} \tag{1.2.}$$

A set of empirical rules, known as Hund's rules, can be used to determine the angular momentum quantum numbers of the ground state of a magnetic system. They deal with the case where the energy of Coulomb repulsion is greater than that arising from spin-orbit interactions, i.e. the LS-coupling regime. Note that they only apply to the ground state, they cannot be used for excited states. The rules are as follows:

1. Maximise the spin. This means that, if we consider adding electrons to the shell, every electron added will increase S by 1/2 until the shell is half-filled. Thereafter each electron added will reduce S by 1/2.

2. Maximise the orbital angular momentum, subject to the first rule. Suppose $l = 2$ (*d*-electrons), then as we add electrons to the shell the first one will have $m_l = 2$, the next $m_l = 1$, until we reach half-filling, where the m_l will have all cancelled out, and then we start the process again.

3. $J = |L - S|$ if the shell is less than half-full, and $J = |L + S|$ if the shell is more than half-full.

1.3.2 Diamagnetism and Paramagnetism

The magnetic moments in a sample are disordered at high temperatures. Such disorder is termed the paramagnetic phase. Disordered magnetic moments tend to align in the presence of an external magnetic field, which causes the sample to become magnetised. The degree to which the sample is magnetised is quantified by the magnetic susceptibility, χ. The magnetic susceptibility, χ is defined as the sample magnetisation (M) divided by the applied field (H); $\chi = \partial M / \partial H$.

Diamagnetism is an ubiquitous effect, although its strength is material dependent. It occurs only when a magnetic field is applied to the material, and acts to oppose the applied field, i.e. the magnetisation is antiparallel to the applied field. The diamagnetic susceptibility of an assembly of N identical ions in a volume V, each with Z electrons of mass m_e, is given by

$$\chi = -\frac{N}{V}\frac{e^2 \mu_0}{6m_e}\sum_{i=1}^{z}\left(r_i^2\right) \tag{1.3}$$

where r_i are the radii or electron orbitals in the material.

Paramagnetism also occurs only when a magnetic field is applied to a material; however the paramagnetic magnetisation will be parallel to the applied field. It arises due to the non-zero angular momentum (spin S and/or orbital L) of the electrons in unfilled shells in a material, and is due to an interaction between individual ions and the applied field. There are assumed to be no interactions between the ions. For a material in which the

total angular momentum, J, of each ion is given by $J = 1/2$ the paramagnetic magnetisation, M, is given by

$$M = N\mu_B \tanh\left(\frac{\mu_B B}{k_B T}\right) \tag{1.4}$$

where N is the number of magnetic ions. In the general case, where $J \neq 0$,

$$M = Ng_J\mu_B JB_J(y) \tag{1.5}$$

where g_J is the Landé g-factor, $y = \frac{g_J\mu_B J}{k_B T}$, and $B_J(y)$ is the Brillouin function,[29] which is given by

$$B_J(y) = \frac{2J+1}{2J}\coth\left(\frac{2J+1}{2J}y\right) - \frac{1}{2J}\coth\left(\frac{y}{2J}\right) \tag{1.6}$$

The variation in susceptibility of a paramagnetic material with temperature can be described by the Curie-Weiss law:

$$\chi = \frac{C}{T-\theta} \tag{1.7}$$

where θ is the Weiss temperature and C the Curie constant given by:

$$C = \frac{N\mu_B^2\mu_{eff}^2}{3k} \tag{1.8}$$

where k_B is the Boltzman constant, N is the number of magnetic ions in the material and μ_{eff} is the effective magnetic moment. μ_{eff} may be predicted from the spin-only (orbital quenching) formula for the first row transition metals:

$$\mu_{eff} = g[S(S+1)]^{1/2} \tag{1.9}$$

The Weiss temperature depends on the interactions between magnetic ions. A positive value indicates a tendency for the magnetic moments to align parallel (FM); a negative

value suggests a tendency for the spins to become opposed to one another (AFM) (Fig. 1.3). [30-32] An ideal paramagnet has zero value of the Weiss temperature. The Curie constant and Weiss temperature can be found by measuring the magnetic susceptibility as a function of temperature.

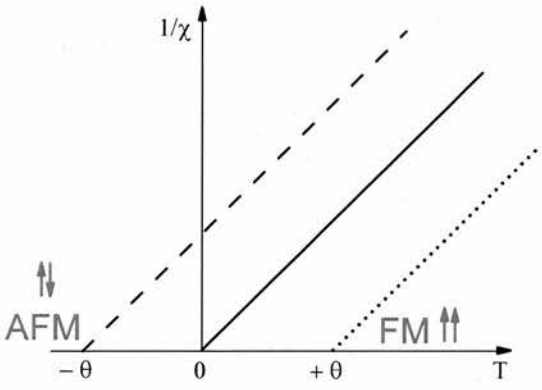

Figure 1.4: Temperature dependence of 1/χ with the intercept on the temperature axis yielding θ

1.3.3 Exchange Interactions

So far we have not considered any inter-site interactions of the magnetic ions, and although this is a good approximation for a lot of materials, there are also many where the magnetic ions do interact. The exchange interaction arises due to Coulomb interactions arising from the overlap of electron wavefunctions in a material. The Heisenberg Hamiltonian, *H*, for exchange interaction terms is given by

$$\mathrm{H} = -\sum_{ij} J_{ij} S_i \cdot S_j \qquad (1.10)$$

where J_{ij} is the exchange constant between the *i*th and *j*th spins, with positive J corresponding to ferromagnetism and negative J corresponding to antiferromagnetism (AFM).

In a ferromagnet (FM) adjacent magnetic moments are aligned parallel, whereas in an antiferromagnet they are antiparallel. The periodicity of ferromagnetic order is equal to the separation of the magnetic moments, whereas for antiferromagnetic order the repeat period is doubled. There are many other magnetic structures that can arise, for a variety

of reasons, where the periodicity is different. For example the magnetic moments may be helically ordered so that along a particular direction neighbouring moments are rotated by a fixed angle relative to their neighbours. Such order can be commensurate, where the period of the magnetic order is equal to an integer number of lattice units or incommensurate where it is not. The simplest case of exchange is direct exchange, where the amount of direct overlap between wavefunctions of neighbouring magnetic ions, and the resulting Coulomb energy, gives rise to the exchange interaction. More usually, and particularly in transition metal oxides, a non-magnetic ion such as oxygen is situated between pairs of magnetic ions whose wavefunctions do not directly overlap. In such cases interaction occurs through superexchange, where each magnetic ion wavefunction overlaps with the wavefunction of a mediating non-magnetic ion. It is usually, although not exclusively, an antiferromagnetic interaction. Considering an M - O - M bond, where M is a magnetic ion and O is non-magnetic, excited states can mix with the ground state for antiferromagnetic interactions, whereas for ferromagnetic interactions they cannot. In the antiferromagnetic case, then, the kinetic energy of the system is lowered and it is stable, whereas in the ferromagnetic case it is not.

For example, in the case of perovskite oxides with the magnetic Cu^{2+} ion in octahedral coordination; e.g. a 180° Cu^{2+}-O^{2-} -Cu^{2+} interaction (via $d_{x^2-y^2}$-O:2*ps*- $d_{x^2-y^2}$ overlap). Weak overlap of the Cu $d_{x^2-y^2}$ and O:2pσ orbitals enables the unpaired spin on one Cu to form a weak 'bond' with the opposite spin O:2p electron. This polarises the spin density in the O:2pσ orbital as shown in Fig. 1.5a, so the second Cu spin must be antiparallel to the first one in order to also form a weak 'bond' with oxygen. The ferromagnetic coupling, in a 90° Cu^{2+}-O^{2-} -Cu^{2+} interaction (via two orthogonal - $d_{x^2-y^2}$O:2pσ overlaps), results from the Hunds rule coupling between the two induced spins. The effective orbital overlapping of 2*p* Oxygen and 3*d* Cu^{2+} orbitals separated by a 90° and 180° bond is shown in Fig. 1.5

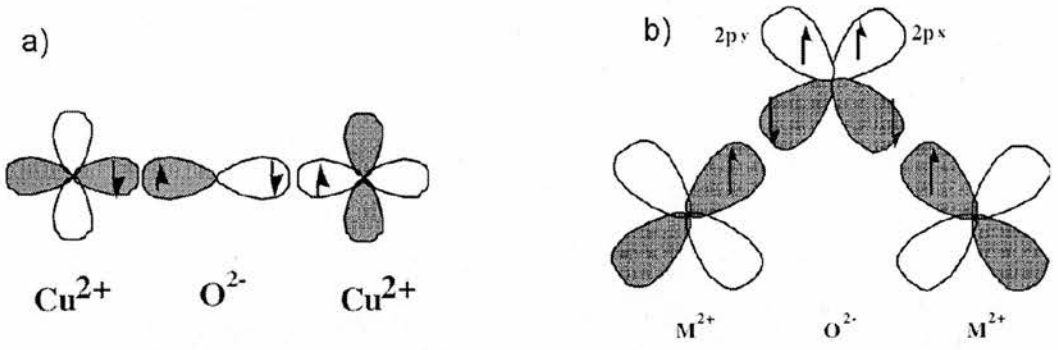

Figure 1.5: The effective orbital overlapping of 2*p* Oxygen and 3*d* Cu^{2+} orbitals separated by a a) 90° and b) 180° bond.

Generally, the Goodenough-Kanamori-Anderson (GKA) rules are a set of guidelines for estimating the sign and relative magnitudes of superexchange interactions,[33-35] and can be summarised as follows

1. Generally interactions in magnetic oxides will be antiferromagnetic.

2. The exchange between e_g electrons on different ions connected by a 180° bond is stronger than that between the t_{2g} electrons.

3. A small ferromagnetic coupling can occur for interaction between t_{2g} electrons separated by a 90° bond, or by e_g and t_{2g} electrons separated by a 180° bond.

4. Completely filled shells with an equal number of up and down spins do not contribute to the superexchange interaction.

Another kind of interaction, the Dzyaloshinskii-Moriya (DM) or anisotropic exchange interaction,[36-38] arises due to spin-orbit coupling. In the case of superexchange there is a mixing of the ground state and excited state of the system due to the presence of a non-magnetic ion such as oxygen, whereas here the spin-orbit interaction can lead to the ground state of one magnetic ion interacting with the spin-orbit excited state of the other magnetic ion. The form of the DM Hamiltonian is;

$$H_{DM} = D \cdot \left(S_i \times S_j \right) \tag{1.11}$$

when acting between the i^{th} and j^{th} spins. The vector D is non-zero provided that the crystal field acting on the two spins does not have an inversion symmetry at the half-way point of the vector joining the two spins. The effect of the DM interaction is for the spins to lie preferentially at right angles to one another, in a plane perpendicular to D. If there are other interactions acting on the system then such a situation may not be realised, and instead the DM interaction may result, for example, in spins lying in the same plane and rotating slightly from site to site.

1.3.4 Itinerant Electron Magnetism

The descriptions of magnetic interactions have so far assumed that all of the magnetic ions were localised (Fig. 1.4) and therefore at fixed distances from each other. It is possible to envisage quite easily a situation in which this assumption is not valid, namely in a metal. Pauli paramagnetism is the paramagnetic response of an electron gas (i.e. a metal) to an applied magnetic field. Its physical origin is distinct from paramagnetism in ionic solids, discussed above, in that it comes about due to splitting of bands with different spin state (spin-up and spin-down) in an applied magnetic field. When a magnetic field is applied, the energy of the electron is raised or lowered depending on its spin (Fig. 1.4). This gives rise to a paramagnetic susceptibility, so-called Pauli paramagnetic susceptibility, which is given by:

$$\chi_p = \frac{M}{H} \approx \frac{\mu_0 M}{B} = \mu_0 \mu_B g_J(E_F) = \frac{3n\mu_0\mu_B^2}{2E_F} \tag{1.12}$$

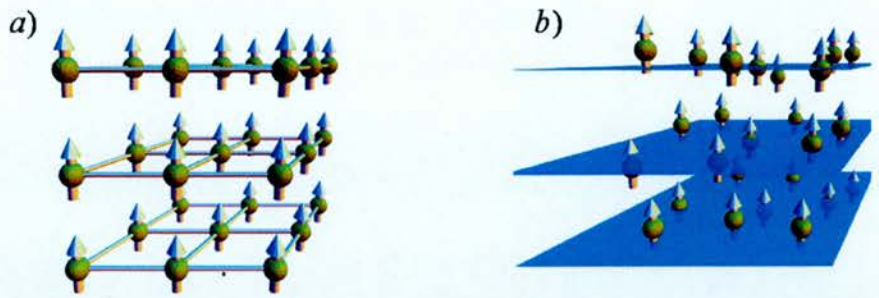

Figure 1.6: Schematic picture of a) localised and b) itinerant system

It is also possible for spontaneous ferromagnetism to occur in metals under certain conditions. If electrons from one spin band are moved into another. The number of electrons moved is $g(E_F)(\delta E)/2$ and they increase in energy by δE (Fig. 1.5). In order to obey the Pauli Exclusion Principle they must gain kinetic energy, hence this is an unfavourable process. However the magnetisation caused by such a move gives rise to an effective magnetic field in the material. This effective field will be strong if there is strong Coulomb interaction in the metal, and it turns out that if the product of the density of states at the Fermi level (E_F) and the Coulomb interaction energy (U_g) is greater than unity, $U_g(E_F) \geq 1$, the system is unstable to ferromagnetism. This instability criterion is known as the Stoner criterion.[39]

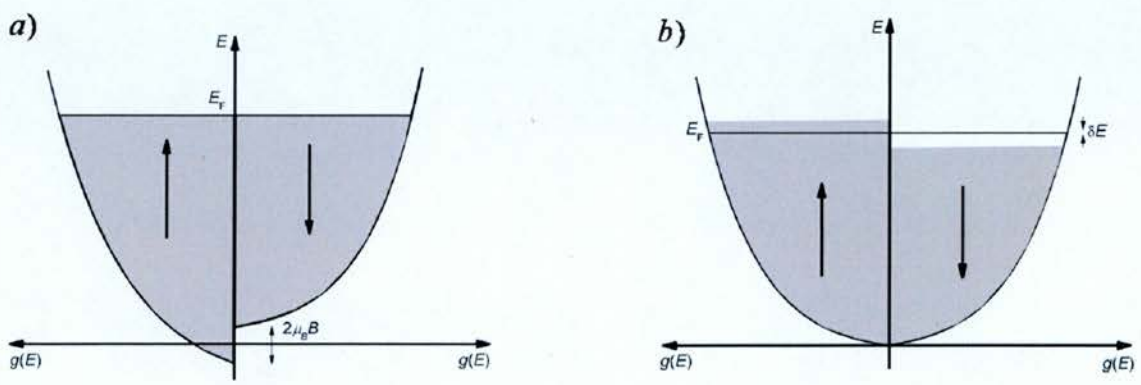

Figure 1.7: Density of states showing a) splitting of energy bands in a field B and b) spontaneous splitting of energy bands.[17]

The magnetic susceptibility χ can be rewritten as

$$\chi = \frac{M}{H} \approx \frac{\mu_0 M}{B} = \frac{\mu_0 \mu_B^2 g_J(E_F)}{1 - U_g(E_F)} = \frac{\chi_P}{1 - U_g(E_F)}. \tag{1.13}$$

In metals the exchange interactions between the magnetic ions can be mediated by the conduction electrons. A localised magnetic moment spin-polarizes the conduction electrons and this polarization in turn couples to a neighbouring localised magnetic moment a distance r away. The exchange interaction is thus indirect because it does not involve direct coupling between the magnetic moments and it is known as RKKY interaction (itinerant exchange).[40, 41] The coupling takes the form of an r-dependent exchange interaction J_{RKKY} (r) given by:

$$J_{RKKY} \propto \frac{\cos(2k_F r)}{r^3} \tag{1.14}$$

at large r (assuming a spherical Fermi Surface of radius k_F). The interaction has an oscillatory dependence on the distance between the magnetic moments.[17]

1.3.5 Spin Excitations in Itinerant Magnets

As has already been discussed previously, there are many magnetic materials in which the electrons are not localised, i.e. in which they are itinerant. In a metallic (itinerant electron) ferromagnet there exist spin-split Stoner bands, separated by a gap Δ. It is possible to transfer an electron from a filled state in one of the spin-split bands to an empty state in the other spin-split band. Such an excitation is known as Stoner excitation in which an electron with wavevector $k+q$ and spin down is excited to a state with wavevector k having spin up (spin flipping). The energy of the excitation is given by

$$\hbar\varpi = E_{k+q} - E_k + \Delta \tag{1.15}$$

where $E_k = \hbar^2 k^2 / 2m_e$ and Δ is the exchange splitting, the energy cost to flip a spin. The spin-split excitations and continuum Stoner excitation is depicted in Fig.1.6.

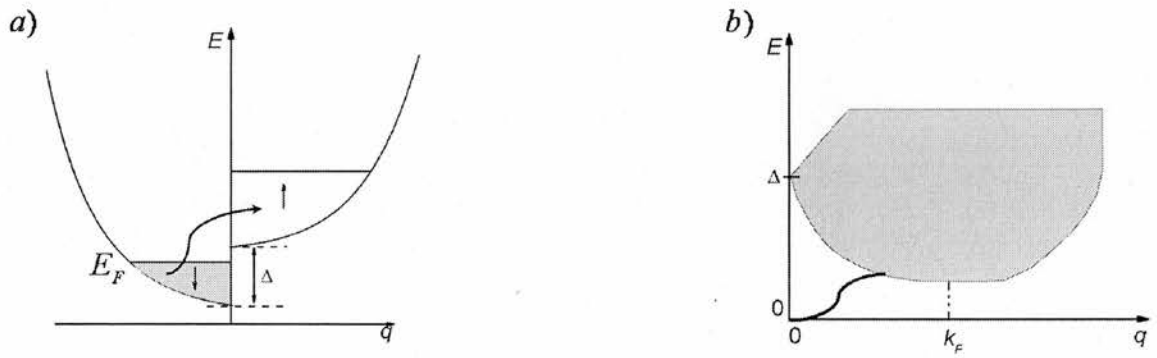

Figure 1.8: a) The single particle spin flip excitation from one band to another in a Fermi gas (metal) and b) magnetic excitations resulting from the spin flip processes (shaded area), and spin wave modes that can still propagate below this continuum (solid line).

While spin fluctuations in localised systems take place in real space, a spin fluctuation in weakly ferromagnetic metal may be regarded as being localised in Q-space with wavevector q. It turns out that Pauli susceptibility is q-dependent and is rewritten as

$$\chi_q = \frac{\chi_p}{1 - U_g(E_F) f(q / 2k_F)}. \tag{1.16}$$

The spins order ferromagnetically with $q = 0$, antiferromagnetically when $|q| = \pi / a$, and $q = 2k_F$ deforms an electron energy and introduces an instability, i.e. wave vector q opens up an energy gap. Formation of the energy gap having electrons with wavevector $q = 2k_F$ near Fermi surface will lead to a lowering of the total energy of the system. The formation of the density wave is said to nest the Fermi surface (FS), i.e. two pieces of FS are translated from one another in k-space by a fixed wavevector q. If the nesting wavevector $|q| = \pi / a$ where a is the spacing between atoms, the spin density wave is commensurate with the lattice and has AFM ordered spins. The spin density wave with $q = 2k_F$ is not a simple multiple of π / a and is thus incommensurate.

1.4 Electronic Properties

1.4.1 Band Theory and Conductivity

The electrons are described by their wave functions. The overlapping of the wave functions of the electrons leads to a formation of the electronic bands. The top filled electronic band is known as the valence band whereas the bottom unoccupied band is called the conduction band. The valence band is separated from the conducting band by the energy gap E_g. The magnitude of E_g depends on the periodicity of the crystal lattice of the solids. The thermal excitation of the electron from the valence band to a conducting band leads to a conductivity of the system. The conductivity σ depends critically on the size of the energy gap which can be described as a fraction of the electrons excited across the energy gap at particular temperature T as

$$\sigma = Ae^{-E_g/2k_BT} \tag{1.17}$$

Substances with large band gaps are insulators, those with smaller band gaps are semiconductors, while conductors either have very small band gaps or none because the valence and conduction bands overlap (Fig. 1.7). Typical room temperature resistivities of metals are ~ 10^{-6} ohm cm, semiconductors are between ~ 10^{-3} and 10^{9} ohm cm; and the resistivity of the insulators can be as large as 10^{22} ohm cm.

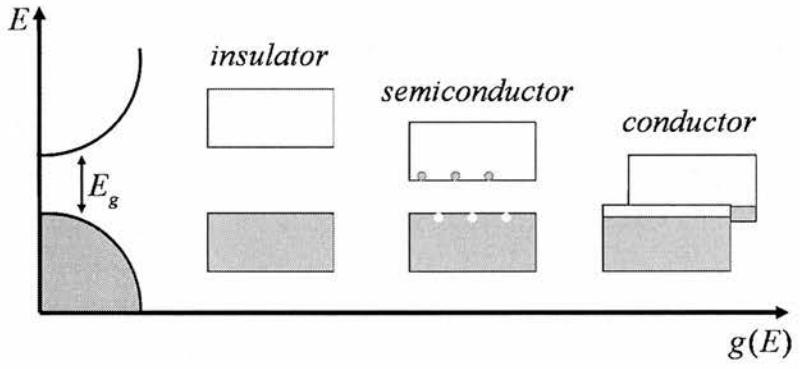

Figure 1.9: Separation of the valence (shaded) and conducting band in insulating, semiconducting and conducting system

The number of the carriers can be increased using doping with impurities. This can happen in two ways, if more electrons are added into the conduction band than holes in the valence band (n-type) or if more holes are added into the valence band than electrons in the conduction band (p-type). In an intrinsic semiconductor or insulator the Fermi level (E_F) lies in between the conduction and valence bands. However the introduction of extra carriers causes a shift of E_F, away from its ideal mid gap position, closer to the conduction band in the n-type semiconductor, or closer to the valence band in the p-type semiconductor.

For simple metals such as the alkali and alkali earth metals the free electron model can be used to describe the electronic conductivity. The valence *s* and *p* orbitals of these metals are very diffuse and there is strong overlap between neighbouring atoms. The bands produced are many electron volts broad and hence the bands formed from *3s*, *3p* and even higher orbitals of sodium overlap in energy and merge into a single conduction band. The atomic orbitals lose their identity, and the electrons in the metal hardly feel the potential of individual atoms. This model however breaks down for the transition metals, in which the narrower bands occur due to a less overlap between *3d* electrons (more contracted than valence *s* and *p*). The simplest approach to the band structure of the transition metal materials follows the Linear Combination of Atomic Orbitals (LCAO), so-called the "tight binding method". The results of band structure calculations are represented in a diagram of band energies *E(k)*, against wavevector *k* or by plotting the total density of states *N(E)*, and are used to locate the Fermi level in the band structure and thus to determine many of the physical properties of the materials.[42]

1.4.2 The Hubbard Model

The electronic ground state in the Fe-based superconductors is generally explained via hopping of the Fe electrons[43] between 3d-3d or 3d-2p-3d orbitals. This can be modelled using the Hubbard model which is based on the correlations between the intra-orbital Coulomb U_{intra}, the inter-orbital Coulomb U_{inter}, the Hund's coupling J^H, and the pair-hopping t parameters. The most important term is the repulsion energy, Coulomb energy, which is the energy cost of putting one electron on a site already occupied. If

the repulsion energy is strong then electrons cannot move freely through the crystal and the metallic behavior breaks down. In structure calculations, the metallic behaviour is generally characterized by the width of the electronic bands, W. The Coulomb energy is given by the parameter U, the so-called Hubbard-U.

With the Hubbard energy, U, much larger than bandwidth, W, the system is known as Mott insulator and shows insulating behavior. As the bandwidth increases each sub-band is broadened by inter-atomic overlap. Eventually the two sub bands meet where the U and W parameter are equal and the system becomes metallic. As the orbitals overlap more, the polarisability of the solid also increases since electron clouds can distort by moving partially between atoms and hence U decreases with increasing bandwidth. Although the 1111- and 122-family of iron-based parent compounds show metallic behaviour down to 2 K, the five-band Hubbard model was found to be an effective tool to interpret the interactions between Fe electrons at the vicinity of the Fermi level, E_F.[22, 44]

1.4.3 Kondo Effect

The electrical resistance of pure metals usually decreases with decreasing temperature. This is a consequence of electron scattering due to lattice vibrations, which are gradually frozen out when reducing the temperature. However, it was discovered that, in some metals containing magnetic impurities, the electrical resistance increases again below a certain temperature, so-called Kondo temperature T_K.[45, 46] Below T_K the interaction between the magnetic moment and the conduction electrons leads to the impurity spin becoming non-magnetic. What is happening is that conduction electrons begin to form a cloud of opposite spin-polarization around the impurity spin resulting in a quasi-bound state. This process of magnetic screening of a magnetic impurity by the conduction electrons is known as Kondo effect.

The influence of the *RE* on the electronic structure of *RE*FeAsO (*RE* = Ce, Pr, Nd, Sm, Y) due to the hybridization between the Fe 3*d* band and the localized 4*f* states of the rare-earth ions has been investigated in the literature.[47] So far, a Kondo screening of the Ce local magnetic moment on the 4*f* shell has been observed in the CeFePO compound,

a homologue of CeFeAsO, with a reported Kondo temperature T_K = 10K.[48] This implies the existence of hybridization between the Fe 3*d* bands in the vicinity of E_F and the localized Ce *4f* states.

1.5 Superconductivity

The phenomenon of superconductivity has been under intensive study since its discovery by Kamerlingh Onnes in 1911. Electrical current flows without resistance in the superconducting state (SCS), that is the electrical resistance of the material falls to extremely low values, very close or equal to zero. Onnes also discovered that the superconducting state can be destroyed if either the magnetic field at the surface of the superconductor or the current flowing through the superconductor reached a critical value. The discovery of the Meissner effect showed that superconductivity is more than just a vanishing of resistance. In 1933, Meissner demonstrated that a superconductor is a perfect diamagnet; magnetic flux is excluded from all but a thin penetration region at a plane surface. The manner in which the penetration occurs depends on the geometry of the sample.

1.5.1 London Equation

Not very long afterwards, London and London proposed a theory in which the superconductivity occurs due to "super electrons".[58] Based on a model of superfluid ^{4}He the London brothers assumed that they can divide the total electron density n_{tot} between normal state n_n and superfluid part n_S as:

$$n_{tot} = n_n + n_S \tag{1.19}$$

A set of equations produced by H. London described the behaviour of these "super electrons" as:

$$J = -\frac{n_S e^2}{m_{eff}} A = -\frac{1}{\mu_0 \lambda_L^2} A \tag{1.20}$$

Where J is the supercurrent; n_S is the number of superfluid electrons per unit volume; e is the electronic charge; m_{eff} is the effective mass of the electrons; A is the magnetic vector potential and λ_L is the London penetration depth of the superconductor,

$$\lambda = \left(\frac{m_{eff}}{\mu_0 n_S e^2} \right)^{1/2}. \tag{1.21}$$

λ_L has dimensions of length and describes the distance inside the surface of the superconductor over which an external magnetic field is screened. The London equation explains the Meissner effect due to keeping the magnetic flux out of the superconductor, and demonstrates that the supercurrent J is related to the magnetic vector potential A.

In 1950, the first quantum mechanical approach developed by Ginzburg and Landau (GL) theory superseded the London theory. This theory claimed that superconducting state must be different from the normal state in the presence of internal order described by using an order parameter, ψ(r). This order parameter may be understood as an effective wave function for the "super electrons" and its square is a measure of their density in the ground state. The London equation can be rewritten then as;

$$J = -\frac{(2e)^2}{2m^*} |\psi|^2 A \tag{1.22}$$

Where the London superfluid density is $n_S = 2|\psi|^2$ and $m^* = 2m_e$ (m_e; bare electron mass) is GL effective mass. The London penetration depth is given by

$$\lambda(T) = \left(\frac{m_e b}{2\mu_0 e^2 \dot{a}(T_C - T)} \right)^{1/2} \tag{1.23}$$

Where $\dot{a}, b$ are GL parameters.

Ginzburg and Landau introduced another very important physical parameter characterizing superconductors called Ginzburg-Landau coherence length, ξ(T). The coherence length is a measure of the distance from the surface over which the order parameter has recovered back to nearly its bulk value and can be written as;

$$\xi(T) = \xi(0)|t|^{-1/2} \tag{1.24}$$

Where $t=(T-T_C)/T_C$ is reduced temperature.

In 1953, Pippard proposed another version of coherence, where he discussed the penetration phenomena.[59] Afterwards the BCS theory was published to explain superconductivity by using an energy-gap model.

1.5.2 BCS Superconductivity

The theory of conventional superconductivity was developed by Bardeen, Cooper and Schrieffer.[49, 50] The starting point is that the interaction between two electrons has an attractive character which can be explained by considering interactions between electrons and a flexible metal lattice. As a negatively charged electron moves through a solid it distorts the positive lattice around it causing lattice vibrations. This leads to areas of increased positive charge and hence the lowering of energy of another electron in the vicinity. This results in the formation of pairs of electrons in the superconducting state known as Cooper pair. The pairs are coupled over a distance called the correlation length, typically of the order of 100 nm, a range of many times the space between atoms in the lattice. The cooper pairs contain electrons of opposite spin and can be treated as individual charge carriers. In contrast to individual electrons these cooper pairs have zero overall spin and are bosons, meaning they can all occupy the same energy level, thus they condense at low temperatures. The energy gain of the superconducting (SC) state is therefore condensation energy of the pairs merging into macroscopic quantum state. This can be measured as an energy gap Δ(T), i.e. the energy required to excite a single electron from the superconducting ground state to the first excited state. This energy gap is highest at low temperatures but vanishes at the transition temperature. At zero-temperature the energy gap is expressed as:

$$\Delta(0) = 1.76 k_B T_C . \tag{1.25}$$

The typical energy scale relevant to superconductivity is very much less than the Debye energy ω_D and can be written as;

$$k_B T_C = 1.13\hbar\omega_D e^{-1/\lambda} \tag{1.26}$$

Where k_B is Boltzmann's constant and $\hbar$ is a Planck's constant.

The BSC theory has been very successful in explaining the critical temperature of the superconductors with T_c up to 30 K. In addition, BCS theory correctly explained the Isotope and Meissner effect. The Meissner effect is explained since the Cooper pairs are destroyed if a magnetic field causes the electron spins to align in any way other than antiparallel. The isotope effect, in which the T_c of different isotopes of a given metallic element varies from one isotope to another, frequently as the inverse square root (~ isotope exponent α) of the ionic mass M is defined as;[51]

$$T_C \propto M^{-\alpha}. \tag{1.27}$$

In other words, T_C dependence on M showed that lattice vibrations and hence electron-lattice interactions are deeply involved in superconductivity.

Since 1962 it has became universally recognized that beside metallic superconductors (type I) new class of superconductors (type II) exist, which are characterized by the fact that they exhibit a new type of reversible magnetic behaviour, the so-called mixed state, also known as Vortex state (Fig. 1.8). Type II superconductor has two critical fields, a lower boundary H_{c1} and an upper limit of H_{c2}. Below the H_{c1} there is penetration of the magnetic field. As the external field is raised to the value between H_{c1} and H_{c2}, there is a partial penetration of flux and the sample exhibits the Vortex state (a microscopic structure of both superconducting and normal regions). At an external field of H_{c2}, the field penetrates the sample completely and it behaves as in the normal state.

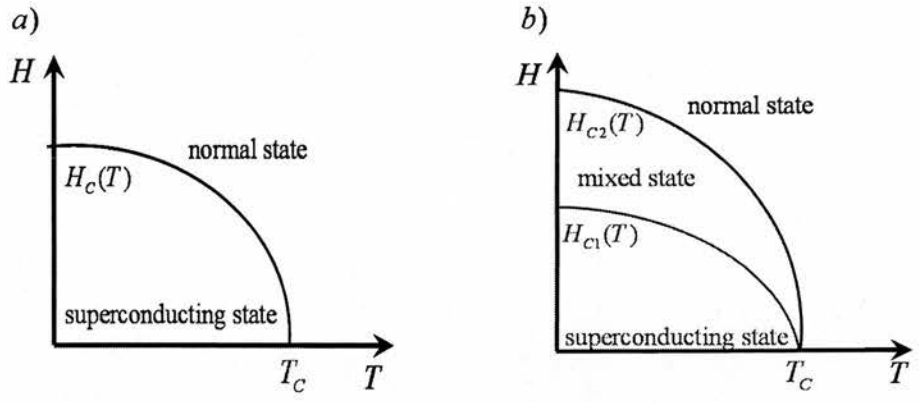

Figure 1.10: Temperature dependence of the thermodynamic states of superconductors a) Type I and b) Type II.

The Werthamer-Helfand-Hohenberg (WHH)[52] model is used, within this thesis, to predict the H_{c2} and slope of the H_{c2} at zero temperature. The WHH equation is given as

$$H_{c2}(0) = -0.693 T_c \left[dH_{c2} / dT \right]. \tag{1.28}$$

1.5.3 Pairing Symmetry

Superconductivity is an "ordered" state. The superconducting order parameter (OP), Δ, is a complex function with both amplitude and phase that describes the macroscopic quantum state of Cooper pairs.

The components of a Cooper pair have the same charge, but the amplitude can be either positive, so-called triplet state (where the electrons in the pair have the same spin; $Cu_xBi_2Se_3$ or single-layered Ruthenates), or negative, so-called singlet state (with electrons having different spin). Thus the amplitude of the Cooper pair bound state will be spin-spin interaction dependent and therefore have different angular momentum, l. The amplitude of the singlet state with $l = 0$ and $l = 2$ is known as *s*-wave and *d*-wave. The amplitude of the triplet state with $l = 1$ and $l = 3$ is known as *p*-wave and *f*-wave, respectively. The system is called *isotropic* if the amplitude of the Cooper pair does not change its sign through its phase component or *anisotropic* if it does. The variation in phase results in a presence of the "zeroes", so-called nodes.

The variation of the amplitude as a function of wavevector k can be probed using techniques as an Angle Resolved Photoemission Spectroscopy (ARPES), SQUID magnetometry (based on Josephson effect), or Nuclear Magnetic Resonance (NMR).[53-59] Using ARPES, an X-ray photon of known energy and wave vector excites an electron out of the surface of the superconductor. By measuring the energy E and parallel components of the wave vector (k_x, k_y) of the emitted electron one can deduce its initial energy and crystal momentum. By comparing the spectra as a function of temperature, one can map out the energy gap $2|\Delta_k|$ at any point on the Fermi Surface.[51]

1.6 Rare-Earth Transition Metal Oxyarsenides

High temperature superconductivity at 26 K was reported by Kamihara *et al.* in fluorine doped LaFeAsO[60]. This original family of iron-based superconductors is now referred to as the 1111 family, based on *RE*FeAsO (*RE* = rare earth metal) or *Ae*FeAsF (*Ae* = Ca, Sr, Ba). Following this discovery, superconductivity has been found in other systems including 122-type $AeFe_2As_2$ (*Ae* = Ca, Sr, Ba), 111-type *A*FeAs (*A* = Li, Na), 11-type $Fe_{1-\delta}Se$ with selenium rather than arsenic and $(Fe_2As_2)(Ae_4M_2O_6)$ (*Ae* = Sr, Ba; *M* = Sc, V, Cr, Mg, Ti), compounds with a perovskite block ($Ae_4M_2O_6$). The structures of the families of all materials are shown in Fig. 1.9. The common feature in these materials is the presence of a Fe_2As_2 (or Fe_2Se_2) plane with the principal difference being the spacer between layers.

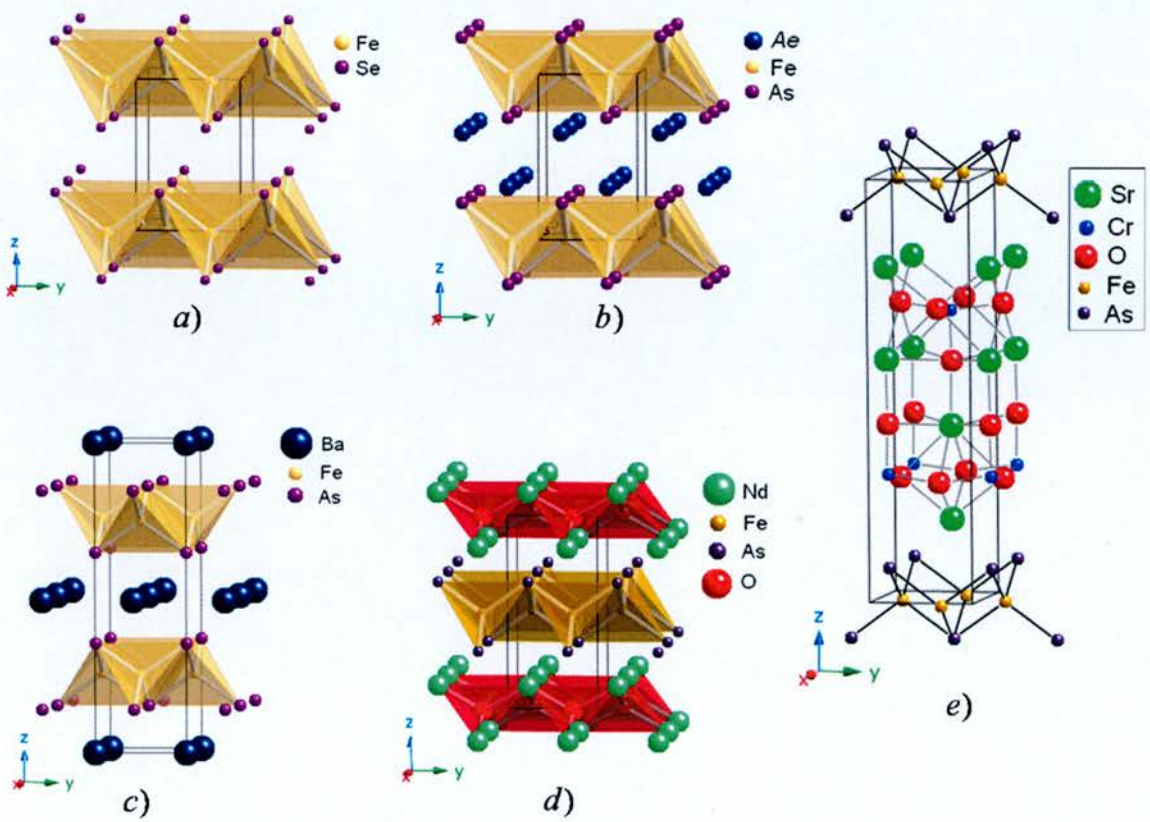

Figure 1.11: Crystal structure of the 11 (a), 111 (b), 122 (c), 1111 (d) and Sr_2CrO_3 (e) materials.

1.6.1 Crystal Structure

The structurally simplest compound is the 11-type, *FeSe* binary system. The structure consists of tetrahedral FeSe layers without any inter-layer atoms. Superconductivity in α-FeSe was first reported by Hsu *et al.*[13] by synthesis of α-$FeSe_{1-x}$ (x=0.03 to 0.12) when reached superconductivity with $T_c = 8$ K at $x = 0.88$. This binary system undergoes a structural transition from tetragonal to orthorhombic *Cmma* at ~ 70 K.[13]

A second family of iron-based superconductors labelled 111 family, independently reported by X.C.Wang et al.[61], S. Clarke et al,[11] and Tapp et al[12] is the *A*FeAs system. *A*FeAs crystallizes into a Cu_2Sb-type tetragonal structure containing a Fe_2As_2 layer with an average Fe^{2+} ion valence like those for 1111 and 122 parent compounds.[10, 11]

The ternary (122) iron-based superconductors,[8, 62] *Ae*Fe_2As_2, exhibit the tetragonal $ThCr_2Si_2$ crystal structure (space group *I4/mmm*). In the *$BaFe_2As_2$* system, the Ba is situated between the Fe_2As_2 planes, and the symmetry is changed from primitive tetragonal to body centred tetragonal (as shown in Fig. 1.9), thus providing a better coordination for Ba. On cooling, the undoped materials undergo a structural transition from tetragonal to orthorhombic *Fmmm*.[63, 64]

The Iron-based compounds with perovskite blocks in between the Fe_2As_2 layers adopt the tetragonal Sr_2GaO_3CuS-type structure (space group *P4/nmm*). The crystal structure of $(Fe_2As_2)(Sr_4Cr_2O_6)$ is shown in Fig. 1.9. No structural phase transition has been observed down to 6.5 K in any compounds with this structure.[65]

The 1111-type iron-based superconductors crystallize in the tetragonal ZrCuSiAs-type structure. These materials can be described with the electron precise formula $RE^{3+}Fe^{2+}As^{3-}O^{2-}$.[66, 67] The structure (Fig. 1.9) is a stacking of alternative positively charged anti-fluorite type layers (RE_2O_2) and negatively charged fluorite type layers (Fe_2As_2) along the c-axis. The *RE* atoms (having *4mm* site symmetry) are coordinated by four As atoms and four O atoms forming distorted square antiprisms. The Fe atoms (*42m*) form square nets perpendicular to c-axis, as depicted in Fig. 1.10. The layers are stacked in an AB-AB sequence. Bonding interactions between atoms of different electronegativities are responsible for a pronounced ionic character of these compounds.

All compounds are stabilized by electron transfer between the layers. The bonds within the transition metal layers have more covalent character than those inside the oxide layers. On cooling the system undergoes a structural phase transition from the tetragonal *P4/nmm* to orthorhombic *Cmma* space group, the so-called T → O structural transition. The relation between the tetragonal and orthorhombic structure is shown in Fig. 1.10. The T → O structural transition precedes the stripe antiferromagnetic (AFM) long range ordering on the iron moments on cooling.[68, 69]

Theoretical studies of these materials showed that the conductivity takes place in Fe_2As_2 layers while the RE_2O_2 layers act as charge reservoir.[26, 70] Based on this, the *RE*-As bond distance and the two-fold As-Fe-As angle (α) are suggested as two crucial parameters to be controlled to enhance superconductivity, i.e. increasing the T_c.[71] Thus systematic changes in the Fe-Fe and *RE*-As atomic distances have been induced by introducing an internal pressure into the TM_2As_2 and RE_2O_2 layers using chemical substitutions. It was found that the systematic replacement of *RE* in $REFeAsO_{1-y}$ (*RE* = La, Ce, Pr, Nd and Sm)[72] resulted in a gradual decrease in the a-axis lattice parameter and a corresponding increase in T_c. The highest T_c is obtained with regular tetrahedron (ie. $\alpha = \beta = 109.47$ °). In addition, Shirage et al. revealed that the a-axis length, corresponding to the distance between Fe atoms, has also a strong correlation with T_c in the 1111 systems.[72] A close-up of the Fe_2As_2 layer and illustration of the two-fold As-Fe-As angle is shown in Fig. 1.10.

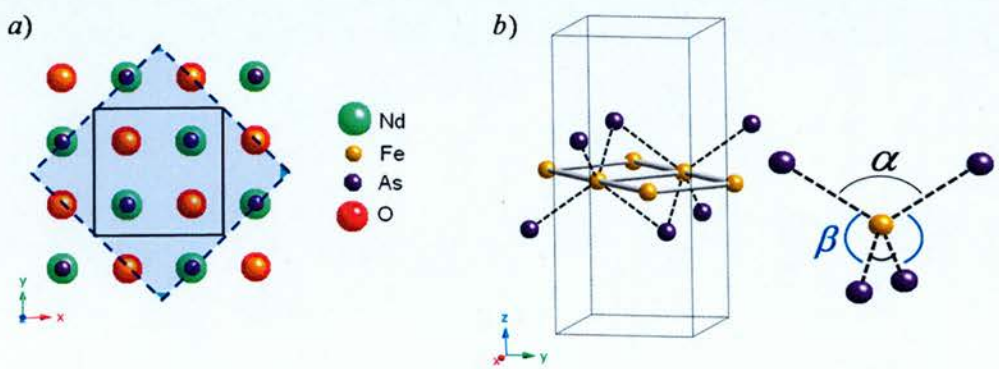

Figure 1.12: a) Top view of the crystal structure from c-direction. The inner square represents the unit cell in the tetragonal phase (*P4/nmm*). The outer square is that in the orthorhombic phase (*Cmma*). b) Schematic diagram of the Fe_2As_2 layer within the tetragonal unit cell and detailed $FeAs_4$ tetrahedron with two-fold (α) and four-fold (β) As-Fe-As angle.

1.6.2 Phase Diagrams

A determination of the structural and magnetic phase transitions in doped transition metal oxides is essential for understanding their electronic properties. For high-transition temperature (high-T_c) copper oxides, the parent compounds are antiferromagnetic (AFM) Mott insulators.[73] When mobile 'electrons' or 'holes' are doped into the parent compounds, the static long-range AFM order is rapidly suppressed and optimal superconductivity emerges after a complete suppression of the static AFM order.[74-76] Much like copper oxide superconductors, high-T_c superconductivity in the Fe-based systems *RE*FeAsO and $(Ba_{1-x}K_x)Fe_2As_2$ are also derived from either electron[7, 77-82] or hole[8, 83] doping of their semimetal parent compounds. The parent compound LaFeAsO also exhibits long range static AFM order that is suppressed upon electron doping to induce superconductivity.[84] The evidence for the interplay between magnetism and superconductivity (in the superconducting rare-earth transition metal oxyarsenides) is the presence of magnetism in the concentration dependent phase diagram. A determination of the structural, magnetic, and superconductivity phase diagram in one of the *RE*FeAsO systems will allow a direct comparison with the phase diagram of high-T_c copper oxides. Such a comparison is important because it might reveal whether the physics of high-T_c superconductivity in the Fe-based materials is fundamentally related to that of the high-T_c copper oxides.

1.6.2.1 1111 Materials

The first evidence for the importance of magnetism in the Fe-based superconductors was the concentration dependent phase diagram presented with the initial discovery of superconductivity in F-doped LaFeAsO.[84] It was soon shown that the undoped LaFeAsO parent compound exhibits spin-density wave (SDW) order below ~150 K consistent with a $\sqrt{2}\times\sqrt{2}\times 2$ unit cell. The low temperature structure was originally described by the monoclinic P112/n space group[68] but it was later clarified that the correct low temperature space group is the orthorhombic space group *Cmma*. The orthorhombic structure extends into the superconducting region and there is some evidence for overlapping magnetic order and superconductivity. It is shown that upon

doping there is competition between magnetism and superconductivity as the magnetically ordered state is destroyed in the fluorine doped superconducting samples.[85] The phase diagrams of REFeAsO$_{1-x}$F$_x$ (RE = La, Ce, Pr and Sm) as a function of doping were experimentally determined using the following techniques: μSR, ^{57}Fe Mossbauer spectroscopy and X-ray diffraction for RE = La[86]; neutron diffraction, resistivity and magnetisation for RE = Ce,[71] Pr[87]; μSR[88] and X-ray diffraction[78] for RE = Sm. A selection of phase diagrams[82] for the Fe-based superconductors are shown in Fig. 1.11.

In all cases (Fig. 1.11a-d), the parent compounds (x = 0) show a structural phase transition (T_{STR} ~150 K) and magnetic ordering with T_N ~140 K. A difference between materials with different RE is observed near the emergence of superconductivity. For REFeAsO with RE = La and Pr, the structural and magnetic transitions vanish in an abrupt step-like manner at the onset of superconductivity. For Ce, the magnetic transition appears to vanish continuously to very low temperatures and superconductivity emerges. This transition has some range of concentrations where superconductivity coexists with the phase transition. Finally, for Sm, both transitions are suppressed gradually and there appears to be overlap between the structural transition and superconductivity. Firstly it was believed that the destruction of the long-range magnetic ordering is a necessary condition for emergence of the superconductivity. However, in some cases the phase diagram shows a region where magnetic ordering coexists with superconductivity (RE = Sm).

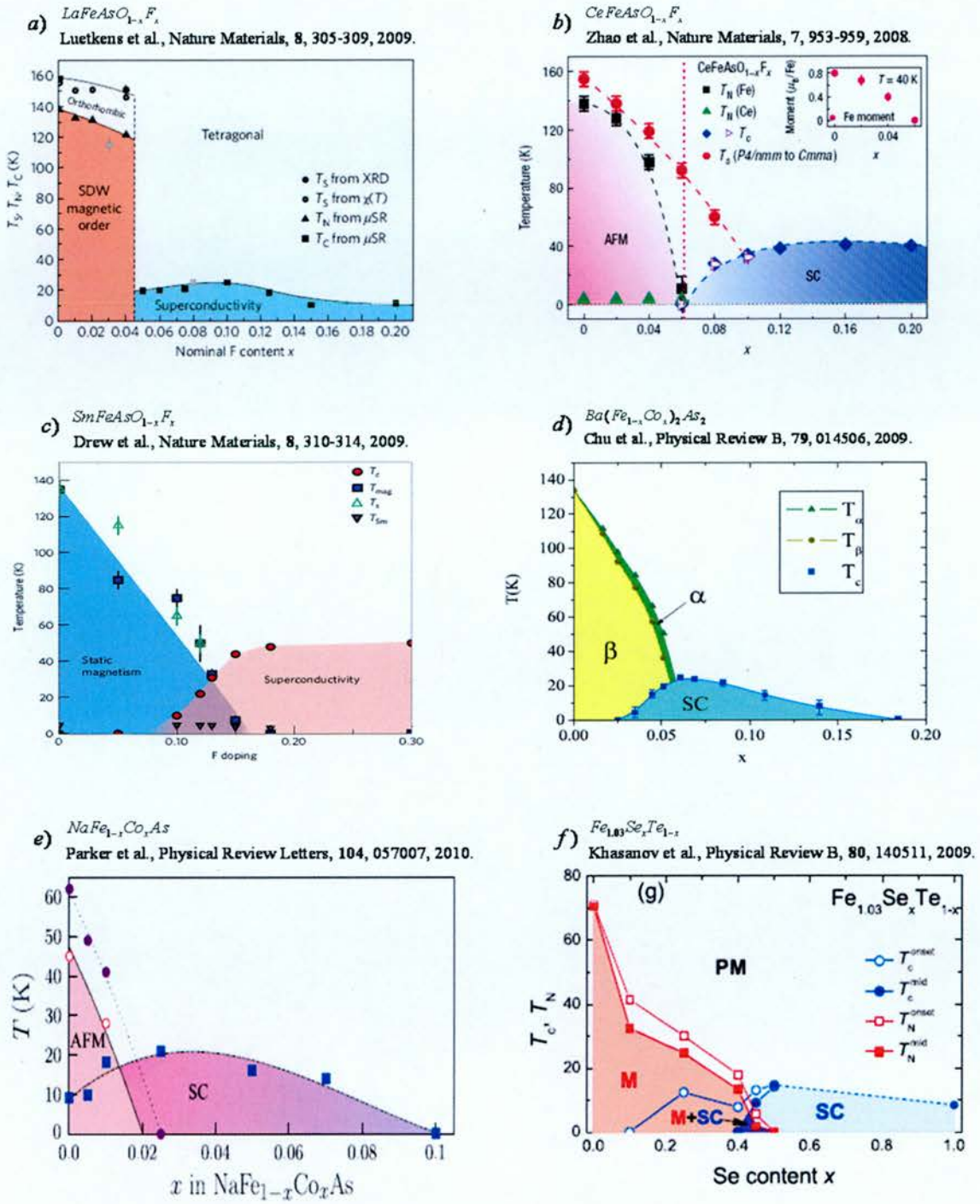

Figure 1.13: Experimentally determined phase diagram for a) $LaFeAsO_{1-x}F_x$,[86] b) $CeFeAsO_{1-x}F_x$,[71] c) $SmFeAsO_{1-x}F_x$,[88] d) $Ba(Fe_{1-x}Co_x)_2As_2$,[89] e) $NaFe_{1-x}Co_xAs$[90] and f) $Fe_{1.03}Se_xTe_{1-x}$.[91]

1.6.2.2 122 Materials

The basic behaviour of the 122-type superconducting materials can be described by considering the phase diagrams for $Ba_{1-x}K_xFe_2As_2$ and $BaFe_{2-x}Co_xAs_2$ (Fig 1.11d). As in the case of the 1111-type parent compounds, 122-type materials exhibit both a structural phase transition (from the room temperature tetragonal *I4/mmm* space group to the low temperature orthorhombic space group *Fmmm*)[8, 62, 92] and a magnetic transition to a long-range ordered, SDW state. However, unlike the 1111-type parent materials, the structural and magnetic phase transitions occur at the same temperature. Doping with either K[93] or Co[92, 94] causes a suppression of the structural and SDW transition. For Co doping, the two transitions no longer appear at the same temperature with the structural transition occurring first upon cooling. A region of phase coexistence of the superconducting and SDW states is observed. This observation raised the question whether the SDW and superconducting states are microscopically coexisting or phase separated. For hole doping with K, ^{75}As NMR[95], μSR[96] and magnetic force microscopy[96] indicate distinct regions which are magnetically ordered and nonmagnetic regions as expected for microscopic phase separation. In contrast, ^{57}Fe Mossbauer measurements indicate a sample which is completely magnetically ordered as expected with microscopic coexistence of the SDW and superconducting states.[97] For Cobalt doping, both ^{75}As NMR and μSR measurements indicate that all the Fe sites participate in the magnetic order as would be expected for the coexistence of SDW and superconductivity.[98] The neutron measurements on the Co doped samples showed that the magnetic Bragg peak intensity of the SDW state is suppressed on entering the superconducting state. This signals strong interaction between the superconducting and SDW states.[99, 100] Rotter et al. compared K and Co doping and concluded there is phase coexistence for the Co doped samples and separation in case of K doping.[97]

1.6.2.3 111 Materials

The *A*FeAs (*A* = Na, Li) materials were experimentally studied using the following techniques: μSR, X-ray diffraction, neutron diffraction, resistivity and magnetisation. All studies showed an extreme sensitivity of these materials to stoichiometry and

synthesis conditions. LiFeAs was reported to be a bulk superconductor in its undoped, stoichiometric form with no sign of a SDW.[61] On the other hand, NaFeAs displays evidence for the coexistence of superconductivity and magnetic ordering.[10] In this study reported by Parker et al., the magnetometry measurements revealed a superconducting behaviour with the onset of perfect diamagnetism below ~9 K. The μSR measurements showed that the magnetic order occurs throughout most of the NaFeAs volume below T_N ~42 K. Similar superconducting behaviour was observed and reported by Chu et al. in Na-deficient sample $Na_{0.9}FeAs$.[101] A comparison of the NaFeAs and $Na_{0.9}FeAs$ compositions suggests that the Na-deficient sample has a higher superconducting volume fraction, whilst the coexistence of magnetic and superconducting states is observed in the stoichiometric material. Recently $NaFe_{1-x}TM_xAs$ (TM = Co, Ni) were synthesised. [90] The highest T_c was observed for $NaFe_{0.975}Co_{0.025}As$ with T_c ~21 K, and for $NaFe_{0.975}Ni_{0.025}$ with T_c ~15 K, respectively. Moreover, high-resolution X-ray diffraction measurements revealed a structural phase transition (T ~ 40K) from tetragonal *P4/nmm* to orthorhombic *Cmma*, signalling the presence of AFM ordering. The coexistence of the AFM and superconducting states in the cobalt doped NaFeAs system was confirmed by μSR measurements.[90] The phase diagram for $NaFe_{1-x}Co_xAs$ is shown in Fig. 1.11e.

1.6.2.4 11 Materials

It has been clarified that the superconducting phase in the 11 family exists only in those samples prepared with intentional Se deficiency. All materials exhibit a SDW state at low concentrations. The superconductivity emerges when the SDW state is suppressed. Initial measurements of the $Fe_{1+y}Te_{1-x}Se_x$ compounds showed superconductivity with T_c up to 15 for x~0.5 existing for all values of x except very near x = 0 where superconductivity is destroyed. However, single crystal specific heat measurements indicate bulk superconductivity only for concentrations near x = 0.5 (Fig 1.11f). Moreover the phase diagram of systems grown with $Fe_{1.1}$ reveals an additional spin glass phase which coexists with superconductivity over much of the measured concentration range. This shows the sensitivity of these materials to stoichiometry and, in particular, the amount of excess Fe present. In a very recent development, a number

of intercalated FeSe compounds with a stoichiometric composition of $A_xFe_{2-y}Se_2$ (A = K, Rb, Cs, Tl) were made, raising the T_c up to ~30 K.

1.6.3 Magnetic Order

1.6.3.1 Iron Magnetic Order

At room temperature all undoped materials are paramagnetic metals with the electronic configuration Fe^{2+} d^6. Upon cooling, two possible types of magnetic ordering of the iron sublattice have been found; stripe antiferromagnetic ordering (SDW), and checkerboard magnetic ordering with spins aligned FM along one direction and AFM along the other. In checkerboard ordering, experiments find that the FM bonds are shorter then the AFM bonds.[102-104] The magnetic ordering in Fe_2As_2 layers is depicted in Fig. 1.12.

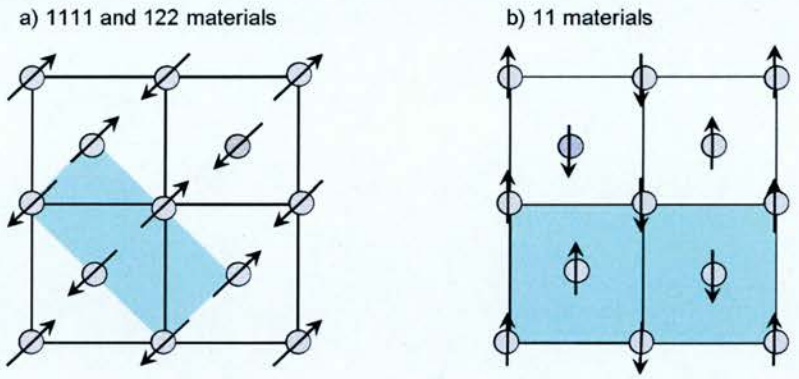

Figure 1.14: Illustration of observed a) SDW and b) checkerboard magnetic ordering in parent compounds. The shaded area indicates the magnetic unit cell.

The 1111 and 122 materials exhibit stripe like SDW below ~160 K (varies with composition). Stripe like character has been confirmed by low-temperature neutron diffraction experiments. The high temperature ($T > T_N$) paramagnetic state is characterized by a magnetic susceptibility with unusual linear temperature behaviour ($\chi \propto T$) and was dubbed as the "nematic" state.[105, 106] The SDW ordering is preceded by a $T \rightarrow O$ structural phase transition at a temperature slightly above the magnetic ordering temperature. The SDW is commensurate with the orthorhombic crystal

structure. The *a*-axis unit cell length becomes typically ~1% longer than that of the *b*-axis at temperature T_{STR}, just above (or at) the antiferromagnetic transition. In this unusual AFM state, each Fe atom along the *b*-axis has parallel spins, whereas those aligned along the *a*-axis is antiparallel. The observed SDW state is induced by Fermi surface nesting. In addition to this Fermi surface nesting scenario, it has been proposed that NN and NNN interactions between local Fe moments are both AFM and of comparable strength leading to magnetic frustration. DFT calculations based on a combination of Fermi surface nesting and superexchange interactions have been used to describe the relation between the structural and magnetic transitions in Fe-based compounds. The magnetic ordering is confirmed by neutron powder diffraction, μSR, NMR, and Mossbauer spectroscopy with an ordered Fe moments of ~ 0.2 - 0.8 μ_B.[48, 107, 108] Electronic structure calculations predicted a large iron moment of 1-2 μ_B. The discrepancies between the observed and the predicted Fe ordered moments have been explained using the previously mentioned "magnetic frustration picture". The SDW magnetic ordering for NdFeAsO and $BaFe_2As_2$ is depicted in Fig. 1.13.

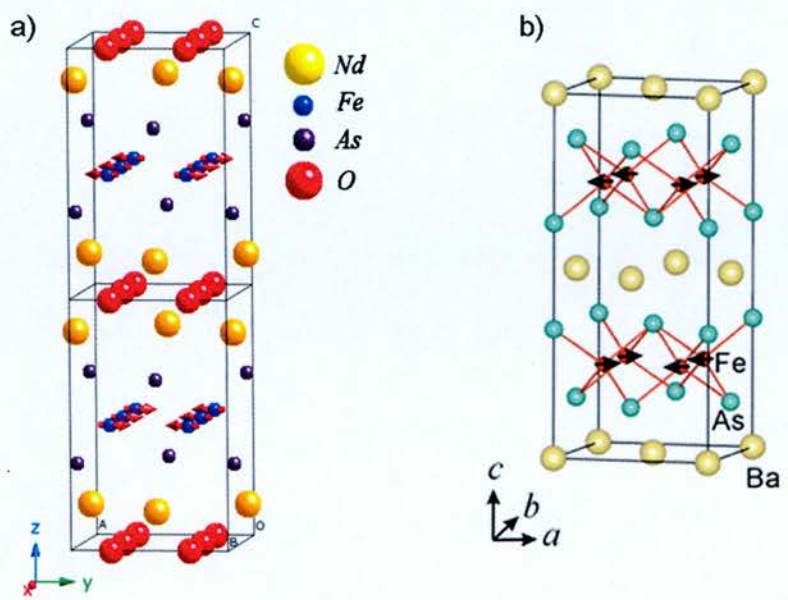

Figure 1.15: Stripe long-range antiferromagnetic ordering of Fe ions in the a) NdFeAsO and b) $BaFe_2As_2$.

1.6.3.2 Rare-Earth Magnetic Order

Compared to other *RE*-Fe systems, *e.g.* Rare-earth orthoferrites $REFeO_3$ or $REFe_{11}Ti$, no Fe spin reorientation was observed upon *RE* ordering. Static magnetic ordering of the *RE* moments in *RE*FeAsO were observed at low temperatures with $T_{N,RE} < 15$ K. The crystal structure remains orthorhombic. No doubling along *c* axis is required which signalises ferromagnetic coupling between planes. This suggests rather weak interplane coupling which is strongly influenced by the *RE* ion and associated with the induced structural changes.

For the parent materials with magnetic rare-earth ions (*RE* = Ce, Nd, Pr and Sm), the rare earth moments order at $T_{N,Ce} = 4.4$ K, $T_{N,Pr} = 11$ K; $T_{N,Sm} < 4.66$ K. For *RE* = Ce and Sm, the neutron and μSR data are consistent with a noncollinear *ab*-plane AFM order of the Ce and Sm moments. Noncollinear *RE* magnetic order arises due to a weak magnetic coupling of the adjacent *RE* planes in the *RE*-O-*RE* layers. For PrFeAsO, Pr moments order AFM along the c axis below 14 K,[109]. The Nd spins in NdFeAsO order at 2 K and form a collinear arrangement with AFM coupling along the orthorhombic b axis. Low temperature magnetic structure with ordered Fe and Nd spins is shown in Fig. 1.14.

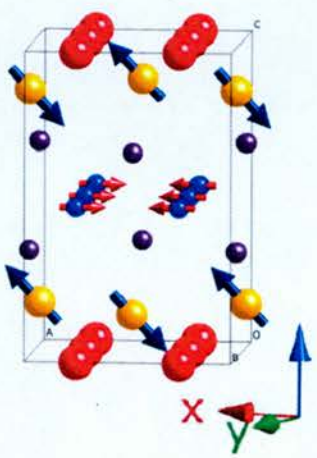

Figure 1.16: Low temperature magnetic structures for NdFeAsO.

1.6.4 Superconducting Properties

1.6.4.1 Chemical Doping

Both electron doping at the oxygen site and hole doping at the lanthanide site in LaFeAsO, was tried first. The T_c shows a trapezoidal dependence of F content with the highest temperature ~26 K in $LaFeAsO_{1-x}F_x$. Fluorine doping helps increase the electron density in the Fe_2As_2 layer. The lattice constants decrease systematically with nominal dopant concentration, indicating the inner chemical pressure. The distance between RE_2O_2 and Fe_2As_2 layers decrease prominently by F doping, suggesting that the electron doping enhances polarization and Coulomb interaction between the layers.[110]

Shortly after the discovery of the Fe-based superconductors, it was found that oxygen deficient samples are also superconducting. The $REFeAsO_{1-y}$ (RE = La, Gd, Sm, Nd, Pr, Ce) samples are prepared using hydrostatic pressure. The highest T_c was found in $SmFeAsO_{1-y}$ with T_c 55 K.[104, 110, 111] The crystal structure of $REFeAsO_{1-y}$ (RE = La, Nd) is modified compared with that of $REFeAsO$. The $FeAs_4$ coordination in $REFeAsO_{1-y}$ transforms into a regular tetrahedron with increasing oxygen deficiency, which is accompanied by an increase in T_c, and T_c reaches a maximum when the $FeAs_4$ lattice forms a regular tetrahedron. Electron doping has also been performed by replacing Fe by another transition metal such as Co, Rh, Ir, Pd, Ni, Ru and Mn in order to induce superconductivity in these materials.[6, 7, 89, 112, 113]

Hole doping was first tried using Ca^{2+} ions in LaFeAsO at the lanthanide site and did not result in superconductivity. On the other hand, strontium doping leads to superconductivity in $La_{1-x}Sr_xFeAsO$ (T_c = 25 K), $Nd_{1-x}Sr_xFeAsO$ (T_c = 13.5 K for x = 0.2) and $Pr_{1-x}Sr_xFeAsO$ (T_c = 16.3 K for x = 0.25). The thorium ion was also chosen as a good candidate for substitution at the rare earth site in order to achieve an even higher T_c. $Gd_{1-x}Th_xFeAsO$ displayed a T_c of 56 K, which was much higher than the F doped $GdFeAsO_{1-x}F_x$ sample.[114] Later, partial substitution of Tb^{3+} by Th^{4+} in TbFeAsO, resulted in superconductivity with a T_c of 50 K.[115]

Replacement of La by smaller *RE* leads to enhanced T_c. The substitution effect in REFeAsO$_{1-x}$F$_x$ with *RE* = Ce, Sm, Nd, Pr, Gd revealed that T_c increases to 41 K for Ce, 41-55 K for Sm, 50 K for Nd, 52 K for Pr and 36 K for Gd substitution. Rare earths with smaller ionic radii, decreased the lattice constants, thereby developing inner chemical pressure leading to higher T_c.[116] Summarizing, doping brings structural modifications such as a reduction in cell volume, a decrease in distance between layers, an increase in distance between RE^{3+} and F^- which enhances spin and charge density fluctuations.[117]

An oxygen-free 1111 material isostructural with the oxypnictide 1111 compounds was reported to be superconducting: The parent material *M*FeAsF (isostructural to LaFeAsO) becomes superconducting when Co is doped onto the Fe site in CaFe$_{1-x}$Co$_x$F with a T_c of 22 K at x = 0.1.[118] An alternative electron-doping method is to replace the divalent metal with a trivalent one as in Sr$_{1-x}$La$_x$FeAsF, which has a T_c of 29.5 K at x = 0.4.[119] These materials are very similar to the 1111-type oxypnictides with the same tetragonal to orthorhombic structural transition and SDW formation at lower temperatures. Both transition temperatures decrease with increasing doping. For CaFe$_{1-x}$Co$_x$F the orthorhombic structure extends into the superconducting region and there is some evidence for overlapping magnetic order and superconductivity in CaFe$_{0.94}$Co$_{0.06}$F, mesoscopic phase separation is cited as the explanation.[120]

1.6.4.2 Upper Critical Field

The upper critical field, H_{c2}, and the critical current density J_c, are the other (in addition to T_c) two important parameters to characterize superconductivity. H_{c2} is an intrinsic property of a type II superconducting material in which the resistive transition (ρ–T) width increases with increasing magnetic field, H. Usually, the H_{c2} of the sample can be measured from the resistive transition (ρ–T) analysis under different magnetic fields. According to the conventional BCS picture, H_{c2} is linear in T near T_c and saturates at the 0 K limit. The H_{c2} (0 K) can be calculated using the one band WHH formula (Eq. 1.28). Extrapolated values of H_{c2} using the WHH model for REFeAsO$_{1-x}$F$_x$ are 36 T for *RE* = La, 150 T for *RE* = Sm, 204 T for *RE* = Nd, 72 T for *RE* = Pr and 107 T for

RE = Ce.[110] The dependence of upper critical field versus temperature for various Fe-based superconductors is shown in Fig. 1.15.

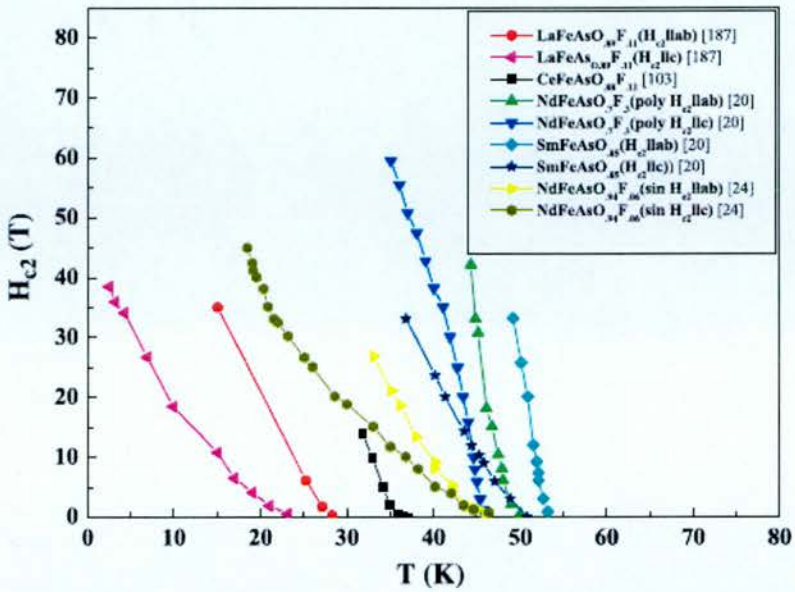

Figure 1.17: Temperature dependence of the in-plane (H_{c2}||ab) and out-of-plane (H_{c2}||c) upper critical field of polycrystalline (poly) and single crystal (sin) *RE*FeAsO$_{1-x}$F$_x$.[110]

1.6.4.3 Critical Temperature

Decreasing the RE^{3+} ionic size has a significant effect on the bands contributing to the Fermi surface. Since the electronically active part of these superconductors is the FeAs layer it is the structure of this which is of particular interest. Several connected parameters are quoted in the literature as definitive of the geometric state or distortion of this tetrahedral layer: Fe-Fe bond length, Fe-As distance and most important two-fold Fe-As-Fe angle, the so-called α-angle. Thus changes of T_c can be demonstrated by plotting T_c against the volume of the unit cell or the two-fold α-angle. In *RE*FeAsO$_{1-x}$F$_x$, prepared at ambient pressure, T_c increases from 28 K for *RE* = La to 53 K for *RE* = Nd. However, in the late *RE* ions, T_c remains constant or decreases. The same up-and-down trend in T_c was found upon applying hydrostatic pressure, where a strong lattice effect is evident at the start of the rare-earth series, as T_c rises from 26 K for LaFeAsO$_{1-x}$F$_x$ to 43 K under pressure.[84, 121] T_c reaches a constant maximum ~50–56 K in the *RE*FeAsO$_{1-x}$F$_x$ and *RE*FeAsO$_{1-\delta}$ series for *RE* = Pr to Gd,[82, 122-125] and decreases from 51 K for *RE* = Tb

to 36 K for $HoFeAsO_{0.9}F_{0.1}$, which has been synthesized under 10 GPa pressure.[117, 126] Variation of the two fold α angle, T_c for different $REFeAsO_{1-x}F_x$ is shown in Fig. 1.16.

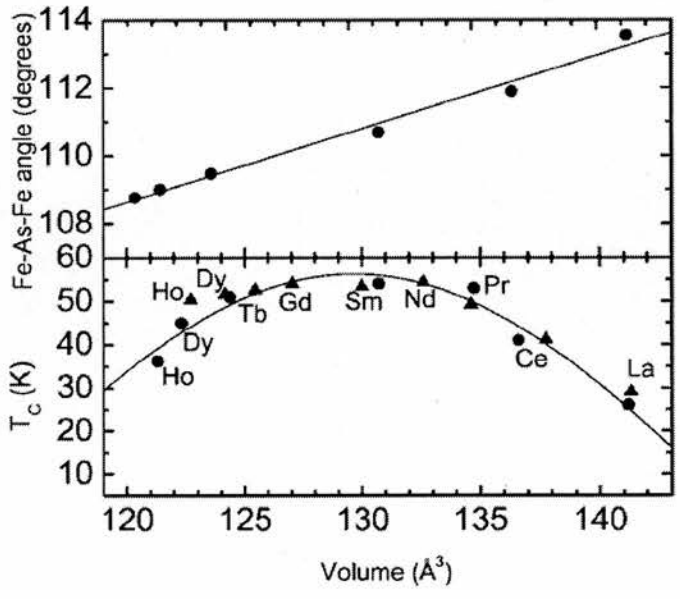

Figure 1.18: Variation in Fe-As-Fe angle (upper panel) and superconducting T_c (lower panel) with unit-cell volume for different $REFeAsO_{1-x}F_x$ (circles) and $RFeAsO_{1-\delta}$ (triangles).[127]

1.7 References

1 Y. Kamihara, T. Watanabe, M. Hirano, and H. Hosono, *Journal of the American Chemical Society* **130**, (11), 3296 (2008).

2 G. F. Chen, Z. Li, D. Wu, G. Li, W. Z. Hu, J. Dong, P. Zheng, J. L. Luo, and N. L. Wang, *Physical Review Letters* **100**, (24), 247002 (2008).

3 X. H. Chen, T. Wu, G. Wu, R. H. Liu, H. Chen, and D. F. Fang, *Nature* **453**, (7196), 761-762 (2008).

4 S. Matsuishi, Y. Inoue, T. Nomura, M. Hirano, and H. Hosono, *Journal of the Physical Society of Japan* **77**, (11), 113709 (2008).

5 S. Matsuishi, Y. Inoue, T. Nomura, H. Yanagi, M. Hirano, and H. Hosono, *Journal of the American Chemical Society* **130**, (44), 14428 (2008).

6 D. Kasinathan, A. Ormeci, K. Koch, U. Burkhardt, W. Schnelle, A. Leithe-Jasper, and H. Rosner, *New Journal of Physics* **11**, (2), 025023 (2009).

7 R. Nath, and et al., *Physical Review B* **79**, (17), 174513 (2009).

8 M. Rotter, M. Tegel, and D. Johrendt, *Physical Review Letters* **101**, (10), 107006-4 (2008).

9 A. S. Sefat, R. Jin, M. A. McGuire, B. C. Sales, D. J. Singh, and D. Mandrus, *Physical Review Letters* **101**, (11), 117004-4 (2008).

10 D. R. Parker, M. J. Pitcher, P. J. Baker, I. Franke, T. Lancaster, S. J. Blundell, and S. J. Clarke, *Chemical Communications*, (16), 2189-2191 (2009).

11 M. J. Pitcher, D. R. Parker, P. Adamson, S. J. C. Herkelrath, A. T. Boothroyd, R. M. Ibberson, M. Brunelli, and S. J. Clarke, *Chemical Communications*, (45), 5918-5920 (2008).

12 J. H. Tapp, Z. J. Tang, B. Lv, K. Sasmal, B. Lorenz, P. C. W. Chu, and A. M. Guloy, *Physical Review B* **78**, (6), 060505 (2008).

13 F.-C. Hsu, J.-Y. Luo, K.-W. Yeh, T.-K. Chen, T.-W. Huang, P. M. Wu, Y.-C. Lee, Y.-L. Huang, Y.-Y. Chu, D.-C. Yan, and M.-K. Wu, *Proceedings of the National Academy of Sciences* **105**, (38), 14262-14264 (2008).

14 G. F. Chen, Z. Li, G. Li, W. Z. Hu, J. Dong, J. Zhou, X. D. Zhang, P. Zheng, N. L. Wang, and J. L. Luo, *Chinese Physics Letters* **25**, (9), 3403-3405 (2008).

15 K. Sasmal, B. Lv, B. Lorenz, A. M. Guloy, F. Chen, Y. Y. Xue, and C. W. Chu, *Physical Review Letters* **101**, (10), 107007 (2008).

16 M. Rotter, M. Tegel, and D. Johrendt, *Physical Review Letters* **101**, (10), 107006 (2008).

17 S. Blundell, *Magnetism in Condensed Matter*. Oxford University Press Inc, New York: Oxford, 2001.

18 R. Arita, and H. Ikeda, *Journal of Physical Society of Japan* **78**, 113707 (2009).

19 J. J. Pulikkotil, M. v. Schilfgaarde, T. Kotani, and V. P. Antropov, *Superconductor Science and Technology* **23**, (5), 054012 (2010).

20 A. V. Chubukov, D. V. Efremov, and I. Eremin, *Physical Review B* **78**, (13), 134512 (2008).

21 K. Kuroki, H. Usui, S. Onari, R. Arita, and H. Aoki, *Physica C: Superconductivity* 470, (Supplement 1), S416-S417

22 S. Graser, T. A. Maier, P. J. Hirschfeld, and D. J. Scalapino, *New Journal of Physics* **11**, (2), 025016 (2009).

23 D. H. Lu, M. Yi, S. K. Mo, A. S. Erickson, J. Analytis, J. H. Chu, D. J. Singh, Z. Hussain, T. H. Geballe, I. R. Fisher, and Z. X. Shen, *Nature* **455**, (7209), 81-84 (2008).

24 P. A. Lee, and X.-G. Wen, *Physical Review B* **78**, (14), 144517 (2008).

25 M. D. Johannes, and I. I. Mazin, *Physical Review B* **79**, (22), 220510 (2009).

26 D. J. Singh, and M. H. Du, *Physical Review Letters* **100**, (23), 237003 (2008).

27 P. Hansmann, R. Arita, A. Toschi, S. Sakai, G. Sangiovanni, and K. Held, *Physical Review Letters* **104**, (19), 197002 (2010).

28 C.-C. Lee, W.-G. Yin, and W. Ku, *Physical Review Letters* **103**, (26), 267001 (2009).

29 L. N. Brillouin, in *Physics*, University of Paris: Paris, 1920; Vol. Doctor.

30 J. R. Hook, *Solid State Physic*. John Wiley&Sons, ltd: 2000.

31 M. T. Weller, *Inorganic Material Chemistry*. Oxford University Press: 2004; p 50-55.

32 A. R. West, *Basic Solid State Chemistry*. John Wiley&Sons, ltd: 1999; p 373-381.

33 P. W. Anderson, *Physical Review* **79**, (2), 350 (1950).

34 J. B. Goodenough, A. Wold, R. J. Arnott, and N. Menyuk, *Physical Review* **124**, (2), 373 (1961).

35 J. Kanamori, *Journal of Physics and Chemistry of Solids* **10**, (2-3), 87-98 (1959).

36 I. Dzyaloshinsky, *Journal of Physics and Chemistry of Solids* **4**, (4), 241-255 (1958).

37 T. Moriya, *Physical Review* **120**, (1), 91 (1960).

38 T. Moriya, *Physical Review Letters* **4**, (5), 228 (1960).

39 E. C. Stoner, in, 1938; Vol. 165, pp 372-414.

40 M. A. Ruderman, and C. Kittel, *Physical Review* **96**, (1), 99 (1954).

41 K. Yosida, *Physical Review* **106**, (5), 893 (1957).

42 J. Singleton, *Band Theory and Electronic Properties of Solids*. Oxfrod University Press Inc.: New York, 2001.

43 E. Manousakis, J. Ren, S. Meng, and E. Kaxiras, *Solid State Communications* 150, 62 (2010).

44 H. Ikeda, R. Arita, and J. Kunescaron, *Physical Review B* **82**, (2), 024508 (2010).

45 J. Kondo, *Progress of Theoretical Physics* **32**, (1), 37-49 (1964).

46 J. Kondo, *Physical Review* **169**, (2), 437 (1968).

47 L. Pourovskii, V. Vildosola, S. Biermann, and A. Georges, *EPL (Europhysics Letters)* **84**, (3), 37006 (2008).

48 E. M. Bruening, C. Krellner, M. Baenitz, A. Jesche, F. Steglich, and C. Geibel, *Physical Review Letters* **101**, (11), 117206 (2008).

49 J. Bardeen, L. N. Cooper, and J. R. Schrieffer, *Physical Review* **108**, (5), 1175 (1957).

50 J. Bardeen, L. N. Cooper, and J. R. Schrieffer, *Physical Review* **106**, (1), 162 (1957).

51 J. F. Annett, *Superconductivity, Superfluids and Condensates*. Oxford University Press Inc.: New York, 2004.

52 N. R. Werthamer, E. Helfand, and P. C. Hohenberg, *Physical Review* **147**, (1), 295 (1966).

53 T. Dong, Z. G. Chen, R. H. Yuan, B. F. Hu, B. Cheng, and N. L. Wang, *Physical Review B* 82, (5), 054522

54 A. J. Drew, F. L. Pratt, T. Lancaster, S. J. Blundell, P. J. Baker, R. H. Liu, G. Wu, X. H. Chen, I. Watanabe, V. K. Malik, A. Dubroka, K. W. Kimouml, M. Hessle, and C. Bernhard, *Physical Review Letters* 101, (9), 097010 (2008).

55 K. Hashimoto, T. Shibauchi, T. Kato, K. Ikada, R. Okazaki, H. Shishido, M. Ishikado, H. Kito, A. Iyo, H. Eisaki, S. Shamoto, and Y. Matsuda, *Physical Review Letters* **102**, (1), 017002 (2009).

56 M. L. Teague, G. K. Drayna, G. P. Lockhart, P. Cheng, B. Shen, H. H. Wen, and N. C. Yeh, *Physical Review Letters* **106**, (8), 087004

57 C. J. van der Beek, G. Rizza, M. Konczykowski, P. Fertey, I. Monnet, T. Klein, R. Okazaki, M. Ishikado, H. Kito, A. Iyo, H. Eisaki, S. Shamoto, M. E. Tillman, S. L. Bud'ko, P. C. Canfield, T. Shibauchi, and Y. Matsuda, *Physical Review B* 81, (17), 174517

58 T. Yokoyama, Y. Tanaka, and A. A. Golubov, *Physical Review B* **78**, (1), 012508 (2008).

59 F. Hunte, J. Jaroszynski, A. Gurevich, D. C. Larbalestier, R. Jin, A. S. Sefat, M. A. McGuire, B. C. Sales, D. K. Christen, and D. Mandrus, *Nature* **453**, (7197), 903-905 (2008).

60 Y. Kamihara, M. Hirano, H. Yanagi, T. Kamiya, Y. Saitoh, E. Ikenaga, K. Kobayashi, and H. Hosono, *Physical Review B* **77**, (21), 214515 (2008).

61 X. C. Wang, Q. Q. Liu, Y. X. Lv, W. B. Gao, L. X. Yang, R. C. Yu, F. Y. Li, and C. Q. Jin, *Solid State Communications* **148**, (11-12), 538-540 (2008).

62 M. Rotter, M. Tegel, D. Johrendt, I. Schellenberg, W. Hermes, and R. Pottgen, *Physical Review B (Condensed Matter and Materials Physics)* **78**, (2), 020503-4 (2008).

63 R. Cortes-Gil, and S. J. Clarke, *Chemistry of Materials* **23**, (4), 1009-1016 (2011).

64 R. Cortes-Gil, D. R. Parker, M. J. Pitcher, J. Hadermann, and S. J. Clarke, *Chemistry of Materials* **22**, (14), 4304-4311 (2010).

65 M. Tegel, F. Hummel, Y. Su, T. Chatterji, M. Brunelli, and D. Johrendt, *Europhysics Letters* **89**, (3), 37006 (2010).

66 P. Quebe, L. J. Terbüchte, and W. Jeitschko, *Journal of Alloys and Compounds* **302**, (1-2), 70-74 (2000).

67 R. Poettgen, and D. Johrendt, *Zeitschrift fur Naturforscung B* **63**, (10), 1135-1148 (2008).

68 C. de la Cruz, Q. Huang, J. W. Lynn, J. Li, W. R. Ii, J. L. Zarestky, H. A. Mook, G. F. Chen, J. L. Luo, N. L. Wang, and P. Dai, *Nature* **453**, (7197), 899-902 (2008).

69 Y. Chen, J. W. Lynn, J. Li, G. Li, G. F. Chen, J. L. Luo, N. L. Wang, P. Dai, C. dela Cruz, and H. A. Mook, *Physical Review B (Condensed Matter and Materials Physics)* **78**, (6), 064515-5 (2008).

70 S. Ishibashi, K. Terakura, and H. Hoson, *Journal of the Physical Society of Japan* **77**, (5), 4 (2008).

71 J. Zhao, Q. Huang, C. de la Cruz, S. Li, J. W. Lynn, Y. Chen, M. A. Green, G. F. Chen, G. Li, Z. Li, J. L. Luo, N. L. Wang, and P. Dai, *Nat Mater* **7**, (12), 953-959 (2008).

72 P. M. Shirage, K. Miyazawa, H. Kito, H. Eisaki, and A. Iyo, *Physical Review B* **78**, (17), 172503 (2008).

73 P. A. Lee, N. Nagaosa, and X.-G. Wen, *Reviews of Modern Physics* **78**, (1), 17 (2006).

74 R. J. Birgeneau, C. Stock, J. M. Tranquada, and K. Yamada, *Journal of the Physical Society of Japan* **75**, (11), 111003 (2006).

75 M. Fujita, T. Kubo, S. Kuroshima, T. Uefuji, K. Kawashima, K. Yamada, I. Watanabe, and K. Nagamine, *Physical Review B* **67**, (1), 014514 (2003).

76 W. Yu, J. S. Higgins, P. Bach, and R. L. Greene, *Physical Review B* **76**, (2), 020503 (2007).

77 K. Pradeep, A. Kumar, S. Saha, D. V. S. Muthu, J. Prakash, U. V. Waghmare, A. K. Ganguli, and A. K. Sood, *Journal of Physics: Condensed Matter* **22**, (25), 255402 (2010).

78 S. Margadonna, Y. Takabayashi, M. T. McDonald, M. Brunelli, G. Wu, R. H. Liu, X. H. Chen, and K. Prassides, *Physical Review B (Condensed Matter and Materials Physics)* **79**, (1), 014503-7 (2009).

79 Y. Qi, Z. Gao, L. Wang, D. Wang, X. Zhang, and Y. Ma, *Superconductor Science and Technology* **21**, (11), 115016 (2008).

80 F. Ronning, N. Kurita, E. D. Bauer, B. L. Scott, T. Park, T. Klimczuk, R. Movshovich, and J. D. Thompson, *Journal of Physics: Condensed Matter* **20**, (34), 342203 (2008).

81 A. S. Sefat, D. J. Singh, R. Jin, M. A. McGuire, B. C. Sales, F. Ronning, and D. Mandrus, *Physica C: Superconductivity* **469**, (9-12), 350-354 (2009).

82 R. H. Liu, and et al., *Phys. Rev. Lett.* **101**, (8), 087001 (2008).

83 K. Sasmal, B. Lv, B. Lorenz, A. M. Guloy, F. Chen, Y.-Y. Xue, and C.-W. Chu, *Physical Review Letters* **101**, (10), 107007-4 (2008).

84 W. T. H. M. a. H. H. Kamihara Y, *J. Am. Chem. Soc.* **130**, (11), 3296 (2008).

85 M. A. McGuire, A. D. Christianson, A. S. Sefat, B. C. Sales, M. D. Lumsden, R. Jin, E. A. Payzant, D. Mandrus, Y. Luan, V. Keppens, V. Varadarajan, J. W. Brill, R. Hermann, euml, P. l, M. T. Sougrati, F. Grandjean, and G. J. Long, *Physical Review B* 78, (9), 094517 (2008).

86 H. Luetkens, H. H. Klauss, M. Kraken, F. J. Litterst, T. Dellmann, R. Klingeler, C. Hess, R. Khasanov, A. Amato, C. Baines, M. Kosmala, O. J. Schumann, M. Braden, J. Hamann-Borrero, N. Leps, A. Kondrat, G. Behr, J. Werner, and B. Buchner, *Nat Mater* **8**, (4), 305-309 (2009).

87 C. R. Rotundu, D. T. Keane, B. Freelon, S. D. Wilson, A. Kim, P. N. Valdivia, E. Bourret-Courchesne, and R. J. Birgeneau, *Physical Review B* **80**, (14), 144517 (2009).

88 A. J. Drew, C. Niedermayer, P. J. Baker, F. L. Pratt, S. J. Blundell, T. Lancaster, R. H. Liu, G. Wu, X. H. Chen, I. Watanabe, V. K. Malik, A. Dubroka, M. Rossle, K. W. Kim, C. Baines, and C. Bernhard, *Nat Mater* **8**, (4), 310-314 (2009).

89 J.-H. Chu, J. G. Analytis, C. Kucharczyk, and I. R. Fisher, *Physical Review B (Condensed Matter and Materials Physics)* **79**, (1), 014506-6 (2009).

90 D. R. Parker, M. J. P. Smith, T. Lancaster, A. J. Steele, I. Franke, P. J. Baker, F. L. Pratt, M. J. Pitcher, S. J. Blundell, and S. J. Clarke, *Physical Review Letters* **104**, (5), 057007

91 R. Khasanov, M. Bendele, A. Amato, P. Babkevich, A. T. Boothroyd, A. Cervellino, K. Conder, S. N. Gvasaliya, H. Keller, H. H. Klauss, H. Luetkens, V. Pomjakushin, E. Pomjakushina, and B. Roessli, *Physical Review B* **80**, (14), 140511 (2009).

92 Q. Huang, Y. Qiu, W. Bao, M. A. Green, J. W. Lynn, Y. C. Gasparovic, T. Wu, G. Wu, and X. H. Chen, *Physical Review Letters* **101**, (25), 257003 (2008).

93 M. Rotter, M. Tegel, and D. Johrendt, *Physical Review Letters* **101**, (10), 107006 (2008).

94 N. Ni, M. E. Tillman, J. Q. Yan, A. Kracher, S. T. Hannahs, S. L. Bud'ko, and P. C. Canfield, *Physical Review B* **78**, (21), 214515 (2008).

95 H. Fukazawa, T. Yamazaki, K. Kondo, Y. Kohori, N. Takeshita, P. M. Shirage, K. Kihou, K. Miyazawa, K. Kito, H. Eisaki, and A. Iyo, *Journal of the Physical Society of Japan* **78**, 033704 (2009).

96 J. T. Park, D. S. Inosov, C. Niedermayer, G. L. Sun, D. Haug, N. B. Christensen, R. Dinnebier, A. V. Boris, A. J. Drew, L. Schulz, T. Shapoval, U. Wolff, V. Neu, X. Yang, C. T. Lin, B. Keimer, and V. Hinkov, *Physical Review Letters* **102**, (11), 117006 (2009).

97 M. Rotter, M. Tegel, I. Schellenberg, F. M. Schappacher, R. Poettgen, J. Deisenhofer, A. Guenther, F. Schrettle, A. Loidl, and D. Johrendt, *New Journal of Physics* **11**, (2), 025014 (2009).

98 C. Bernhard, A. J. Drew, L. Schulz, V. K. Malik, M. Roessle, C. Niedermayer, T. Wolf, G. D. Varma, G. Mu, H.-H. Wen, H. Liu, G. Wu, and X. H. Chen, *New Journal of Physics* **11**, (5), 055050 (2009).

99 A. D. Christianson, M. D. Lumsden, S. E. Nagler, G. J. MacDougall, M. A. McGuire, A. S. Sefat, R. Jin, B. C. Sales, and D. Mandrus, *Physical Review Letters* **103**, (8), 087002 (2009).

100 D. K. Pratt, W. Tian, A. Kreyssig, J. L. Zarestky, S. Nandi, N. Ni, S. L. Bud'ko, P. C. Canfield, A. I. Goldman, and R. J. McQueeney, *Physical Review Letters* **103**, (8), 087001 (2009).

101 C. W. Chu, F. Chen, M. Gooch, A. M. Guloy, B. Lorenz, B. Lv, K. Sasmal, Z. J. Tang, J. T. Tapp, and Y. Y. Xue, *arXiv:0902.0806v1*, (2009).

102 J. Paglione, and R. L. Greene, *Nature Physics* **6**, (9), 645-658 (2010).

103 I. I. Mazin, and J. Schmalian, *Physica C: Superconductivity* **469**, (9-12), 614-627 (2009).

104 Z.-A. Ren, G.-C. Che, X.-L. Dong, J. Yang, W. Lu, W. Yi, X.-L. Shen, Z.-C. Li, L.-L. Sun, F. Zhou, and Z.-X. Zhao, *EPL (Europhysics Letters)* **83**, (1), 17002 (2008).

105 C. Fang, H. Yao, W.-F. Tsai, J. Hu, and S. A. Kivelson, *Physical Review B* **77**, (22), 224509 (2008).

106 T. M. Chuang, M. P. Allan, J. Lee, Y. Xie, N. Ni, S. L. Budko, G. S. Boebinger, P. C. Canfield, and J. C. Davis, *Science* **327**, (5962), 181-184 (2010).

107 I. Pallecchi, C. Fanciulli, M. Tropeano, A. Palenzona, M. Ferretti, A. Malagoli, A. Martinelli, I. Sheikin, M. Putti, and C. Ferdeghini, *Physical Review B* **79**, (10), 104515 (2009).

108 A. Iadecola, S. Agrestini, M. Filippi, L. Simonelli, M. Fratini, B. Joseph, D. Mahajan, and N. L. Saini, *EPL (Europhysics Letters)* **87**, (2), 26005 (2009).

109 S. A. J. Kimber, D. N. Argyriou, F. Yokaichiya, K. Habicht, S. Gerischer, T. Hansen, T. Chatterji, R. Klingeler, C. Hess, G. Behr, A. Kondrat, uuml, and B. chner, *Physical Review B* **78**, (14), 140503 (2008).

110 P. M. Aswathy, J. B. Anooja, P. M. Sarun, and U. Syamaprasad, *Superconductor Science and Technology* **23**, (7), 073001 (2010).

111 J. Yang, Z. C. Li, W. Lu, W. Yi, X. L. Shen, Z.-A. Ren, G. C. Chen, X. L. Dong, L. L. Sun, F. Zhou, and Z. X. Zhao, *Superconductor Science and Technology* **21**, (8), 082001 (2008).

112 E. D. Bauer, F. Ronning, B. L. Scott, and J. D. Thompson, *Physical Review B (Condensed Matter and Materials Physics)* **78**, (17), 172504 (2008).

113 C. Guanghan, J. Shuai, L. Xiao, W. Cao, L. Yuke, R. Zhi, T. Qian, F. Chunmu, D. Jianhui, X. Zhu'an, and Z. Fu-Chun, *Physical Review B (Condensed Matter and Materials Physics)* **79**, (17), 174505 (2009).

114 C. Wang, L. Li, S. Chi, Z. Zhu, Z. Ren, Y. Li, Y. Wang, X. Lin, Y. Luo, S. Jiang, X. Xu, G. Cao, and Z. a. Xu, *EPL (Europhysics Letters)* **83**, (6), 67006 (2008).

115 Z. Li, G. Chen, J. Dong, G. Li, W. Hu, D. Wu, S. Su, P. Zheng, T. Xiang, N. Wang, and J. Luo, *Physical Review B (Condensed Matter and Materials Physics)* **78**, (6), 060504-4 (2008).

116 J.-W. G. Bos, G. B. S. Penny, J. A. Rodgers, D. A. Sokolov, A. D. Huxley, and J. P. Attfield, *Chemical Communications*, (31), 3634-3635 (2008).

117 J. A. Rodgers, G. B. S. Penny, A. Marcinkova, J.-W. G. Bos, D. A. Sokolov, A. Kusmartseva, A. D. Huxley, and J. P. Attfield, *Physical Review B* **80**, (5), 052508 (2009).

118 S. Matsuishi, Y. Inoue, T. Nomura, H. Yanagi, M. Hirano, and H. Hosono, *Journal of the American Chemical Society* **130**, (44), 14428-14429 (2008).

119 X. Zhu, F. Han, P. Cheng, G. Mu, B. Shen, L. Fang, and H.-H. Wen, *EPL (Europhysics Letters)* **85**, (1), 17011 (2009).

120 S. Matsuishi, Y. Inoue, T. Nomura, M. Hirano, and H. Hosono, *Journal of the Physical Society of Japan* **77**, (11), 113709 (2008).

121 H. Takahashi, K. Igawa, K. Arii, Y. Kamihara, M. Hirano, and H. Hosono, *Nature* **453**, (7193), 376-378 (2008).

122 Z. A. Ren, J. Yang, W. Lu, G. C. Che, X. L. Dong, L. L. Sun, and Z. X. Zhao, *Materials Research Innovations* **12**, 105-106 (2008).

123 Z.-A. Ren, J. Yang, W. Lu, W. Yi, X.-L. Shen, Z.-C. Li, G.-C. Che, X.-L. Dong, L.-L. Sun, F. Zhou, and Z.-X. Zhao, *EPL (Europhysics Letters)* **82**, (5), 57002 (2008).

124 X. H. Chen, T. Wu, G. Wu, R. H. Liu, H. Chen, and D. F. Fang, *Nature* **453**, (7196), 761-762 (2008).

125 Z. A. Ren, and et al., *Chin. Phys. Lett.* **25**, (6), 2215 (2008).

126 J.-W. G. Bos, G. B. S. Penny, J. A. Rodgers, D. A. Sokolov, A. D. Huxley, and J. P. Attfield, *Chemical Communications* **31**, 3634 (2008).

127 J. P. Attfield, *Journal of Materials Chemistry* 21, (13), 4756-4764 (2011).

CHAPTER 2

Experimental Techniques

This research is primarily concerned with the structural, magnetic and superconducting (SC) properties of 1111-type transition metal oxyarsenides. Initial phase analysis of all prepared materials was done using laboratory powder X-ray diffraction on a Bruker D8 AXS diffractometer. Variable temperature structural studies were done at the European Synchrotron Radiation Facility (ESRF) in Grenoble using the high-resolution synchrotron powder diffraction beamline ID31. Thus the X-ray scattering theory, techniques used, and X-ray data analysis are described within sections 2.1-2.3. In order to describe the magnetism and the magnetic interactions in the 1111-type transition metal oxyarsenides, neutron scattering experiments have been performed. The Rietveld refined magnetic moments give information about the nature and occupancy of the *d*-orbitals and *f*-orbitals. Neutron diffraction studies were carried out using the high-resolution neutron powder diffractometer D2B and the high-intensity two-axis neutron diffractometer D20 at Institute Laue Langevin (ILL) in Grenoble, France. The neutron powder diffraction (NPD) study of NdNiAsO was preformed using the WISH time-of-flight (TOF) neutron powder diffractometer at ISIS, Rutherford Appleton laboratories, Didcot, UK. The theory of neutron scattering and the neutron diffractometers used are explained in sections 2.4 and 2.5. The structural and magnetic data obtained from scattering experiments has been complemented with property measurements carried out using a Quantum Design Magnetic Property Measurement System (MPMS) and Quantum Design Physical Property Measurement System (PPMS). In addition the SARA*h* and GSAS programmes are described within this chapter.

2.1 X-ray Diffraction

Powder diffraction by X-rays is one of the most powerful and widely used techniques available to material scientists. An excellent description of the function of synchrotron

light sources, as well as scattering theory for x-rays, may be found in the books by J. Als-Nielsen and D. McMorrow[1] or by R. E. Dinnebier and S. J. Billinge.[2]

2.1.1 X-ray Diffraction Theory

All crystalline solids consist of a three-dimensional periodic array of atoms. One of the most important techniques for probing the crystalline structure is diffraction. If an incident beam of radiation, with wavelength comparable to the inter-atomic spacing of the lattice, hits a crystalline sample, the atoms in the sample act as scattering centers and can reflect the radiation. If we consider two planes within the crystalline sample to be separated by a distance, d, it is clear that two beams reflected by adjacent planes at D and B will have a path difference of AB + BC = $2dsin\theta$, where θ represents the angle made between the incident beam and the plane (Fig. 2.1).

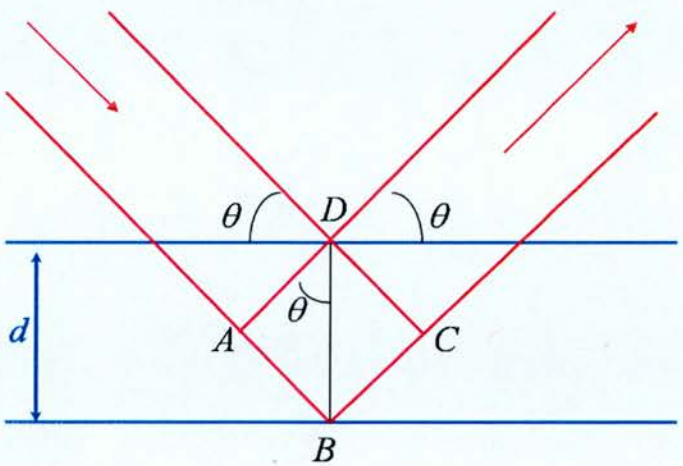

Figure 2.1: Reflection of X-rays from two lattice planes belonging to the family of lattice planes with indices *h,k,l*. d is the planar spacing.

If the path difference between two reflected beams is an integral numbers of wavelengths, constructive interference is observed. This is described by Bragg's law:

$$2d\sin\theta = n\lambda \tag{2.10.}$$

An extension of Bragg's Law, used to relate the atomic planes described above to the lattice parameters of the unit cell of a given crystalline solid, involves the use of Miller indices. The Miller indices of a plane are given by the ratios $h = a/x, k = b/y,\ l = c/z$, where a, b and c are the lattice parameters of the unit cell and x, y and z are the points at which that plane intersects the crystallographic axis. They are commonly written *(hkl)*. The distance between a family of *(hkl)* planes, *d(hkl)*, can now be considered in the Bragg equation:

$$2d_{hkl}\sin\theta = \lambda \tag{2.11}$$

The d-spacing for the tetragonal lattice can be given as:

$$\frac{1}{d} = \frac{h^2 + k^2}{a^2} + \frac{l^2}{c^2} \tag{2.12}$$

The lattice parameters a and c can be calculated using:

$$\frac{4\sin^2\theta}{\lambda^2} = \frac{h^2 + k^2}{a^2} + \frac{l^2}{c^2} \tag{2.13}$$

The positions of Bragg reflections thus allow the determination of the dimension of the unit cell. However, in order to describe the crystal structure fully (determine atomic positions) we must measure the reflection intensities. The measured intensity of the Bragg reflection I_{hkl} is proportional to the square of the structure factor F_{hkl} and because the atoms in the solid do not interact with radiation to the same extent, and to take account of this, we introduce an atomic scattering factor, f_j, to describe this interaction for an every atom j. Due to the scattering factor f_j, a structure factor F_{hkl} can be given as:

$$F_{hkl} = \sum_{j=1}^{N} f_j \exp\left[2\pi i(hx_j + ky_j + lz_j)\right]\exp\left[-W_j(\sin^2\theta)/\lambda^2\right] \tag{2.14}$$

Where x_j, y_j, and z_j are the fractional coordinates of an atom j; and $\left[-W_j(\sin^2\theta)/\lambda^2\right]$ is the Debye - Waller factor which is used to account for the thermal motion (which increases with temperature) of atoms in the solid. B_j is the atomic temperature factor of atom j, and is related to the mean squared thermal displacement factor, U_j, by the formula $B = 8\pi^2 U$. The intensity of a particular reflection *(hkl)* is then given: $\left|F_{hkl}^2\right|$.[2-4]

When the magnitude of the X-ray energy coincides with the magnitude of the binding energy of the electrons in the atom, the scattering process is affected by the possible absorption of the photon and subsequent ejection of the electron. This leads to a rise in the X-ray absorption with increasing photon energy at each of the electron binding energies (absorption edges). The result is a shift in the phase between the incident wave and the scattered wave. This phase shift creates an imaginary component (f') to the atomic scattering factor as well as a modification of the real part (f''). Therefore the scattering factor f_j is described as;

$$f_j = f_0 + f' + f'' \tag{2.15}$$

Where f_0 is an atomic constant corrected for valence charge; f' and f'' are tabulated for the commonly used characteristic X-ray wavelengths.

All samples synthesized and studied within this thesis are polycrystalline powders. In a crystalline powder, a large number of randomly oriented crystals are present. These materials can be measured using powder diffraction techniques which have been developed by Debye and Scherrer. These methods can be classified as 'fixed λ with varying θ' in which the varying θ is achieved by large number of randomly orientated crystal with *hkl* planes that will be orientated, by chance, at the appropriate Bragg angles for reflection. All the planes of a given d_{hkl}-spacing reflect at the same 2θ angle to the direct beam and all these reflected beams lie on a cone (Fig. 2.2) of semi-angle 2θ about the direct beam. The diffracted intensities in the cones will be uniform in a case in which the sample contains the crystals arranged at every possible orientation, therefore just part of the cones need to be recorded.[2, 5, 6]

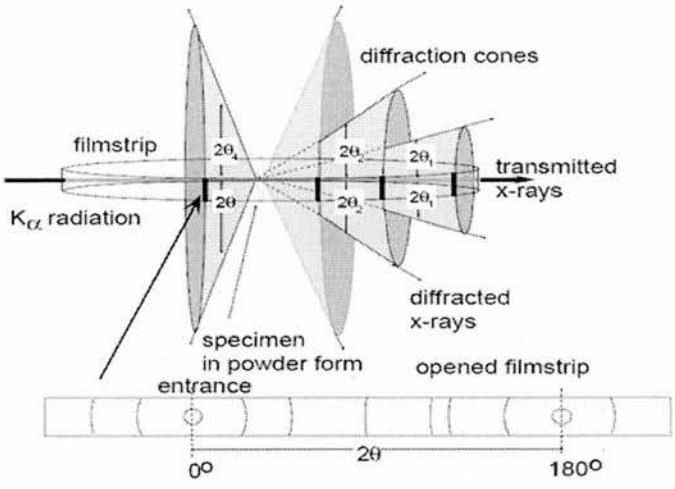

Figure 2.2: Debye-Sherrer powder setup and analysis

2.1.2 Laboratory X-ray Instruments

The laboratory powder diffraction data included in this thesis were collected on a Bruker D8 Advance diffractometer.[7] The X-rays are produced in a sealed X-ray tube, where electrons accelerated by a potential (in our case of 60 kV) bombard a Copper (Cu) metal anode inside the vacuum tube. At higher acceleration voltages the electrons have enough energy to eject electrons from the core levels of the target material. The electromagnetic radiation (X-rays) is emitted when the electrons from the higher energy orbitals (L-shell: $2p_{3/2}$, $2p_{1/2}$ or M-shell: $3p_{3/2}$, $3p_{1/2}$) fill the holes in the core level. Produced X-rays have a particular wavelength which depends on the metal of the anode and on the voltage of the X-ray generator used. In the characteristic X-ray spectrum of copper, two emission lines ($K\alpha_1$, $K\alpha_2$), which correspond to electrons decaying from $2p \rightarrow 1s$, are observed. Two different wavelength caused by spin-orbital splitting of the *2p* orbitals in Cu can be separated using monochromator or suitable filter. In the case of D8 Advance diffractometer, the beam is monochromated by an angled crystal of germanium, which is oriented such that only the desired Bragg reflection is used to measure the sample, which consists solely of Cu $K\alpha_1$ with $\lambda = 1.54056$ Å. The samples were run in reflection Bragg-Brentano geometry using the form of a flat plate. In Bragg-Brentano setup, the sample is irradiated from a fixed source with divergent beam which converges post-diffraction as a fixed radius from the sample, where the detector is

located. The divergence of the incident and diffracted beam is controlled using slits. The D8 Advance diffractometer uses a Braun position sensitive detector (PSD) in which the potential exists across a volume of methane gas. X-rays ionise the methane and the resulting current can be measured, giving the X-ray intensity. To obtain a good powder average with this geometry, the sample was spun.

2.1.3 The Synchrotron Source

The basic principle of a synchrotron light source is very simple, a beam of electrons (although they could be any charged particles) is accelerated in a linear accelerator and then again in a circular accelerator to near light speeds (~ 6GeV) and is then injected into a storage ring (circumference 844m at ESRF) and allowed to travel at constant speed around an approximately circular path. The acceleration of the electrons as they travel on their curved path results in emission Bremsstrahlung X-rays. In reality, the circular path is made up of many straight sections, and at the end of each one there is a magnetic field which bends the electrons into the next straight section, a so-called bending magnet. The bending magnet is simply a static magnetic field that affects the electron path (describing a circular arc) due to the Lorentz force. Upon bending the electrons are accelerated and therefore emit radiation in the form of Bremsstrahlung X-rays. The energy (ξ_e) of the electron in the storage ring and the radius of the curvature (ρ) can be described using following equation;

$$\rho[m] = \frac{3.3\xi_e[GeV]}{B[T]} \tag{2.16}$$

where B is the constant magnetic field applied by the bending magnet. The characteristic energy ($\hbar\omega$), of the emitted electrons, i.e. the energy at which the flux is the greatest is given by:

$$\hbar\omega_c[keV] = 0.665\xi_e^2[GeV]B[T] \tag{2.17}$$

and the radiated power (P) is given by

$$P[kW] = 1.266 \xi_e^2 [GeV] B^2 [T^2] L[m] I[A], \tag{2.18}$$

where the L is the length of the section over which the electron experiences magnetic field, and I is the current of the electrons in the storage ring. The synchrotron light can be also produced in the straight sections, so-called insertion devices (ID), in which the electron beam passes through wigglers or undulators. A wiggler is a periodic array of alternating magnetic fields which cause the electron path to bend in alternate directions. In principle, the electrons undergo the same process as with a bending magnet, but several times. Therefore the emerging radiation is the incoherent sum of $2n$ bending magnets, if the wigglers have n magnet periods. For an array of n magnet periods with the overall length L the electrons will see an array of magnets of length L/γ, with a period of $L/n\gamma$. Undulators are similar to a wiggler but work in a slightly different way. While using the bending magnets and wigglers, the synchrotron light is spread out in a horizontal fan, whereas the undulator radiation is concentrated into a central on-axis cone surrounded by additional weaker rings. Thus the overall intensity of the radiation arriving at the sample, rather than striking the walls of the electron beam pipe, is higher for undulators. The magnetic field applied to the electrons using undulators, perpendicular to the plane of the undulations is given

$$B_Z = B_0 \sin(2\pi s / \lambda_u) \tag{2.19}$$

where s is the spatial co-ordinate in the direction of the unbent electron path, λ_u is the period of the magnetic field, and B_0 is the maximum applied field. All synchrotron X-ray experiments described within this thesis done at insertion device beamline were performed on undulator beamline ID31. A schematic of a typical synchrotron storage ring is shown in Fig. 2.3.

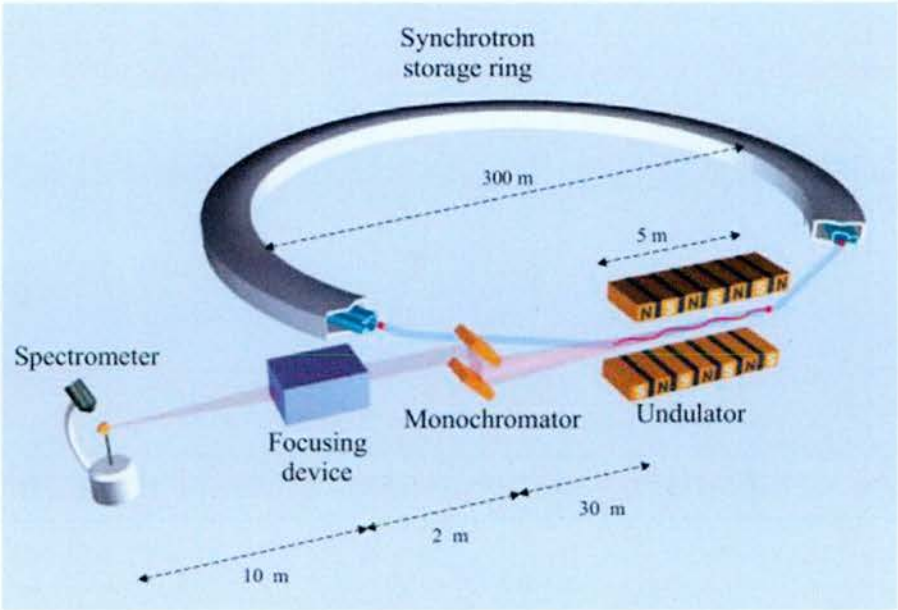

Figure 2.3: A schematic of a typical X-ray beamline at a third generation X-ray source.[1]

2.1.4 Synchrotron Instruments

Synchrotron X-ray powder diffraction experiments were performed at the ESRF on High-resolution Synchrotron powder diffraction beamline ID31. This beamline is built on a straight part of the electron beam, where the X-rays are produced by three undulator magnets. This undulator source gives a large enhancement in the incident X-ray flux and lower divergence in the incident beam. The beam source size is ~2.5 x 1.5 mm^2 with FWHM (full width at half-maximum) around 0.003° 2θ. The diffractometer was used with a bank of nine detectors with a nine-crystal analyser stage placed in between the detectors and the sample.[8] The crystal analyser stage consists of the nine Si(111) crystals (separated by approximately 2° intervals) which define the angle of light accepted by the detectors to a much higher degree of accuracy than the detector slits in a conventional diffractometer.[8, 9] The samples were finely ground and placed in a 0.6 mm diameter borosilicate glass capillary, which was then mounted on the axis of the diffractometer about which it was spun. For low temperature diffraction measurements, a rotating rod with the sample capillary was spun inside a liquid-helium cooled flow cryostat. The wavelength used was ~ 0.4 Å. Finally, the measured scans at RT and 4 K were collected for 1-2 hrs at a rate of 2° degrees per minute, while variable

temperature scans collected in between 4 K and 300 K were collected for 35 min at a rate of 3° degrees per minute. The data were summed and rebinned to a constant step size of 0.002°.

2.2 Neutron Diffraction

In X-Ray diffraction measurements the radiation is scattered by electrons in orbitals surrounding the nucleus. Due to the similarity of distances between these electrons with the magnitude of the X-ray wavelengths, the scattering power of an atom is strongly dependent on the scattering angle (form factor). In regard of this fact, the X-ray scattering of an atom will be also dependent on the number of electrons present around the atomic nucleus. It means that light atoms such as H, Li or O have scattering powers very much smaller that those of heavier metals such as Fe, Au and U. In neutron diffraction, the scattering process involves the interaction between the nucleus and neutrons (nuclear scattering), the distance of this interaction (~ fm) is shorter than the neutron's wavelength which means that the neutron diffraction and the scattering power is dependent on properties of the nucleus itself (Fig. 2.4).[2]

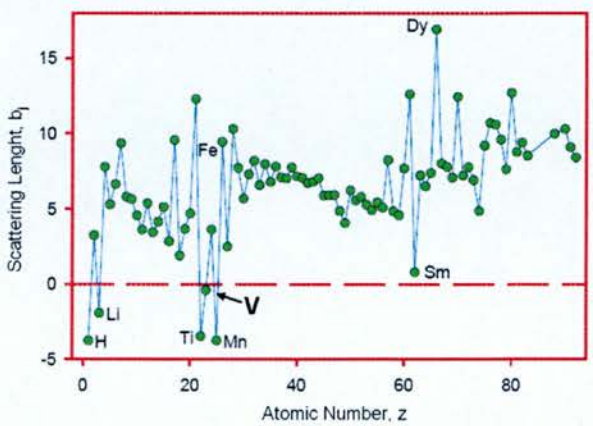

Figure 2.4: Variation of neutron scattering length with atomic number

The second interaction is that neutrons interact with unpaired electrons via the magnetic dipole interaction, so-called magnetic scattering. Thus information can be gained about both the crystal structure of a material from diffraction of the neutron with the atomic

nuclei and the magnetic structure by interaction between the neutrons magnetic moments and those of the atoms/ions with unpaired electrons.

2.2.1 The Neutron Source

There are two methods currently employed to generate neutrons for use in scattering experiments, namely, a nuclear reactor and a spallation source. Much of the description that follows is specific to the nuclear reactor at the ILL in Grenoble, and to the spallation source at ISIS in Didcot, UK.

The first method is nuclear fission,[10] occurring in a traditional nuclear reactor with uranium as the fuel.

$$^{235}U + n \rightarrow 2.5n + 200MeV + nuclei \tag{2.20}$$

Before reaching the scattering instruments the neutrons pass through a moderator which modifies their energy spectrum, the precise choice of moderator material and temperature determining the resulting spectrum. The primary coolant uses heavy water (D_2O) at about 35°, which also acts as a reflector, concentrating the neutrons in a small space. Neutrons which undergo several scattering processes in the moderator tend to be more likely to enter such waveguides than unscattered fast neutrons (i.e. high energy neutrons), which are radiated radially from the reactor core. The main advantage of a reactor source is that it produces a high flux of neutrons at a steady rate.

The other method of generating neutrons for scattering is with a spallation source. Accelerated protons strike a heavy metal target. The spallation process is the excitation and neutron emission of the target until it achieves a stable nuclear state. The spectrum of the neutrons, as with in the reactor, is modified by moderators. Such a source typically produces a much lower flux of neutrons than a reactor, however if the proton beam, and hence the neutron beam, is pulsed then so-called ´time-of-flight´ instruments can be used.

One of the main advantages of neutrons is that they interact rather weakly with matter, and that their interaction with magnetic moments is not immeasurably weak. This does,

however, present a problem when it comes to detecting scattered neutrons. Since neutrons have no charge and are non-ionizing they cannot be detected using radiation detectors which rely on direct gas ionisation. Instead the neutrons need to cause some other atom to emit charged particles which will ionise a gas and therefore be electronically detectable. The standard way of doing this is to use a chamber filled with ^{3}He gas, which then undergoes the following reaction:

$$\begin{aligned} {}^3He + {}^1n &\rightarrow {}^3H + p + E(MeV) \\ {}^3H &\rightarrow {}^3He + e^- + \bar{\nu}_e \end{aligned} \tag{2.21}$$

so that the charged decay products ionise the gas and give rise to a signal, which can be distinguished from signals at different energies arising from gamma rays entering the detector. The ^{3}H nucleus eventually decays to form another ^{3}He nucleus and an electron, so the supply of helium in the detector does not need to be replenished.

2.2.2 Neutron Powder Diffraction Theory

The De Broglie equation is used to describe the relation between the neutron's velocity (v) and its wavelength (λ);

$$\lambda = \frac{h}{p} = \frac{h}{m_n v} \tag{2.22}$$

where h is Planck's constant, p is the momentum of the particle and m_n is the mass of the neutron.

Further, neutrons have a spin quantum number of a half, and possess a magnetic moment. The electromagnetic interaction between the neutron and the nuclei with spin depends on the spin state of the nucleus. If a material is paramagnetic, then the magnetic scattering is incoherent, and will only manifest itself in an increase in the background intensity. Ferromagnetic of Antiferromagnetic ordering of the magnetic moments results in the magnetic diffraction. Ferromagnets produce magnetic peaks, which are superimposed on the nuclear peaks since the periodicity of the magnetic moments and

the atoms are the same. Extra magnetic reflections occur upon neutron scattering of antiferromagnets due to the supercell of the nuclear cell, i.e. if the antiferromagnetic magnetic ordering results in the doubling of the unit cell in all three directions then one of the extra peaks will be $(hkl)=(½,½,½)$.[2, 5] Generally, the intensity of a Bragg reflection for non polarized neutrons is given by:

$$F^2 = F_N^2 + F_M^2 \tag{2.23}$$

F_N^2 is the nuclear structure factor and F_M^2 is the magnetic structure factor. In order to fully describe the character of the magnetic elastic scattering, one has to describe firstly the neutron scattering cross section.

2.2.2.1 Neutron Scattering Cross Sections

A neutron scattering theory is based on the fact that both momentum and energy of the incident and scattered beam of the neutrons must be conserved. Energy conservation is given by:

$$E_i - E_s = \frac{\hbar^2}{2m_N}(k_i^2 - k_s^2) = \hbar\omega \tag{2.24}$$

Where E_i and E_s are the incident and final energies of the neutron, k_i and k_s are the incident and final neutron wavevectors and $\hbar\omega$ is the energy of the excitation in the sample. This allows us to define the scattering wavevector, Q, as:

$$Q = k_i - k_s . \tag{2.25}$$

The scattered neutrons are collected by a detector which counts all the neutrons arriving within a solid angle ($d\Omega$) around $\Omega(\theta,\Phi)$. Such a counting rate is normalized to incident flux (Φ). The quantity measured during the neutron scattering experiment is the double differential cross section, which is defined as:

$$\frac{d^2\sigma}{d\Omega dE} = \frac{\text{number of the neutrons scattered per unit time into the solid angle d}\Omega \text{ in the direction } \theta, \Phi \text{ with E and E+dE}}{dE \; \text{d}\Omega \; \Phi} \tag{2.26}$$

If instead all neutrons are collected without energy analysis, the measured quantity is called differential cross section ($\frac{d\sigma}{d\Omega}$) and represents the counting rate. All neutron scattering experiments done on 1111-type transition metal oxyarsenides were elastic, therefore in both nuclear and magnetic elastic scattering it is ($\frac{d\sigma}{d\Omega}$) that is of the interest.

2.2.2.2 Nuclear Elastic Scattering

The coherent nuclear elastic scattering cross section is given by:

$$\frac{d\sigma}{d\Omega} = N\frac{(2\pi)^3}{V_0}\left|F_N(Q)\right|^2 \tag{2.27}$$

Where N is the number of unit cells in the crystal, V_0 is the Volume of the unit cell and F_N is the nuclear structure factor.

$$F_N(Q) = \sum_j \bar{b}_j \exp^{iQ.r_j} \exp^{-W_j(Q,T)} \tag{2.28}$$

Where the sum runs over all atoms j, r_j is the position of the j^{th} atom, $\bar{b}_j$ is the nuclear scattering length of the j^{th} atom and W_j is the Debye-Waller factor. The Debye-Waller factor is included because the atoms are not frozen to their lattice sites, but rather they undergo a certain amount of thermal motion about an equilibrium position;

$$W_j(Q,T) = \frac{1}{2}\left\langle \left(Q \cdot \mu_j(T)\right)^2 \right\rangle \tag{2.29}$$

$\mu_j(T)$ is the thermal displacement of atom j from its equilibrium position.

2.2.2.2 Magnetic Elastic Scattering

Unlike the nuclear elastic scattering, the magnetic elastic scattering is spin-spin correlations dependable. When the magnetic moments order at low temperature then spins are correlated. If these correlations persist for infinite time then scattering is purely elastic and correlations are time independent. The differential magnetic cross section can be written as:

$$\frac{d\sigma}{d\Omega} = N_{mag}\frac{(2\pi)^3}{V_{mag}}\left(\frac{\gamma r_0}{2}\right)^2 \sum_{\tau_M}\left|F_M(\tau_M)\right|^2 \delta(Q-\tau_M) \tag{2.30}$$

Where N_{mag} is the number of the magnetic unit cells, V_{mag} is the volume of the magnetic unit cell, $\gamma = 1.91$ is a gyromagnetic ratio, $r_0 = 2.8\times10^{-15} m$ is the classical electron radius.

$$F_M(Q) = \sum_j \mu_j f_j \exp^{iQ.r_j} \exp^{-W_j(Q,T)} \tag{2.31}$$

is the magnetic structure factor, where μ_j is the magnetic moment of the j^{th} atom, and f_j is the magnetic form factor of the j^{th} atom. Magnetic form factors may be regarded as a characteristic function of each magnetic ion. It is necessary to know the magnetic form factor for each ion in order to calculate the magnetic cross sections. The accurate measurement of f_j is also necessary in order to reveal fine details of the magnetic distribution on the different atoms in a particular crystal. τ_M is the reciprocal lattice vector of the magnetic structure which can be written as $\tau_{\mathbf{M}} = \tau \pm \mathbf{k}$. The vector k characterizes the periodicity and is called the propagation or wave vector of the magnetic structure. The reciprocal lattice vector $\tau = ha* + kb* + lc*$, where $a*$, $b*$, $c*$ are the reciprocal unit cell vectors. If $\mathbf{k} = 0$, the magnetic reflections are on the nodes of the reciprocal lattice and the magnetic diffraction peaks therefore overlap with the nuclear peaks, increasing those peaks below the ordering temperature. When $|\mathbf{k}| > 0$, the magnetic intensities do not overlap with the nuclear intensities and additional peaks are observed in the diffraction pattern below the ordering temperature.

2.2.3 Constant Wavelength Neutron Instruments

Neutron powder diffraction (NPD) experiments in this work were all performed at ILL using mainly the High-flux two-axis neutron diffractometer D20 and the High-resolution two-axis neutron powder diffractometer D2B. High neutron flux on the sample, a wide band of wavelengths and very large detector, are the main features that make these diffractometers highly sensitive.[11]

Due to the high incident neutron flux and a large detector solid angle, D20 provides the fastest counting rate of any reactor-based neutron diffractometer, which is desirable when limited sample volumes are available. The three different monochromators Cu(200), highly oriented pyrolitic graphite-HOPG(002) and Ge(*hhl*) allow one to tailor the wavelength in the range 1-2.4 Å, depending on the *d*-spacing range of interest. The wavelengths used in the NPD experiments performed in this work were 2.41 Å with HOPG(002) monochromator at 42° take-off angle. In the case of the $NdFe_{1-x}Co_xAsO$ sample, room temperature (RT) of NPD patterns were collected using wavelength 1.3 Å with Cu(002) monochromator with the average high-resolution configuration of $\Delta d/d \sim 1.6\times10^{-3}$. The resolution of D20 is slightly lower than that of D2B instrument with $\Delta d/d \sim 5\times10^{-4}$. In order to cover a continuous 2θ range of 153.6°, a position sensitive detector (PSD), composed of 48 black-glass plate, each plate of 32 cells, is used. The D20 instrument has several dedicated sample environments: a large vacuum vessel to reduce air-scattering for RT experiments and an Orange cryostat (1.7 K to 300 K) with a choice of ϕ25 mm and ϕ50 mm vanadium tails. Moreover all sample environments at D20 are mounted on an *x*-*y*-*z* translation stage, which itself is mounted on a 360° ω-axis. [12]

The D2B diffractometer is characterized by a very high take-off angle (135°). As mentioned above, D2B has much higher resolution, thus it is suitable for the detailed structural studies of crystalline compounds. D2B is suitable for measuring very large *d*-spacings using wavelengths of between 2.4 Å and 6 Å, which can be easily changed by rotation within the Ge(*hhl*) plane. D2B's 2D Multidetector consists of 128 cells spaced at 1.25° intervals. Data collected on D2B were recorded between $5° \leq 2\theta \leq 140°$ with a step size of 0.05°. The neutron wavelengths used were λ = 1.594 Å and 2.4 Å.

Finally, all samples were finely ground and mounted in 6 mm diameter cylindrical vanadium cans. The layout of D2B and D20 instrument is depicted in Fig. 2.5.

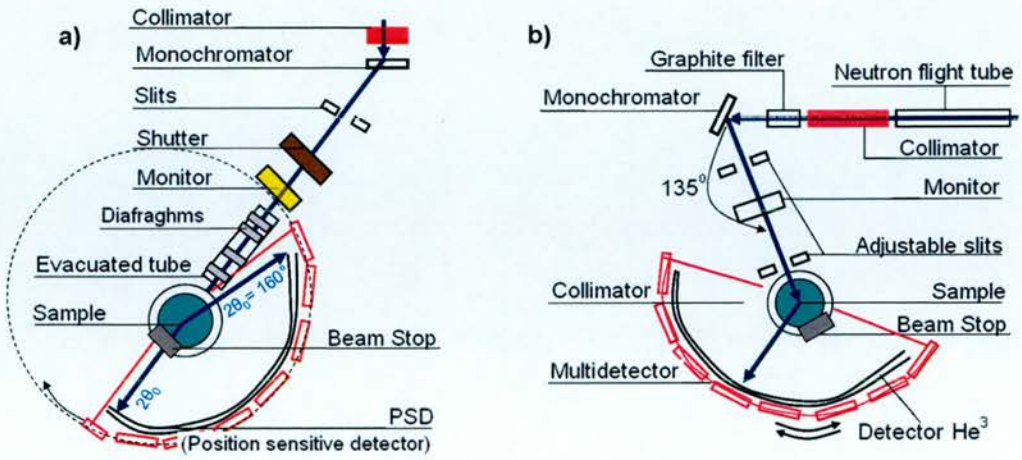

Figure 2.5: Instrumental arrangement for a) D20 and b) D2B

2.2.4 Time of Flight Neutron Diffraction

The time of flight method has been used to obtain neutron powder diffraction data on the NdNiAsO sample. A brief elaboration of the method is given here. The scattering angle is constant (detector held in a fixed position)and a white beam is used. The wavelength of the neutron is effectively varied by measuring the time taken for the neutron to travel from the target to the detector. Bragg's law may be formulated in terms of the time of flight as:

$$\lambda = 2d\sin\theta = h/p = h/mv = \frac{ht}{mL} \Rightarrow t = \frac{2mL}{h} d\sin\theta \qquad (2.32)$$

Where t is the measured time of flight, m is the mass of the neutron, L is the total flightpath and v is the neutron velocity. The De Broglie relationship, where the neutron's wavelength is inversely proportional to its velocity, has been used. By recording the arrival time of each neutron of a particular pulse in the detector the corresponding d-spacing can be calculated from Eq. 2.16.

The resolution function of the time of flight diffractometers depends mainly on the neutron's flight path and on its uncertainties in time of flight (δt) path length (δL) and scattering angle ($\delta\theta$), respectively. Therefore the Eq.2.16 can be rewritten as;

$$\left(\frac{\delta d}{d}\right)^2 = \left(\frac{\delta t}{t}\right)^2 + \left(\frac{\delta L}{L}\right)^2 + \left(\cot\theta\delta\theta\right)^2 \qquad (2.33).$$

The angle term dominates the resolution function at low scattering angles. The $\cot\theta$ term is close to zero at $\theta = 180°$, therefore the back-scattering detectors provide data with the highest resolution. The uncertainty in scattering angle depends as well on the size of the sample and can be reduced by increasing secondary flight path (L_2, sample-to-detector distance). However with increasing L_2 the solid angle seen by the detectors decreases. The high d-spacing resolution can be achieved via tuning the distance of the flight path (longer L, better d-spacing resolution, but longer t) and via positioning the detectors at high scattering angles.[9, 13]

2.2.5 Time of Flight Neutron Intruments

Time of flight neutron diffraction experiments were carried out at ISIS, Rutherford Appleton laboratories, Didcot, UK, which is a spallation neutron source. Briefly; protons are accelerated to high energies in a small synchrotron ring (163m circumference), and extracted in pulses or packets by powerful magnets. The high energy proton packets are directed into one of two tungsten targets where they eject neutrons from the tungsten nuclei. The neutrons are slowed to useful velocities with water moderator (ambient temperature), liquid methane moderator (100 K) and liquid hydrogen moderator (20 K). The moderator temperature determines the spectral distributions of neutrons produced and this can be tailored for different types of experiments. Slowed neutrons are then directed to a variety of instruments distributed radially around the two target stations (TS-I, TS-II).

WISH (Wide angle In a Single Histogram) is a High-resolution magnetic TOF diffractometer placed in TS-II designed for powder diffraction at long d-spacing (0.5-50 Å) using incident wavelengths of between 1.5 Å and 15 Å.[14] WISH uses a decoupled

methane moderator and is situated with an incident flight path of 50 m and a post sample flight path to the various detectors of 1.0 – 2.5 m. The beam on WISH is a maximum size of 40 mm high and 20 mm and can be changed using focusing snout to 1 mm high and 1 mm wide. The sample was inserted into a copper can and variable temperature neutron diffraction patterns were collected for total proton beam currents of 100 μA hours for T = 0.3 K and 1.5 K, and of 30 μA hours for temperatures in between from the 26, 58, 90, 121 and 153° 2θ detector banks. Each bank is fitted with ZnS scintillators which are positioned to have the same resolution function. The detector layout of the WISH diffractometer is shown in Fig. 2.6.

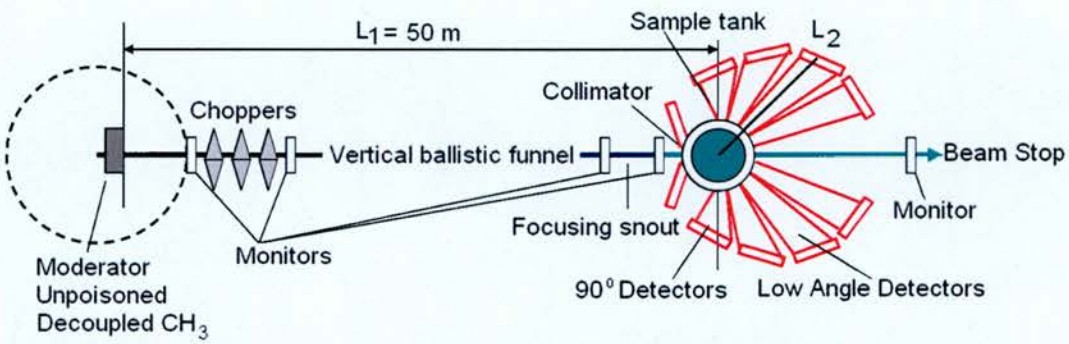

Figure 2.6: The instrument layout of the WISH diffractometer

2.3 Rietveld Method

Once the powder X-ray or Neutron diffraction data are collected, the crystal structure may be refined, and the most widely used technique is the Rietveld method. The principle of the Rietveld Method devised by Hugo Rietveld (1969)[15, 16] is to minimize a function M which represents the difference between a calculated profile y^{calc} and the observed data y^{obs}. Rietveld defined such an equation as:

$$M = \sum_i W_i \left\{ y_i^{obs} - \frac{1}{c} y_i^{calc} \right\}^2 \qquad (2.34)$$

Where W_i is the statistical weight and c is an overall scale factor such that $y^{calc} = cy^{obs}$. At the beginning the method requires some starting parameters: the space group, the lattice parameters (which determine the positions of the reflections) and some instrumental details.[4]

The observed intensity y_i can be defined as:

$$y_i = y_i(background) + \sum_i y_i^{(i)}(Bragg) \tag{2.35}$$

Where $y_{i(background)}$ is the background intensity and $\sum_i y_i^{(i)}{}_{(Bragg)}$ is the sum of the contributions of reflections close to the powder pattern step, i. The contribution of all nearby Bragg reflection K including the background contribution are involved in the calculated intensity as well. It's given by:

$$y_{calc} = S\sum_K L|F_K|^2 \phi(S_i - S_K)P_K A + y_{i,bkg} \tag{2.36}$$

where S is the scale factor, L contains Lorentz and Polarisation factors, F_K is the structure factor, $\phi(S_i - S_K)$ is the peak shape function, which models the effect of the instrument and the sample itself on the profile, P_K is the preferred orientation function, A is the absorption factor and $y_{i,bkg}$ is the background intensity at point i in the diffraction pattern. Each of these parameters may be varied during the refinement cycle to improve the match between calculated and observed diffraction patterns.

2.3.1 Background Intensity

The background intensity at every step i can be fitted in any of three ways, from a linear interpolation between selected points in the pattern, secondly from a table of intensities provided by the user or from a specified background function, such as a cosine Fourier series or power series. All of the parameters described above can be refined, along with the cell parameters and atomic positions, atomic thermal factors (U), site occupancies. If

the starting structure model becomes close to the correct structure, then the global minimum is reached.

2.3.2 Intensity Correction Factors

Generally, the intensities of the observed neutron/X-ray peaks depend on the sample, the instrument geometry, and the type of radiation. The intensity correction factors, K_{ph}, can be related using:[17, 18]

$$K = \frac{E_{ph} A_h O_p M_p L}{V_p} \tag{2.37}$$

Where E_{ph} is an extinction correction (crystal grains), A_h is an absorption correction, O_p is the preferred orientation correction, M_p is the reflection multiplicity, L is the angle dependent correction (Lorentz-polarization), and V_p is the unit cell volume for the phase. In this work, the A_h, L and O_p corrections have been used. Thus more detailed description of these three intensity correction factors is given below.

2.3.2.1 Lorentz, Polarisation Correction

Although Lorentz and polarization term in powder diffraction experiments are of different origins, they are usually coupled into a single term. The Lorentz factor is used to correct for the angle dependence of the intensities for both neutron and X-rays, while polarization term arises from the wavelike nature of the radiation used in the experiment. The Lorentz-Polarization factors for neutron diffraction experiments are given as:

$$LP(CW) = \left(2\sin^2\theta\cos\theta\right)^{-1} \tag{2.38}$$

$$LP(TOF) = d^4\sin\theta \tag{2.39}$$

For X-ray diffraction experiments, LP single term is more complicated due to the fact that the polarization term depends on the properties of the monochromator crystal as

well as the monochromator angle. For synchrotron X-rays the polarization depends on the properties of the incident beam and the monochromator used.

2.3.2.2. Absorption Correction

During the X-ray or neutron measurement, some of the x-rays or neutrons can be absorbed by atoms. Due to this absorbance that is dependent on the type of atom a reduction of measured intensities will be observed. In the case of data collected in Debye - Sherrer (cylindrical) geometry, the wavelength dependence, $A = \mu R/\lambda$, is observed. For TOF data, the linear absorption of all components in the sample varies with 1/velocity. For CW data, the absorption coefficient (A) is related to the value for 1 Å neutrons. Generally for cylindrical sample, the absorption correction can be calculated as:

$$A = \exp\left[-(1.7133 - 0.0368\sin^2\theta)\mu R + (0.0927 + 0.3750\sin^2\theta)(\mu R)^2\right] \qquad (2.40)$$

A is the absorption coefficient, and R is the radius of the cylindrical sample. This function is only correct for small values of μR (<2). The quantity μR can either be refined, or calculated using the following equation a) for X-ray experiment, b) for neutron experiment:

$$a) \qquad \mu R = \frac{\sum_{cell} \mu_i \rho_i}{\rho} pR \qquad (2.41)$$

$$b) \qquad \mu R = \frac{\sum_{cell} \sigma_i}{V_{cell}} pR \qquad (2.42)$$

where the absorption coefficients, σ_i (barns) and μ_i (cm^{-1}) for atom i are specific to the atom, and dependent on the wavelength of the X-rays or neutrons used, ρ_i (g/cm^3) is the density of atom i in the sample, p is the packing density of the sample in the cylindrical holder (if not measured, this is taken to be 0.5 as standard).

2.3.2.3 Preferred Orientation Correction

The preferred orientation coefficient (O_p) of neutron/X-rays experiments depends on both the diffraction geometry and the crystallite shape, and is given as:

$$O_{ph} = \frac{1}{M_p}\sum_{j=1}^{M_p}\left(R_0^2\cos^2 A_j + \frac{\sin^2 A_j}{R_0}\right)^{-3/2} \tag{2.43}$$

Where A_j is the angle between the preferred orientation axis and reflection vector h_p. It assumes that the preferred orientation axis of the sample lies within the diffraction plane ($R_0 > 1$) or coincides with the diffraction vector ($R_0 < 1$). R_0, the refinable coefficient, gives the effective sample compression or extension along the cylinder axis.

2.3.3 Peak Shape Function

The peak shape function is designed to model the effects that the instrument and sample have on the shape and position of a Bragg reflection.[18] For constant neutron wavelength experiments, the profile function could be almost described as a fully Gaussian function, S_{ik} with Full Width at Half Maximum (FWHM), as given below:

$$H_K^2 = U\tan^2\theta + V\tan^2\theta + W \tag{2.44}$$

where U, V and W are refinable parameters. For high resolution instruments, peak widths are often sufficiently narrow for sample effects, such as microstrain and particle size, to have a noticeable effect in broadening the profile. Problems with more complicated peak-shapes can be solved by using the Thompson, Cox and Hastings modified Pseudo-Voigt function.[19]

The pseudo-Voigt function takes into account both the sample (Lorentzian, L) and instrumental (Gaussian, G) broadening:

$$\phi(2\theta_I - 2\theta_k) = \eta L + (1-\eta)G \tag{2.45}$$

Where η is a complex function which depends in the FWHM's for the Gaussian (Γ_{GK}) and Lorentzian (Γ_{LK}) broadening of the K^{th} Bragg reflection.

$$(\Gamma_{GK}) = \left(U \tan^2 \theta_K + V \tan \theta_K + W + \frac{Z}{\cos^2 \theta_K} \right)^{1/2} \tag{2.46}$$

$$(\Gamma_{LK}) = X \tan \theta_K + \frac{Y}{\cos \theta_K} \tag{2.47}$$

Z is the Sherrer coefficient for Gaussian particle size broadening; X and Y model the Lorentzian strain and Sherrer broadening respectively.

For TOF neutron experiments, the peak shape fitting is more complicated due to the highly asymmetric nature of the neutron pulse coming from the moderator. Such an asymmetry is observed in the pattern, where the edge of the Bragg intensity is very sharp whereas the trailing edge decays depending on the moderator size and temperature. Therefore a model using a convolution of rising and falling exponentials, to describe the time dependence of the initial neutron pulse, with the above described Pseudo-Voigt function is used to fit the peak shape of the TOF data.

$$\phi(T_i - T_K) = \int E(\tau) \phi_{pv} (\Delta T - \tau) d\tau \tag{2.48}$$

ΔT is the difference in TOF between the reflection position and the profile point, $E(\tau)$ is described in terms of the exponential rise and decay constants, α and β:

$$E(\tau) = \frac{\alpha\beta}{\alpha + \beta} \exp(\alpha\tau) \tag{2.49}$$

$$E(\tau) = \frac{\alpha\beta}{\alpha + \beta} \exp(-\beta\tau) \tag{2.50}$$

The maximum of the neutron pulse occurs at $\tau = 0$, $\alpha = \alpha_0 + \alpha_1/d$ and $\beta = \beta_0 + \beta_1/d$.[17, 20, 21] The FWHM's due to the Gaussian and Lorentzian broadening of the pseudo-Voigt function are:

$$(\Gamma_{GK}) = \sigma = \left(\sigma_0^2 + \sigma_1^2 d_K^2 + \sigma_2^2 d_K^4\right)^{1/2} \tag{2.51}$$

$$(\Gamma_{LK}) = \gamma = \gamma_0 + \gamma_1 d_K + \gamma_2 d_K^2 \tag{2.52}$$

2.3.4 Indicators of Fit

As discussed above, the Rietveld method tries to minimize the difference between the calculated and observed diffraction patterns. The goodness of fitted model is described by several residual functions:

- Structure factor, R_F: $$R_F = \frac{\sum \left| I_{K,obs}^{1/2} - I_{K,calc}^{1/2} \right|}{\sum I_{K,obs}^{1/2}} \tag{2.53}$$

- R-pattern, R_p: $$R_p = \frac{\sum \left| y_{i,obs} - y_{i,calc} \right|}{\sum y_{i,obs}} \tag{2.54}$$

- R-weighted pattern, R_{wp}: $$R_{wp} = \left[\frac{\sum w_i (y_{i,obs} - y_{i,calc})^2}{\sum w_i (y_{i,obs})^2} \right]^{1/2} \tag{2.55}$$

- Goodness of fit parameter, χ^2: $$\chi^2 = \frac{\sum_i w_i (y_{i,obs} - y_{i,calc})^2}{N - p + C} \tag{2.56}$$

where $I_k(obs)$ and $I_k(calc)$ are the observed and calculated intensities assigned to the kth Bragg reflection at the end of the refinement cycle. $(N - p + C)$ is the number of degrees of freedom, p and C are the total number of observations, refined parameters and constraints respectively.

Generally R_{wp} and χ^2 are the most commonly used regarded residuals for powder diffraction experiments, as they contain the expression being minimised in the refinement process, S_y, as the numerator. The value of R_{wp} can be increased by the presence of additional weak peaks or by the presence of the second phase in the pattern.

The value of χ^2 depends on the intensity of background or poor counting statistics. However they do provide an excellent tool in comparison of two structural models in a given experiment.[19]

2.4 GSAS Program Package

Rietveld refinement of the X-ray and Neutron patterns within this thesis was carried out using the computer program GSAS & EXPQUI (General Structure Analysis System) - the PC Windows version developed by A. C. Larson and R. B. Von Dreele.[19] GSAS works with both X-ray and Neutron data, either angle or wavelength dispersive and can work with multiple data sets simultaneously, as well as with diffraction data from mixtures of phases. It is sub-divided into a number of smaller individual programs, each of which is designed for a specific task or crystallographic calculation.

2.5 Magnetic Symmetry

The magnetic moments of atoms are disordered at elevated temperatures and may become ordered on a crystal lattice at certain temperature (ordering temperature). Such a magnetic structure is commonly represented as a set of arrows associated with the magnetic moments, with magnitudes and orientations characteristic of the particular structure. The symmetry of the magnetic structure and the positions of ordered magnetic moments can be described using space groups listed in International Tables of Crystallography. Such an approach cannot be used to fully define the direction of magnetic moments; therefore alternative methods have to be applied. So far two different approaches have been proposed: magnetic Shubnikov groups[22, 23] and Group Representational Analysis.[24] The Group Representational Analysis involves first the determination of the space group symmetry elements. This leads to define the irreducible representations of any space group and together with the propagation vector may be used to classify the magnetic structure. For structures which arise through a second order phase transition, only one irreducible representation may arise, according to the Landau theory of phase transitions. (However, real structures are not limited to single second order phase transition). The Shubnikov groups can only be used in the

special case of commensurate magnetic structures. Representational Analysis has been used to characterise all magnetic structures described within this thesis and the theory underlying this method is explained in subchapter 2.5.1.

2.5.1 Representational Analysis

Crystal structures are constructed from the nuclear unit cell that is repeated along the three directions of the crystal axes. The same approach can be used to describe the magnetic structures consisting of the magnetic unit cell. For convenience, a description based on the nuclear unit cell and a "propagation vector", *k*, that describes the relation between moment orientations of equivalent magnetic atoms in different unit cells can be used. The magnetic moment can be thus described in terms of projections along the crystallographic axes, and is given by a "basis vector", Ψ, which has components along these axes. The real basis vector corresponding to the projection of the moment along the different crystallographic axes can be written as;

$$\vec{M}_j = \vec{\Psi}_j \tag{2.57}$$

However, in general the projections of the moment are described not just by one basis vector, but by a linear combination of the basis vectors as:

$$\vec{\Psi}_j = \sum_v C_v \vec{\Psi}_v \tag{2.58}$$

Where $\vec{\Psi}_v$ is used to represent the v components of $\vec{\Psi}_j$ for a given propagation vector **k**. For single magnetic structures (all magnetic structures discussed within this thesis are all described by a single magnetic propagation vector), the magnetic ordering of atom j in the magnetic structure can be described as:

$$\vec{M}_j = \vec{\Psi}_j \exp(-2\pi i \vec{k} \cdot \vec{t}) \tag{2.59}$$

This equation characterises the translational properties in real space of the basis vector Ψ_j, which can be thought of as the projection of the magnetic moment along the a, b, c crystallographic axes in the *zero*th (nuclear) cell.

Representational analysis based on Group theory can be used to derive symmetry allowed magnetic structures from knowledge of the propagation vector and the nuclear cell. This involves firstly the determination of the space group symmetry elements that leave the magnetic propagation vector **k** invariant: these form the little group G_k. For a magnetic structure to be possible it must be compatible with all symmetry operations of G_k simultaneously. The operations of all the symmetry elements of the group on all the atomic positions and all of the displacement vectors can be described using a set of matrices so called the magnetic representation (Γ_{mag}). Γ_{mag} is reducible and can be written in terms of the irreducible representations (IRs) of the little group, G_k as:

$$\Gamma_{mag} = \sum_{v} n_v \Gamma_v^{\mu} \tag{2.60}$$

where n_v is the number of times the irreducible representation Γ_v appeared.

For a second-order transition a powerful simplification of the number of possible structures arises as a consequence of the Landau theory: the ordering transition can involve only a single IR. Accordingly, the basis vectors involved in the structure are limited to those associated with a single IR. In addition, the number of "symmetry-allowed" magnetic structures is the number of nonzero IRs in the decomposition of its magnetic representation. This greatly reduces the number of possible magnetic models and the number of parameters involved in their refinements. Within this thesis representational analysis was carried out using the SARA*h* Representational Analysis programme. This programme also contains an introduction to Representational analysis and Group symmetry.[24]

2.5.2 SARA*h* Representation Analysis Program

The SARA*h* program was used to calculate possible magnetic structures. The SARA*h* Representation Analysis program is written by A.S. Wills.[24] The input required are the propagation vector k, the crystallographic space group and the atomic coordinates of the magnetic atoms. As has been written in sub-chapter 2.5.1, the calculations determine firstly the small group (G_k) followed by the decomposition of the magnetic representation of a crystallographic site (Γ_{mag}) into the IRs of the small group (G_k).

2.6 Bulk Property Measurements

2.6.1 Magnetisation Measurements Using a SQUID

The magnetisation measurements with variable temperature and field experiments were carried out using a Quantum Design Magnetic Property Measurement System (MPMS), which contains a Superconducting Quantum Interference Device (SQUID).[25] Any magnetisation in the sample changes the magnetic flux through the sensing coil, inducing a supercurrent which in turn changes the flux through the SQUID, thereby producing a change in the SQUID output signal.[81]

The SQUID detection system is a superconducting ring, containing a weak link that is capable of amplifying any small changes in magnetic field into large electrical signals. It is coupled, through superconducting circuitry, to a superconducting sensing coil which surrounds the sample. A superconducting magnet is used to generate a highly uniform magnetic field in the magnetometer, and the sample is moved through the detection coils in discrete steps. Any magnetisation in the sample changes the magnetic flux through the sensing coil, inducing a supercurrent which in turn changes the flux through the SQUID, thereby producing a change in the SQUID output signal. The output of the SQUID is recorded as a function of sample position and the response curve analyzed by a computer to derive a corresponding magnetic moment.

The SQUID measurements can be performed in two modes, DC - and AC - mode. Direct-current (DC) magnetometry, in which the sample is magnetized by a constant magnetic field, is used to establish the equilibrium value of the magnetization in a sample. Alternating-current (AC) magnetic measurements provide information on magnetization dynamics since the sample moment is time dependent. AC measurements give two values of magnetisation per measurement, an in-phase and out-of-phase or real and imaginary part referred to as M' and M'' respectively.

The SQUID device is highly sensitive, measuring the sample magnetisation to a moment sensitivity of 10^{-7} emu. The values of magnetisation per unit mass, m (emu/g) were then used to calculate the molar magnetic susceptibility, where H is the applied magnetic field and M_w the molecular weight:

$$\chi_m = \frac{mM_W}{H} \tag{2.61}$$

Where χ_m is the molar susceptibility; m is the magnetisation per unit mass (emu/g); M_w is the molecular weight (g) and H is applied magnetic field (gauss).

For the SQUID measurements approximately 20 mg of the sample was placed in a plastic capsule.

2.6.2 Electrical Resistivity Measurements Using a PPMS

The electrical resistivity of samples was measured on polycrystalline bars using the conventional four-probe technique. Current contacts were made at the two ends of the sample bars, and the voltage contacts at approximately 1/3 and 2/3 of the sample length. All contacts were made with silver epoxy (highly conductive adhesive) to ensure a homogeneous current distribution. The sample resistivity, ρ, was then calculated from the measured resistance given;

$$\rho = \frac{RA}{l} \tag{2.62}$$

Where R is resistivity in Ω, A is cross-sectional area of the sample bar in cm^2, and l is a distance between two current wires. Sample resistivity was measured under different conditions. These included varying the temperature (from 5K to 350K) while keeping the magnetic field constant (zero field or 1T), varying the magnetic field (±7 T) while keeping the temperature constant. The temperature dependence of resistivity was measured using generally a sweep rate of 1 K per minute. Data were collected on both cooling and heating to confirm there was no temperature hysteresis.

2.6.3 Heat Capacity Measurements Using a PPMS

The heat capacity (HC) was measured using the Quantum Design HC option. The sample puck consists of a microcalorimeter platform which is suspended by eight thin wires that serve as the electrical leads for an embedded heater and thermometer. The wires provide a well-defined thermal connection between the sample platform and the puck. Samples were attached to this platform using vacuum grease. The heat capacity measurement consists of several steps. Firstly the puck has to be "calibrated" (i.e. measured empty) then the sample is mounted and the measurement is repeated.

Generally, power is applied to the microcalorimeter platform heater for a predetermined length of time, causing the platform temperature to rise. When the power is terminated, the temperature of the sample platform relaxes toward the puck temperature. The sample platform temperature is monitored throughout both heating and cooling, providing the raw data of the heat capacity calculation. Each measurement is analyzed using a *two-τ model*[26] to accurately simulate the effect of the heat flow between the microcalorimeter platform and the sample (τ_2) as well as the heat flow between the platform and puck stage (τ_1). *Two-τ model* assumes that the sample is in good thermal contact with the sample platform. A second analysis is also performed using a model that assumes perfect thermal coupling between the sample and the sample platform. The heat capacity software determines which model best fits the measured data and automatically saves the values of the sample heat capacity, addenda (puck with grease on the platform) heat capacity, thermal coupling between the sample and the platform, thermal time-constants, and other information to the data file.

2.7 References

1 J. Als-Nielsen, and D. McMorrow, *Elements of Modern X-Ray Physics*. John Wiley & Sons; 1 edition: New York, NJ, USA, 2001.

2 R. E. Dinnebier, and S. J. L. Billinge, *Powder diffraction Theory and Practice*. The Royal Society of Chemistry: Cmabridge, 2008.

3 C. Hammond, *The basics of Crystallography and Diffraction-2nd ed.* Oxford Science Publication: 2001.

4 W. I. F. David, K. Shankland, and L. B. McCusker, *Structure Determination from Powder Diffraction Data* Oxford Science Publication: 2002.

5 D. L. Bish, and J. E. Post, *Modern powder diffraction*. Mineralogical Society of America: Washington D.C., 1989.

6 E. W. Nuffield, *X-Ray Diffraction Methods*. John Wiley&Sons, ltd.: 1966.

7 in *http://www.bruker-axs.de/d8_advance.html (15/12/2010)*.

8 H. Jean-Louis, B. Patricia, M. Anne, A. Prat, A. N. Fitch, E. Dooryhee, G. Vaughan, and K. F. Andreas, in, eds. Albert, T. M.; Andreas, K. F.; Tetsuya, I.; Dennis, M. M., Society of Photo-Optical Instrumentation Engineers: 1998; Vol. 3448, pp 353-361.

9 J. P. Wright, G. B. M. Vaughan, and A. N. Fitch, *IUCr Computing Commisiion Newsletter* **1**, (92), (2003).

10 L. A. Turner, *Reviews of Modern Physics* **12**, (1), 1 (1940).

11 A. W. Hewat, *Physica B-Condensed Matter* **385-86**, 979-984 (2006).

12 in *http://www.ill.eu (15/12/2010)*.

13 C. G. Windsor, *Pulsed neutron scattering*. Taylor and Francis Ltd.: London, 1989.

14 in *http://www.isis.stfc.ac.uk/instruments/wish/technical/wish-technical-information7362.html (15/12/2010)*.

15 H. Rietveld, *Acta Crystallographica* **22**, (1), 151-152 (1967).

16 H. Rietveld, *Journal of Applied Crystallography* **2**, (2), 65-71 (1969).

17 R. B. Von Dreele, J. D. Jorgensen, and C. G. Windsor, in *Journal of Applied Crystallography*, 1982; Vol. 15, pp 581-589.

18 R. A. Young, and D. B. Wiles, *Journal of Applied Crystallography* **15**, (4), 430-438 (1982).

19 A. C. Larson, and R. B. Von Dreele, in *General Structure Analysis System (GSAS)*, ed. Los Alamos National Laboratory Report LAUR 86-748, 2004.

20 O. Halpern, and M. H. Johnson, *Physical Review* **55**, (10), 898 (1939).

21 S. Ikeda, and J. M. Carpenter, *Nuclear Instruments and Methods in Physics Research Section A: Accelerators, Spectrometers, Detectors and Associated Equipment* **239**, (3), 536-544 (1985).

22 W. Opechowski, and R. Guccione, *"Magnetic Symmetry" in Magnetism*. Academic Press: 1965; Vol. Volume II, Part A, p 105-165.

23 W. Opechowski, *Crystallography and Metacrystallographic groups*. Elsevier Science Publishiers B.V.: Amsterdam, 1986.

24 A. S. Wills, *Physica B: Condensed Matter* **276-278**, 680-681 (2000).

25 M. McElfresh, in, ed. University, P., Quantum Design, Inc.: 1994.

26 J. S. Hwang, K. J. Lin, and C. Tien, *Review of Scientific Instruments* **68**, (1), 94-101 (1997).

CHAPTER 3

The Synthesis, Structure and Physical Properties of NdMnAsO

3.1. Introduction

The manganese (Mn) analogues of the 1111-type *RE*FeAsO have generated interest because the Mn^{2+} ion has an odd number of 3d electrons and is expected to form different spin configuration (high spin $3d^5$, hall-filled pseudoclosed shells) from the analogues with Fe^{2+} ($3d^6$), Co^{2+} ($3d^7$), Ni^{2+} ($3d^8$) and Zn^{2+} ($3d^{10}$) analogues.[1-5] Difference in transport properties compared to other iron based compounds has been attributed to a much stronger hybridization between Mn *3d* and pnictogen *4p* states.[6]

The best characterized system is $BaMn_2As_2$, which has a *G*-type (i.e. AF ordering in all three dimensions) magnetic structure with moments aligned along the c-axis ($\mu = 3.88(4)\,\mu_B$ at 10 K) and a Neél temperature of 625(1) K. Heat capacity and electrical resistivity measurements revealed a Sommerfeld coefficient being close to zero; a metallic temperature dependence and a room temperature (RT) resistivity of 165 mΩ cm.[6, 11, 12]

LaMnPO shows a similar magnetic structure to $BaMn_2As_2$, but with parallel alignment of the nearest neighbor (NN) Mn moments along the c-axis. Transport measurements on polycrystalline samples revealed Arrhenius type semiconducting behaviour between 200-300 K with a RT resistivity value of 2 kΩ cm. First principle calculations performed on BaMnPF show that the *3d* bands of Mn are split by the magnetic exchange with a calculated magnetic moment of $3.35\mu_B$ per Mn atom. These calculations also showed the presence of a bandgap at Fermi level consistent with the observed insulating behaviour.[13]

A combination of synchrotron X-ray, neutron powder diffraction, magnetisation and electrical resistivity measurements have been used to study the NdMnAsO system. Neutron diffraction on NdMnAsO revealed G-type checkerboard AF magnetic ordering with an ordered moment $m_{z,Mn} = 2.41(6)\,\mu_B$ at room temperature. The Mn spins are aligned parallel to the c-axis down to 23 K when a spin reorientation (SR) transition of Mn moments into the *ab*-plane is observed.

3.1 Synthesis

A 2 gram polycrystalline NdMnAsO sample was prepared using solid state chemistry methods. Stoichiometric quantities of NdAs and MnO were mixed together using mortar and pestle, pressed into pellets and heated for 24 hrs at 1100 °C. MnO (99.999%) was obtained from Sigma Aldrich. NdAs was prepared from a stoichiometric mixture of Nd (Sigma Aldrich, 99.99%) and As (Sigma Aldrich, 99.9%) which was heated for 2 hrs at 500 °C in an evacuated quartz tube, immediately followed by 16 hrs at 900 °C.

3.2 Structural Analysis

High-resolution synchrotron powder diffraction measurements were done on the ESRF beam line ID31 at 4, 8, 12, 16, 20, 24, 28, 32, 50, 75, 100, 150, 200 and 250 K. The sample was contained in a 0.6 mm diameter borosilicate capillary. For all temperatures, the capillary was spun to improve the powder averaging of the crystallites, inside a liquid-helium-cooled flow cryostat. The X-ray wavelength used was 0.3998 Å. A linear absorption correction $\mu_r = 1.5$ was applied. The counts from the nine detectors of the various scans were normalized, summed, rebinned to a constant step size of 0.002° and then fitted using the GSAS program. Variable temperature neutron powder diffraction patterns were collected on the ILL beamline D20. The instrument was used in the high-flux setting with $\lambda = 2.41$ Å. The sample was contained in a 6 mm diameter cylindrical vanadium can. Between 1.6-30 K, 30 min data sets were collected at a fixed temperature. From 30-300 K, 5 min data sets were collected on a ramp of 1.25 K/min. A linear absorption correction $\mu_r = 0.3$ was applied. Rietveld analysis of the collected

powder diffraction data was done using the GSAS program. A pseudo-Voigt function was used to describe the peak shape for both types of data.

3.2.1 Variable Temperature High-resolution Synchrotron Powder Diffraction

Inspection of the high resolution data revealed that NdMnAsO has the tetragonal structure (SG *P4/nmm*) down to 4 K. The fit to the 4 K dataset is given in Fig. 3.1. A summary of the fitted parameters and selected bond distances and angles at 4, 100 and 250 K is given in Table 3.1.

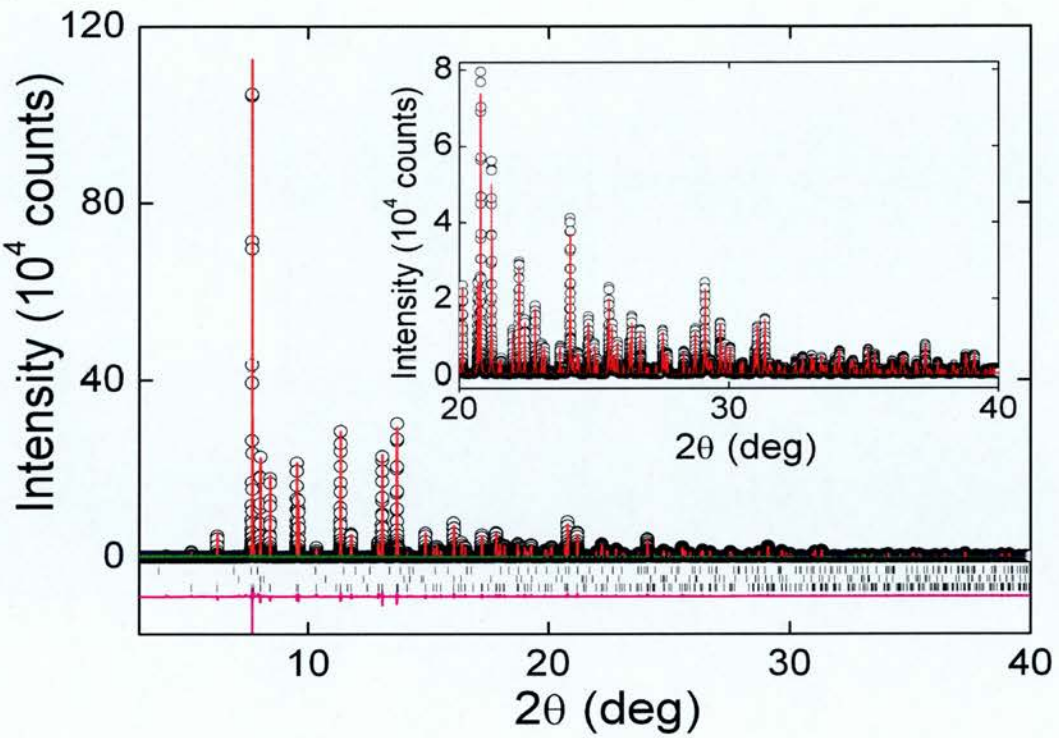

Figure 3.1: Rietveld fit against 4 K synchrotron X-ray powder diffraction data for NdMnAsO. Observed data are indicated by open circles, the fit by the solid line, and the difference curve is shown at the bottom. The Bragg markers are for NdMnAsO (bottom), MnAs (middle) and Nd_2O_3 (top).

Table 3.1: Refined lattice constants, atomic parameters, selected bond lengths (Å) and angles (°), and fit statistics for NdMnAsO from Rietveld fits against synchrotron X-ray powder diffraction data.

T (K)		4	100	250
SG		*P4/nmm*	*P4/nmm*	*P4/nmm*
a-axis (Å)		4.04446(1)	4.04503(1)	4.04979(5)
c-axis (Å)		8.87383(2)	8.88258(2)	8.89935(2)
Volume (Å^3)		145.16	145.34	145.97
Nd	U_{iso}(Å^2)	0.0010(1)	0.0025(1)	0.0053(1)
	Z	0.12991(5)	0.12992(4)	0.12976(4)
	Frac	1.00	1.00	1.00
Mn	U_{iso}(Å^2)	0.0017(1)	0.0039(2)	0.0073(2)
	Frac	1.00	1.00	1.00
As	U_{iso}(Å^2)	0.0013(1)	0.0044(2)	0.0071(2)
	Z	0.6737(1)	0.6736(1)	0.6736(1)
	Frac	1.00	1.00	1.00
O	U_{iso}(Å^2)	0.0041(1)	0.0046(1)	0.009(1)
	Frac	1.00	1.00	1.00
d(Nd-O) (Å)		2.3277(2)	2.3286(2)	2.3308(2)
∠Nd-O-Nd (°) 2x		120.63(2)	120.58(2)	120.63(2)
∠Nd-O-Nd (°) 4x		104.22(2)	104.22(2)	104.21(2)
d(Mn-As) (Å)		2.5456(5)	2.5424(4)	2.5468(4)
∠As-Mn-As (°) 2x		111.65(2)	111.54(1)	111.59(2)
∠As-Mn-As (°) 4x		105.20(3)	105.41(2)	105.32(2)
d(Mn-Mn) (Å)		2.85983(1)	2.86027(1)	2.86364(1)
χ^2		5.1	4.7	5.1
R_{wp} (%)		12.8	14.1	15.0
R_p (%)		8.3	9.6	9.6
R_F^2 (%)		4.3	5.5	5.1

Nd: 2c(¼, ¼, z); Mn: 2b(¾, ¼, ½); As: 2c(¼, ¼, z); O: 2a(¾, ¼, 0)

Impurities: 1.5(1) wt% Nd_2O_3, 1.0(1) wt% MnAs.

Upon cooling, the lattice contracts gradually and uniformly along *a*- and *c*-axis down to 4 K. The temperature evolution of the lattice constants is given in Fig. 3.2, 3.3. A typical Debye-like positive thermal expansion of the unit cell is observed with increasing temperature and can be adequately described by

$$V(T) = V_0 + A\coth\left(\frac{T_D}{T}\right) \tag{3.1}$$

Where $T_D = 204.1(2)$ K is the Debye temperature, $V_0 = 145.1(2)$ Å^3 is the unit cell volume at T→0, and A = 0.35(1) is a constant. The intraplanar Mn-Mn distance is found to elongate from $d_{Mn\text{-}Mn} = 2.8599(1)$ Å to $d_{Mn\text{-}Mn} = 2.8636(1)$ Å between 4 K and room temperature. The two-fold α (As-Mn-As) angle remains almost same with slight decrease from α = 111.65(2)° to α = 111.59(2)° upon cooling. The c/a ratio shows a slight discontinuity at 23 K, which may be related to the magnetic transition. No phase transitions are observed on cooling. Small impurity peaks have been observed due to the presence of Nd_2O_3 (1%). Refinement of the atomic site occupancies confirmed the nominal composition.

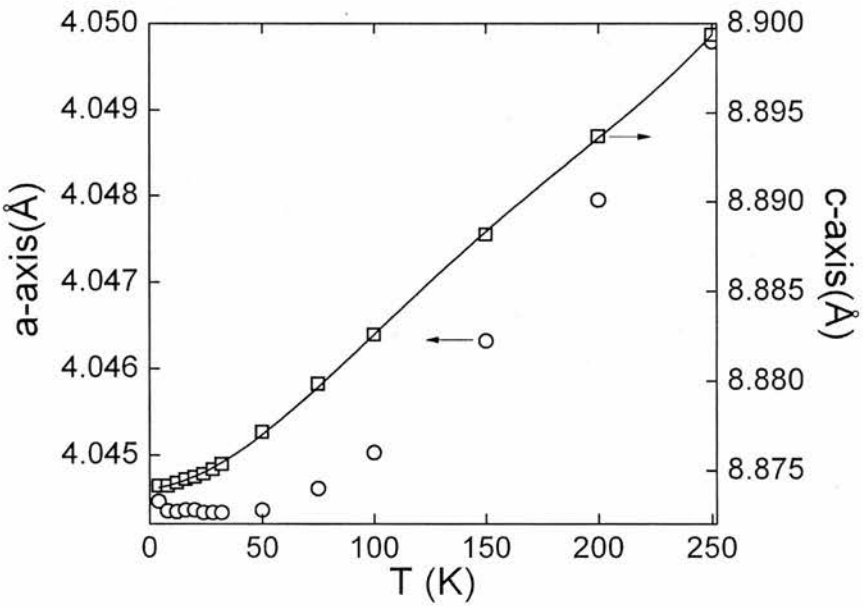

Figure 3.2: Temperature dependence of the crystallographic *a*- and *c*-axes for NdMnAsO. (The solid line is a guide to the eye).

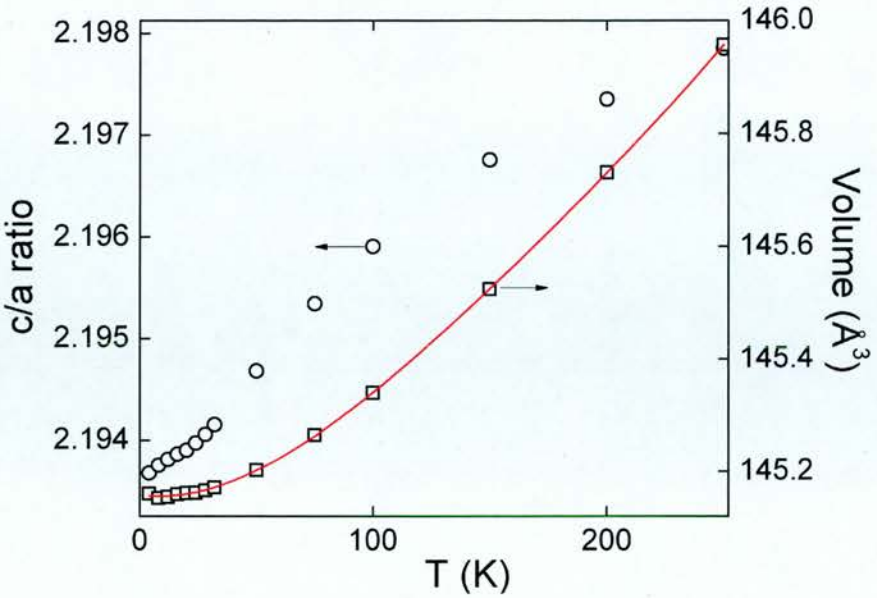

Figure 3.3: Temperature dependence of the unit cell volume and the *c/a* ratio for NdMnAsO. The solid line is fit to $V(T) = V_0 + A\coth\left(T_D/T\right)$.

3.2.2 High-flux Neutron Diffraction

NPD data were collected from 1.6 K up to 400 K. In the angular range displayed, the magnetic reflections (002) at 31.48°, (100) at 34.48°, (101) at 38.18° and (003) at 60.08° were observed below 360 K. Minor magnetic contributions were observed for (200) at 73.23° and (004) at 76.47°. The two most intense magnetic peaks have comparable intensities down to 23 K. Below this temperature, the presence of a third magnetic reflection (38.18°) is observed. This can be due to the differences in the magnetic ordering below and above this temperature. The NPD patterns collected at 1.6 K, 30 K, 300 K and 360 K are shown in Fig. 3.4. No phase transition is observed in the temperature range 1.6 K – 400 K. Small impurity peaks of Nd_2O_3 (3 %) and MnAs(1 %) are observed.

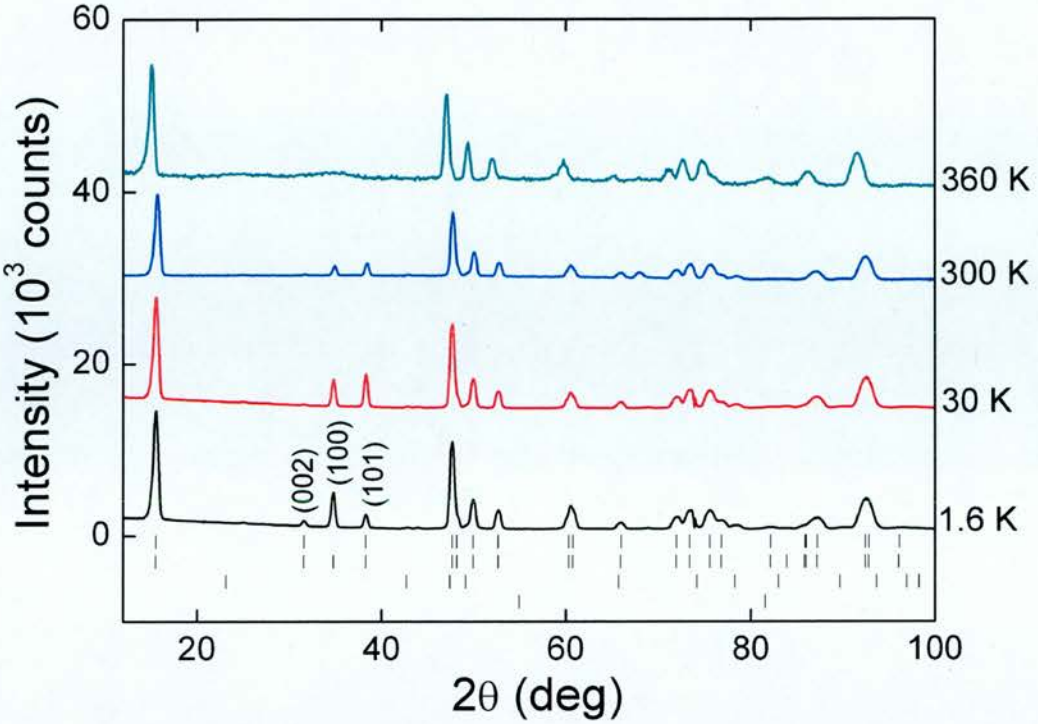

Figure 3.4: Comparison of the neutron powder patterns collected at different temperatures. From top to bottom: Bragg markers are for NdMnAsO, the magnetic phase, Nd_2O_3 and MnAs.

3.3 Magnetic Susceptibility

The DC magnetic susceptibility shown in Fig. 3.5 revealed a Curie-Weiss type paramagnetic behavior. The presence of Nd and Mn moments makes interpretation of the $\chi(T)$ data difficult. In particular, the data in Fig. 3.5 cannot be modelled using a single Curie-Weiss term, $\chi(T) = C/(T-\theta_W)$, unless χ_{Mn}(T) is negligible. To obtain an indication of the relative importance of the Nd and Mn contributions, $1/\chi$ was fitted to a single Curie-Weiss term between 125 and 300 K. This yields C = 2.39(2) emu $K^{-1}mol^{-1}$ and θ_W = - 43.1(8) K. The Curie constant (C) corresponds to an effective magnetic moment μ_{eff} = 4.37(3) μ_B. The fitted Curie constant is larger than the expected for $^4I_{9/2}$ Nd^{3+} (C = 1.6 emu K^{-1} mol^{-1}) which suggests that both Nd and Mn contribute to the $\chi(T)$ in this temperature interval. The negative Weiss temperature signals the presence of AFM interactions. Two magnetic transitions are evident. The first at 23 K, the second at 4 K. The neutron powder diffraction experiment allowed the transition at 23 K to be

assigned to a Nd induced spin-reorientation (TSR) transition, while the transition at 4 K corresponds to the saturation of the ordered Nd moments. The latter transition cannot be attributed to the magnetic impurities present (Table 3.1) as Nd_2O_3 does not order down to at least 1.8 K, and MnAs is a FM with a Curie temperature above RT. The field dependence of the magnetisation is shown in Fig. 3.6. Magnetic field dependence of the magnetisation showed linear behaviour in full range.

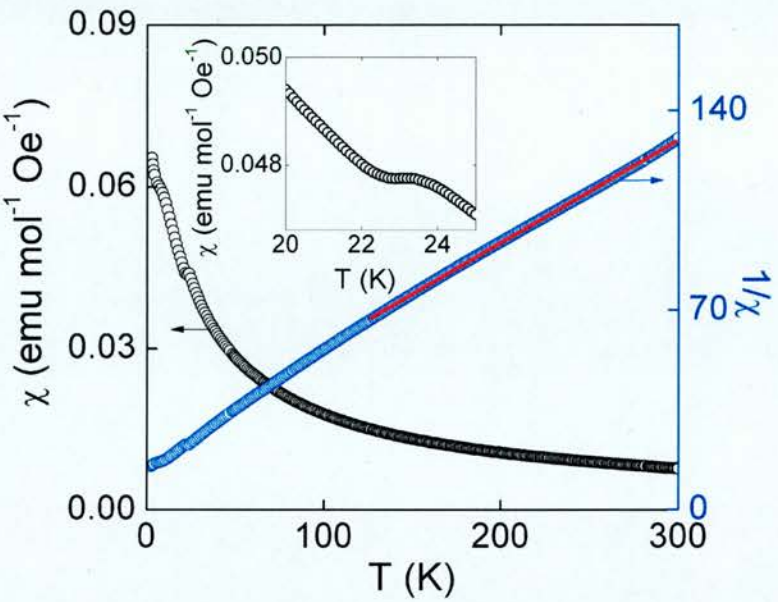

Figure 3.5: Temperature dependence of the zero field cooling (ZFC) magnetic and inverse magnetic susceptibilities for NdMnAsO. The solid line is a fit to the Curie-Weiss law.

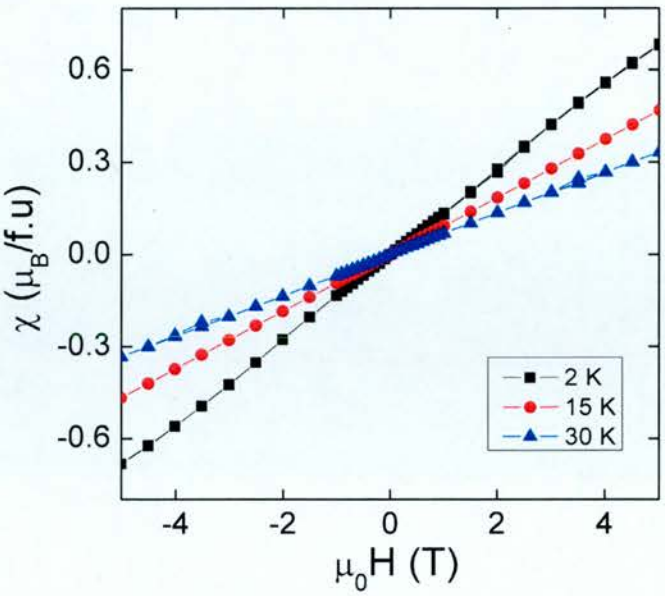

Figure 3. 6: Field dependence of the magnetisation at 2, 15 and 30 K.

3.4 Magnetic Structure

To recall, neutron data revealed magnetic contributions to the nuclear (102) and (103) reflections, and completely magnetic (100) and (101) reflections in the neutron-diffraction patterns from 300-25 K. Below 25 K, a magnetic contribution to the (002) reflection develops and there is a clear change in the relative intensities of the other magnetic reflections. In all cases, the magnetic reflections are indexed on the nuclear cell and the magnetic propagation vector $\vec{k} = (000)$ at all measured temperatures. The symmetry-allowed magnetic structures of NdMnAsO material were deduced using the SARA*h* Representational Analysis program.[15] The decomposition of the magnetic representation (Γ_{Mag}) into the irreducible representations (IRs) of $G_{\mathbf{k}}$ gave $\Gamma_3^1 + \Gamma_6^1 + \Gamma_9^2 + \Gamma_{10}^2$ for the Mn sites and $\Gamma_2^1 + \Gamma_3^1 + \Gamma_9^2 + \Gamma_{10}^2$ for the Nd sites. The representations used are after Kovalev,[16] and the character table can be found in Ref.[17] The symmetry allowed basis vectors are given in Table 3.2. These models have been refined using Rietveld least square fitting.

Table 3. 2: Basis vectors $[m_x, m_y, m_z]$ for space group *P4/nmm* with k = 0

	Γ_2^1	Γ_3^1	Γ_6^1	Γ_9^2	Γ_{10}^2
Mn1	-	[0 0 m_z]	[0 0 m_z]	[m_x m_y 0]	[m_x m_y 0]
Mn2	-	[0 0 m_z]	[0 0 -m_z]	[m_x m_y 0]	[-m_x -m_y 0]
Nd1	[0 0 m_z]	[0 0 m_z]	-	[m_x m_y 0]	[m_x m_y 0]
Nd2	[0 0 -m_z]	[0 0 m_z]	-	[m_x m_y 0]	[-m_x -m_y 0]
R_{wp} (1.6K)	10.5	-	9.3	-	5.4
R_{wp} (30K)	31.7^{US*}	-	5.1	-	16.3

* US: unstable, Mn1: (0.75, 0.25, 0.5), Mn2: (0.25, 0.75, 0.5), Nd1: (0.25, 0.25, 0.139) and Nd2: (0.75, 0.75, 0.861).

3.4.1 High-Temperature Magnetic Model

According to the negative Weiss temperature associated with AFM ordered Mn spins the basis vectors involved in the magnetic structure appeared to be limited to those associated with the IR Γ_6^1, Γ_2^1 (Mn site) and Γ_2^1, Γ_{10}^1 (Nd site). The AFM models differ in the magnetization direction, which is either along the *c*-axis or in the basal plane. NPD data were fitted firstly with models based on single IR because according to Landau theory, only a single IR becomes critical in a 2nd order phase transition. The magnetic peaks were best fitted with model (Γ_6^1) as shown in Fig. 3.7, i.e. using only AFM ordered Mn moments along *c*-axis down to 25 K. At room temperature the Mn moments are aligned parallel to the *c*-axis and nearest neighbour (NN) spins order AF within the MnAs layer, as depicted in Fig. 3.7. Trial refinements using linear combination of Γ_2^1 and Γ_6^1 models did not give a satisfactory fit. There is no evidence for Nd ordering above 23 K. The magnetic moment at RT has been found to be $m_{z,Mn} = 2.41(6)\ \mu_B$. The evolution of the Mn magnetic moment over the temperature interval 30-400 K is shown in Fig. 3.8. A fit to $M = M_0 * (1 - T/T_N)^{\beta}$ for $M_{Z,Mn}^{2+}$ yields $M_0 = 3.85(2)\ \mu_B$, $T_N = 354 \pm 5$ K, and $\beta = 0.27$ (1).

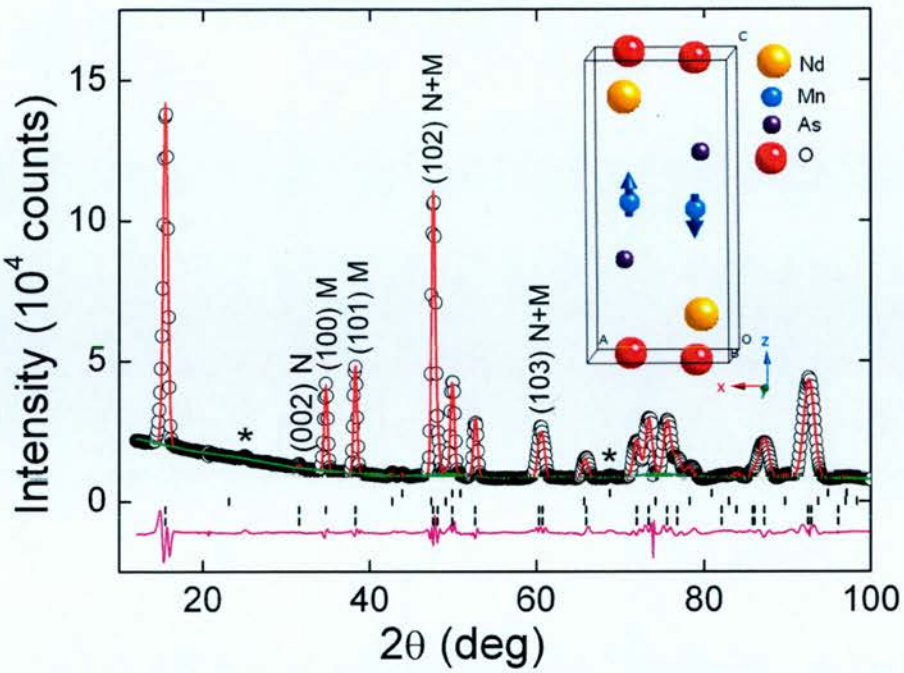

Figure 3.7: Rietveld fit against 30 K neutron powder diffraction data for NdMnAsO. The observed data are indicated by open circles, the fit by the solid line, and the difference curve is shown at the bottom. From bottom to top: Bragg markers are for NdMnAsO, the magnetic phase, Nd_2O_3 (2.0(2) wt%) and MnAs (1.0(2) wt%), (R_{wp} = 5.1%, R_p = 3.2% and R_F^2 = 3.4%). The inset shows a graphic representation of the fitted magnetic structure. *peaks represent unknown impurities.

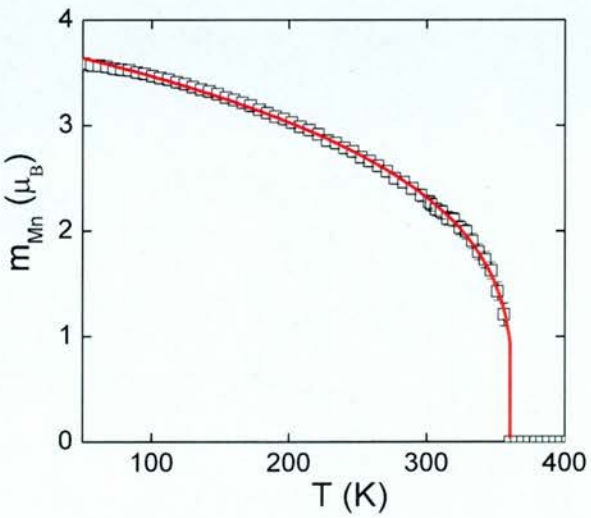

Figure 3.8: **Temperature evolution of the Mn moment between 50 K and 360 K. A solid line is fit to** $M = M_0 * (1 - T/T_N)^{\beta}$.

3.4.2 Low-Temperature Magnetic Model

For NPD patterns collected below 20 K, the magnetic peaks were well fitted using the Γ_{10}^{2} model with ordered Mn and Nd moments, which are both constrained to the basal plane (Fig. 3.9.). The ordered moments at 1.6 K are 3.72(1) μ_B for Mn and 1.941(1) μ_B for Nd. Rietveld refinements using models with an out-of-plane component on the Nd and/or the Mn sublattice did not result in an improvement, and were generally unstable.

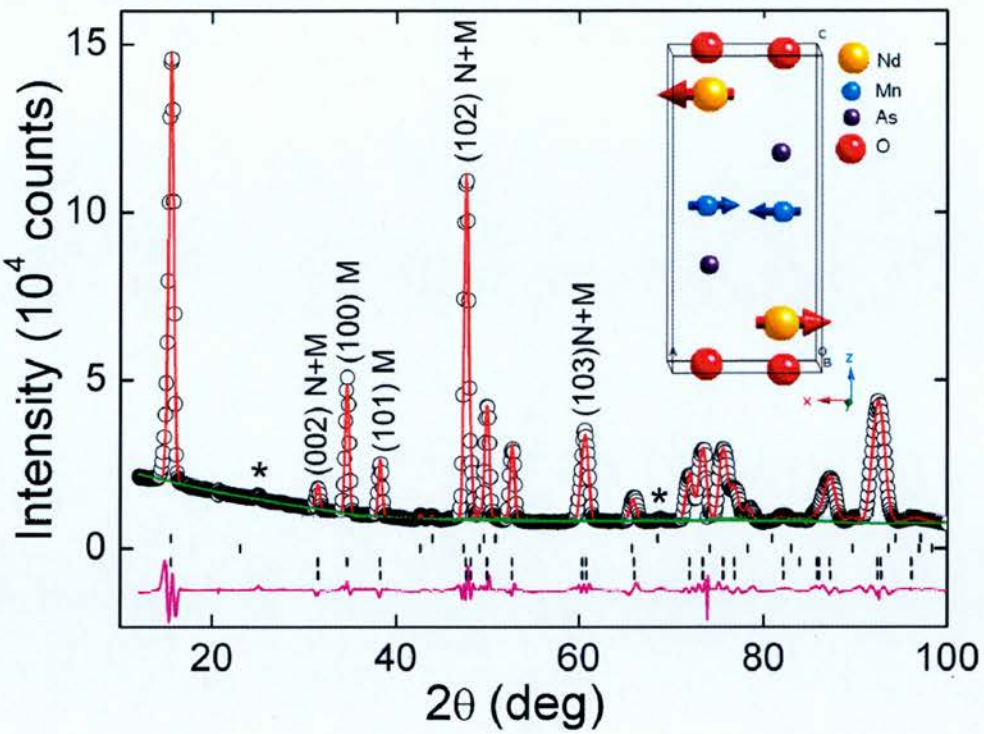

Figure 3.9: Rietveld fit against 1.6 K neutron powder diffraction data for NdMnAsO. The observed data are indicated by open circles, the fit by the solid line, and the difference curve is shown at the bottom. From bottom to top: Bragg markers are for NdMnAsO, the magnetic phase, Nd_2O_3 and MnAs, (R_{wp} = 5.5%, R_p = 3.1 % and R_F^2 = 5.1 %). The inset shows the graphic representation of the fitted magnetic structure.

3.4.3 Spin-Reorientation Transition

The transition between the HT (Γ_6^1) and LT (Γ_{10}^2) magnetic model occurs in a narrow temperature interval (20 K< T < 25 K) which is in good agreement with magnetic susceptibility and heat capacity measurements. In this temperature interval, the best fit was obtained using a model based on linear combination of the HT and LT models. This suggests that the Mn spin-reorientation transition (TSR) is induced by the ordering of Nd moments. The temperature evolution of the moments is shown in Fig. 3.10. First, a rapid increase of Nd component consistent with 2nd order transition is seen up to 0.9 μB followed by a gradual evolution to its maximum value 1.9 μB at 4 K, which corresponds to the second magnetic transition observed in magnetic susceptibility. No significant changes in magnetic intensities are observed above and below 4 K and the fit statistics using same magnetic model are comparable. Thus there is no evidence for a phase transition to a different magnetic structure at 4 K. The rotation angles (ϕ_{Mn}) of the Mn moment with respect to the c-axis are 12(10)° at 23.6(2) K, 29(5)° at 21.7(2) K, and 80(9)° at 19.9(2) K. The temperature evolution of the Mn/Nd moments is depicted in Fig. 3.10.

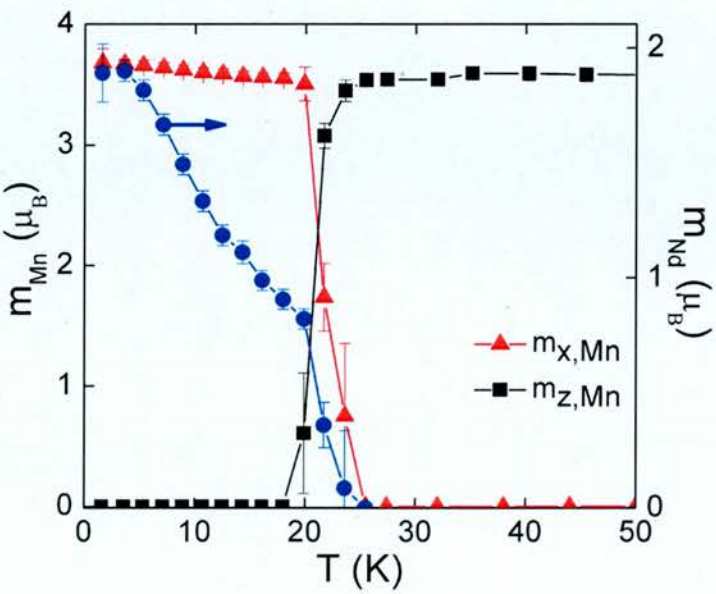

Figure 3.10: Temperature evolution of the Mn and Nd moments between 1.6 K and 50 K.

To further analyze the observed magnetic ordering, a schematic representation of the main magnetic interactions in NdMnAsO is shown in Fig. 3.11. Within the unit cell, the magnetic ions form a diamond shape with Nd at the top and bottom corners. The interaction between NN Mn-Mn moments (J_1) ($d = 2.86$ Å, shortest through-space distance is dominant and leads to the observed checkerboard magnetic ordering. Within the Nd-O_2-Nd blocks there are two main interactions: J_3 which cuts across the block Nd1-Nd2, ($d = 3.68$ Å), and J_4 which is along the block (Nd*n*-Nd*n*), $n = 1,2$, $d = 4.04$ Å). From our analysis, the interaction J_4 (Nd*n*-Nd*n*) within the Nd plane, is FM, while the J_3 interaction is AFM. The interaction between the Nd and Mn sublattices proceeds via four identical paths (J_2, $d = 3.86$ Å), which leads to a frustrated arrangement of symmetric Heisenberg exchange interactions between local moments. This leaves the weaker antisymmetric (Dzyaloshinsky-Moriya) exchange as the strongest magnetic interaction, and a postulated perpendicular orientation of the ordered Mn and Nd moments. Unfortunately, due to the tetragonal symmetry (which means the orientation of the magnetic moments within the *ab*-plane is not known) this cannot be verified experimentally.

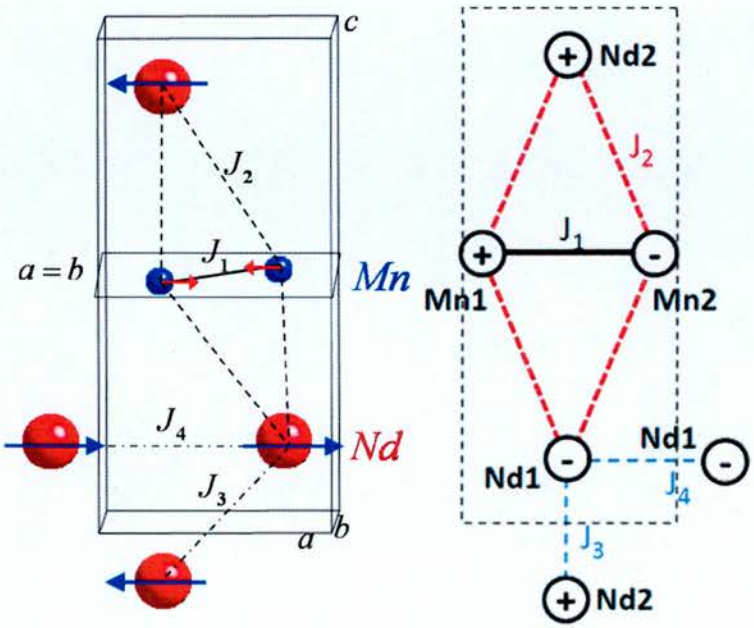

Figure 3.11: Representation of the magnetic interaction for NdMnAsO (left) within the tetragonal unit cell, (right) schematic representation. The orientation of the magnetic moments within the *ab*-plane is not known.

3.5 Electrical Resistivity

The temperature dependence of the electrical resistivity (ρ) is shown in Fig. 3.12. The magnitude of the resistivity falls between 25 and 50 Ω cm, which places NdMnAsO in the semiconducting regime. The temperature dependence is characterized by a broad hump at 250 K, above which semiconducting behavior is found, while below a metallic temperature dependence is evident. At the transition, TSR, the resistivity shows a moderate upturn, which may be due to increased spin scattering. The magnetoresistance (MR) was obtained from the symmetric part of R(H) curves measured between $9\ T \leq \mu_0 H \leq 9\ T$ and is depicted in Fig. 3.13. This was done to eliminate Hall effect contributions due to misalignment of the contact electrodes. At low temperatures ($T <$ 30 K), the field dependence shows a rapid drop followed by a saturation at the 1-2 percent level. At higher temperatures, the field dependence is linear with a similar MR of 2% in 9 T observed at 250 K.

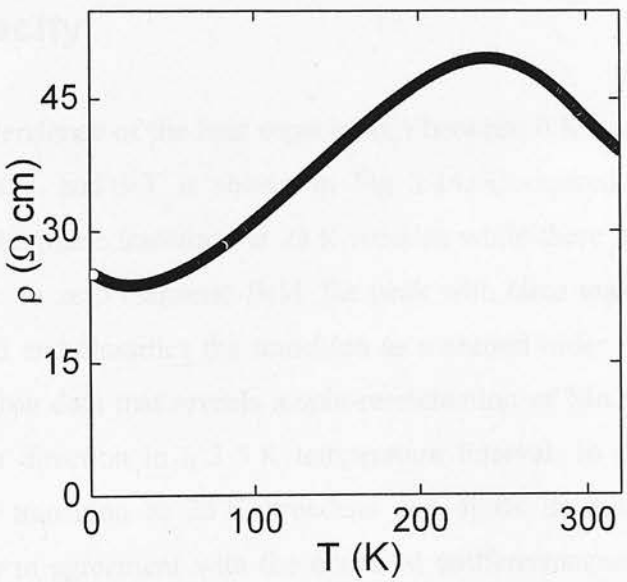

Figure 3. 12: Temperature dependence of the electrical resistivity for NdMnAsO

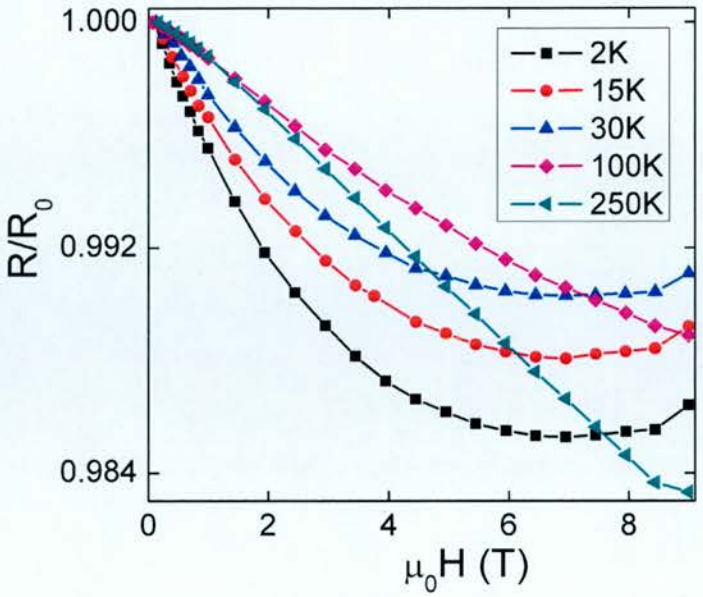

Figure 3.13: Field dependence of the normalized resistivity R/R_0 at 2, 15, 30, 100 and 250 K of NdMnAsO.

3.6 Heat Capacity

The temperature dependence of the heat capacity (C) between 0 K and 35 K in applied magnetic fields of 0 T and 9 T is shown in Fig 3.14. Compared to the magnetic susceptibility data, the phase transition at 23 K remains while there is no evidence for the transition at 4 K. In zero magnetic field, the peak with clear maximum at 23 K is somewhat broadened and classifies the transition as a second order transition. This is consistent with neutron data that reveals a spin-reorientation of Mn spins from c-axis direction into a-axis direction in a 3-5 K temperature interval. In the presence of a magnetic field, the transition at 23 K broadens and shifts its maximum to lower temperature. This is in agreement with the observed antiferromagnetic ordering. The inset (to Fig. 3.14) shows a typical linear fit to C/T versus T^2 at low temperatures, which indicates that the Sommerfeld coefficient is close to zero ($\gamma = 1.2(8)$ J mol^{-1} K^{-2}). This is in good agreement with the observed semiconducting behaviour.

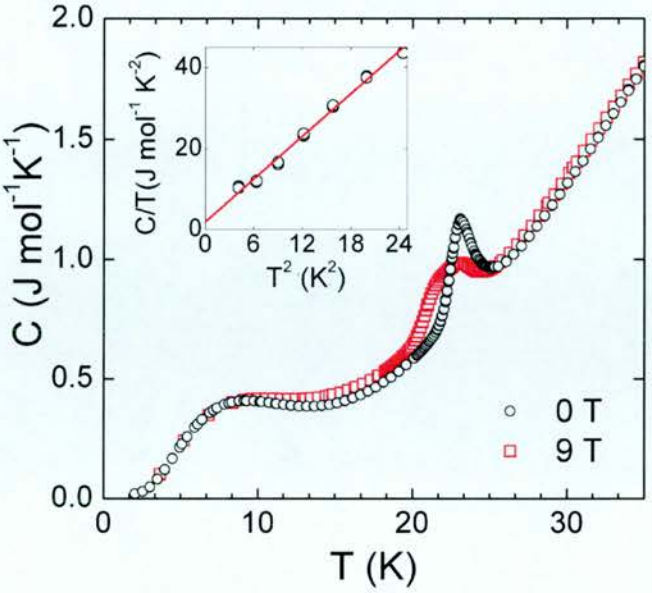

Figure 3.14: The temperature dependence of the heat capacity between 0 K and 35 K in applied magnetic fields of 0 T and 9 T. The inset shows a linear fit to C/T vs. T^2 in 0 T.

3.7 Discussion

The structures and properties of polycrystalline NdMnAsO have been studied using high-resolution synchrotron powder diffraction, neutron powder diffraction, magnetic susceptibility, electrical resistance and heat capacity measurements. Analysis of the room temperature crystal structure revealed that NdMnAsO has a tetragonal structure (SG *P4/nmm*), composed of alternating tetrahedral Mn-As and O-Nd layers. The crystallographic *a*-, *c*-axis and volume decrease smoothly upon cooling. The electronically important two-fold tetrahedral As–Mn–As angle (α) is 111.59(2)° at 300 K. This is similar to the literature values for LaMnPO (111.24°), but slightly bigger than the value for LaMnAsO (110.71°). The distance between two nearest Mn atoms has been found to be $d_{Mn\text{-}Mn}$ = 2.86364(1) Å, which is shorter than the Mn-Mn bond in NdMnPO [$d_{Mn\text{-}Mn}$ = 2.945(1) Å] but longer than that in NdMnSbO [$d_{Mn\text{-}Mn}$ = 2.821(1) Å]. On the other hand in the 122-type Mn analogues the Mn-Mn bond has been found to be generally longer, $d_{Mn\text{-}Mn}$ = 2.9475(2) Å in $BaMn_2As_2$, $d_{Mn\text{-}Mn}$ = 3.004(2) Å in $CaMn_2As_2$ and $d_{Mn\text{-}Mn}$ = 3.046(2) Å in $SrMn_2As_2$.

Rietveld fits to the NPD data between 360 K and 30 K revealed an AFM coupling of the Mn spins aligned along the c-axis and FM ordering between adjacent Mn planes. The refined magnetic moment at RT is $M_{,Mn}$ = 2.41(6) μ_B which is bigger that the magnetic moment in LaMnPO [$M_{,Mn}$ = 2.26(2) μ_B]. The extrapolated moment at 0 K is m_0 = 3.85(2) μ_B which is comparable to $m_{,Mn}$ = 3.88(4) μ_B in $BaMn_2As_2$. The Neél temperature [T_N = 359(2) K] is heavily reduced compared to $BaMn_2As_2$ with T_N = 625(1) K and $BaMn_2P_2$ with T_N > 750 K.[6, 11, 12] In addition, the critical exponent β = 0.27(1) is lower than reported for $BaMn_2As_2$ β = 0.35(2), which is close to the expected value for a three-dimensional Heisenberg magnet β = 0.367. At low temperatures (~23 K) NPD data revealed a SR transition of Mn spins aligned along the *c*-axis into the basal plane induced by the Nd ordering. This transition suggests a strong coupling between the Mn and Nd sublattices and occurs in a narrow temperature window (less than 3 K). The intermediate phase (20 K < *T* > 25 K) consists of the linear combination of the HT and LT model with the Φ_{Mn} being between 0°-90° with respect to the c-axis. This is in good agreement with a report on PrMnSbO[18] that shows an

identical SR transition occurring over a much wider temperature window (< 10 K). The narrow SR transition for NdMnAsO is in good agreement with magnetic susceptibility and heat capacity measurements that evidence a 2nd order transition. The probable cause of the SR transition is the competition between the single-ion anisotropy of Nd^{3+} and Mn^{2+} ions.[19] The Mn^{2+} ion (free ion values S = 5/2 and L = 0) prefers to order along the c-axis while Nd^{3+} prefers to be aligned within *ab*-plane (free ion values S = 3/2 and L = 6). Since single-ion anisotropy of Nd^{3+} dominates that of Mn^{2+} (L = 0): the SR transition of Mn moments can occur as soon as an ordered moment develops in the Nd sublattice.

Transport measurements revealed semiconducting behaviour for NdMnAsO with no evidence of significant magnetoresistance. The temperature dependence of the resistivity, described within this chapter, is suggestive of a degenerate semiconductor with a 290 K resistivity of ~40 Ω.cm and a maximum -MR of 2% is in an 9 T field. This contrasts to a study of (La,Nd)OMnAs systems published by Emery et al.,[20] where NdMnAsO is a disordered semiconductor (290 K resistivity = 1268 Ω.cm) with a sizeable -MR over a wide temperature range and exhibits an electronic transition at 150 K which appears to be coupled to the crystal lattice. Both samples are of similar quality (1.5 weight % MnAs) and the only difference appears to be the non-stoichiometry of the *RE* site in GMR *RE*MnAsO samples (*RE* = Nd and La).

The observed semiconducting behaviour is consistent with heat capacity measurements and gave a Sommerfeld coefficient close to zero [$\gamma = 1.2(8)$ J mol^{-1} K^{-2}].

3.8 References

1 D. Bérardan, L. Pinsard-Gaudart, and N. Dragoe, *Journal of Alloys and Compounds* **481**, (1-2), 470-472 (2009).

2 A. S. Sefat, A. Huq, M. A. McGuire, R. Jin, B. C. Sales, D. Mandrus, L. M. D. Cranswick, P. W. Stephens, and K. H. Stone, *Physical Review B (Condensed Matter and Materials Physics)* **78**, (10), 104505-9 (2008).

3 G. Cao, S. Jiang, X. Lin, C. Wang, Y. Li, Z. Ren, Q. Tao, C. Feng, J. Dai, Z. a. Xu, and F.-C. Zhang, *Physical Review B* **79**, (17), 174505 (2009).

4 H. Yanagi, R. Kawamura, T. Kamiya, Y. Kamihara, M. Hirano, T. Nakamura, H. Osawa, and H. Hosono, *Physical Review B* **77**, (22), 224431 (2008).

5 G. Cao, S. Jiang, X. Lin, C. Wang, Y. Li, Z. Ren, Q. Tao, C. Feng, J. Dai, Z. a. Xu, and F.-C. Zhang, *Physical Review B (Condensed Matter and Materials Physics)* **79**, (17), 174505-6 (2009).

6 J. An, A. S. Sefat, D. J. Singh, and M.-H. Du, *Physical Review B* **79**, (7), 075120 (2009).

7 A. S. Sefat, R. Jin, M. A. McGuire, B. C. Sales, D. J. Singh, and D. Mandrus, *Physical Review Letters* **101**, (11), 117004 (2008).

8 F. Ronning, E. D. Bauer, T. Park, N. Kurita, T. Klimczuk, R. Movshovich, A. S. Sefat, D. Mandrus, and J. D. Thompson, *Physica C: Superconductivity* **469**, (9-12), 396-403 (2009).

9 K. Sasmal, B. Lv, B. Lorenz, A. M. Guloy, F. Chen, Y.-Y. Xue, and C.-W. Chu, *Physical Review Letters* **101**, (10), 107007-4 (2008).

10 A. Leithe-Jasper, W. Schnelle, C. Geibel, and H. Rosner, *Physical Review Letters* **101**, (20), 207004-4 (2008).

11 S. L. Brock, J. E. Greedan, and S. M. Kauzlarich, *Journal of Solid State Chemistry* **113**, (2), 303-311 (1994).

12 Y. Singh, A. Ellern, and D. C. Johnston, *Physical Review B* **79**, (9), 094519 (2009).

13 H. Kabbour, L. Cario, and F. Boucher, *Journal of Materials Chemistry* **15**, (34), 3525-3531 (2005).

14 H. F. Wang, K. F. Cai, H. Li, L. Wang, and C. W. Zhou, *Journal of Alloys and Compounds* **477**, (1-2), 519-522 (2009).

15 A. S. Wills, *Physica B: Condensed Matter* **276-278**, 680-681 (2000).

16 O. V. Kovalev, *Representations of the Crystallographic Space Groups*. 2nd ed.; Gordon and Breach Science Publishers: Switzerland, 1993.

17 A. Marcinkova, D. A. M. Grist, I. Margiolaki, T. C. Hansen, S. Margadonna, and J. W. G. Bos, *Physical Review B* **81**, (6), 064511 (2010).

18 S. A. J. Kimber, A. H. Hill, Y. Z. Zhang, H. O. Jeschke, R. Valenti, C. Ritter, I. g, W. Hermes, R. Poettgen, and D. N. Argyriou, *Physical Review B* **82**, (10), 100412 (2010).

19 R. Sachidanandam, T. Yildirim, A. B. Harris, A. Aharony, and O. Entin-Wohlman, *Physical Review B* **56**, (1), 260 (1997).

20 N. Emery, E. J. Wildman, J. M. S. Skakle, G. Giriat, R. I. Smith, and A. C. McLaughlin, *Chemical Communications* **46**, (36), 6777-6779 (2010).

CHAPTER 4

Response of the Crystal Structure and Electronic Properties to Calcium Doping in NdFeAsO

4.1 Introduction

Most of the discovered 1111-type superconductors are characterized as electron-doped materials including substitutions such as $(O_{1-x}F_x)$,[1-3] (O_{1-d}),[4, 5] or by direct doping on the Fe site, $Fe_{1-x}T_{Mx}$, by for example T_M = Co, Ni, Ru, Rh.[6-9] Hydrostatic pressure has also been used to suppress the magnetic ordering and induce superconductivity.[10-12] Hole-doped 1111-type superconductors are less common. Iron-based materials are limited to strontium doped $La_{1-x}Sr_xFeAsO$ (with T_c = 25 K for x = 0.13),[13] $Nd_{1-x}Sr_xFeAsO$ (with T_c = 13.5 K for x = 0.2)[14] and $Pr_{1-x}Sr_xFeAsO$ (with T_c = 16.3 K for x = 0.25).[15] In other systems, $La_{1-x}Sr_xNiAsO$, in which the parent material was already found to be superconducting, Sr^{2+} doping led to an increase of T_c from 2.4 K to ~3.8 K.[16]

Other divalent cations that could be used as possible dopants are Ca^{2+} and Ba^{2+}. Superconductivity was achieved by substituting Tb^{3+} with Ca^{2+} in TbFeAsO system. The maximum superconducting transition temperature T_c = 15.6 K is found for x = 0.44.[17] The positive Hall coefficient, R_H, in a wide low-temperature range suggests that the hole-type charge carriers dominate the conduction in this system. The upper critical field, H_{c2}, of this sample using WHH model was estimated to be ~77T with the slope H_{c2}(T) of -7.1(1) T K^{-1}. No superconductivity has been found in calcium doped $RE_{1-x}Ca_xFeAsO$ (RE = La and Pr) samples above 1.8 K in quite a wide doping range ($0.10 \leq x \leq 0.50$).[17] In a superconducting LaFePO material (with T_c 2.4–5.5 K), Ca^{2+} doping increases T_c up to 7 K.[18] The observed T_c variation is presumably due to changes in the lattice parameters or carrier density caused by the compositional deviation from stoichiometry. In addition, a linear correlation was found between the T_c increase and unit cell volume.[18]

Factors which prevent calcium doped $RE_{1-x}Ca_xFeAsO$ (RE = La, Nd, Pr)[14, 15] materials from superconducting could be explain by structural differences between calcium systems and their strontium superconducting analogues.[19] Another very important factor is the difference of the ionic size of the RE and Sr/Ca elements.

4.2 Synthesis

Polycrystalline samples of $Nd_{1-x}Ca_xFeAsO$ (x = 0.025, 0.05, 0.075, 0.1, 0.125, 0.15 and 0.2) were prepared using standard solid state chemistry methods. Stoichiometric amounts of NdAs, FeAs, Fe, Fe_2O_3 and CaO were mixed using mortar and pestle and pressed into dense pellets. These were heated for 24 hours at 1150 °C with one intermediate regrinding. All chemicals were obtained from Sigma Aldrich with at least 99.9% purity and all sample manipulations were done inside an Ar filled glovebox. The precursors FeAs and NdAs were prepared from stoichiometric mixtures of the elements heated in evacuated quartz tubes for 2 hours at 500 °C, followed by 16 hours at 900 °C for NdAs and 750 °C for FeAs. The initial exploration of these materials was done on a 0.5 g scale. For x = 0 and x = 0.05, 2 g samples were prepared for neutron powder diffraction measurements.

4.3 Structural Analysis

High-resolution synchrotron powder diffraction measurements were done on the ESRF beam line ID31. The prepared samples were measured during two experiments; the first with $\lambda = 0.39986$ Å was done on compositions x = 0, 0.05, and 0.10; the second with $\lambda = 0.40030$ Å was done on x = 0.025, 0.05, 0.075, and 0.15. The x = 0.05 sample was measured in both experiments for scaling purposes. Variable-temperature high-resolution neutron powder diffraction data were collected on the ILL high-resolution super-D2B powder diffractometer. Data sets were collected between $2° \leq 2\theta \leq 40°$ and binned with a step size of 0.002° and then fitted using GSAS program. Data sets were recorded at 1.6 K and 175 K for x = 0 and x = 0.05. The instrument was used without additional collimation and with a large diameter beam to maximize the number of neutrons on the sample. The neutron wavelength used was $\lambda = 1.594$ Å. Data were

recorded at $5 \leq 2\theta \leq 160°$ with a stepsize of 0.05°. High-flux neutron powder diffraction experiments were performed on the ILL D20 instrument. The instrument was set up in the highest flux mode with $\lambda = 2.41$ Å. Data sets were collected over 4 h each at 1.6, 30, and 175 K in the $5° \leq 2\theta \leq 150°$ interval using a position sensitive detector.

4.3.1 High-resolution Synchrotron X-ray Powder Diffraction

The synchrotron diffraction data were used to follow the x-dependence of the room temperature crystal structure. The Rietveld fit for the x = 0.05 sample is shown in Fig. 4.1. Rietveld fitting of these data sets showed that the solubility of calcium is limited to x = 0.05. (by refinement of the Nd/Ca occupancies). Increasing the Ca^{2+} content leads to an expansion of the *ab*-plane, whereas the c-axis initially contracts and then increases slightly for x = 0.05 (Table 4.1). This results in an initial drop in cell volume followed by a modest increase (Table 4.1) and is consistent with the behaviour observed in the $Nd_{1-x}Sr_xFeAsO$ series.[14] In contrast to these changes, the modification of the FeAs tetrahedral layers upon doping is systematic (Fig. 4.2): First, the Fe-As distance decreases linearly upon increasing x, as is expected for hole doping (partial oxidation of Fe^{2+} to Fe^{3+}). Secondly, the Fe-As-Fe angle increases linearly, leading to a compression of the FeAs layer. The net effect of the shortened Fe-As bond and increase in Fe-As-Fe angle is a linear decrease in the FeAs layer thickness. The changes to the (Nd/Ca)-O and (Nd/Ca)-As bond lengths and angles are not linear but follow an increase-decrease (or decrease-increase) pattern, and are given in Table 4.1.

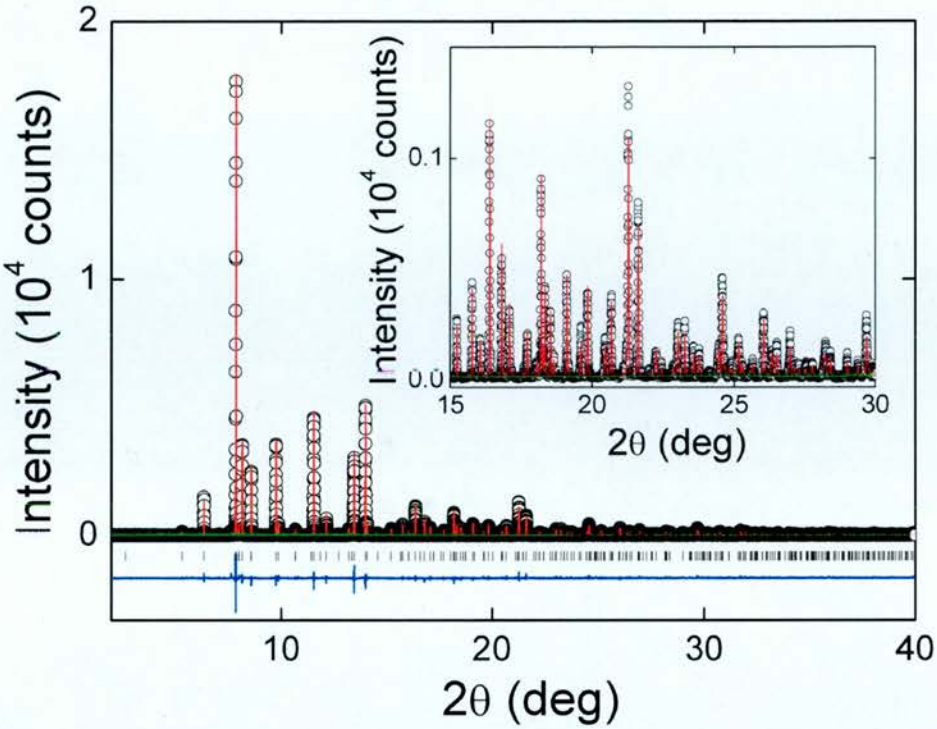

Figure 4.1: Rietveld refinement against RT synchrotron X-ray powder diffraction data for $Nd_{0.95}Ca_{0.05}FeAsO$. Observed data are indicated by open circles, the fit by the solid line, and the difference curve is shown at the bottom.

Table 4.1: Room temperature lattice constants, atomic parameters, selected bond lengths (Å) and angles (°), and fit statistics for the $Nd_{1-x}Ca_xFeAsO$ series.

$Nd_{1-x}Ca_xFeAsO$		x = 0	x = 0.025	x = 0.05
a-axis (Å)		3.96594(1)	3.96773(1)	3.96805(1)
c-axis (Å)		8.59786(5)	8.58658(5)	8.58668(5)
volume ($Å^3$)		135.233(1)	135.177(1)	135.201(1)
Nd	z	0.13888(6)	0.13935(6)	0.13894(7)
	frac	1.00	0.969(4)	0.950(5)
	Uiso ($Å^2$)	0.0068(2)	0.0057(2)	0.0045(2)
Ca	z	-	0.13935(6)	0.13894(7)
	frac	-	0.031(4)	0.050(5)
	Uiso ($Å^2$)	-	0.0057(2)	0.0045(2)
Fe	Uiso ($Å^2$)	0.0062(2)	0.0059(4)	0.0046(4)
As	z	0.6575(1)	0.6572(1)	0.6568(1)
	Uiso ($Å^2$)	0.0062(3)	0.0074(3)	0.0057(3)
O	Uiso ($Å^2$)	0.003(1)	0.016(2)	0.018(2)
d(Fe-As) (Å)		2.4010(5)	2.3996(6)	2.3979(7)
∠As-Fe-As (°)		111.36(4)	111.53(4)	111.66(5)
		108.54(2)	108.45(2)	108.39(2)
d(Nd-As) (Å)		3.3061(5)	3.3045(6)	3.3087(7)
∠As-Nd-As (°)		116.04(3)	116.18(3)	115.99(4)
d(Nd-O) (Å)		2.3147(3)	2.3168(3)	2.3151(3)
∠O-Nd-O (°)		117.89(2)	117.81(2)	117.96(2)
χ^2		2.0	2.1	2.1
wR_p (%)		15.2	18.1	18.1
R_p (%)		11.7	11.8	12.7
R_F^2 (%)		7.61	5.6	5.1

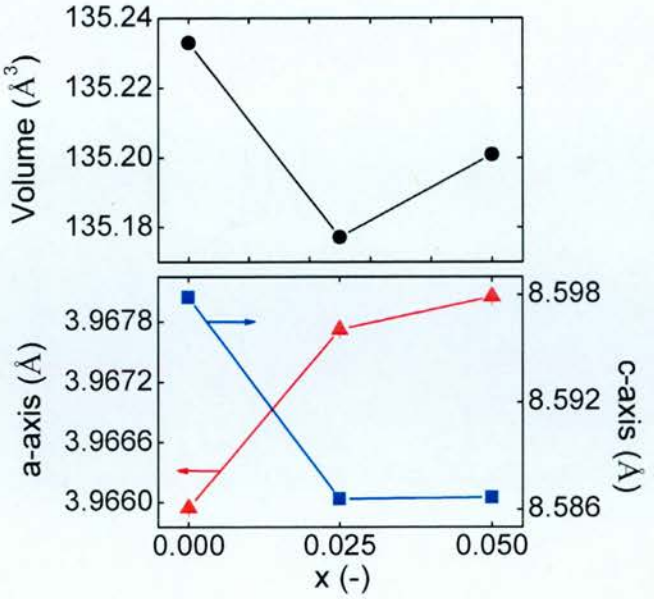

Figure 4. 2: Doping dependence of the cell volume, a and c axes of the $Nd_{1-x}Ca_xFeAsO$.

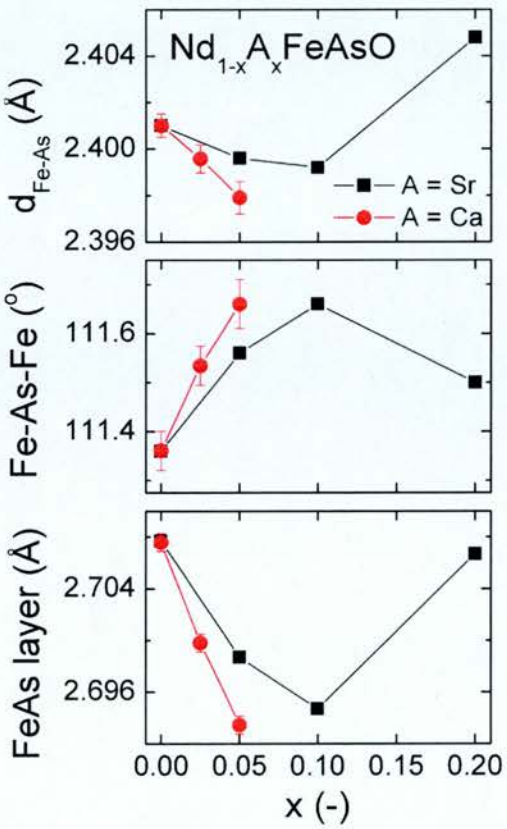

Figure 4. 3: Doping dependence of the Fe-As bond distance, As-Fe-As tetrahedral angle, and FeAs layer thickness of the $Nd_{1-x}A_xFeAsO$ (A = Sr, Ca). Sr data taken from the literature.[14]

4.3.2 Variable Temperature High-resolution Neutron Diffraction

High-resolution neutron powder diffraction has been used to follow the temperature dependence of the lattice parameters of $Nd_{1-x}Ca_xFeAsO$ for x = 0 and 0.05, respectively. The datasets collected at 175 K confirmed the tetragonal *P4/nmm* structure with atomic positions given in Table 4.2. On cooling to 4 K, a structural phase transtion from tetragonal to orthorhombic (SG *Cmma*) occurs. The refined lattice constants, atomic parameters and selected bond length and angles for x = 0 and x = 0.05 at 1.6 and 175 K are given in Table 4.2. The Rietveld fit to the 1.6 K D2B neutron powder diffraction pattern for $Nd_{0.95}Ca_{0.05}FeAsO$ is shown in Fig. 4.4.

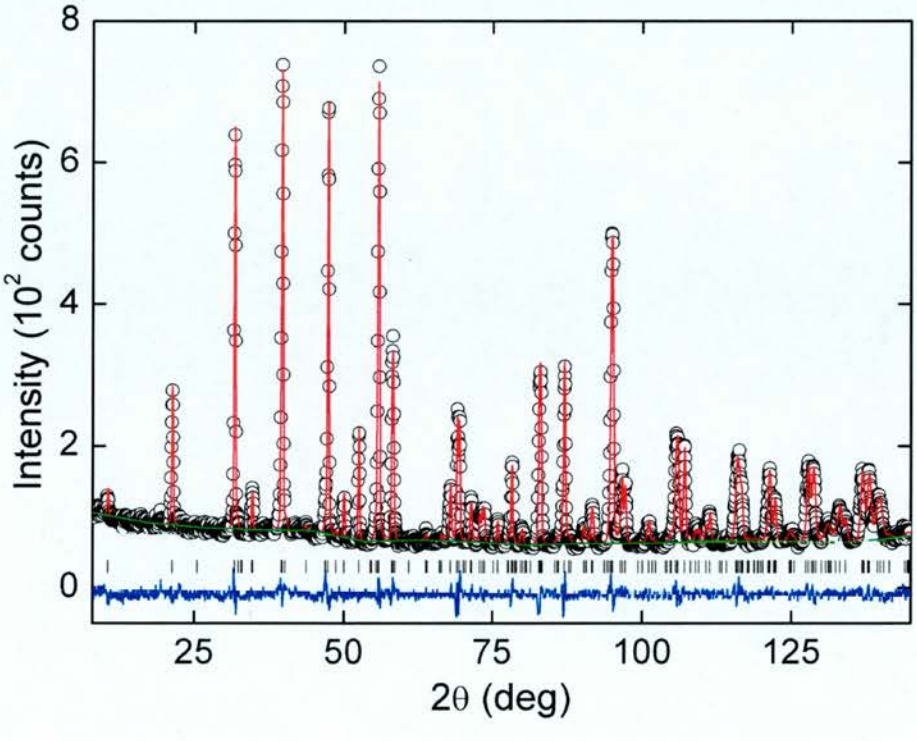

Figure 4.4: Rietveld refinement against 1.6 K D2B neutron powder diffraction data for $Nd_{0.95}Ca_{0.05}FeAsO$. The observed data are indicated by open circles, the fit by the solid line, and the difference curve is shown at the bottom.

Table 4.2: Lattice constants, atomic parameters and selected bond lengths (Å) and angles (°) for $Nd_{1-x}Ca_xFeAsO$ from variable temperature D2B neutron powder diffraction data.

$Nd_{1-x}Ca_xFeAsO$		x = 0		x = 0.05	
T (K)		175	1.6	175	1.6
Space group		P4/nmm	Cmma	P4/nmm	Cmma
a-axis (Å)		3.96133(4)	5.6154(1)	3.96351(5)	5.6157(1)
b-axis (Å)			5.5856(1)		5.5908(1)
c-axis (Å)		8.5772(2)	8.5591(2)	8.5662(2)	8.5479(2)
volume ($Å^3$)		134.597(3)	268.461(7)	134.570(5)	268.372(6)
Nd/Ca	z	0.1389(2)	0.1390(2)	0.1388(2)	0.1389(2)
	Uiso($Å^2$)	0.0036(7)	0.0004(6)	0.0023(6)	0.0005(6)
Fe	Uiso($Å^2$)	0.0076(6)	0.0062(6)	0.0079(5)	0.0061(6)
As	z	0.6582(3)	0.6587(3)	0.6574(3)	0.6578(3)
	Uiso($Å^2$)	0.0078(7)	0.0059(7)	0.0072(7)	0.0043(8)
O	Uiso($Å^2$)	0.0061(8)	0.0049(8)	0.0050(7)	0.0049(6)
χ^2		2.4	2.4	2.9	2.8
$_wR_p$ (%)		5.2	5.2	5.9	5.7
R_p (%)		4.1	4.1	4.6	4.5
R_F^2 (%)		4.1	4.3	4.2	4.6
d(Fe-As) (Å)		2.401(2)	2.401(2)	2.397(2)	2.397(2)
∠As-Fe-As (°)		111.2(1)	111.1(1)	111.5(1)	111.5(1)
		108.64(5)	108.45(5)	108.45(5)	108.28(5)
			108.89(5)		108.65(5)
d(Nd-O) (Å)		2.311(1)	2.310(1)	2.311(1)	2.310(1)
d(Nd-As) (Å)		3.298(1)	3.299(1)	3.302(1)	3.302(1)
			3.286(1)		3.292(1)
d(Fe-Fe) (Å)		2.80108(3)	2.80771(6)	2.80263(3)	2.80785(5)
			2.79280(6)		2.79538(5)

4.4 Magnetic Susceptibility

The inverse magnetic susceptibilities of the $Nd_{1-x}Ca_xFeAsO$ samples (Fig. 4.5) revealed paramagnetic behavior throughout the temperature range 2 K-300 K. A fit to $\chi = C/(T-\theta)$ yields C = 2.05(1) emu K^{-1} mol^{-1} and θ = -25.9(1) K for x = 0, C = 1.62 (2) emu K^{-1} mol^{-1} and θ = -30.9(1) K for x = 0.025, and C = 1.39(2) emu K^{-1} mol^{-1} and θ = -34.8(1) K for x = 0.05. For x = 0, 0.025 , the inverse magnetic susceptibilities are dominated by the paramagnetic Nd^{3+} moments and the fitted Curie constants are larger than the expected one (dash-dot line, Fig. 4.5) for paramagnetic $^4I_{9/2}$ Nd^{3+} [C = 1.6 emu K^{-1} mol^{-1}] which suggest that both Nd and Fe contribute to $\chi(T)$ in this temperature interval. In x = 0.05 sample, decrease of the Curie constant is a result of decreasing paramagnetic Nd^{3+} content. The fitted Curie constants are shown in the inset to Fig. 4.5 and reveal a linear decrease which can be explained by replacing magnetic Nd^{3+} by diamagnetic Ca^{2+}. Negative Weiss temperatures (θ) indicate an antiferromagnetic interaction between Nd^{3+} spins.

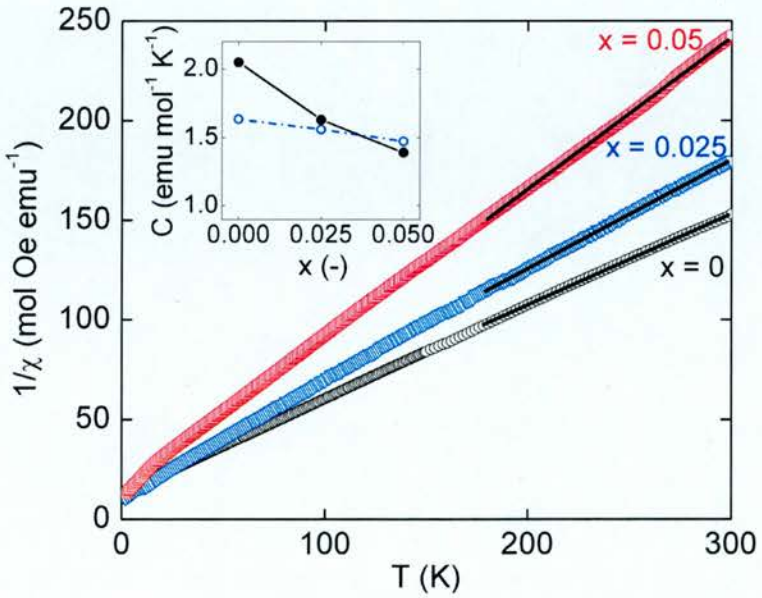

Figure 4.5: Temperature dependence of inverse magnetic susceptibility for the $Nd_{1-x}Ca_xFeAsO$ serie. The inset shows the experimental (solid line) and calculated Curie constant (dash-dot line) for Nd^{3+} ($^4I_{9/2}$).

4.5 Magnetic Structure

High-flux neutron powder diffraction patterns collected at 1.6, 30 and 175 K have been subtracted in order to separate the magnetic scattering from the structural contribution. The 2 K-30 K difference NPD pattern consists of two strong and five small magnetic reflections. For x = 0, possible magnetic structures are discussed in chapter 5.3.2. For x = 0.05, the 2-30 K difference pattern (Fig. 4.6) shows an identical magnetic diffraction pattern to that observed for x = 0. The reduction in intensities is consistent with a slightly lower ordering temperature of the Nd-sublattice resulting from the dilution of the magnetic Nd^{3+} lattice by non-magnetic Ca^{2+}. All magnetic peaks can be index using the orthorhombic nuclear cell and magnetic model proposed by Qiu et al was used to refine magnetic Nd/Fe magnetic moments. The refined magnetic moments for $Nd_{0.95}Ca_{0.05}FeAsO$ are $m_x = 0.26(6)\ \mu_B$, $m_z = 0.42(5)\ \mu_B$ and $m = 0.50(2)\ \mu_B$ for Nd and $m_x = 0.27(5)\ \mu_B$ for Fe. The Rietveld fits to 2-30 K neutron powder diffraction patterns for x = 0 and x = 0.05 are shown in Fig 4.6.

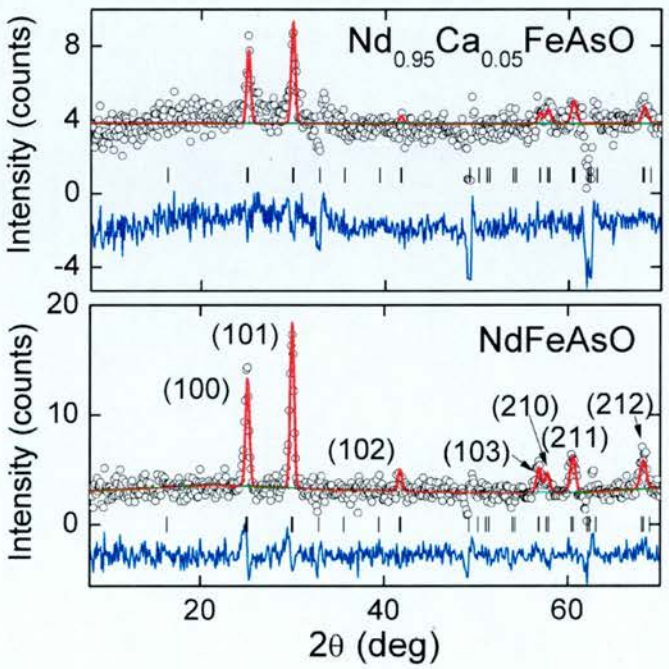

Figure 4.6: The Rietveld fit against 2 K-30 K difference neutron powder pattern for $Nd_{0.95}Ca_{0.05}FeAsO$ and parent material NdFeAsO.

4.5 Electrical Resistivity

The temperature dependence of the resistance for $Nd_{1-x}Ca_xFeAsO$ is shown in Fig. 4.7. For x = 0, the resistance is dominated by a drop, which occurs below $T \sim 160$ K with maximum slope at ~140 K. This is associated with the $T \rightarrow O$ structural transition, which is caused by the SDW transition and occurs around 140 K. Upon Ca^{2+} substitution, the temperature dependence of the resistance changes from metallic (x = 0) to semiconducting (x = 0.025) and remains semiconducting for x = 0.05. Moreover, the drop is almost suppressed for x = 0.025 and re-appears for x = 0.05. In fact, for x = 0.025 dR/dT < 0 indicating semiconducting behavior over the entire temperature range, while the maximum slope occurs around ~ 126 K. For x = 0.05, $T_{max} \sim 146$ K while $(dR/dT)_{max} = 132$ K.

The magnetic field dependence of the resistance of the $Nd_{1-x}Ca_xFeAsO$ samples has been measured between -9 T ≤ $\mu_0 H$ ≤ 9 T. The symmetric part of the magnetoresistance ($MR = R/R_0$) is shown in Fig. 4.8. The inset in Fig 4.8 shows the as measured R(H) curves, which were found to be a bit asymmetric due to the slight misalignment of the contact electrodes. For x = 0, the MR curve shows H^2 dependence typical for metals in applied magnetic field below H = 1 T. With increasing magnitude of the H the R/R_0 can be fitted to a power law with an exponent n=1.44 (1) (see Fig. 4.8.). Upon doping with Ca^{2+}, the magnitude of the MR is reduced dramatically. The MR at 9 T is 1.6 for x = 0, while it drops to 1.03 for x = 0.025 and 1.06 for x = 0.05, respectively. Moreover, at low magnetic fields, the MR does not follow a H^2 dependence and is no longer typical of metal. Furthermore, a discontinuity in field dependence is visible at ~ 5.5 T for x = 0.025 and ~ 4 T for x = 0.05 (Fig 4.7). For x = 0.025 power law fits yield n = 1.38(1) for $0 \leq \mu_0 H \leq 5.5$ T and n = 1.15(3) for $5.5 < \mu_0 H \leq 8.5$ T. For x = 0.05, the values are n = 1.22(1) for $0 \leq \mu_0 H \leq 4$ T and n = 0.94(3) for $4 < \mu_0 H \leq 8.5$ T. In larger magnetic fields the MR becomes more linear for x > 0.

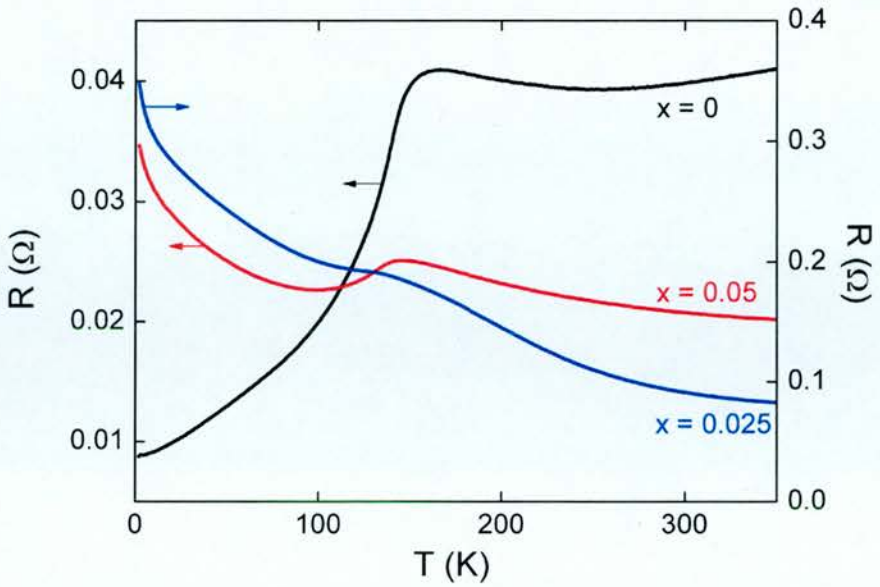

Figure 4.7: The temperature dependence of the resistance for $Nd_{1-x}Ca_xFeAsO$

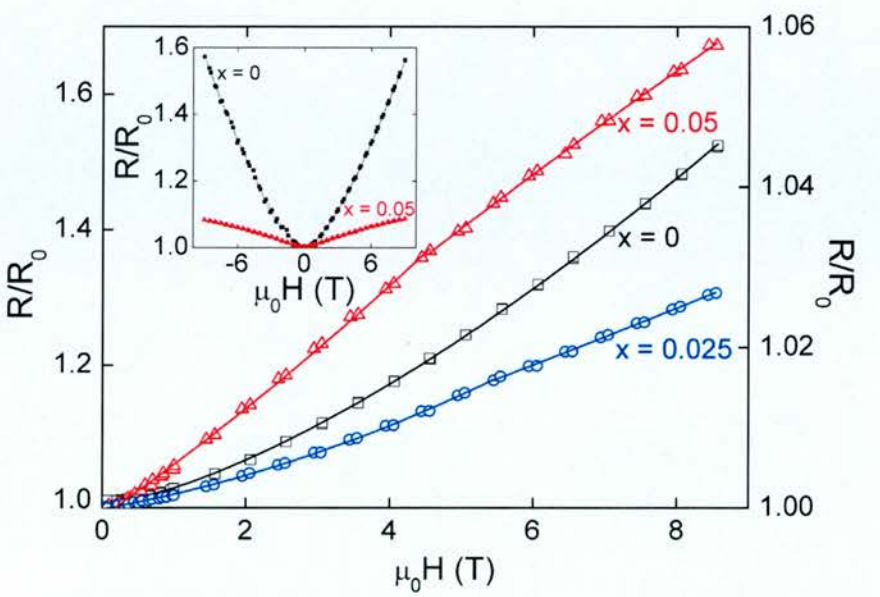

Figure 4.8: Magnetic field dependence of the magnetoresistance for $Nd_{1-x}Ca_xFeAsO$. The solid lines represent fits to power laws. The inset shows raw data collected for x = 0 and 0.05.

4.6 Discussion

The structure and properties of polycrystalline $Nd_{1-x}Ca_xFeAsO$ samples have been studied using high-resolution synchrotron powder diffraction, neutron powder diffraction, magnetic susceptibility, electrical resistance measurements. Analysis of the room temperature Synchrotron powder X-ray diffraction data revealed that the $Nd_{1-x}Ca_xFeAsO$ series forms for $0 \leq x \leq 0.05$. Hole doping via Ca^{2+} results in a formal $Fe^{(2+x)+}$ and with increasing x a linear contraction in FeAs layer thickness is observed up to $x = 0.05$ above which the structure is no longer stable. The electronically important two-fold angle (α) remains almost unchanged and is $\alpha = 111.36(4)$ for $x = 0$ and $\alpha = 111.66(5)$ for $x = 0.05$ at room temperature, respectively.

The decrease in the FeAs layer thickness for $Nd_{1-x}Ca_xFeAsO$ is consistent with hole doping of the anti-bonding iron bands at the Fermi level. This results in a depletion of *n*-type charge carriers as evidenced by the transition from metallic to semiconducting behaviour (Fig. 4.7). Upon doping the SDW remains, but $(dR/dT)_{max}$ follows decrease-increase trend with $(dR/dT)_{max} = 140$ K for $x = 0$, $(dR/dT)_{max} = 126$ K for $x = 0.025$ and $(dR/dT)_{max} = 130$ K for $x = 0.05$. The investigation of the magnetoresistance reveals that the Ca^{2+} doping dramatically changes the magnitude and shape of the MR. The field dependence changes from $\propto H^2$ behaviour ($x = 0$) to an almost linear behaviour at higher applied magnetic fields (x= 0.025, 005), with transitions at ~ 5.5 T for $x = 0.05$ and ~ 4 T for $x = 0.025$. This change in the magnitude and shape of the MR could be related to the SDW and to the number of free carriers. The magnitude of the MR has been found to be larger for the of 1111-*RE*FeAsO materials than for the 122-*Ae*Fe_2As_2 group. For example the MR for NdFeAsO is 1.35 while that for $BaFe_2As_2$ is only ~1.1 (both at 5 K and 6.5 T). This suggests that there might be a correlation with the ordered iron moment found from neutron powder diffraction, which is typically lower for the *RE*FeAsO samples [0.25(7) μ_B for NdFeAsO compared to 0.87(3) μ_B for $BaFe_2As_2$]. Generally, materials with stronger fluctuations (lower ordered Fe moment) have larger positive MR. It is worth pointing out that the MR

shows an anomaly at the *RE*-sublattice ordering temperature for *RE* = Ce, Pr, and Nd, despite the absence of significant bonding between (RE_2O_2) and (Fe_2As_2) layers.

The reduction in magnetic intensities (Fig. 4.5) is consistent with a slightly lower ordering temperature of the Nd-sublattice resulting from the dilution of the magnetic Nd^{3+} lattice by non-magnetic Ca^{2+}. Furthermore simultaneous Fe- and Nd-spin order is observed at 1.6 K while no SDW ordering of the Fe-spins could be detected at 30 K, revealing that ordering of the rare-earth sublattice strongly enhances the ordered iron moment.

4.7 References

1 K. Kuroki, S. Onari, R. Arita, H. Usui, Y. Tanaka, H. Kontani, and H. Aoki, *Physical Review Letters* **101**, (8), 087004 (2008).

2 S. Margadonna, Y. Takabayashi, M. T. McDonald, M. Brunelli, G. Wu, R. H. Liu, X. H. Chen, and K. Prassides, *Physical Review B (Condensed Matter and Materials Physics)* **79**, (1), 014503-7 (2009).

3 I. I. Mazin, D. J. Singh, M. D. Johannes, and M. H. Du, *Physical Review Letters* **101**, (5), 057003 (2008).

4 H. Kito, H. Eisaki, and A. Iyo, *Journal of the Physical Society of Japan* **77**, (6), (2008).

5 Z.-A. Ren, G.-C. Che, X.-L. Dong, J. Yang, W. Lu, W. Yi, X.-L. Shen, Z.-C. Li, L.-L. Sun, F. Zhou, and Z.-X. Zhao, *EPL (Europhysics Letters)* **83**, (1), 17002 (2008).

6 D. Kasinathan, A. Ormeci, K. Koch, U. Burkhardt, W. Schnelle, A. Leithe-Jasper, and H. Rosner, *New Journal of Physics* **11**, (2), 025023 (2009).

7 Y. Qi, Z. Gao, L. Wang, D. Wang, X. Zhang, and Y. Ma, *Superconductor Science and Technology* **21**, (11), 115016 (2008).

8 A. Marcinkova, D. A. M. Grist, I. Margiolaki, T. C. Hansen, S. Margadonna, and J. W. G. Bos, *Physical Review B* **81**, (6), 064511 (2010).

9 J. Yang, Z. C. Li, W. Lu, W. Yi, X. L. Shen, Z.-A. Ren, G. C. Chen, X. L. Dong, L. L. Sun, F. Zhou, and Z. X. Zhao, *Superconductor Science and Technology* **21**, (8), 082001 (2008).

10 J. W. G. Bos, G. B. S. Penny, J. A. Rodgers, D. A. Sokolov, A. D. Huxley, and J. P. Attfield, *Chemical Communications* **31**, 3634 (2008).

11 S. Margadonna, Y. Takabayashi, Y. Ohishi, Y. Mizuguchi, Y. Takano, T. Kagayama, T. Nakagawa, M. Takata, and K. Prassides, *Physical Review B (Condensed Matter and Materials Physics)* **80**, (6), 064506-6 (2009).

12 J. A. Rodgers, G. B. S. Penny, A. Marcinkova, J.-W. G. Bos, D. A. Sokolov, A. Kusmartseva, A. D. Huxley, and J. P. Attfield, *Physical Review B* **80**, (5), 052508 (2009).

13 H.-H. Wen, G. Mu, L. Fang, H. Yang, and X. Zhu, *EPL (Europhysics Letters)* **82**, (1), 17009 (2008).

14 K. Kasperkiewicz, J.-W. G. Bos, A. N. Fitch, K. Prassides, and S. Margadonna, *Chemical Communications*, (6), 707-709 (2009).

15 G. Mu, B. Zeng, X. Zhu, F. Han, P. Cheng, B. Shen, and H.-H. Wen, *Physical Review B* **79**, (10), 104501 (2009).

16 L. Fang, H. Yang, P. Cheng, X. Zhu, G. Mu, and H.-H. Wen, *Physical Review B* **78**, (10), 104528 (2008).

17 G. Mu, P. Zeng, P. Cheng, X. Zhu, F. Han, B. Shen, and H. H. Wen, *EPL (Europhysics Letters)* **89**, (2), 27002 (2010).

18 Y. Kamihara, T. Watanabe, M. Hirano, and H. Hosono, *Journal of the American Chemical Society* **130**, (11), 3296-3297 (2008).

19 G. F. Chen, Z. Li, D. Wu, G. Li, W. Z. Hu, J. Dong, P. Zheng, J. L. Luo, and N. L. Wang, *Physical Review Letters* **100**, (24), 247002-4 (2008).

CHAPTER 5

Magnetism and Superconductivity in $NdFe_{1-x}Co_xAsO$ ($0 \leq x \leq 1$)

5.1 Introduction

Superconductivity induced by Co doping was first reported for the 1111-type material $LaFe_{1-x}Co_xAsO$.[1] Upon Co doping, the stripe-like AFM order is destroyed and superconductivity is observed at $T_c = 11.2$ K for x = 0.05, at $T_c = 14.3$ K for x = 0.11 and at $T_c = 6$ K for x = 0.15. The superconducting (SC) transition widths are 3.2, 2.3, and 3.9 K, respectively. Other well characterized 1111-type superconductors include $SmFe_{1-x}Co_xAsO$ (with $T_c = 17.2$ K for x = 0.1)[2] and 1111-type $CaFe_{1-x}Co_xAsF$ (with $T_c = 22$ K for x = 0.1).[3] In the 122-type $AE(Fe_{1-x}Co_x)_2As_2$ (AE = Ba, Sr, and Ca) superconductors, cobalt doping led to higher T_c's. In $Ba(Fe_{1-x}Co_x)_2As_2$ the superconductivity is observed at $T_c = 22$ K for x = 0.2. The transition width is estimated to be 0.6 K.[4] Kim et al. reported a study on $Sr(Fe_{1-x}Co_x)_2As_2$ single crystals which have a slightly smaller value of $T_c \sim 20$ K for x = 0.2.[5] In $Ca(Fe_{1-x}Co_x)_2As_2$, superconductivity is observed at $T_c = 20$ K for x = 0.06. The upper critical field, $H_{c2}(T)$, at zero temperature is estimated to be ~27 T and the coherence length is 40 Å.[6] It has been suggested that the *RE*-As distance and Fe-As-Fe angle are the two crucial parameters in the structure of *RE*FeAsO that control the effective bandwidths in these materials and, hence, the superconductivity. It is found that the twofold tetrahedral As-Fe-As angle (α) is an important electronic parameter and with higher T_c's α tends to the ideal tetrahedral value (109.5°).[7, 8] Most forms of chemical doping result in a reduction in α and values closer to 109.5°. For example, indirect electron doping of NdFeAsO (α = 111.4°) via F substitution or O deficiency reduces α by ~0.4° and ~1° for optimally doped samples.[9, 10] This is also true for hole-doped 122 systems such as $Ba_{1-x}K_xFe_2As_2$ where α = 109.5° for samples with $T_c = 38$ K (x = 0.4) compared to α = 111.2° for the parent material.[11] In contrast, it is common for cobalt doping that α increases with cobalt

substitution, which is expected to have an unfavourable effect and reduce T_c. The fully substituted x = 1 samples are also of considerable interest. LaCoPO and LaCoAsO are itinerant ferromagnets[1, 12] with room temperature resistivity of $\sim 3\times10^{-4}\ \Omega$ cm.[12] Ferromagnetic transitions occur at 43 K for LaCoPO, 66 K for LaCoAsO[12] and 90 K for LaCoAsO with spontaneous magnetic moments of $\sim 0.4\ \mu_B$.[1] $BaCo_2As_2$ is not ferromagnetic (FM) but is in close proximity to a FM quantum critical point.[13] The presence of Nd in the current x = 1 composition offers the prospect of studying the interplay between rare-earth and transition-metal magnetism.

5.2 Synthesis

Polycrystalline $NdFe_{1-x}Co_xAsO$ samples ($x_{nominal}$ = 0, 0.05, 0.075, 0.10, 0.125, 0.15, 0.175, 0.20, 0.25, 0.50, and 1) were prepared using solid state chemistry methods. Stoichiometric quantities of NdAs, Fe_2O_3, Fe, Co_3O_4, and Co powders of at least 99.9% purity were mixed together using mortar and pestle, and pressed into pellets. The pellets were vacuum sealed into quartz tubes and heated for 48 hrs at 1150 °C for $0 \le x_{nominal} \le 0.25$ and at 1050 °C for $x_{nominal}$ = 0.5 and 1. The reactions were initially done on a 0.5 gram scale. Larger 2 gram samples of $x_{nominal}$ = 0.075, 0.125, 0.175 and 1 were prepared for neutron powder diffraction. The starting material NdAs was prepared by heating stoichiometric mixture of Nd and As pieces at 500 °C for 2 hrs in an evacuated quartz tube, immediately followed by 16 hrs at 900 °C.

5.3 Antiferromagnetism in NdFeAsO

5.3.1 Structure and Physical Properties of NdFeAsO

Variable temperature synchrotron X-ray diffraction was used to follow the *P4/nmm* to *Cmma* transition associated with the AFM ordering that occurs in 1111-type parent materials. In case of NdFeAsO ($x = 0$), a broad transition with initial broadening of Bragg reflections at ~160 K followed by a full splitting at ~140 K (Fig. 5.1) is observed

and is in good agreement with previously reported results.[14] The latter temperature corresponds to the onset of long-range AFM order of the Fe spins.

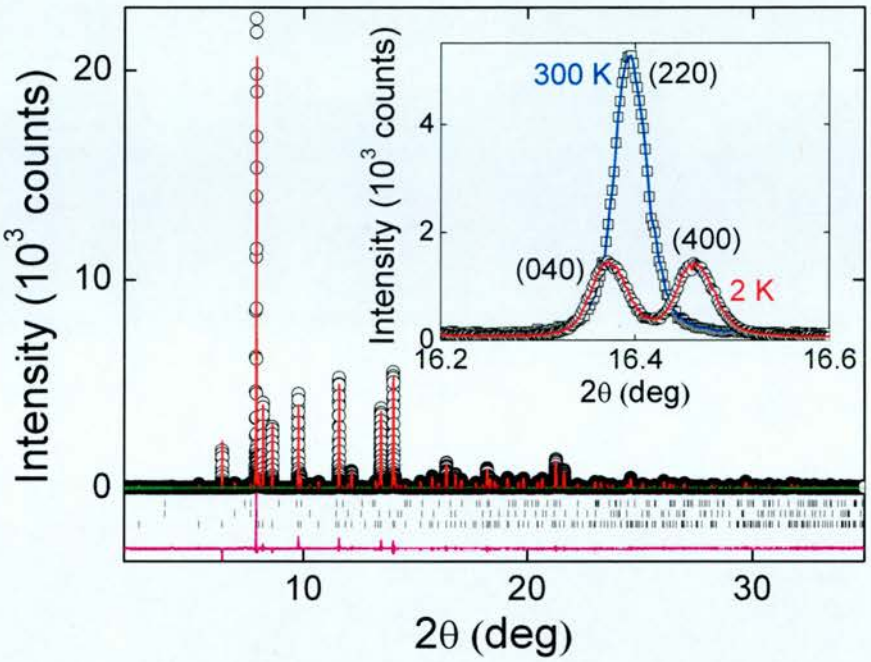

Figure 5.1: Rietveld refinement against room temperature synchrotron X-ray powder diffraction data for NdFeAsO. The observed data are indicated by open circles, the fit by the solid line and the difference curve is shown at the bottom. Bragg position markers are for NdFeAsO (bottom), NdAs (middle) and Nd_2O_3 (upper). The inset shows full splitting of the (220) Bragg reflection typical for T → O structural transition.

The magnetic susceptibility for NdFeAsO shows paramagnetic behavior and is given in Fig. 4.5 (chapter 4). The normalized resistance $R/R_{300\ K}$ for NdFeAsO is given in Fig. 5.12. The normal state resistance for $x = 0$ shows the familiar drop below ~160 K with the maximum slope dR/dT at 140 K. These temperatures correspond to the onset of the $T \rightarrow O$ transition and AFM order, respectively. The observed transport properties in NdFeAsO are in good agreement with previously reported results.[15, 16]

5.3.2 Magnetic Structure of NdFeAsO

The magnetic ordering in NdFeAsO was investigated using high-flux neutron powder diffraction on the D20 instrument at the ILL. Patterns were collected for 2 hrs each at

1.7, 30 and 175 K. These were carefully subtracted to separate the magnetic scattering from the structural contributions.

5.3.2.1 Magnetic Order of the Iron Spins

Unfortunately, the 30 K–175 K difference pattern showed no evidence for magnetic reflections within the experiment accuracy. However, *Chen et al.* published the Fe AFM order in NdFeAsO. [15] The reported magnetic structure is shown in Fig. 5.2. The magnetic unit cell for this magnetic structure is doubled along the *c* direction with respect to the orthorhombic crystallographic (nuclear) unit cell and yields the observed magnetic Bragg peaks at positions indexed by a propagation vector of $\mathbf{k} = (1\ 0\ ½)$. The Fe moment is determined to be 0.25(7) μ_B.[15] The Fe moments are collinearly aligned along the *a*-axis with AFM arrangement in the *a*- and *c*- directions and FM in the *b* direction. The possible AFM magnetic structures were analyzed using representational analysis.[17] The decomposition of the magnetic representation Γ_{Mag} in terms of the irreducible representations (IRs) of G_k for the Fe site is $1\Gamma_1^1 + 1\Gamma_3^1 + 1\Gamma_7^1$. The reported magnetic model corresponds to the Γ_3 solution. The resulting basis vectors for the two independent iron atoms are given in Table 5.5.[15, 16]

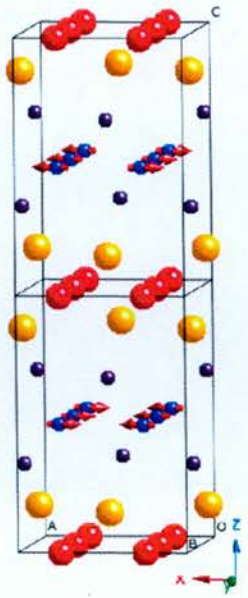

Figure 5.2: A schematic representation of the stripe-like magnetic ordering of Fe spins in NdFeAsO.

5.3.2.2 Magnetic Order of the Neodymium and Iron Spins

The magnetic 2-30 K difference pattern can be indexed using a magnetic unit-cell identical to the orthorhombic crystallographic unit cell. In particular, no doubling along the *c* direction is now required, signalling a change from AFM ordering in this direction to FM ordering. The observed magnetic Bragg peaks can be indexed by a propagation vector of $\mathbf{k} = (1\ 0\ 0)$. At 2 K, the decomposition of the magnetic representation is $\Gamma_{Mag} = 1\Gamma_1^1 + 1\Gamma_2^1 + 1\Gamma_3^1 + 1\Gamma_4^1 + 1\Gamma_5^1 + 1\Gamma_6^1$ and $\Gamma_{Mag} = 1\Gamma_2^1 + 1\Gamma_3^1 + 1\Gamma_5^1 + 1\Gamma_6^1 + 1\Gamma_7^1 + 1\Gamma_8^1$ for the Fe and Nd sites, respectively. The unit cell contains two independent Fe and two independent Nd sites with basis vectors as given in Table 5.1. The Γ_1^1, Γ_3^1 and Γ_5^1 IRs for the Fe1 (¼, 0, ½) and Fe2 (¾, 0, ½) atoms are FM and may therefore be excluded. For the Nd1 (0 , ¼, 0.14) and Nd2 (0, ¾, 0.86) atoms only the Γ_2^1, Γ_6^1 and Γ_8^1 IRs with AFM structures are considered. In case of a second-order phase transition, Landau theory states that only a single IR becomes critical. This leaves the Γ_2^1 and Γ_6^1 symmetries for combined Nd and Fe ordering. The Γ_2^1 solution has spin-stripe AFM ordered Fe planes with moments constrained along the *a* direction and AFM ordered Nd

planes with moments constrained along the c direction, respectively. The Γ_6^1 solution has spin-stripe AFM ordered Fe planes with moments constrained along the c direction and AFM ordered Nd planes with moments constrained along the a direction. Neutron powder diffraction data were fitted (Fig. 5.3) using the Γ_2^1, Γ_6^1 models and a model consisting of a linear combination of $\Gamma_2^1 \times \Gamma_6^1$. These models have been compared to the published magnetic model ("PRL model").[16,18]

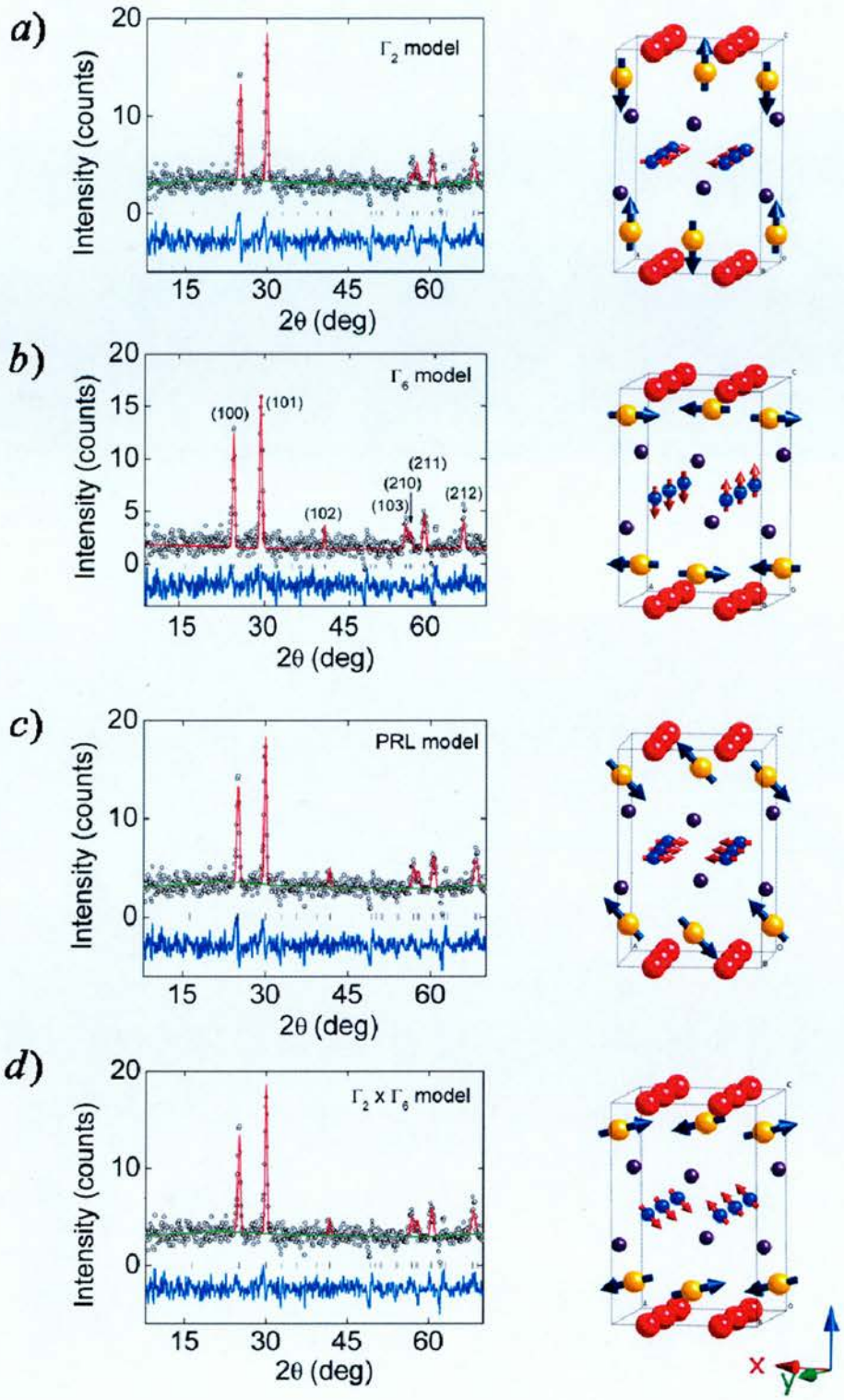

Figure 5.3: Possible magnetic models of NdFeAsO and their Rietveld fits to the 1.6-30 K difference neutron powder diffraction data.

Table 5.1: Basis vectors [m_x, m_y, m_z] for the space group *Cmma* with k = (1 0 ½) and k = (1 0 0). Fe1: (1/4 , 0, 1/2); Fe2: (3/4 , 0, 1/2); Nd1: (0, 1/4, 0.14); Nd2: (0, 3/4, 0.86); coordinates in crystallographic cell.

	k = (1 0 ½)			k = (1 0 0)	
	Γ_1	Γ_3	Γ_7	Γ_2	Γ_6
Fe1	[0 m_y 0]	[m_x 0 0]	[0 0 m_z]	[m_x 0 0]	[0 0 m_z]
Fe2	[0 -m_y 0]	[-m_x 0 0]	[0 0 -m_z]	[-m_x 0 0]	[0 0 -m_z]
Nd1	-	-	-	[0 0 m_z]	[m_x 0 0]
Nd2	-	-	-	[0 0 -m_z]	[-m_x 0 0]

Comparison of magnetic models and the values of magnetic moments are shown in Table 5.2. The first model, Γ_2^1, yields the total Fe magnetic moment of 0.92(7) μ_B and 1.81(3) μ_B per Nd. The value of the normalized χ^2 (1.05) is the highest, which can be seen as well from the Rietveld fit to the difference neutron powder diffraction pattern in Fig. 5.3 (a). The best Rietveld fit with the lowest value of χ^2 (0.96) is achieved using the Γ_6^1 model in which the AFM ordered Fe spins are aligned along *c*-axis, whilst the AFM ordered Nd spins are aligned along *a*-axis. The Fe total magnetic moment is m = 1.30(7) μ_B which is slightly larger compared to the PRL model. On the other hand, the Nd magnetic moment decreases from m = 1.81(3) μ_B (PRL model) to m = 1.46(6) μ_B. The linear combination of the two magnetic models ($\Gamma_2^1 \times \Gamma_6^1$) gives the lowest value of the normalized χ^2, it yields the value of z-component of the Nd magnetic moment $m_z \sim 0$ μ_B. In addition, the most intense (1 0 0) and (1 0 1) magnetic intensities have not been fitted satisfactorily. The total magnetic moments are 1.77(8) μ_B per Iron and 1.29(8) per Nd.

Further analysis is required in order to collect better data and to distinguish between the magnetic models. The Rietveld fits to neutron powder diffraction datasets and the schematic representations of each magnetic model are shown in Fig. 5.3.

Table 5.2: Comparison of magnetic models fitted to the 1.6-30 K difference neutron powder diffraction data. For Nd/Fe the labels correspond to Nd1 (0, ¼, 0.14), Nd2 (0, ¾, ~0.86), Fe1 (¼, 0, ½) and Fe2 (¾, 0, ½). Reported magnetic moments are in μ_B. χ^2 is normalized using the *PRL* fit value.

		k = (1 0 0)			
		Γ_2	Γ_6	*PRL*	$\Gamma_2 \times \Gamma_6$
Fe1	m_x	0.92(7)	0	1.25(9)	1.1(1)
	m_z	0	1.30(7)	0	1.39(7)
	m	0.92(7)	1.30(7)	1.25(9)	1.77(8)
Nd1	m_x	0	1.46(6)	1.25(8)	1.28(8)
	m_z	1.81(3)	0	1.31(7)	-0.2(1)
	m	1.81(3)	1.46(6)	1.81(3)	1.29(8)
χ^2/χ^2_{PRL}		1.05	0.96	1.00	0.92

5.4 Superconductivity in $NdFe_{1-x}Co_xAsO$

5.4.1 Structural Analysis

Combined neutron and synchrotron X-ray Rietveld refinements have been performed on the $NdFe_{1-x}Co_xAsO$ series in order to refine the Fe/Co occupancies and to study the structural changes upon increasing Co content. High-resolution Synchrotron powder diffraction measurements were done on the ID31 beamline at the ESRF. The X-ray wavelength used was 0.3994 Å. Room temperature patterns were collected for all prepared samples while selected samples ($x_{nominal}$ = 0.05, 0.075, 0.125,1) were studied as a function of temperature using shorter scans. Room temperature neutron powder diffraction patterns for $x_{nominal}$ = 0.075, 0.125, 0.175 and 1 were collected on the ILL beamline D20. The instrument was used in the high-flux setting with wavelength λ = 1.37 Å. The variable temperature data were collected between 4 K and 100 K for NdCoAsO at wavelength λ = 2.41 Å.

5.4.1.1 Combined Synchrotron X-ray and Neutron Powder Diffraction

Inspection of the synchrotron X-ray powder diffraction patterns revealed that all prepared samples have the tetragonal *P4/nmm* structure at room temperature (RT). The lattice constants obtained from the Rietveld refinements showed that the *c/a*-ratio varies linearly with x over the entire composition range ($0 \leq x \leq 1$), as shown in Fig. 5.4. Closed circles indicate samples where the Rietveld fits to synchrotron and neutron powder diffraction data sets confirmed the nominal composition. The linear dependence suggests that the *c/a* ratio can be used as an experimental measure of the composition. The fitted line is $c/a = -0.0809(7)x + 2.1679(2)$. For most compositions, the agreement between the nominal and calculated (c/a-derived) compositions is within 1-3 esd's (Table 5.3). For some samples, e.g. $x = 0.1$, a larger deviation is found. This signals the formation of impurities that change the stoichiometry of the main phase. The application of the calculated compositions results in a smoother x-dependence of the refined lattice constants, bond lengths and angles. Moreover it differentiates between samples having the same nominal composition but different SC transition temperatures. Thus the compositions used within this chapter are the ones calculated from the *c/a*-ratio. The a-axis is constant for low doped samples but increases slightly for $x > 0.25$ (Fig. 5.4). In contrast, the c-axis contracts rapidly. The (Fe/Co)-As bond lengths show a gradual contraction from 2.40 Å to 2.35 Å upon doping, while the tetrahedral angle increases from 111.9 ° to 115.9 ° as depicted in Fig. 5.5.

Table 5.3: Crystallographic *c/a*-ratios, compositions from *c/a*-ratio (x_{calc}), compositions from Rietveld fits ($x_{Rietveld}$) for the $NdFe_{1-x}Co_xAsO$ series.

$x_{nominal}$	c/a	x_{calc}*	$x_{Rietveld}$
0	2.1680(1)	0	
0.05	2.1642(1)	0.046(3)	
0.075 (NPD)	2.1627(1)	0.064(3)	0.075(5)
0.075	2.1618(1)	0.075(3)	
0.1	2.1584(1)	0.121(3)	
0.125 (NPD)	2.1581(1)	0.122(3)	0.126(5)
0.125	2.1580(1)	0.117(3)	
0.15	2.1555(1)	0.154(3)	
0.175 (NPD)	2.1540(1)	0.172(3)	0.176(7)
0.2	2.1512(1)	0.206(3)	
0.25	2.1473(1)	0.255(3)	
0.5	2.1285(1)	0.488(3)	
1	2.0866(1)	1	0.996(2)

* $x_{calc} : c/a = -0.0809(7)x + 2.1679(2)$

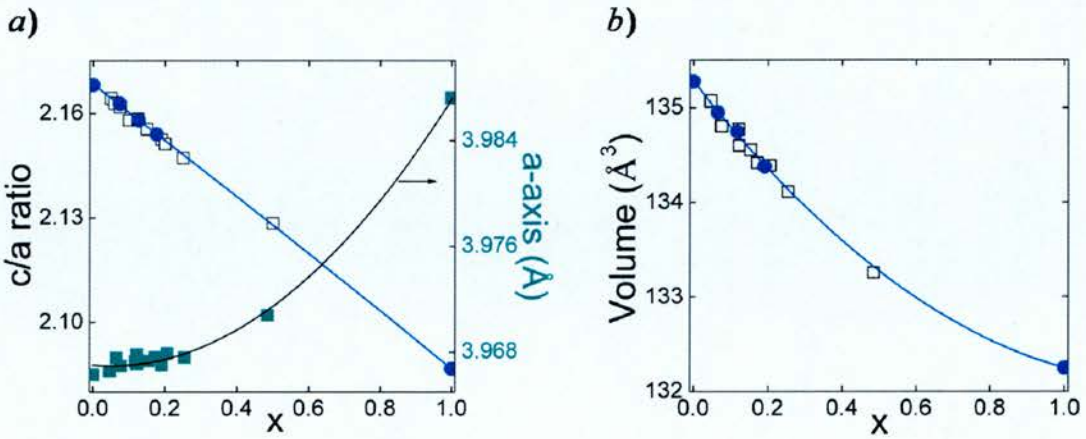

Figure 5.4: a) Left axis – crystallographic *c/a*-ratio versus $x_{nominal}$ for $NdFe_{1-x}Co_xAsO$. The fitted line is $c/a = -0.0809(7)x + 2.1679(2)$. Right axis – the *a*-axis versus the composition derived from the *c/a*-ratio (x_{calc}). The solid line is the fit to 2nd order polynomial. b) Volume versus $x_{nominal}$ for $NdFe_{1-x}Co_xAsO$. The solid line is the fit to 2nd order polynomial.

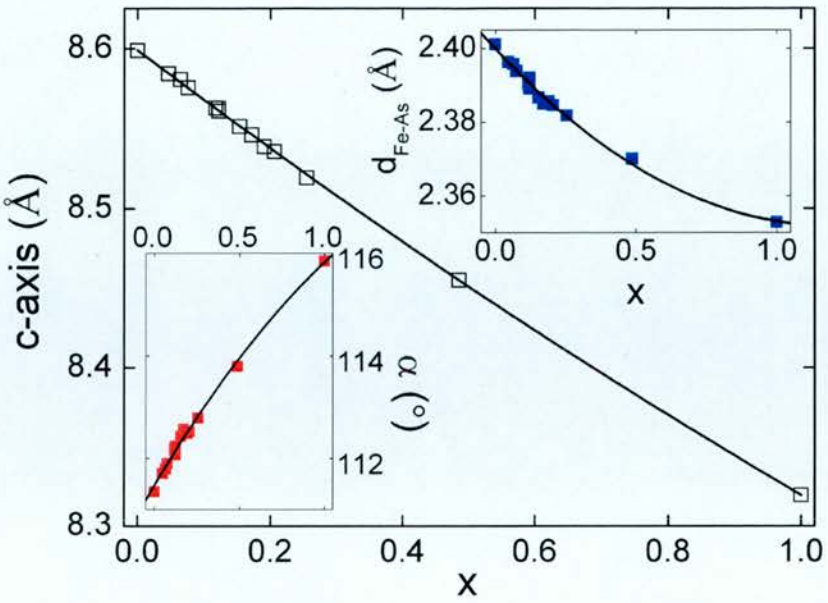

Figure 5.5: A fit against Crystallographic *c*-axis plotted versus *x*. The insets show the x-dependence of the FeAs bond distance and the twofold tetrahedral As-Fe-As angle for the $NdFe_{1-x}Co_xAsO$. The solid lines are fits to 2nd order polynomials.

In order to confirm the composition of selected samples, combined Rietveld refinements of room temperature synchrotron X-ray and neutron powder data were undertaken. This allows the simultaneous refinement of the total transition metal site occupancy and the iron to cobalt ratio. The total occupancy is effectively obtained from the Rietveld fits to Synchrotron x-ray data with no significant scattering difference between Fe and Co, while the different neutron scattering length Fe = 9.45 fm, Co = 2.49 fm] of the elements allows the determination of Fe/Co ratio. Four compositions were studied with $x_{nominal}$ = 0.075, 0.125, 0.175 and 1. In these combined refinements, the lattice constants were kept at the synchrotron X-ray values and the neutron wavelength was refined to fit the neutron powder diffraction data. The Rietveld fits to the X-ray and neutron powder data for $x_{nominal}$ = 0.075, 0.125 and 0.175 is shown in Fig. 5.6-5.8. The results of the combined fits are summarized in Table 5.4 and the Rietveld fits for other samples are shown in an appendix 1. They revealed that the total occupancy of the transition metal site is unity in all cases, and that the refined Fe and Co fractions are within a single standard deviation of the nominal composition.

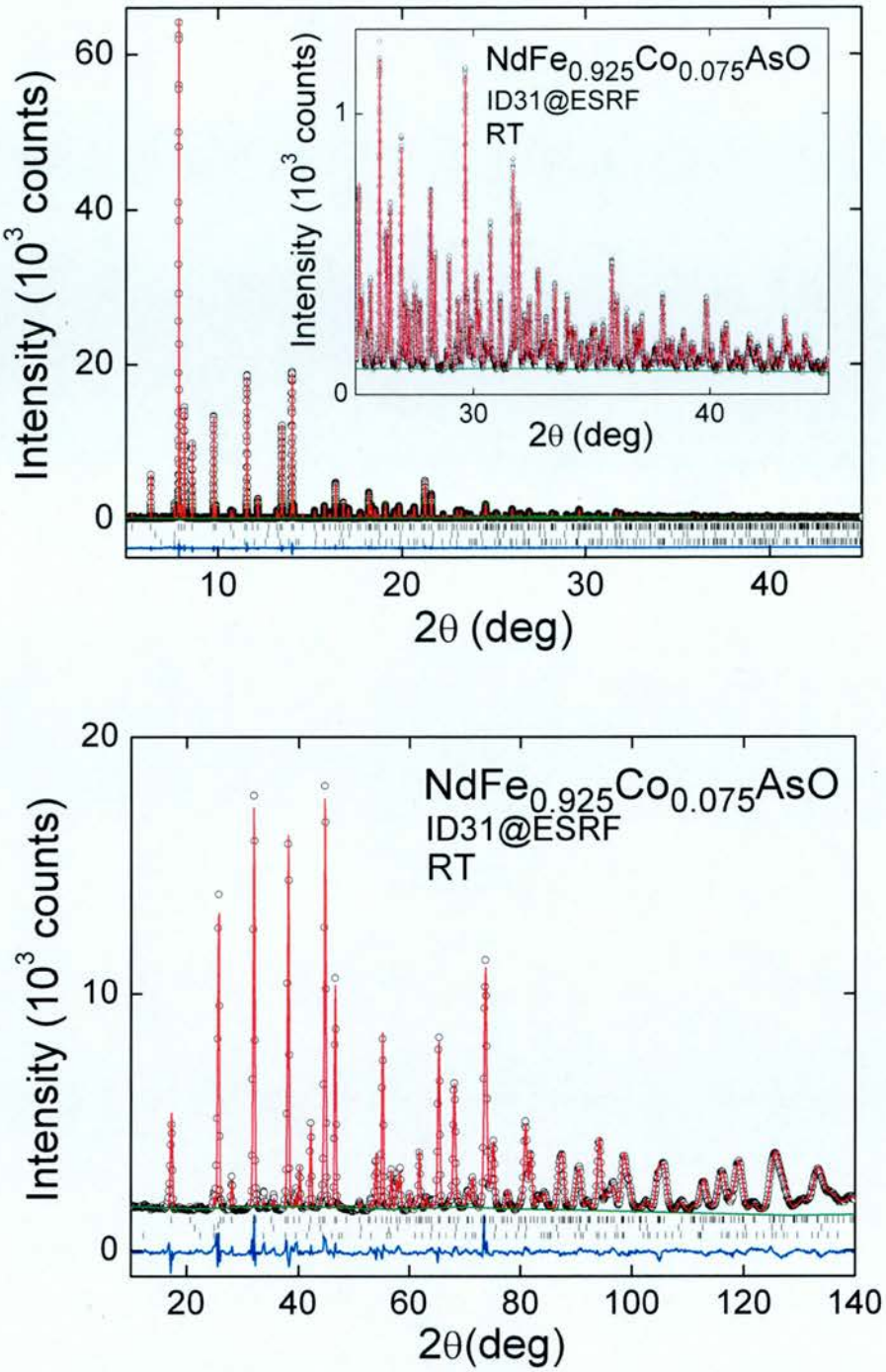

Figure 5.6: Combined Rietveld refinement against room temperature synchrotron X-ray (upper) and neutron (bottom) powder diffraction data for a sample with $x_{nominal} = 0.075$ composition. The observed data are indicated by open circles, the fit by the solid line and the difference curve is shown at the bottom. Bragg position markers are for $NdFe_{0.925}Co_{0.075}AsO$ (top), NdAs (middle) and Nd_2O_3 (bottom).

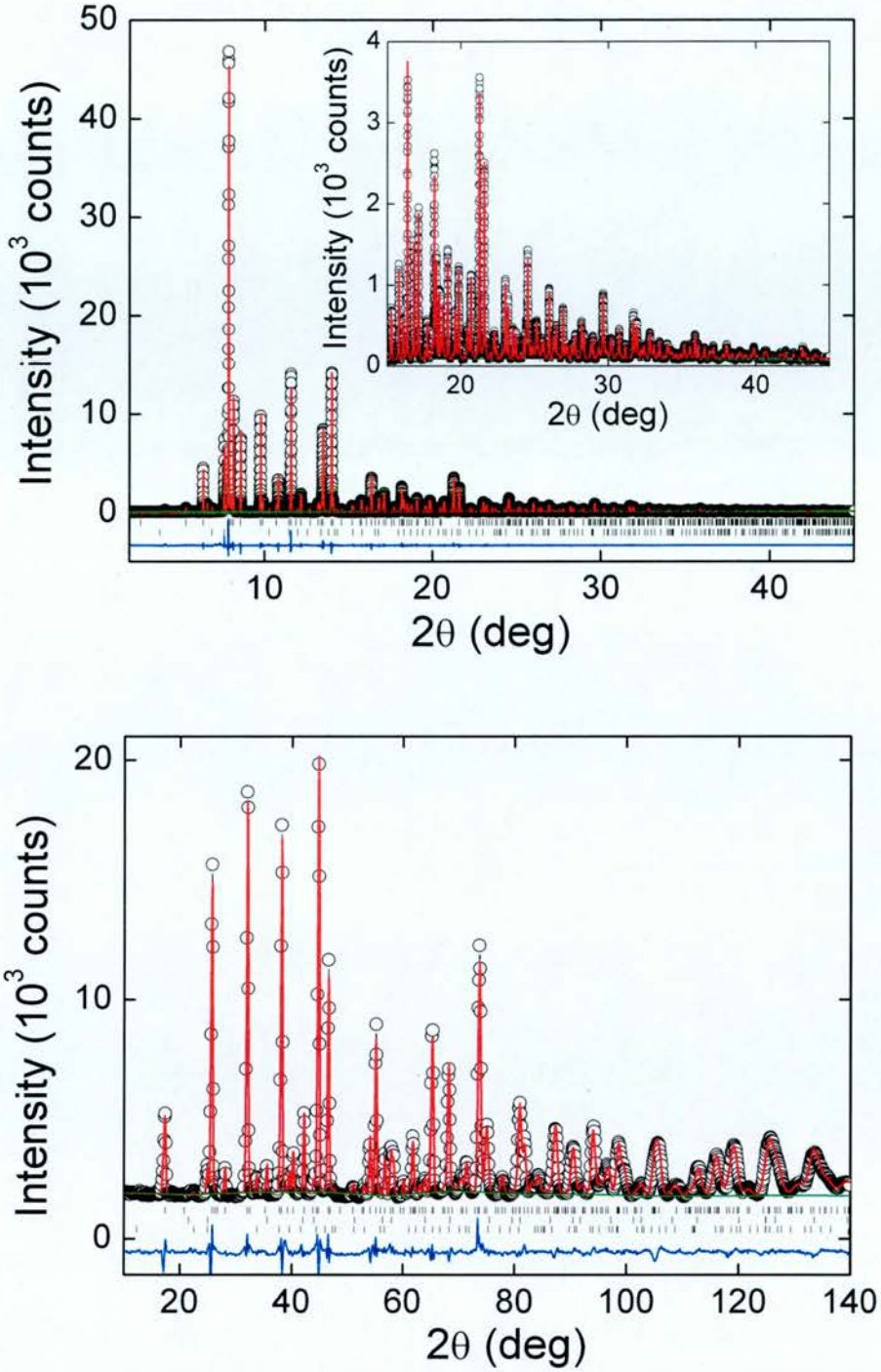

Figure 5.7: Combined Rietveld refinement against room temperature synchrotron X-ray (upper) and neutron (bottom) powder diffraction data for a sample with $x_{nominal} = 0.125$ composition. The observed data are indicated by open circles, the fit by the solid line and the difference curve is shown at the bottom. Bragg position markers are for $NdFe_{0.875}Co_{0.125}AsO$ (top), NdAs (middle) and Nd_2O_3 (bottom).

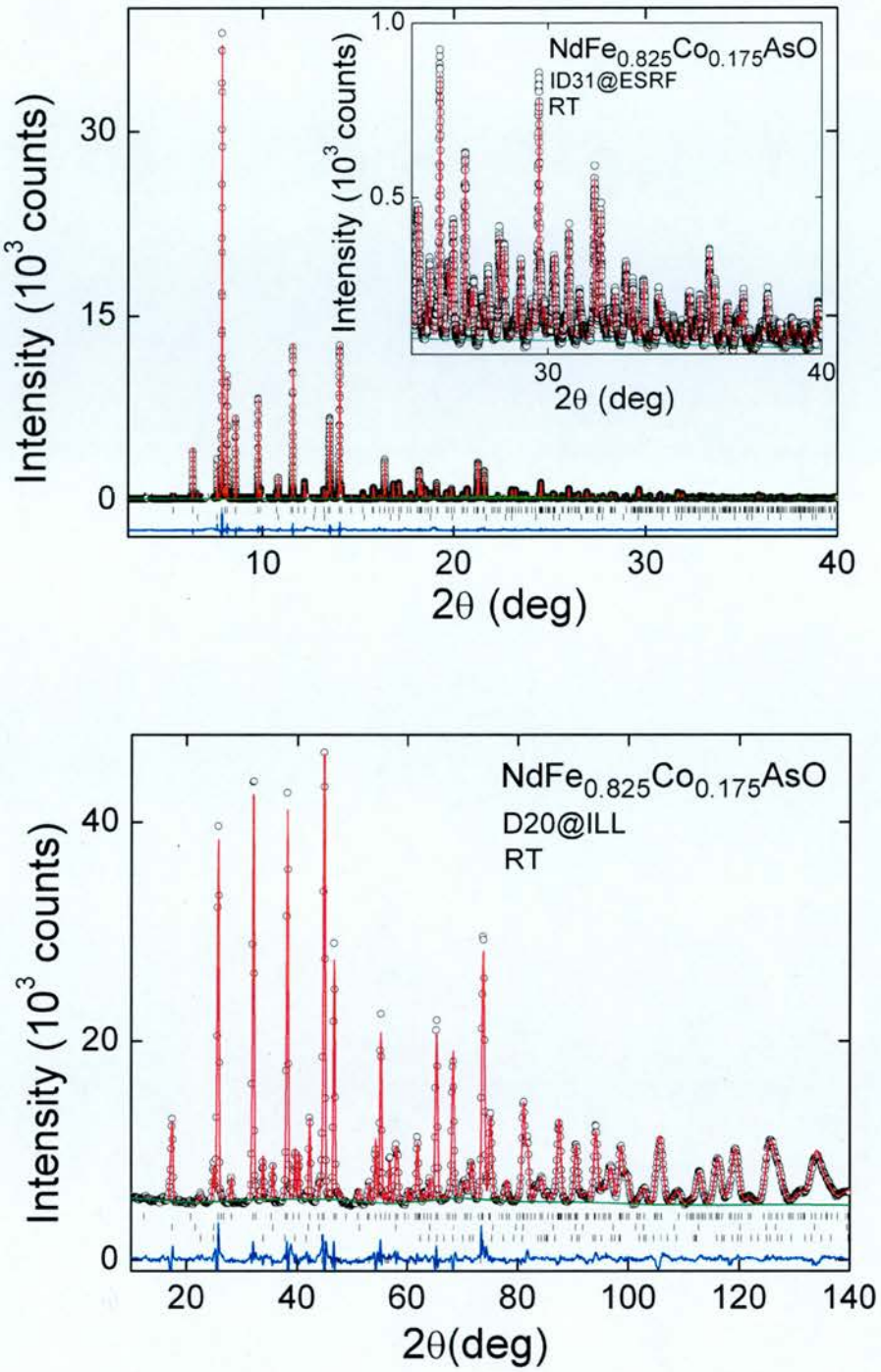

Figure 5.8: Combined Rietveld refinement against room temperature synchrotron X-ray (upper) and neutron (bottom) powder diffraction data for a sample with $x_{nominal} = 0.175$ composition. The observed data are indicated by open circles, the fit by the solid line and the difference curve is shown at the bottom. Bragg position markers are for $NdFe_{0.825}Co_{0.175}AsO$ (top), NdAs (middle) and Nd_2O_3 (bottom).

Table 5.4: Lattice constants, refined atomic parameters, selected bond distances and angles, and fit statistics for the combined Rietveld fits to synchrotron X-ray and neutron powder diffraction data for selected $NdFe_{1-x}Co_xAsO$ compositions. Space group *P4/nmm*; Nd on *2c*(1/4,1/4,*z*); Fe/Co on *2b*(3/4,1/4,1/2); As on *2c*(1/4,1/4,*z*); O on *2a*(1/4,3/4,0).

$x_{nominal}$		0.075	0.125	0.175	1.00
a-axis (Å)		3.96754(1)	3.96711(3)	3.96759(4)	3.98724(1)
c-axis (Å)		8.58069(5)	8.5611(1)	8.5462(1)	8.31835(4)
Volume (Å^3)		135.072(1)	134.734(1)	134.532(1)	132.246(1)
Nd	U_{iso} (Å^2)	0.0041(1)	0.0046(1)	0.0049(1)	0.0060(1)
	z	0.13911(3)	0.13973(5)	0.14012(6)	0.14223(5)
	Occ.	1.00	1.00	1.00	1.00
Fe/Co	U_{iso} (Å^2)	0.0049(2)	0.0050(2)	0.0049(3)	0.0066(2)
	Fe-occ.	0.918(4)	0.886(6)	0.831(7)	0
	Co-occ.	0.076(4)	0.123(6)	0.180(8)	0.996(2)
	Tot-occ.	0.994(5)	1.009(8)	1.007(11)	0.996(2)
As	U_{iso} (Å^2)	0.0018(1)	0.0021(1)	0.0017(2)	0.0033(1)
	z	0.65673(5)	0.65557(8)	0.6549(1)	0.65063(8)
	Occ.	1.011(2)	1.024(3)	1.019(3)	1.003(2)
O	U_{iso} (Å^2)	0.0047(3)	0.0048(4)	0.0029(6)	0.0036(3)
	Occ.	0.978(4)	0.962(6)	0.980(8)	1.000(4)
$x_{Rietveld}$		0.076(4)	0.122(6)	0.178(8)	0.996(2)
d(Fe/Co-As) (Å)		2.3966(3)	2.3892(4)	2.3841(5)	2.3546(3)
∠As-(Fe/Co)-As		111.73(2)	112.24(3)	112.63(4)	115.70(3)
∠As-(Fe/Co)-As		108.35(1)	108.10(1)	107.91(2)	106.45(1)
χ^2		3.1	3.2	5.2	3.1
NPD	wR_p (%)	3.6	3.6	3.3	3.0
	R_p (%)	2.5	2.5	2.4	2.3
	R_F^2 (%)	2.9	2.5	2.8	3.0
XRD	wR_p (%)	7.9	8.7	12.9	10.1
	R_p (%)	5.4	6.2	8.7	6.8
	R_F^2 (%)	2.5	2.7	7.8	3.5
NdAs (wt%)		1.4(1)	6.3(1)	3.4(1)	8.6(1)
CoAs (wt%)					7.3(3)
Nd_2O_3 (wt%)		1.1(1)	3.4(1)	2.3(1)	

(for x = 0 see Table 4.2, Chapter 4, section 4.3.2)

5.4.1.2 Variable Temperature High-resolution Synchrotron Powder Diffraction

For $NdFe_{1-x}Co_xAsO$ [$x = 0.047(2)$, $x = 0.065(2)$, and $x = 0.123(2)$], synchrotron powder diffraction data were collected on heating from 4 K. At low temperatures a broadening of reflections with Miller indices (*hkl*) ($h + k = 2n$) consistent with the well established $T \rightarrow O$ transition, was evident (Fig. 5.7). However, no peak splitting occurs down to the lowest measured temperatures. Structural refinements using the orthorhombic *Cmma* model showed a clear divergence of the *a*- and *b*-axes for $x = 0.047(2)$ and $x = 0.065(2)$, respectively. In contrast, refinements for $x = 0.122(2)$ showed no evidence for a structural distortion as Rietveld fits with the *P4/nmm* and *Cmma* structural models gave the same residuals and almost identical *a*- and *b*-axes. The temperature dependence of the lattice constants is shown in Fig. 4.8, where the a_0, b_0 are the orthorhombic cell constants. The lattice constants above the $T \rightarrow O$ transition were obtained from fits to the *P4/nmm* structural model. The transition temperatures were taken from the onset temperature of orthorhombic strain, $s = (a_O - b_O)/(a_O + b_O)$, and are 72(2) K [$x = 0.047(2)$] and 64(2) K [$x = 0.065(2)$], respectively (Fig. 5.9).

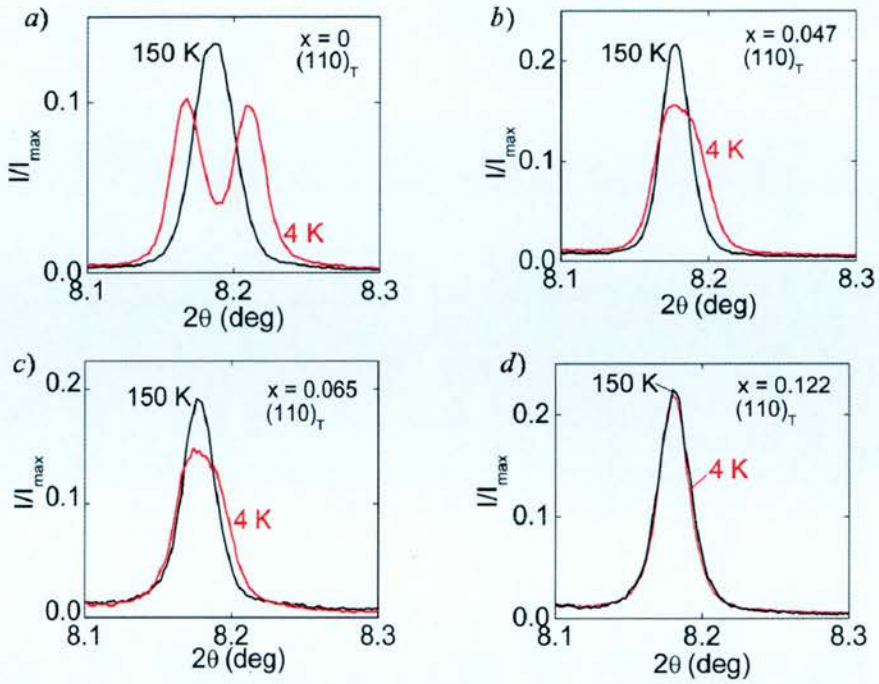

Figure 5.9: Full splitting in a) NdFeAsO and broadening in b) $NdFe_{0.953}Co_{0.047}AsO$, c) $NdFe_{0.945}Co_{0.065}AsO$ of the tetragonal (1 1 0) reflection for $NdFe_{1-x}Co_xAsO$ series indicative of the T→ O structural transition.

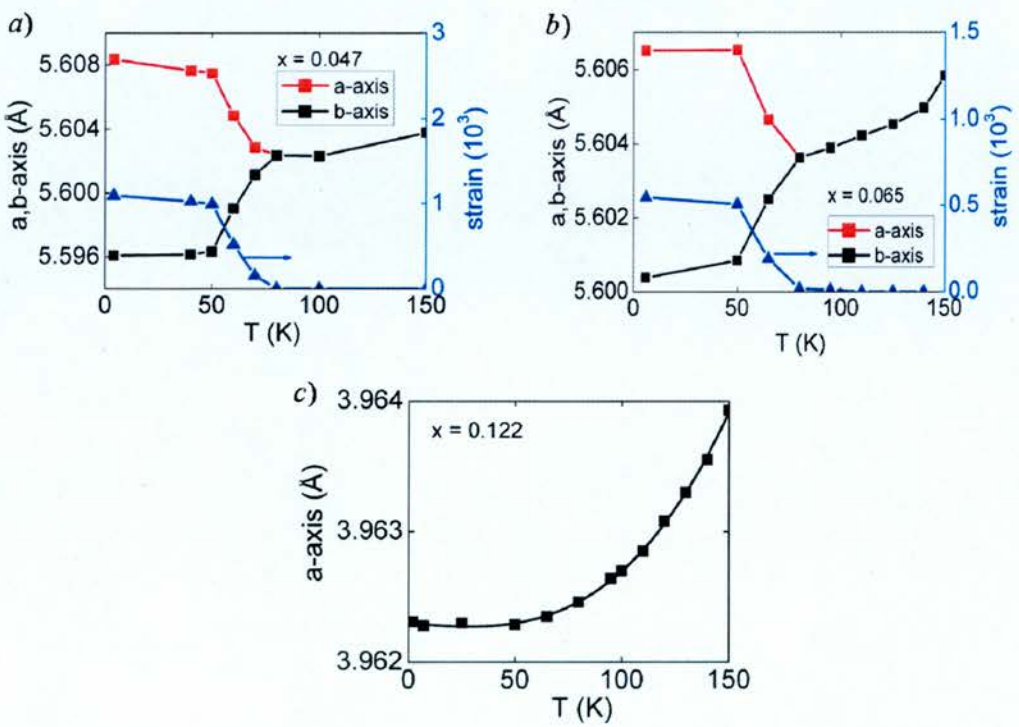

Figure 5.10: Temperature dependence of the crystallographic basal plane lattice constants and orthorhombic strain for $NdFe_{1-x}Co_xAsO$ where a) x = 0.047, b) x = 0.065 and c) x = 0.122.

5.4.2 Magnetic Susceptibility

The low field ZFC susceptibilities for the $NdFe_{1-x}Co_xAsO$ solid solution series are given in Fig. 5.11. Superconducting transitions are observed for samples with $0.065(2) \leq x \leq 0.172(2)$. The transition temperatures were taken from the diamagnetic onset temperature and are summarized in Table 5.5. This reveals almost identical values of 16.5(2) K for optimally doped samples near $x = 0.12$ [$x = 0.118(2)$, $x = 0.122(2)$, and $x = 0.123(2)$]. The diamagnetic shielding fractions (SF) can be calculated according to:

$$SF(\%) = \frac{4\pi * [M(30K) - M(2K)] * \rho}{H * m} * 100\% \qquad (5.1)$$

Where M (emu) is the magnetization, ρ (g cm^{-3}) is the packing density (in calculations $\rho = 7$ g cm^{-3} was used), H (Oe) is the applied magnetic field and m (g) is the mass. The SF vary from 20-70% of $4\pi\chi$ for samples with $x = 0.12$ and are lower on the underdoped and overdoped sides as are the critical temperatures (Table 5.5, Fig. 5.9). The SC transitions were confirmed by electrical resistance measurements.

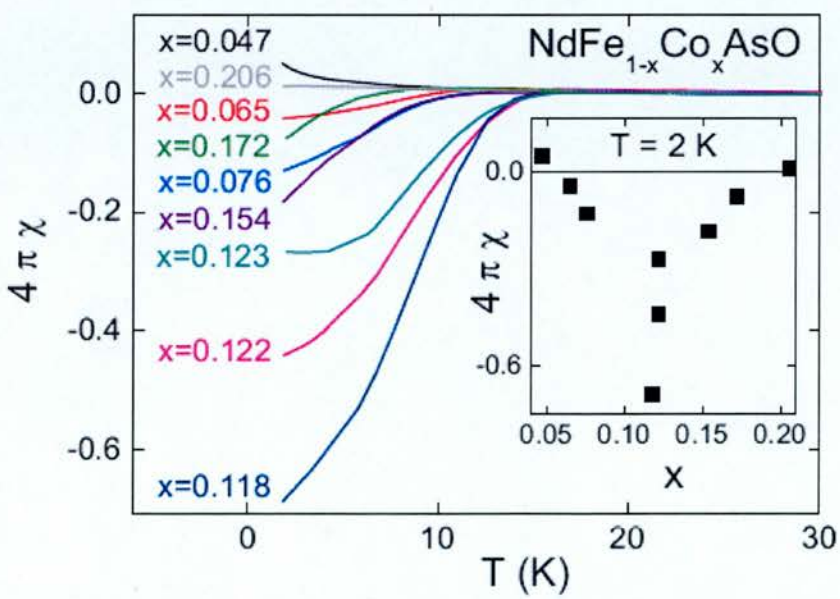

Figure 5.11: Temperature dependence of the low field magnetic susceptibilities for $NdFe_{1-x}Co_xAsO$. The inset shows the x dependence of the diamagnetic fraction at 2 K.

Table 5.5: Critical temperatures from the onset of diamagnetism, resistive transition midpoint, diamagnetic shielding fraction (SF, %), critical field (H_{c2}) and coherence length (ξ) for the $NdFe_{1-x}Co_xAsO$ series.

x_{calc}	T_c, χ_{onset} (K)	T_c, R_{mid} (K)	SF (%)	H_{c2}(T)	ξ ( )
0.0647	12.8	9.2	3	14(1)	49(1)
0.0760	15.0	14.2	9.5		
0.1217	16.7	16.2	46.0		
0.1178	16.5	16.0	70.0	26(1)	36(1)
0.1225	16.6		28		
0.1539	15.1		18		
0.1721	13.4	12.6	5.5	21(1)	40(1)

5.4.3 Electrical Resistance and Superconductivity

5.4.3.1 Electrical Resistance

The normalized resistances $R/R_{300\,K}$ are given in Fig. 5.12. The 300 K resistivities fall between 5 mΩ cm for $x = 0$ and 2 mΩ cm for $x = 1$. Samples with $x > 0.2$ have metallic temperature dependences indicating a transition to more conventional metallic behavior on the overdoped side. On the underdoped side, increasing x suppresses the SDW transition and no large anomaly in $R(T)$ is evident for any of the SC samples. At low temperatures SC transitions are evident. The transition temperatures were taken from the 50% of normal state resistance values ($0.5R_N$) and are listed in Table 5.5. The obtained values are in good agreement with the values from the magnetic susceptibility measurements.

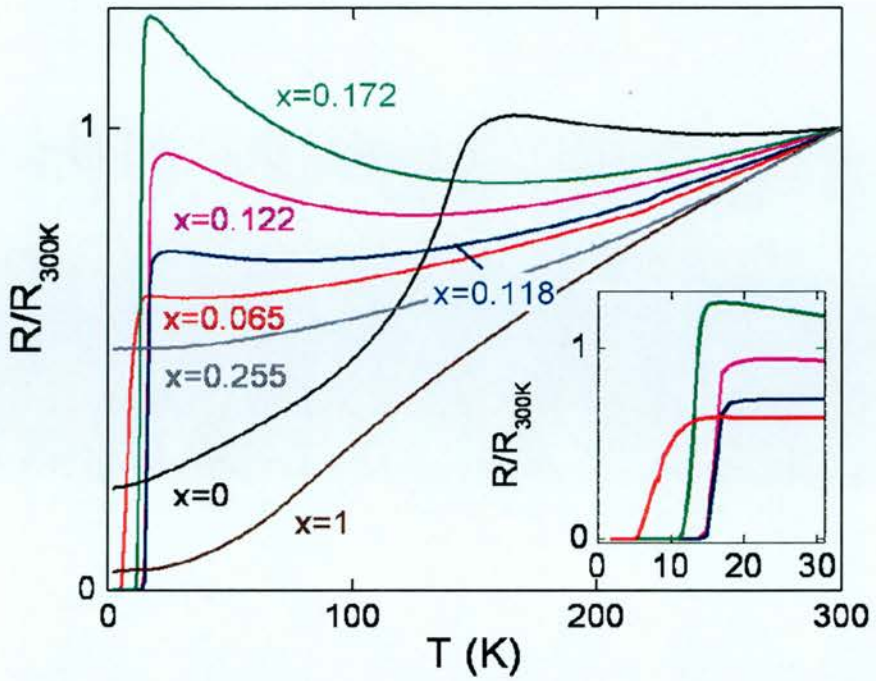

Figure 5.12: Temperature dependence of normalised resistance R/R300K for $NdFe_{1-x}Co_xAsO$. The inset illustrates superconducting transitions.

5.4.3.2 Superconducting Properties

The widths of the resistive transitions were determined by taking the difference between $0.9R_N$ and $0.1R_N$ and are ~2 K wide for the optimally doped samples ($x = 0.12$), ~5 K for $x = 0.065(2)$, and ~3 K for $x = 0.0172(2)$. This is comparable to other polycrystalline 1111-type cobalt-doped superconductors including $LaFe_{1-x}Co_xAsO$ and $SmFe_{1-x}Co_xAsO$,[2, 19] and polycrystalline samples of $Ba(Fe_{1-x}Co_x)As_2$.[20] The field dependence of $R(T)$ in the vicinity of the SC transition was studied up to 9 T for samples with $x = 0.065(2)$, $x = 0.118(2)$, and $x = 0.172(2)$. The results are shown in the Fig. 5.13 and reveal a significant suppression of T_c with applied magnetic field.

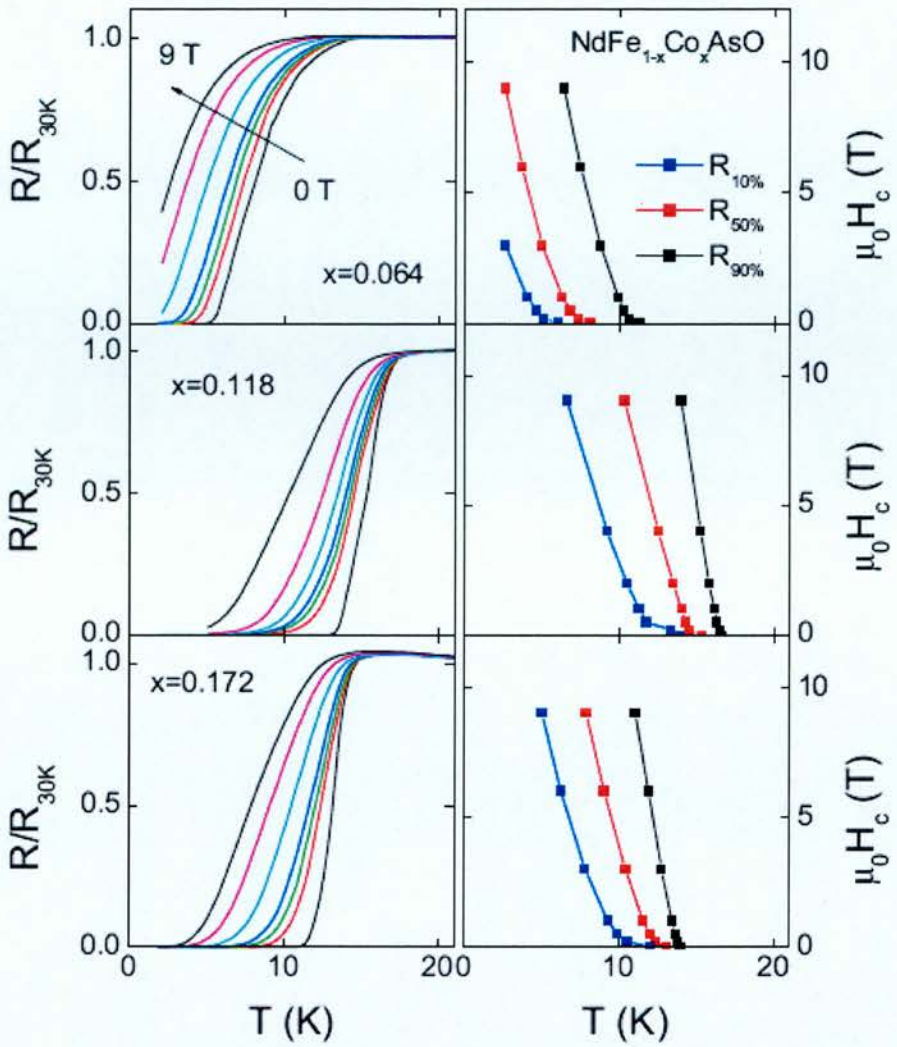

Figure 5.13: Temperature and field dependences of the electrical resistance for selected $NdFe_{1-x}CoxAsO$ compositions. H_{c2}(T) derived from 10% ($0.1R_N$), 50% ($0.5R_N$), and 90% ($0.9R_N$) resistance drops are shown on the right-hand side.

The upper critical fields were determined at the temperatures of the 10%, 50%, and 90% reduction in the normal state resistance. The results are plotted Fig. 5.13. In all samples, an initial rapid reduction in small applied fields $\mu_0 H < 0.5$ T is evident. This is followed by an approximately linear decrease for $\mu_0 H > 1$ T, which shows no sign of saturation. The dependence of $0.1R_N$, $0.5R_N$ and $0.9R_N$ slopes signalling a broadening of the transition in applied magnetic fields. This is characteristic for type-II superconductors and was also observed in the $LaFe_{1-x}Co_xAsO$ series.[1] Using the $0.5R_N$ criterion, almost identical slopes of $-2.5(1)$ T K^{-1} [$x = 0.065(2)$], $-2.3(1)$ T K^{-1} [$x = 0.118(2)$], and $-2.3(1)$ T K^{-1} [$x = 0.172(2)$] were obtained from

linear fits between $1 \leq \mu_0 H \leq 9$ T. The linear dependence of $H_{c2}(T)$ near T_c suggests that the Werthamer-Helfand-Hohenberg model, which predicts $H_{c2}(0)=0.69\ T_c[dH_{c2}/dT]$, can be used to estimate the upper critical field at zero temperature.[21] The SC coherence length, ξ, is given by $\xi^2(0) = \Phi_0/2\pi H_{c2}(0)$, where $\Phi_0 = 2.07 \times 10{-}7$ Oe cm^2. The critical field, H_{c2}, and coherence length, ξ, of the representative samples are summarized in Table 5.5.

5.5 Ferromagnetism in NdCoAsO

5.5.1 Structural Analysis

The temperature dependence of the crystal structure of NdCoAsO was followed between 5 K and room temperature using synchrotron x-ray powder diffraction. No structural transition was observed down to 5 K (Fig. 5.14 inset) and the structure was described using the *P4/nmm* structural model reported by Quebe et al. The RT lattice constants, atomic parameters, selected bond lengths, and fit statistics are summarized in Table 5.4. The refined lattice constants and fractional coordinates at 5 K are as follows: $a = 3.97940(1)$ Å, $c = 8.29849(3)$ Å, $z_{Nd} = 0.14264(4)$, and $z_{As} = 0.65071(7)$, *wRp* (9.5%), *Rp* (6.2%), and R_F^2 (2.4%). The Co-As bond distance contracts moderately from 2.3546(3) Å at RT to 2.3501(3) Å at 5 K, while the tetrahedral angle remains almost constant with RT and 5 K values of 115.70(3)° and 115.69(4)°, respectively. The Rietveld fit to the room temperature synchrotron X-ray powder diffraction is shown in Fig. 5.14.

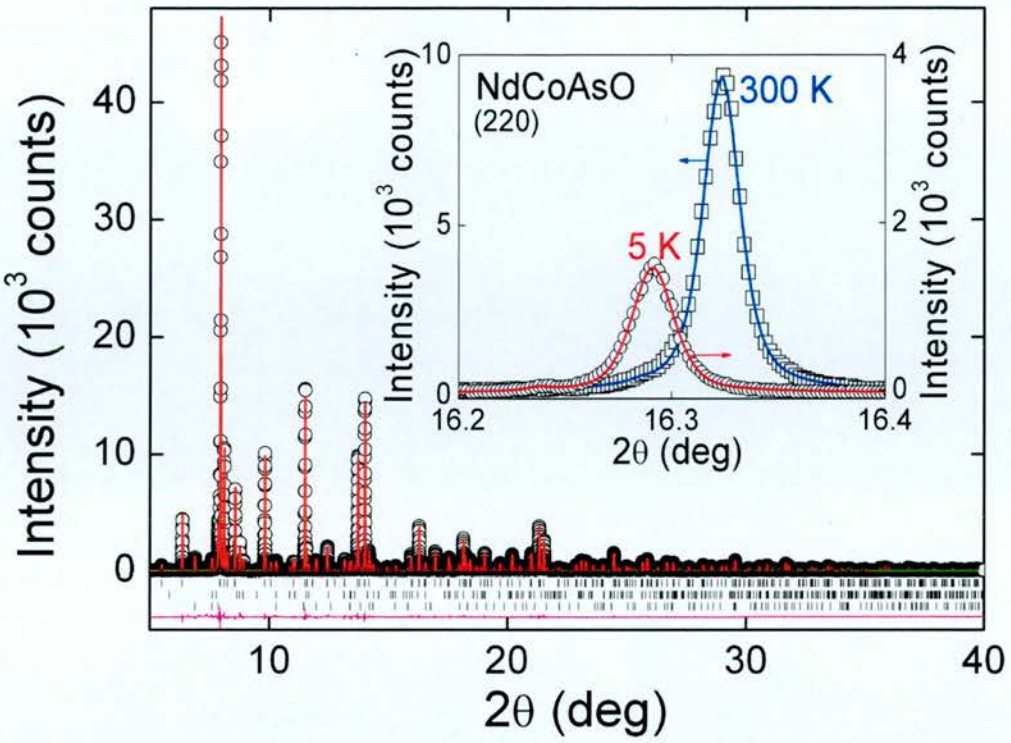

Figure 5.14: Combined Rietveld refinement against room temperature synchrotron X-ray powder diffraction data for NdCoAsO. The observed data are indicated by open circles, the fit by the solid line and the difference curve is shown at the bottom. Bragg position markers are for NdCoAsO (top), NdAs (middle) and Nd_2O_3 (bottom). The inset shows the Bragg reflection (220) at room and base temperature. The difference between the intensities of the Bragg peaks collected at 300 K and 5 K is due to different counting time.

5.5.2 Magnetic Susceptibility

The DC magnetic susceptibility is shown in Fig. 5.15 and reveals a FM divergence of the susceptibility with $T_c = 85$ K followed by a transition to an AFM state at $T_N = 9$ K. The Curie temperature was determined from the local maximum in $d\chi / dT$, while the Néel temperature was taken when $d\chi / dT$ changes sign (Fig. 5.13). Zero-field-cooled and field-cooled curves collected in 1 T do not show any thermal hysteresis. The high-temperature susceptibility does not follow the Curie-Weiss law.

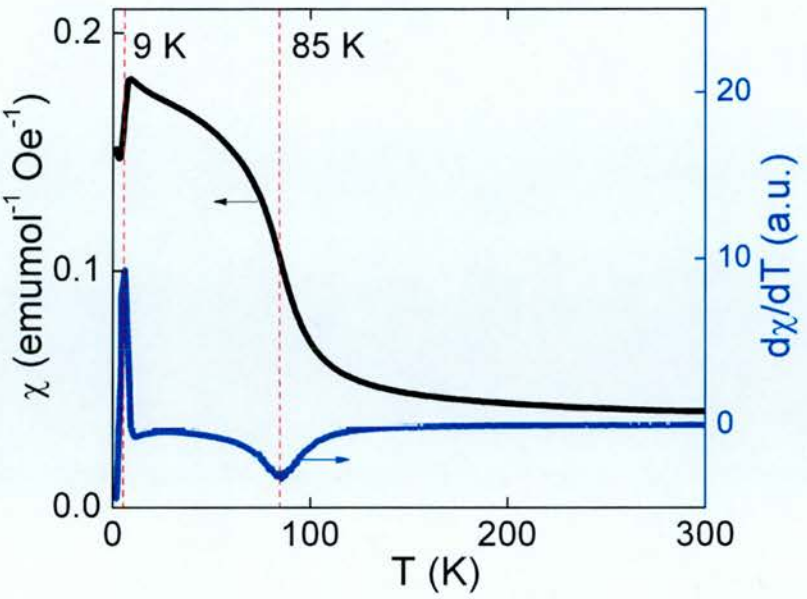

Figure 5.15: Temperature dependence of the ZFC magnetic susceptibility and its derivative for NdCoAsO.

To further investigate the magnetic properties, *M(H)* isotherms were collected at 1.7, 50, and 100 K. These data are shown in the inset of Fig. 5.16. The main panel shows the derived Arrott plots, M^2 versus H/M, that were used to determine the nature of the magnetic ground state.[22] Extrapolation of the linear high-field behavior for a ferromagnet yields a negative H/M-axis intersect, while the same extrapolation for AFM and paramagnetic (PM) states intersect the H/M axis at a positive value. At 1.7 and 100 K, the Arrott plots clearly indicate the absence of ferromagnetism and are consistent with antiferromagnetism and paramagnetism, respectively. At 50 K, the Arrott plot indicates a FM ground state. The isothermal *M(H)* measurements are therefore consistent with a PM to FM to AFM sequence of ordering transitions upon cooling from RT. No magnetic hysteresis is evident from the measurement at 50 K indicating that NdCoAsO is an extremely soft ferromagnet without any sizable remnant magnetization.

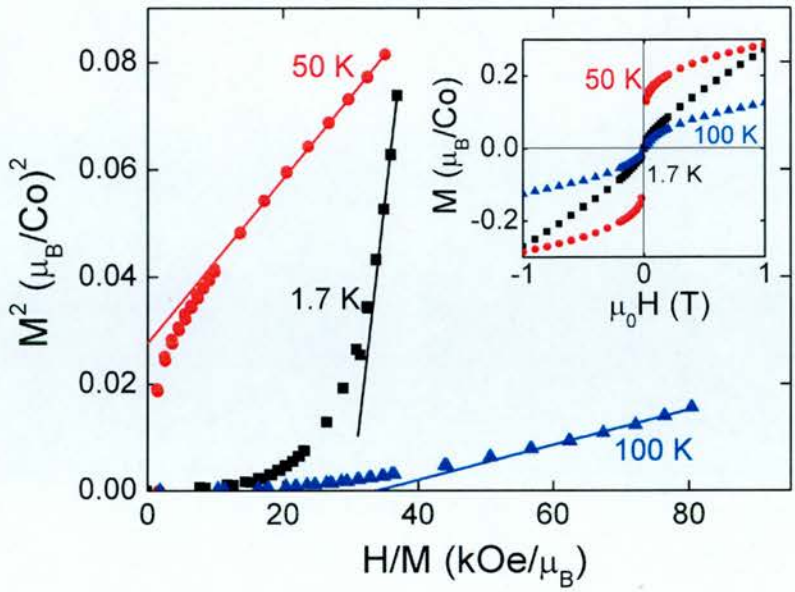

Figure 5.16: Arrot plots derived from the M(H) isotherms (showed as inset) of NdCoAsO.

5.5.3 Electrical Resistivity

The temperature dependence of the electrical resistivity of NdCoAsO is typical of that of a good metal with RRR = 25 (Fig. 5.17). The magnetic ordering transitions do not result in large anomalies in *R(T)* but are evident in *dR/dT*, which shows a maximum at ~85 K and a minimum at ~9 K (Fig. 5.17). The slope remains positive throughout revealing that the sample is metallic over the entire temperature range.

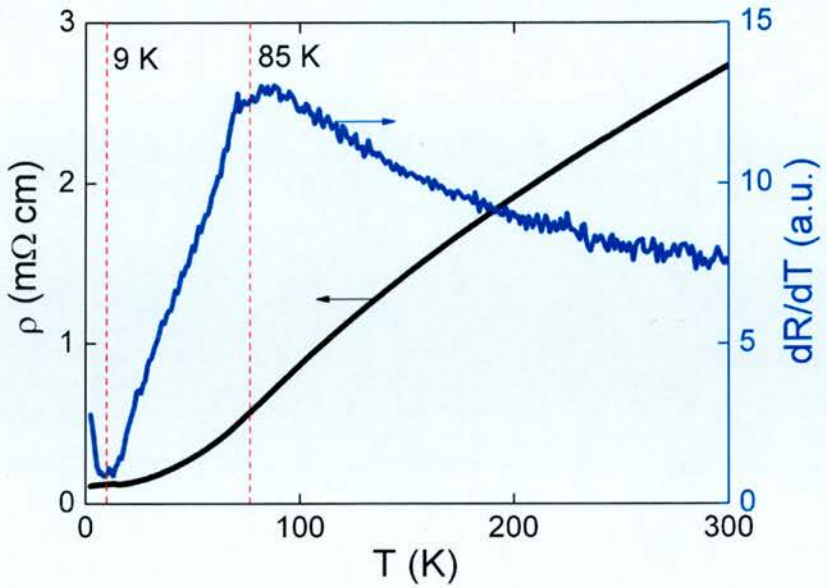

Figure 5.17: Temperature dependence of the electrical resistivity and its derivative for NdCoAsO.

5.5.4 Magnetic Structure of NdCoAsO

The magnetic ordering in NdCoAsO was investigated using high-flux neutron powder diffraction on the D20 instrument at ILL. Patterns were collected for 2 hrs each at 1.7, 15, 40, 70, and 100 K. At 1.7 K, long-range AFM order was confirmed by the presence of magnetic Bragg reflections that were not present in the 5 K synchrotron powder diffraction pattern. These reflections were all indexed on a tetragonal cell doubled along the crystallographic c direction ($a_M = a_N$, $c_M = 2c_N$, where the subscript M denotes magnetic and N the nuclear cell). The indexing of the most prominent magnetic reflections is given in Fig. 5.18. Upon heating to 15 K, the AFM reflections disappear in agreement with the magnetic susceptibility data. Careful subtraction of the 100 and 15 K data revealed weak magnetic contributions to the nuclear (0 0 1) and (0 0 2) Bragg reflections. Similar FM intensities were also evident in the 40 K pattern but at 70 K there is no evidence for magnetic Bragg diffraction. The possible FM and AFM magnetic structures were analyzed using representational analysis. In both the FM ($\mathbf{k} = 0$) and AFM [$\mathbf{k} = (0\ 0\ 1/2)$] states all 16 symmetry elements of the $P4/nmm$ space group leave the magnetic

propagation vector (**k**) invariant or transform it into an equivalent vector and thus constitute the small group G_k. In the FM state, the decomposition of the magnetic representation Γ_{Mag} in terms of the irreducible representations (IRs) of G_k for the Co site is $1\Gamma_3^1 + 1\Gamma_6^1 + 1\Gamma_9^2 + 1\Gamma_{10}^2$. The resulting basis vectors for the two independent cobalt atoms are given in Table 5.6.

Table 5.6: Basis vectors [m_x, m_y, m_z] for the space group *P4/nmm* with $k = 0$ and $k = (0\ 0\ ½)$. Co1: (1/4 , 3/4, 1/2); Co2: (3/4 , 1/4, 1/2); Nd1: (1/4 , 1/4, 0.14); Nd2: (3/4 , 3/4, 0.86); coordinates in crystallographic cell.

	k = 0				**k = (0 0 ½)**		
	Γ_3^1	Γ_6^1	Γ_9^2	Γ_{10}^2	Γ_2^1	Γ_9^2	Γ_{10}^2
Co1	[0 0 m_z]	[0 0 m_z]	[m_x m_y 0]	[m_x m_y 0]	[0 0 m_z]	[m_x m_y 0]	[m_x m_y 0]
Co2	[0 0 m_z]	[0 0 -m_z]	[m_x m_y 0]	[-m_x -m_y 0]	[0 0 m_z]	[-m_x -m_y 0]	[m_x m_y 0]
Nd1			-	[m_x m_y 0]	[0 0 m_z]	[m_x m_y 0]	[m_x m_y 0]
Nd2			-	[m_x m_y 0]	[0 0 m_z]	[-m_x -m_y 0]	[m_x m_y 0]

The allowed models correspond to an easy-axis ferromagnet (Γ_3^1), an easy-plane ferromagnet (Γ_9^2), and two checkerboard antiferromagnets with moments along the c direction (Γ_6^1) or in the basal plane (Γ_{10}^2), respectively. The solutions with moments in the basal plane are no longer tetragonal and therefore independent m_x and m_y components are allowed. The absence of a measurable lattice distortion, however, prevents their unique determination. In the AFM state the decomposition is $\Gamma_{Mag} = 1\Gamma_2^1 + 1\Gamma_7^1 + 1\Gamma_9^2 + 1\Gamma_{10}^2$ and $\Gamma_{Mag} = 1\Gamma_2^1 + 1\Gamma_3^1 + 1\Gamma_9^2 + 1\Gamma_{10}^2$ for the Co and Nd sites, respectively. In the case of a second-order phase transition, Landau theory states that only a single IR becomes critical. This leaves the Γ_2^1, Γ_9^2, and Γ_{10}^2 symmetries for combined Nd and Co ordering. The unit cell contains two independent Co and two independent Nd sites with basis vectors as given in Table 4.6. The Γ_2^1 and Γ_{10}^2 solutions have FM Co and FM Nd planes (coupled AFM) with moments constrained along the c direction and in the basal plane, respectively. The

Γ_9^2 solution has AFM Co planes and FM Nd planes (coupled AF). The presence of only magnetic (0 0 l) reflections in the FM state reveals that the ordered moment is constrained to the basal plane and that the Γ_9^2 solution is the correct one. Rietveld fitting gives an ordered moment of 0.30(1) μ_B at 15 K and 0.26(1) μ_B at 40 K. Attempts to fit the magnetic intensities to any of the other three models in Table 5.6 were not successful. Subtraction of the 15 and 1.7 K data showed that the FM contribution to the (0 0 l) reflections has disappeared at base temperature. Trial Rietveld refinements quickly established that the Γ_2^1 and Γ_9^2 models do not give good fits to the observed magnetic intensities. The Γ_{10}^2 solution in contrast yields an excellent fit to the data. In this model, adjacent FM Nd layers couple AFM, and the FM Co layer at $z = 1/4$ couples AFM with the FM Co layer at $z = 3/4$, and adjacent Co and Nd moments are antiparallel. All moments are constrained to the basal plane and Rietveld fitting gives m_{Co}=0.26(6) μ_B and m_{Nd}=1.39(4) μ_B at 1.7 K. The final Rietveld fits and a schematic representation of the magnetic structure are given in Fig. 5.18, Fig. 5.19.

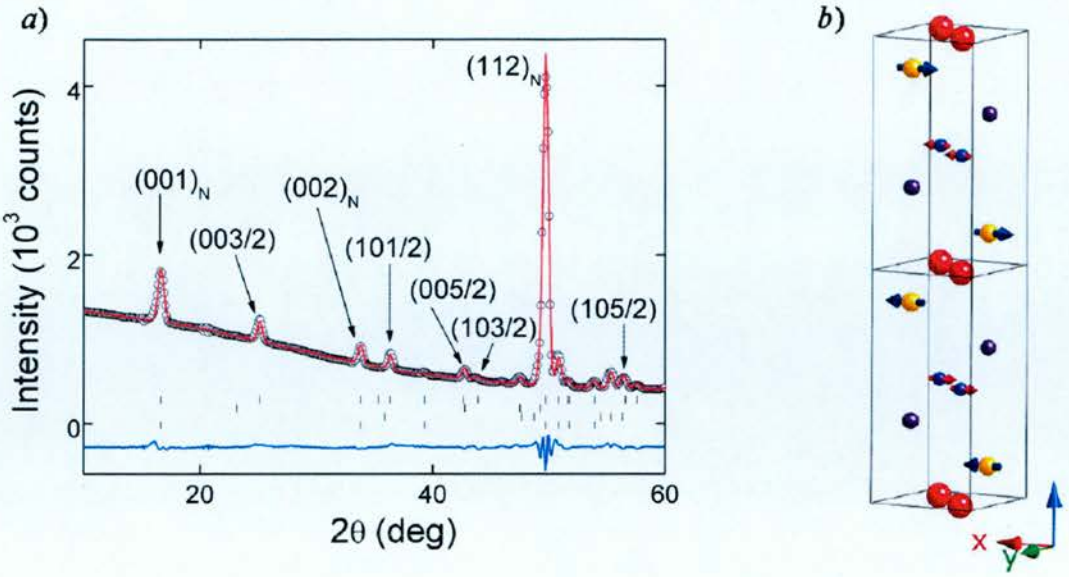

Figure 5.18: a) Rietveld fit against 1.7 K neutron powder diffraction data. The tick marks are from the bottom to top: NdCoAsO, CoAs, NdAs and magnetic phase (wRp = 3.5%, Rp = 2.3%, R_F^2 = 8.4%,). b) The representation of the magnetic structure at that temperature.

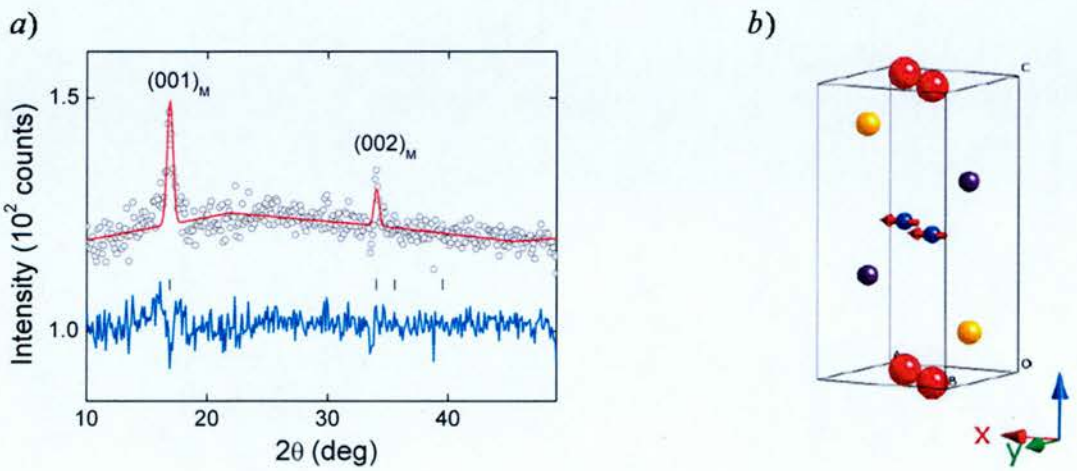

Figure 5.19: a) Rietveld fit against the 15-100 K difference neutron powder diffraction data and b) a schematic representation of the fitted ferromagnetic magnetic structure.

5.6 Discussion

5.6.1 NdFeAsO

The experimental studies revealed that in the NdFeAsO material the ordering of the iron spins occurs at T ~ 140 K and is connected with a structural transition from tetragonal (*P4/nmm*) to orthorhombic (*Cmma*). The $T \rightarrow O$ phase transition has been confirmed by splitting of the tetragonal (2 2 0) Bragg reflection into the orthorhombic (4 0 0) and (0 4 0) Bragg peaks.[15] However, our neutron powder diffraction data collected at 30 K did not show any magnetic peaks. The magnetic model published by Chen et al. has been adopted, where the ordering temperature of iron spins is $T_{N,\,Fe} \sim 141(6)$ K with the Fe magnetic moment ~ 0.25(7) μ_B.. In 2010, Tian et al. published a neutron diffraction study on aligned NdFeAsO single crystals. This study confirmed that the Fe spins order in the stripe-like structure proposed by Chen et al. The Fe magnetic moment $m_{Fe} = 0.54(3)\ \mu_B$ is larger than the one reported on the powder sample. The Néel temperature is determined as $T_{N,\,Fe} \sim 137$ K. In addition, a second magnetic transition was observed at $T_N \sim 15$ K. At this temperature, no doubling along the c direction is required and the Fe stripe-like order in the *ab*-plane remains unchanged. It is rather interesting that a similar second order transition has also been observed in the NdCoAsO material with $T_N \sim 14$ K.[23]

Coupled Nd and Fe spin order in NdFeAsO was observed at $T_N = 1.96(3)$ K,[16] $T_N = 1.7$ K,[18] and at $T_N \sim 6$ K in a single crystal, respectively. Upon Nd ordering the magnetic cell is indexed by a propagation vector of **k** = (1 0 0). In the model proposed by Qiu et al. (PRL model), the AFM Fe moments are constrained along *a* direction, whilst AFM ordered Nd moments are aligned in between the *a* and *c* directions. The total magnetic moments are 1.55(4) μ_B per Nd and 0.9(1) μ_B per Fe.[24] However, our symmetry analysis revealed that the PRL model is not symmetry allowed. In addition, the Rietveld fits using the symmetry allowed Γ_2^1, Γ_6^1, and $\Gamma_2^1 \times \Gamma_6^1$ models gave better fit statistics. The Rietveld fit to difference 1.6-

30 K neutron powder diffraction data using Γ_6^1 yields the lowest value of χ^2. In addition, the most intense (1 0 0) and (1 0 1) magnetic intensities have been fitted satisfactorily. Compared to the high-temperature ordering, the Fe magnetic moment was found to increase from ~ 0.5 μ_B to 1.3 μ_B. This increase suggests that Fe moment is enhanced by Nd spin ordering. Generally, it is found that in the *RE*FeAsO materials the Fe spins order in a striped pattern with a small ordered moment of ~0.4 μ_B for all *RE* from spectroscopic methods such as Mossbauer and μSR.[25] Neutron powder diffraction, in contrast, suggests a wider spread of 0.3–0.8 μ_B,[26] which Maeter et al. have attributed to an induced magnetization on the *RE* sublattice below T_{SDW} that contributes to the "Fe" magnetic Bragg reflections.[25,27] Mazin and Johannes have suggested that iron in fact has a large moment but that this appears strongly reduced because of fluctuations caused by antiphase boundaries and stacking faults along the z-direction. In this scenario, ordering of the Nd sublattice provides enhanced three-dimensional coherency and leads to observation of a larger Fe moment in neutron powder diffraction.[28]

5.6.2 NdCoAsO

Like the isostructural *RE*FeAsO high-*T*c parent materials NdCoAsO exhibits significant interplay between the rare earth and transition-metal sublattices. Below 85 K, NdCoAsO is an itinerant FM with a small ordered cobalt moment of 0.3 μ_B constrained to the *ab* plane. This is analogous to LaCoAsO, which has a Curie temperature of ~60 K and a moment of 0.5 μ_B,[1, 12] and consistent with calculations for LaCoAsO that reveal a spin-polarized band structure with a small ordered moment.[12] Our Arrott plots suggest a linear dependence of M^2 on H/M in large fields typical of weak itinerant ferromagnets such as $ZrZn_2$ but different to the "anomalous" M^4 dependence reported for LaCoAsO.[29] More extensive measurements are needed to investigate this. Below 9 K, Nd spin ordering transforms NdCoAsO to an AF metal. Both the FM and AFM transitions are evident in the temperature derivative of the resistance but do not result in large anomalies as observed for *RE*FeAsO. The almost constant Co moment between 1.7 and 40 K (~0.3 μ_B) suggests that there is no significant induced "Nd contribution",

and the available evidence points toward an unchanged Co moment. However, it is important to note that in symmetry unrestricted refinements (i.e., by allowing canting out of the basal plane) it is possible to obtain solutions with $m_{Co} = 0.9(2)\ \mu_B$ but these are characterized by large correlations and large estimated standard deviations. Trial refinements with noncollinear *RE* ordering analogous to that reported for CeFeAsO[8] did not give satisfactory fits to the data. The fitted Nd moment is $1.39(4)\ \mu_B$, which is comparable to the value for NdFeAsO ~$1.55(4)\ \mu_B$.[16, 30]

5.6.3 $NdFe_{1-x}Co_xAsO$

The lattice constants, bond distances, and angles for $NdFe_{1-x}Co_xAsO$ change gradually, signalling the formation of a solid solution, as confirmed by Rietveld refinement of the Fe/Co occupancies of selected samples against neutron and synchrotron x-ray data. Furthermore, the structural analysis reveals that the *c/a* ratio can be used as an experimental measure of the composition (Fig. 5.4). This is valid because the combined x-ray and neutron refinements presented in Table 5.4 confirm that the only significant compositional change throughout the series is the Fe/Co ratio. The twofold As-Fe-As tetrahedral angle (α), defined in Fig. 5.5 increases with x. This is in contrast to most other forms of chemical doping and may in part explain why cobalt doping has not yielded the high T_c's observed in other electron-doped superconductors, such as $NdFeAsO_{1-x}F_x$ and $NdFeAsO_{1-d}$, despite having the same nominal amount of doping. The chemical disorder introduced by mixing Fe/Co on the same crystallographic site is also expected to have a detrimental effect on the maximum attainable T_c's. The variable temperature synchrotron diffraction study reveals subtle structural distortions consistent with the well established $T \rightarrow O$ structural transition upon cooling for samples with $x = 0.046(2)$ and $x = 0.065(2)$. This confirms that replacement of Fe with Co suppresses the $T \rightarrow O$ transition and the associated SDW. The phase diagram is presented in Fig. 5.18 and reveals the presence of a SC dome with limiting compositions $0.05 \leq x \leq 0.20$. The maximum critical temperature is 16.5(2) K for $x = 0.12$. The underdoped samples ($x \leq 0.075$) have the orthorhombic

Cmma structure. The presence of a "dome" and possible overlap between magnetic and SC regions is consistent with results published for other 1111- and 122-type cobalt-doped superconductors although the existence of phase coexistence is still under debate.[2, 3, 31, 32] The critical field, H_{c2}(T), increases by approximately 2.3(1) T K^{-1} for the three measured compositions upon cooling below T_c. This is smaller than for "indirect" (not Fe-site) electron-doped superconductors, such as $NdFeAsO_{1-x}F_x$, where values of 4–5 T K^{-1} have been observed.[33] However, similar values are reported for other cobalt-doped superconductors[34, 35] suggesting that the superconductivity in these materials is less robust against applied magnetic fields.

5.6.4 Phase Diagram

The phase diagram for low cobalt substitutions is presented in Fig. 5.18 and reveals the presence of a SC dome with limiting compositions $0.05 \leq x \leq 0.20$. Our NdCoAsO shows one FM-AFM transition ($T_N = 9$ K) upon cooling. This is in good agreement with published data on another NdCoAsO powder sample.[23] In this study, a second AFM transition has been observed at $T_N = 14$ K (we did not collect the NPD data between 1.7 and 15 K).[36] The magnetic structure at this temperature is similar to one at 2 K. The FM ordered Co moments rearrange into a layered AFM structure, with simultaneous ordering of small Nd moments on Nd. The value of the Nd magnetic moments develops with decreasing temperature and achieves the saturation at 3.5 K. Moreover, McGuire et al. performed Fe doping in NdCoAsO. Increasing Fe content suppressed the FM-AFM ordering in the sample. $NdCo_{1-x}Fe_xAsO$ becomes paramagnetic at $x = 0.2$ (Fig. 5.20).[36]

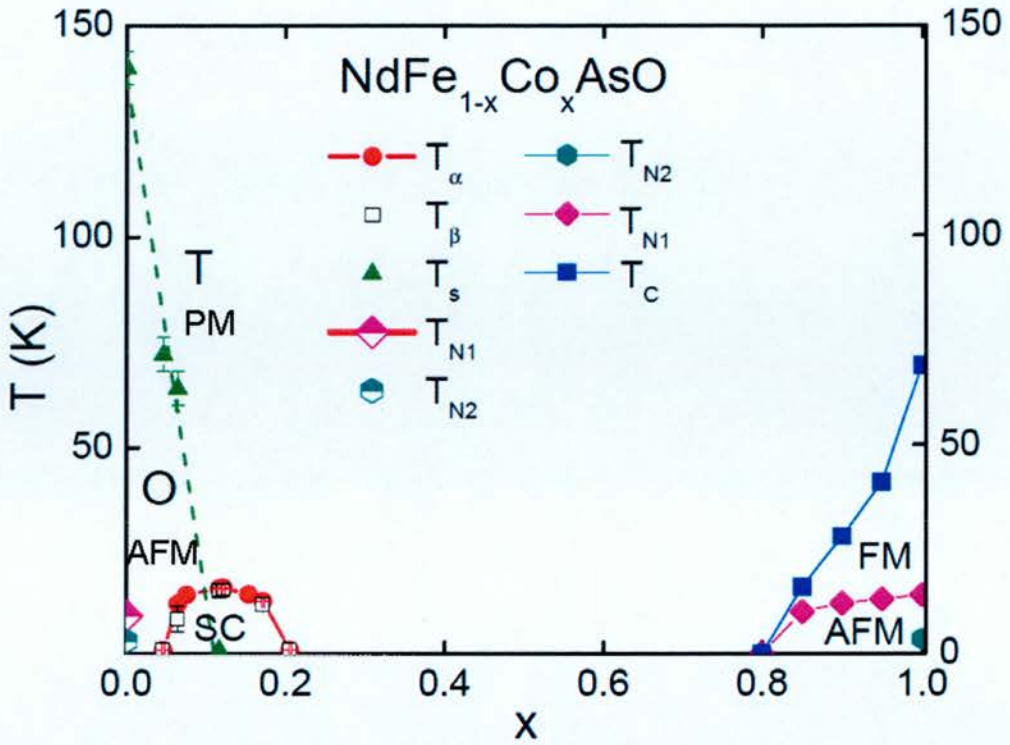

Figure 5.20: Temperature-composition phase diagram for $NdFe_{1-x}Co_xAsO$ showing the suppression of the structural T→O phase transition with increasing Co concentration and the superconducting dome. The data points for the T→O structural transition (Ts) were obtained from synchrotron X-ray powder diffraction, while the superconducting Tc values were obtained from the diamagnetic onset temperatures; (Tα; red circles) and midpoint resistances (T_β; black squares). Error bars indicate 10% and 90% of the resistive transition. The green dotted line is a linear fit to the Ts data. NdCoAsO show FM/AFM transition (T_c/T_{N1}) upon cooling. Increasing Fe content led to a suppression of the FM/AFM.[36]

5.7 References

1 A. S. Sefat, A. Huq, M. A. McGuire, R. Jin, B. C. Sales, D. Mandrus, L. M. D. Cranswick, P. W. Stephens, and K. H. Stone, *Physical Review B* **78**, (10), 104505 (2008).

2 C. Wang, Y. K. Li, Z. W. Zhu, S. Jiang, X. Lin, Y. K. Luo, S. Chi, L. J. Li, Z. Ren, M. He, H. Chen, Y. T. Wang, Q. Tao, G. H. Cao, and Z. A. Xu, *Physical Review B* **79**, (5), 054521 (2009).

3 S. Matsuishi, Y. Inoue, T. Nomura, H. Yanagi, M. Hirano, and H. Hosono, *Journal of the American Chemical Society* **130**, (44), 14428-14429 (2008).

4 A. S. Sefat, R. Jin, M. A. McGuire, B. C. Sales, D. J. Singh, and D. Mandrus, *Physical Review Letters* **101**, (11), 117004 (2008).

5 J. S. Kim, S. Khim, H. J. Kim, M. J. Eom, J. M. Law, R. K. Kremer, J. H. Shim, and K. H. Kim, *Physical Review B* **82**, (2), 024510

6 N. Kumar, R. Nagalakshmi, R. Kulkarni, P. L. Paulose, A. K. Nigam, S. K. Dhar, and A. Thamizhavel, *Physical Review B* **79**, (1), 012504 (2009).

7 C. H. Lee, A. Iyo, H. Eisaki, H. Kito, M. T. Fernandez-Diaz, T. Ito, K. Kihou, H. Matsuhata, M. Braden, and K. Yamada, *Journal of the Physical Society of Japan* **77**, (8), 083704 (2008).

8 J. Zhao, Q. Huang, C. de la Cruz, S. Li, J. W. Lynn, Y. Chen, M. A. Green, G. F. Chen, G. Li, Z. Li, J. L. Luo, N. L. Wang, and P. Dai, *Nat Mater* **7**, (12), 953-959 (2008).

9 P. JegliC, J. W. G. Bos, A. Zorko, M. Brunelli, K. Koch, H. Rosner, S. Margadonna, and D. ArCon, *Physical Review B (Condensed Matter and Materials Physics)* **79**, (9), 094515-7 (2009).

10 C. H. Lee, and et al., *Phys. Soc. Jpn.* **77**, (8), 083704 (2008).

11 M. Rotter, M. Tegel, and D. Johrendt, *Physical Review Letters* **101**, (10), 107006-4 (2008).

12 H. Yanagi, R. Kawamura, T. Kamiya, Y. Kamihara, M. Hirano, T. Nakamura, H. Osawa, and H. Hosono, *Physical Review B* **77**, (22), 224431 (2008).

13 A. S. Sefat, D. J. Singh, R. Jin, M. A. McGuire, B. C. Sales, F. Ronning, and D. Mandrus, *Physica C: Superconductivity* **469**, (9-12), 350-354 (2009).

14 M. Fratini, R. Caivano, A. Puri, A. Ricci, Z. A. Ren, X.-L. Dong, J. Yang, W. Lu, Z.-X. Zhao, L. Barba, G. Arrighetti, M. Polentarutti, and A. Bianconi, *Superconductor Science and Technology* **21**, (9), 092002 (2008).

15 Y. Chen, J. W. Lynn, J. Li, G. Li, G. F. Chen, J. L. Luo, N. L. Wang, P. Dai, C. dela Cruz, and H. A. Mook, *Physical Review B (Condensed Matter and Materials Physics)* **78**, (6), 064515-5 (2008).

16 Y. Qiu, W. Bao, Q. Huang, T. Yildirim, J. M. Simmons, M. A. Green, J. W. Lynn, Y. C. Gasparovic, J. Li, T. Wu, G. Wu, and X. H. Chen, *Physical Review Letters* **101**, (25), 257002-4 (2008).

17 A. S. Wills, *Physica B: Condensed Matter* **276-278**, 680-681 (2000).

18 A. Marcinkova, D. A. M. Grist, I. Margiolaki, T. C. Hansen, S. Margadonna, and J.-W. G. Bos, *Physical Review B* **81**, (6), 064511

19 A. S. Sefat, R. Jin, M. A. McGuire, B. C. Sales, D. J. Singh, and D. Mandrus, *Physical Review Letters* **101**, (11), 117004-4 (2008).

20 C. W. Chu, and B. Lorenz, *Physica C: Superconductivity* **469**, (9-12), 385-395 (2009).

21 N. R. Werthamer, E. Helfand, and P. C. Hohenberg, *Physical Review* **147**, (1), 295 (1966).

22 A. Arrott, *Physical Review* **108**, (6), 1394 (1957).

23 M. A. McGuire, A. S. Sefat, B. C. Sales, and D. Mandrus, *Physical Review B* **82**, (9), 092404

24 Y. Qiu, B. Wei, Q. Huang, T. Yildirim, J. M. Simmons, M. A. Green, J. W. Lynn, Y. C. Gasparovic, J. Li, T. Wu, G. Wu, and X. H. Chen, *Physical Review Letters* **101**, (25), 257002 (2008).

25 H. Maeter, H. Luetkens, Y. G. Pashkevich, A. Kwadrin, R. Khasanov, A. Amato, A. A. Gusev, K. V. Lamonova, D. A. Chervinskii, R. Klingeler, C. Hess, G. Behr, B. Buechner, and H. H. Klauss, *Physical Review B* **80**, (9), 094524 (2009).

26 J. W. Lynn, and P. Dai, *Physica C: Superconductivity* **469**, (9-12), 469-476 (2009).

27 Y. Chen, J. W. Lynn, J. Li, G. Li, G. F. Chen, J. L. Luo, N. L. Wang, P. Dai, C. dela Cruz, and H. A. Mook, *Physical Review B* **78**, (6), 064515 (2008).

28 I. I. Mazin, and M. D. Johannes, *Nat Phys* **5**, (2), 141-145 (2009).

29 H. Ohta, and K. Yoshimura, *Physical Review B* **79**, (18), 184407 (2009).

30 A. Marcinkova, E. Suard, A. N. Fitch, S. Margadonna, and J. W. G. Bos, *Chemistry of Materials* **21**, (13), 2967-2972 (2009).

31 J.-H. Chu, J. G. Analytis, C. Kucharczyk, and I. R. Fisher, *Physical Review B (Condensed Matter and Materials Physics)* **79**, (1), 014506-6 (2009).

32 C. Lester, J.-H. Chu, J. G. Analytis, S. C. Capelli, A. S. Erickson, C. L. Condron, M. F. Toney, I. R. Fisher, and S. M. Hayden, *Physical Review B* **79**, (14), 144523 (2009).

33 J. Jaroszynski, F. Hunte, L. Balicas, Y.-j. Jo, I. RaiCevic, A. Gurevich, D. C. Larbalestier, F. F. Balakirev, L. Fang, P. Cheng, Y. Jia, and H. H. Wen, *Physical Review B (Condensed Matter and Materials Physics)* **78**, (17), 174523-9 (2008).

34 N. Ni, M. E. Tillman, J. Q. Yan, A. Kracher, S. T. Hannahs, S. L. Bud'ko, and P. C. Canfield, *Physical Review B* **78**, (21), 214515 (2008).

35 A. S. Sefat, A. Huq, M. A. McGuire, R. Jin, B. C. Sales, D. Mandrus, L. M. D. Cranswick, P. W. Stephens, and K. H. Stone, *Physical Review B (Condensed Matter and Materials Physics)* **78**, (10), 104505-9 (2008).

36 M. A. McGuire, A. S. Sefat, B. C. Sales, and D. Mandrus, *Physical Review B* **82**, (9), 092404 (2010).

CHAPTER 6

Crystal Structure and Superconductivity of NdNiAsO

6.1 Introduction

In contrast to the 1111-type *RE*FeAsO materials, the Nickel (Ni) analogues have no magnetically ordered parent material, but are found to superconduct, albeit with much lower transition temperatures (≤ 4 K).[1-6] This suggest that the superconductivity in the Ni materials is of different origin. The absence of the magnetically ordered parent materials is consistent with electronic band structure calculations that show that Fermi surface nesting of electron and hole pockets, which is considered to cause AFM and superconductivity in the Fe-based superconductors, is destroyed by increased band filling. Both, electron- and hole-doping (F^- and Sr^{2+}) in LaNiAsO resulted in increase of T_c from 2.4 K to ~ 3.8 K.[7, 8]

Nickel based superconductors reported so far include 1111-type LaNiPO ($T_C = 4.2$ K), LaNiAsO ($T_C = 2.4$ K), 122-type $BaNi_2P_2$ ($T_C = 2.7$ K), $SrNi_2P_2$ ($T_C = 1.4$ K), $BaNi_2As_2$ ($T_C = 0.68$ K), $SrNi_2As_2$ ($T_C = 0.62$ K), and the mixed 122/1111-type $La_3Ni_4P_4O_2$ ($T_C = 2.2$ K).[9-13]

6.2 Synthesis

A polycrystalline NdNiAsO sample was synthesised from stoichiometric amounts of NdAs and NiO. NiO (99.999%) was obtained from Sigma Aldrich. NdAs was prepared from a stoichiometric mixture of Nd (Sigma Aldrich, 99.99%) and As (Sigma Aldrich, 99.9%) which was heated for 2 hrs at 500 °C in an evacuated quartz tube, immediately followed by 16 hrs at 900 °C. NdAs and NiO were mixed using mortar and pestle,

pressed into pellets and heated for 24 hrs at 1100 °C. All sample manipulations were done in an Ar filled glovebox.

6.3 Structural Analysis

Laboratory X-ray powder diffraction data were collected on a Bruker AXS D8 Advance diffractometer using Cu $K\alpha_1$ radiation. Neutron powder diffraction data were collected at 2 K, 50 K and 175 K on the ILL D2B powder diffractometer. Data were recorded between $5° \leq 2\theta \leq 140°$ with a step size of 0.05°. The neutron wavelength used was $\lambda = 1.594$ Å. The sample was contained in a 6 mm diameter cylindrical vanadium can.

Low temperature (< 2 K) neutron powder data were collected on the time of flight WISH powder diffractometer at the ISIS, UK. Data were collected in the temperature range 0.3 K-1.5 K in the series of *d*-spacing ranges 0.9-4.8 (bank 1), 1.0-5.6 (bank 2), 1.4-7.5 (bank 3), 1.9-12 (bank 4) and 2.6-19.6 Å (bank 5). Data were collected for total proton beam currents of 100 μA hours for T = 0.3 K and 1.5 K, and of 30 μA hours for temperatures in between. After normalization using the spectra from a main beam monitor and correction for the wavelength dependence of the detector, the spectral ranges were finally merged to provide a composite pattern covering the range 20 to 100 ms time of flight, equivalent to 0.9 Å to 12 Å in *d*-spacing. No diffraction peaks were observed at longer *d*-spacings up to the limit of observation at 12 Å. The DIF C, DIF A and Zero parameters for each bank are summarized in table 6.1. The sample was contained in a 6 mm diameter cylindrical copper can. The GSAS suite of programs and the EXPGUI graphical user interface were used for Rietveld fitting of neutron powder diffraction data.

Table 6.1: The summarized WISH NPD parameters (DIF C, DIF A and Zero) for bank 1-5 for NdNiAsO.

Bank number	Scattering angle (°)	DIF C	DIF A	Zero
Bank 1	152.827	20767.998	-4.635	-9.241
Bank 2	121.660	18658.109	-4.086	-10.937
Bank 3	90.000	15110.570	-2.922	-13.934
Bank 4	58.330	10344.771	-0.585	-16.157
Bank 5	26.660	4926.100	+1.390	-18.525

6.3.1 Variable Temperature High-resolution Neutron Powder Diffraction

Laboratory X-ray and neutron powder diffraction confirmed the tetragonal *P4/nmm* structure with RT lattice constants a = 4.0496(1) Å and c = 8.0537(2) Å. No phase transitions are observed on cooling, and the structure is described in the *P4/nmm* space group throughout. Further proof of the absence of the tetragonal to orthorhombic (*Cmma*) transition that occurs in the *RE*FeAsO parent materials comes from the temperature evolution of the full width half maximum (FWHM) of the (220) reflection, which remains constant at 0.236(3)° (Table 6.2). The Rietveld refinement of the occupancies, which are equal to each other within 3 estimated standard deviations, resulted in a composition of $Nd_{1.01(1)}Ni_{0.97(1)}As_{0.97(1)}O_{1.00(1)}$. The gain in goodness of fit compared to the nominal composition is negligible. The refined structural parameters, selected bond lengths and angles and fit statistics are presented in Table 6.1. The Rietveld fit to the 2 K D2B neutron powder diffraction pattern is shown in Fig. 6.1. The electronically important twofold angle is α = 118.8(2)° at 1.8 K and the Ni-Ni distance (d_{Ni-Ni}) is 2.856 Å. From laboratory powder X-ray diffraction, the RT value for α = 120.1(2)° and d_{Ni-Ni} = 2.864 Å. The NPD data did not revealed any magnetic peaks down to 1.6 K.

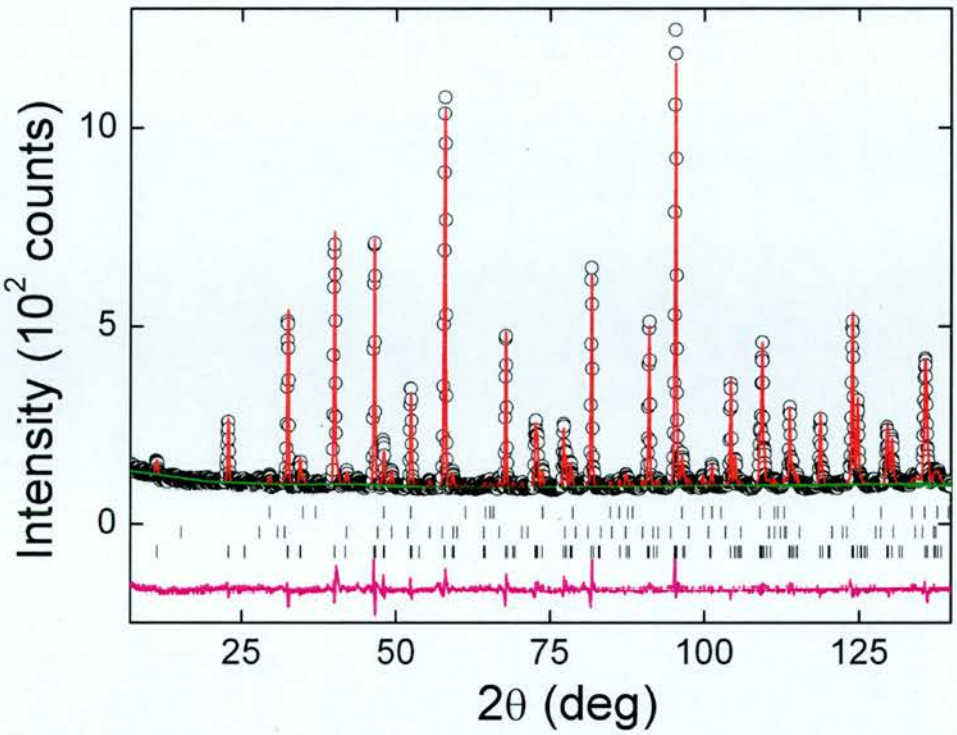

Figure 6.1: Rietveld fit against 2 K D2B neutron powder diffraction data for NdNiAsO. Observed data are indicated by open circles, the fit by the solid line, and the difference curve is shown at the bottom. From bottom to top: The Bragg markers are for NdNiAsO, Nd_2O_3 and NiAs.

Table 6.2: Refined lattice constants, atomic parameters, selected bond lengths (Å) and angles (°), and fit statistics for NdNiAsO from Rietveld fits against D2B neutron powder diffraction data.

T (K)		2	50	150
SG		*P4/nmm*	*P4/nmm*	*P4/nmm*
a-axis (Å)		4.03941(4)	4.03979(4)	4.04279(4)
c-axis (Å)		8.0397(1)	8.0407(1)	8.0454(1)
Volume (Å^3)		131.182(3)	131.223(3)	131.495(3)
FWHM (220) (°)		0.236(3)	0.239(3)	0.232(3)
Nd	U_{iso}(Å^2)	0.0002(3)	0.0009(3)	0.0036(3)
	Z	0.1430(4)	0.1432(4)	0.1434(4)
	Occ.	1.01(1)	1.02(1)	1.01(1)
Ni	U_{iso}(Å^2)	0.0002(3)	0.0009(3)	0.0036(3)
	Occ.	0.97(1)	0.97(1)	0.96(1)
As	U_{iso}(Å^2)	0.0002(3)	0.0009(3)	0.0036(3)
	Z	0.6486(5)	0.6483(5)	0.6471(6)
	Occ.	0.96(1)	0.96(1)	0.95(1)
O	U_{iso}(Å^2)	0.0002(3)	0.0009(3)	0.0036(3)
	Occ.	1.00(1)	1.00(1)	1.00(1)
d(Nd-O) (Å)		2.324(2)	2.325(2)	2.2983(4)
∠O-Nd-O (°)		120.7(1)	120.6(1)	120.6(2)
∠O-Nd-O (°)		104.16(6)	104.19(6)	104.23(7)
d(Ni-As) (Å)		2.347(2)	2.345(2)	2.342(2)
∠As-Ni-As (°)		118.8(2)	118.9(2)	119.3(2)
∠As-Ni-As (°)		105.02(7)	104.97(8)	104.79(8)
d(Ni-Ni) (Å)		2.85629(2)	2.85656(2)	2.85868(3)
χ^2		3.4	3.3	3.2
wR_p (%)		4.9	4.8	4.7
R_p (%)		3.8	3.7	3.7
R_F^2 (%)		4.5	4.3	5.0

Nd: 2c(¼, ¼, z); Ni: 2b(¾, ¼, ½); As: 2c(¼, ¼, z); O: 2a(¾, ¼, 0)

Impurities: 1.0(3) wt% Nd_2O_3, 1.0(2) wt% NiAs.

6.3.2 Variable temperature Time-of-flight Neutron Powder Diffraction

NPD data were collected from 0.3 K up to 1.5 K. Rietveld fitting confirmed the tetragonal structure down to 0.3 K. The site occupancies were kept at 1.00 for all elements. The Rietveld fit to the 0.3 K WISH NPD pattern is shown in Fig. 6.2. The most intense Bragg peaks from the copper can have been fitted using the fully weighted Le Bail method. A trial Rietveld fit with preferred orientation for the copper phase lead to unstable refinement. The absence of the structural transition is confirmed by the constant lattice parameters over the 0.3 K< T < 1.5 K temperature range.

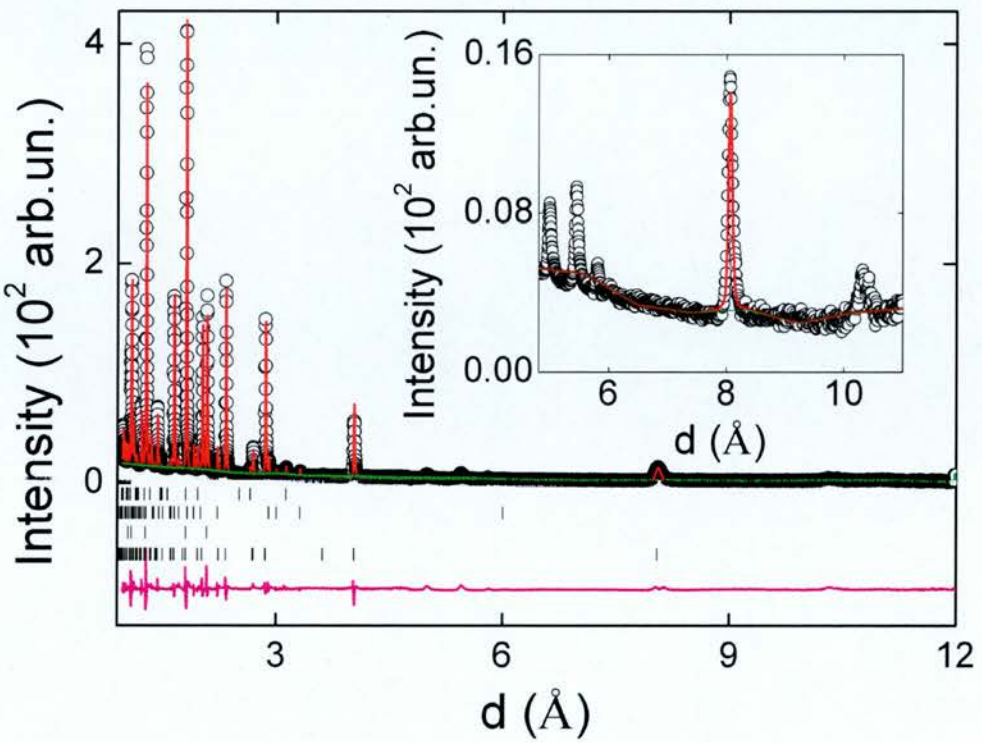

Figure 6.2: Rietveld fit against 0.3 K WISH neutron powder diffraction data for NdNiAsO. Observed data are indicated by open circles, the fit by the solid line, and the difference curve is shown at the bottom. From bottom to top: The Bragg markers are for NdNiAsO, copper, Nd_2O_3 and NiAs. The inset shows the first four magnetic peaks for NdNiAsO.

6.4 Magnetic Susceptibility

The ZFC magnetic (χ) and inverse ($1/\chi$) magnetic susceptibilities are shown in Fig. 6.3. The temperature dependence of χ is Curie-Weiss between RT and 30 K, and is dominated by the paramagnetic contribution of Nd^{3+}. A fit to $\chi = C/(T-\theta)$ yields $C = 1.77(5)$ emu $K^{-1}mol^{-1}$ and $\theta_W = -21(1)$ K. The Curie constant (C) corresponds to an effective magnetic moment $\mu_{eff} = 3.76(3)\ \mu_B$, which is in good agreement with the expected value for Nd^{3+} ($^4I_{9/2}$, 3.62 μ_B). Below 30 K, a decrease in $1/\chi$ is observed, which may be related to neodymium 4f crystal field effects also observed in heat capacity measurements. The negative Weiss temperature (θ_W) indicates antiferromagnetic interactions between local Nd^{3+} moments.

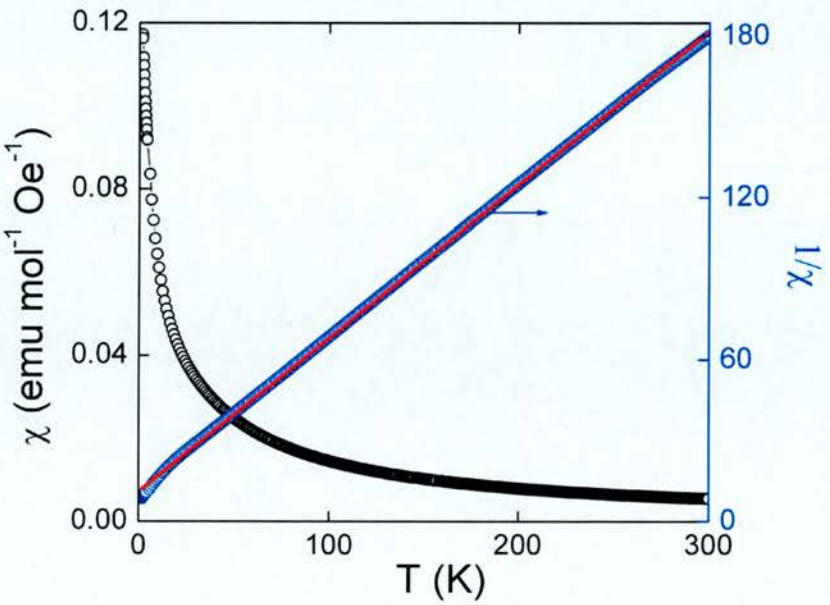

Figure 6.3: Temperature dependence of the ZFC magnetic and inverse magnetic susceptibilities for NdNiAsO. The solid line is a fit to the Curie-Weiss law.

6.5 Magnetic Structure

In the d-spacing range displayed (Fig. 6.2), the magnetic reflections at 10.121 Å, 5.784 Å, 5.428 Å and 4.984 Å were observed at 0.3 K. Small magnetic peaks were observed at 3.763 Å, 3.437 Å and 3.056 Å. The WISH NPD patterns collected at 0.3 K and 1.5 K are shown in Fig. 6.4. The three most intense magnetic peaks appear at 1.25(6) K, other two small ones (3.763 Å, 3.473 Å) at 0.7 K, and a final small magnetic peak at $d = 4.984$ Å appears at 0.5 K. The integrated peak intensity for each magnetic reflection is shown in Fig. 6.4. This suggests existence of three magnetic transitions, which is consistent with heat capacity measurements (see Fig. 6.7).

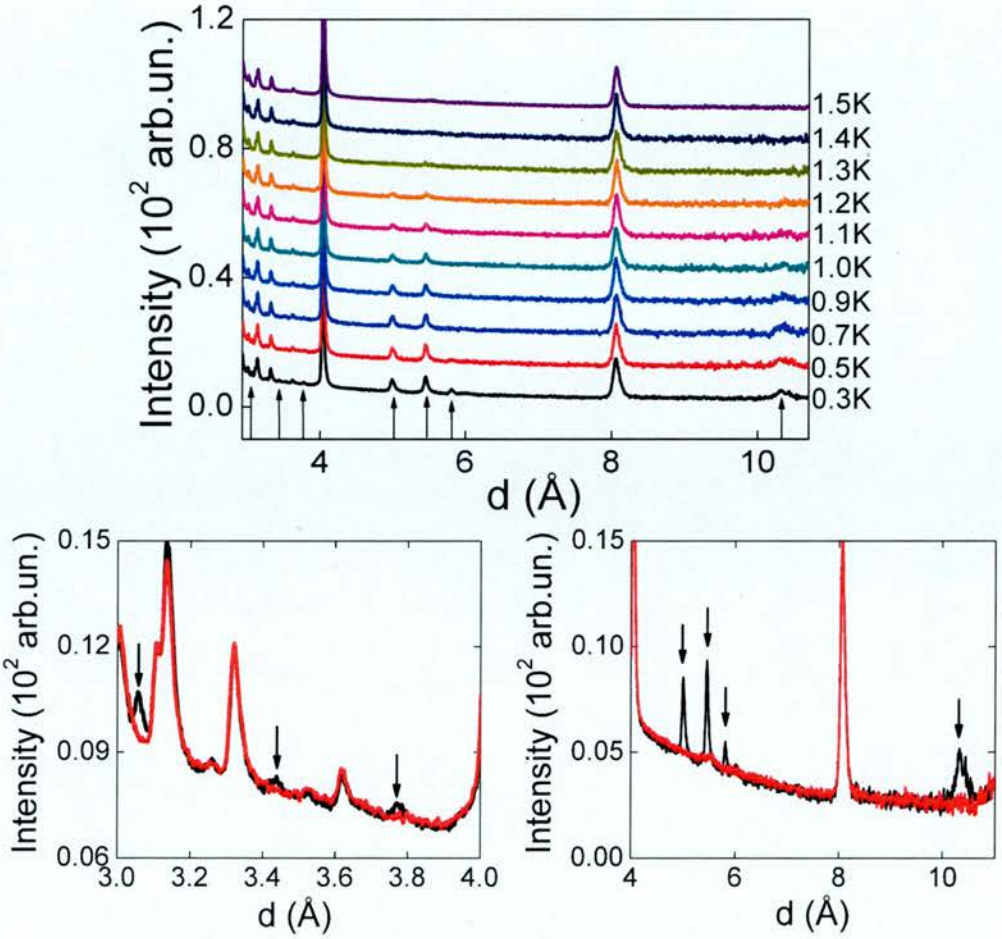

Figure 6.4: (upper) The comparison of WISH neutron powder data collected between 0.3-1.5 K. (bottom) Detailed comparison of WISH neutron powder data collected at 0.3 K (black line) and 1.5 K (red line). The arrows indicate magnetic reflections.

None of the magnetic peaks can be indexed on a commensurate superstructure related to NdNiAsO or any of the containing impurities (NiAs, Nd_2O_3). The K-search package in FullProf program found two possible **k**-vectors; **k** = (0, ~0.30, ½), which index the three main magnetic reflections. The second possible **k**-vector is **k** = (~1/4, ~0.3, 0). These possible solutions can be compared to those magnetic structures in *RE*$CuSb_2$ proposed by M. Kolenda et al.[14, 15] The integrated intensities of the Bragg magnetic peaks (Fig. 6.5) are comparable to those observed In NdFeAsO suggesting that the magnetic intensities of the 3 most intense peaks are due to the main phase.

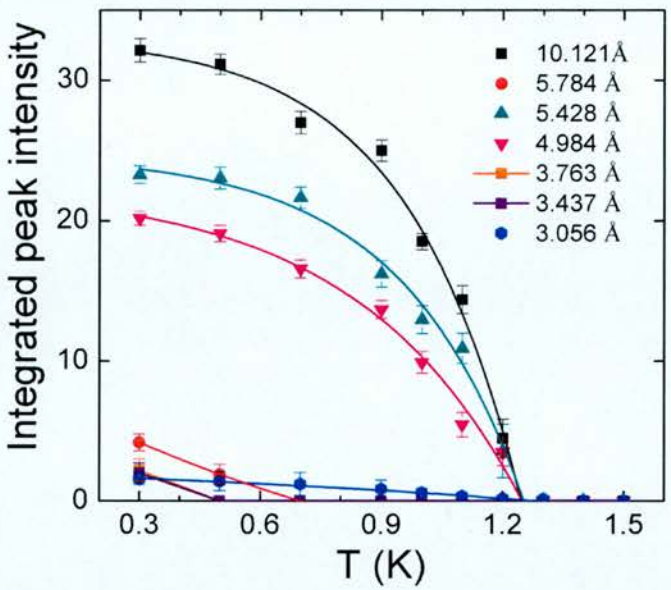

Figure 6.5: The temperature dependence of the magnetic reflections in the temperature range 0.3 K-1.5 K for NdNiAsO WISH NPD data.

6.6 Electrical Resistivity

The electrical resistivity was measured by a conventional four-probe method between 1.7 and 300 K using the resistance option of a Quantum Design Physical Property Measurement System (PPMS). A dilution fridge was used to measure the four point resistivity below 1.8 K. The temperature dependence of the electrical resistivity (ρ) is shown in Fig. 6.6. NdNiAsO exhibits metallic behaviour down to 1.3 K. A fit to $\rho(T) = \rho_0 + \alpha T^n$ from 2 K to 50 K gives $\rho_0 = 0.108(3)$ mΩ cm, $\alpha = 0.001(1)$ and

n = 1.89(3). The observed exponent is in good agreement with the expected value for a Fermi liquid (n = 2). The residual resistivity ratio (RRR) is 12. The inset shows the data measured below 2 K in the dilution fridge. This reveals a superconducting transition with an onset temperature $T_{c,onset}$ = 1.2 K and zero resistance at $T_{c,zero}$ = 1.0 K ($T_{c,\ midpoint}$ = 1.1 K).

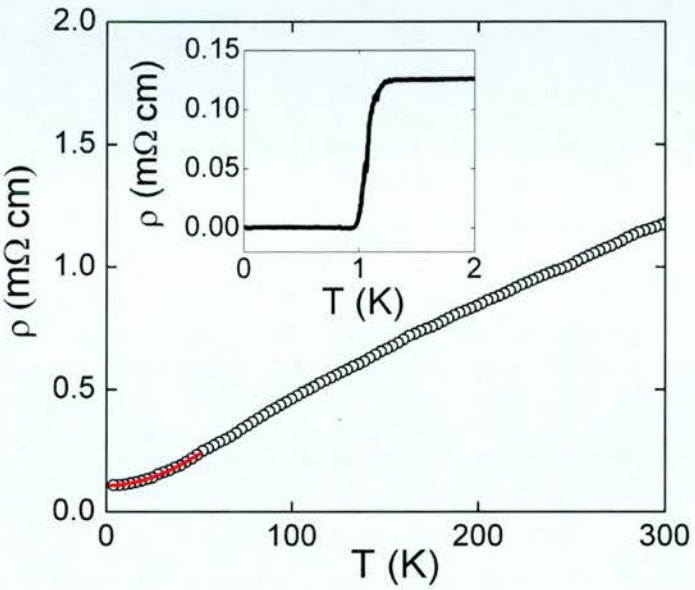

Figure 6.6: The temperature dependence of the electrical resistivity between 1.3 K and 300 K for NdNiAsO. The inset shows the temperature dependence of the electrical resistivity between 0 K and 1.3 K.

6.7 Heat Capacity

The heat capacity was measured between 0.3-30 K using the PPMS heat capacity option and Helium-3 refrigeration system. The heat capacity measurement was performed in absence of a magnetic field. The results are summarized in Fig. 6.7 and Fig 6.8. Three transitions (Fig. 6.7) with their maxima at 0.48(1) K, 0.65(1) K and 1.27 K were revealed by plotting C/T as a function of temperature, T. All three transition have been observed in the WISH NPD data and are therefore of magnetic origin. The electronic term was isolated by plotting C/T as a function of T^2 (Fig. 6.7 inset). This yields a Sommerfeld coefficient γ = 18.3 ±2.2 mJ mole^{-1} K^{-2}, 2-3 times larger than that reported for LaNiAsO (5-7 mJ mole^{-1} K^{-2}).[16] The Debye expression was used to estimate the

phonon heat capacity. This is shown as the red curve in Fig. 4b, where the Debye temperature $\theta_D = 223(2)$ K gives a good match to the experimental data between 27-30 K. The difference between the measured heat capacity and the phonon contribution at lower temperatures is solely due to the electronic and magnetic contributions (blue line). The initial discrepancy below 27 K is due to the crystal field splitting of the Nd^{3+} 4f states, and the magnitude is modelled well using a Schottky anomaly. Below 5 K, the heat capacity shows a lambda transition revealing a long range magnetic ordering transition at 1.3 K. The magnetic entropy associated with this peak is close to Rln2, indicating a S = ½ ground state, which has also been observed for *RE*FeAsO (*RE* = Nd, Sm).[17]

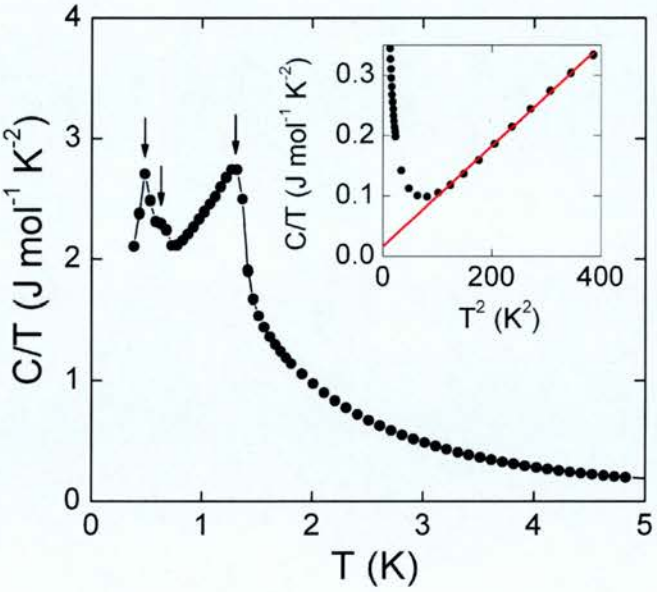

Figure 6.7: The temperature dependence of the C/T between 0.3-30 K. The inset shows C/T as a function of T^2. The solid red line is a linear fit.

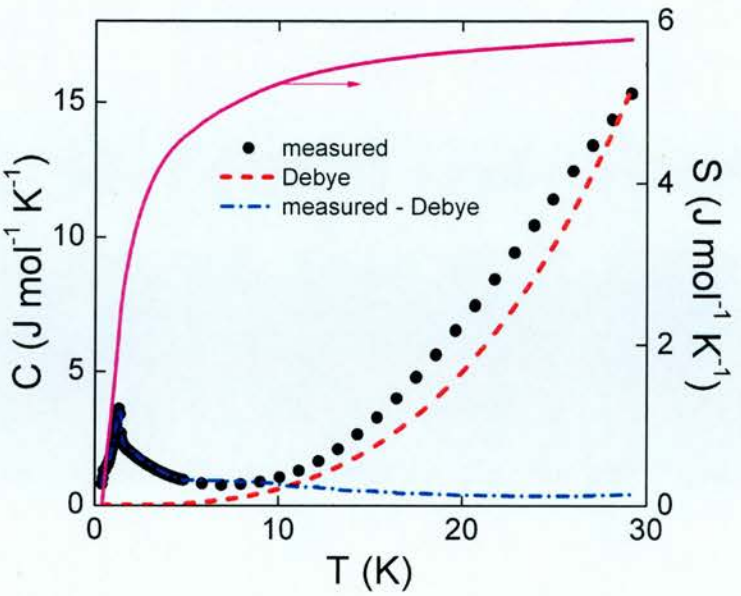

Figure 6. 8: The temperature dependence of the heat capacity (black circles) for NdNiAsO illustrating the lattice contribution modelled using the Debye model (red dash line), the electronic heat capacity obtained by subtracting the Debye contribution (blue short dash dot line). The solid (pink) line shows magnetic and electronic entropy.

6.8 Discussion

The structures and properties of polycrystalline NdNiAsO have been studied using laboratory x-ray powder diffraction, neutron powder diffraction, magnetic susceptibility, electrical resistance and heat capacity measurements. The NdNiAsO sample was prepared and characterised for the first time, thereby extending the *RE*NiAsO family of superconductors towards smaller and magnetic *RE*-ions. The NPD data revealed that NdNiAsO has tetragonal structure (*SG P4/nmm*). The crystal lattice parameters and electronically important two-fold angle showed typical thermal dependence with increasing temperature (Tab. 6.2). There is no evidence for a structural transition in the temperature interval 0.3 K to 150 K. It is well established that the electronic properties in these compounds are very sensitive to any changes in the covalent *TM-Pn* (*TM* = Fe, Co, Ni; *Pn* = P, As) layers.[18] In the nickel based superconductors, higher T_c are observed for compounds with more distorted As–Ni–As angles (α) compared to the ideal angle. The two-fold tetrahedral As–Ni–As angle is 119.3(2)° in NdNiAsO (T_c~1.1 K); 122.95° in LaNiAsO (T_c~2.4 K)[8] and 126.5(2)° in LaNiPO (T_c~4 K).[12, 13] This opposes the trend observed in the Fe-based analogues.

None of the measurements done on NdNiAsO reveal any evidence of magnetic ordering of the nickel spins as observed in the high-T_c iron based superconductors. The magnetic susceptibility is consistent with local Nd^{3+} ($^4I_{9/2}$) spins and itinerant non-magnetic nickel spins. The electrical resistivity reveals typical metallic behaviour down to 2 K, and the superconducting transition with $T_{c,midpoint}$ = 1.1 K, which is two times reduced compared to LaNiAsO sample (T_c = 2.4 K).

Heat capacity measurements reveal three magnetic transitions at ~ 1.3 K, 0.7 K and 0.5 K. All of them have been observed on Neutron powder diffraction data and are therefore of magnetic origin. The magnetic ordering transition observed at 1.3 K with an associated magnetic entropy is due to the ordering of localized S = 1/2 Nd^{3+} states. The reduction to S = ½ from the free ion value was also reported for NdFeAsO and SmFeAsO, and therefore appears intrinsic to this particular crystal field. Sommerfeld coefficient γ = 18.3 ±2.2 mJ mol^{-1} K^{-2} is almost three times larger than the reported for LaNiAsO (5-7 mJ mol^{-1} K^{-2}),[16] which does not contain a magnetic 4f element. It is also

larger than reported for $BaNi_2As_2$ (10.8 ± 1.0 mJ mol^{-1} K^{-2})[19] and $SrNi_2As_2$ (8.7 ± 1.0 mJ mol^{-1} K^{-2}).[20] The larger The Sommerfeld coefficient for NdNiAsO suggests a possible weak hybridization between the Nd *4f* states and Ni *3d* states and therefore Nd *4f* states might play a role in the electronic transport properties. In contrast, strongly correlated systems have much bigger Sommerfeld coefficients. In 1111-type materials, strong correlations between *4f* and *3d* states have been observed in CeFePO ($\gamma \sim 700$ mJ mol^{-1} K^{-2})[21] via heat capacity measurements.[22]

6.9 References

1 E. D. Bauer, F. Ronning, B. L. Scott, and J. D. Thompson, *Physical Review B (Condensed Matter and Materials Physics)* **78**, (17), 172504 (2008).

2 V. Keimes, D. Johrendt, A. Mewis, C. Huhnt, and W. Schlabitz, *Zeitschrift für anorganische und allgemeine Chemie* **623**, (11), 1699-1704 (1997).

3 F. Lei, Y. Huan, C. Peng, Z. Xiyu, M. Gang, and W. Hai-Hu, *Physical Review B (Condensed Matter and Materials Physics)* **78**, (10), 104528 (2008).

4 T. M. McQueen, T. Klimczuk, A. J. Williams, Q. Huang, and R. J. Cava, *Physical Review B (Condensed Matter and Materials Physics)* **79**, (17), 172502-4 (2009).

5 F. Ronning, E. D. Bauer, T. Park, S. H. Baek, H. Sakai, and J. D. Thompson, *Physical Review B (Condensed Matter and Materials Physics)* **79**, (13), 134507-7 (2009).

6 F. Ronning, N. Kurita, E. D. Bauer, B. L. Scott, T. Park, T. Klimczuk, R. Movshovich, and J. D. Thompson, *Journal of Physics: Condensed Matter* **20**, (34), 342203 (2008).

7 L. Fang, H. Yang, P. Cheng, X. Zhu, G. Mu, and H.-H. Wen, *Physical Review B* **78**, (10), 104528 (2008).

8 Z. Li, G. Chen, J. Dong, G. Li, W. Hu, D. Wu, S. Su, P. Zheng, T. Xiang, N. Wang, and J. Luo, *Physical Review B* **78**, (6), 060504 (2008).

9 E. D. Bauer, F. Ronning, B. L. Scott, and J. D. Thompson, *Physical Review B* **78**, (17), 172504 (2008).

10 T. Klimczuk, T. M. McQueen, A. J. Williams, Q. Huang, F. Ronning, E. D. Bauer, J. D. Thompson, M. A. Green, and R. J. Cava, *Physical Review B* **79**, (1), 012505 (2009).

11 F. Ronning, E. D. Bauer, T. Park, N. Kurita, T. Klimczuk, R. Movshovich, A. S. Sefat, D. Mandrus, and J. D. Thompson, *Physica C: Superconductivity* **469**, (9-12), 396-403 (2009).

12 M. Tegel, D. Bichler, and D. Johrendt, *Solid State Sciences* **10**, (2), 193-197 (2008).

13 T. Watanabe, H. Yanagi, T. Kamiya, Y. Kamihara, H. Hiramatsu, M. Hirano, and H. Hosono, *Inorganic Chemistry* **46**, (19), 7719-7721 (2007).

14 M. Kolenda, A. Oles, and A. Szytula, *Journal of Alloys and Compounds* **322**, (1-2), 55-58 (2001).

15 A. Szytula, M. Kolenda, and A. Oles, *Journal of Alloys and Compounds* **383**, (1-2), 224-227 (2004).

16 Z. Li, G. F. Chen, J. Dong, G. Li, W. Z. Hu, D. Wu, S. K. Su, P. Zheng, T. Xiang, N. L. Wang, and J. L. Luo, *Physical Review B* **78**, (6), 060504 (2008).

17 P. J. Baker, S. R. Giblin, F. L. Pratt, R. H. Liu, G. Wu, X. H. Chen, M. J. Pitcher, D. R. Parker, S. J. Clarke, and S. J. Blundell, *New Journal of Physics* **11**, 025010 (2009).

18 K. Ishida, Y. Nakai, and H. Hosono, *Journal of the Physical Society of Japan* **78**, (6), 062001 (2009).

19 F. Ronning, N. Kurita, E. D. Bauer, B. L. Scott, T. Park, T. Klimczuk, R. Movshovich, and J. D. Thompson, *Journal of Physics-Condensed Matter* **20**, (34), 342203 (2008).

20 E. D. Bauer, F. Ronning, B. L. Scott, and J. D. Thompson, *Physical Review B* **78**, (17), 172504 (2008).

21 E. M. Bruning, C. Krellner, M. Baenitz, A. Jesche, F. Steglich, and C. Geibel, *Physical Review Letters* **101**, (11), 117206 (2008).

22 M. G. Holder, A. Jesche, P. Lombardo, R. Hayn, D. V. Vyalikh, S. Danzenbacher, K. Kummer, C. Krellner, C. Geibel, Y. Kucherenko, T. K. Kim, R. Follath, S. L. Molodtsov, and C. Laubschat, *Physical Review Letters* **104**, (9), 096402 (2010).

CHAPTER 7

Conclusions

In this thesis a detailed investigation of the properties of several 1111-type rare-earth transition metal oxyarsenides and their doped analogues was undertaken. The Nd*TM*AsO (*TM* = Mn, Fe, Co and Ni), Ca doped $Nd_{1-x}Ca_xFeAsO$ ($0 \leq x \leq 0.05$) and Co doped $NdFe_{1-x}Co_xAsO$ ($0 \leq x \leq 1$) series have been synthesized. Synchrotron X-ray powder diffraction, magnetic susceptibility and transport property measurements were employed to characterise these systems. In addition, neutron powder diffraction was used to describe the magnetic structures. The synthesis and characterisation of the Nd*TM*AsO series demonstrates that changes in chemical composition can induce significant changes in the electronic and magnetic properties of these compounds. As demonstrated through whole thesis, Nd*TM*AsO and its doped analogues show a remarkably wide range of interesting properties, including spin-density-wave antiferromagnetism (NdFeAsO), ferromagnetism (NdCoAsO), and both conventional (NdNiAsO) and unconventional superconductivity ($NdFe_{1-x}Co_xAsO$).

7.1. Crystal Structure

The synthesis, structure and physical properties of new 1111-type rare-earth transition oxyarsenides Nd*TM*AsO (*TM* = Mn, Fe, Co and Ni) have been studied in order to learn more about the electronic and magnetic properties. Structural studies reveal that all these materials crystallise with the 1111-type ZrCuSiAs structure. Upon cooling, NdFeAsO undergoes a symmetry-lowering crystallographic phase transition (T → O). No structural transition has been observed down to 2 K in the Mn, Co or Ni analogues. The lattice constants, twofold α tetrahedral angle, *TM-As* distance and height of the arsenic atom are shown in Fig. 7.1 as a function of the ionic radii of the transition metal. At room temperature, the c-axis increases linearly with increasing *TM* ionic radius, whilst the a-axis initially shrinks and then expands (Fig. 7.1). This results in an anomalously large volume for Mn (146 $Å^3$), which is much larger than expected based

on a simple extrapolation of the values for NdFeAsO (135 $Å^3$), NdCoAsO (132 $Å^3$) and NdNiAsO (131 $Å^3$). The expansion of the unit cell, along the a-axis is due to the corresponding variation of the density of states within basal plane. In other words, the ab-plane expands due to the increasing number (Fe → Ni) of the delocalized 3d electrons in the *TM* band at Fermi level. Due to the contraction of the unit cell along c-axis the layer-layer distance is reduced and As is pushed towards the Fe plane. This can be demonstrated by the arsenic height parameter that is given as $h_{Pn} = (z_{Pn} - 0.5) * c$ shown in Fig. 7.1. The electronically important twofold tetrahedral As–*TM*–As angle (α) decreases with increasing *TM* ionic radius and is 119.3(2)° in NdNiAsO, 111.36(4)° in NdFeAsO, 115.70(3)° in NdCoAsO and 111.59(2)° in NdMnAsO.

Structural analysis confirmed the tetragonal space-group *P4/nmm* for the prepared samples of $Nd_{1-x}Ca_xFeAsO$ (x = 0.025 and 0.05) and $NdFe_{1-x}Co_xAsO$ ($0 \leq x \leq 1$) at room temperature. In addition the tetragonal to orthorhombic structural transition was observed at low temperatures ($T \leq 175$ K) for $Nd_{1-x}Ca_xFeAsO$ (x = 0.025 and 0.05) and $NdFe_{1-x}Co_xAsO$ (x = 0.047 and 0.065). In the $Nd_{1-x}Ca_xFeAsO$ serie, the two-fold tetrahedral As-Fe-As angle (α) and h_{Pn} remains almost unchanged upon doping; α = 111.53(4)° with h_{Pn} = 1.350 Å (x = 0.025) and α = 111.66(5)° with h_{Pn} = 1.346 Å (x = 0.05). In $NdFe_{1-x}Co_xAsO$ (x = 0.064, 0.118, 0.172) materials, α increases with increasing Co content from 111.73(2)°(x = 0.064), to 112.24(3)° (x = 0.118) and 112.63(4)° (x = 0.172). The h_{Pn} decreases with increasing x and is 1.346 Å for x = 0.064, 1.334 Å for x = 0.118 and 1.324 Å for x = 0.172.

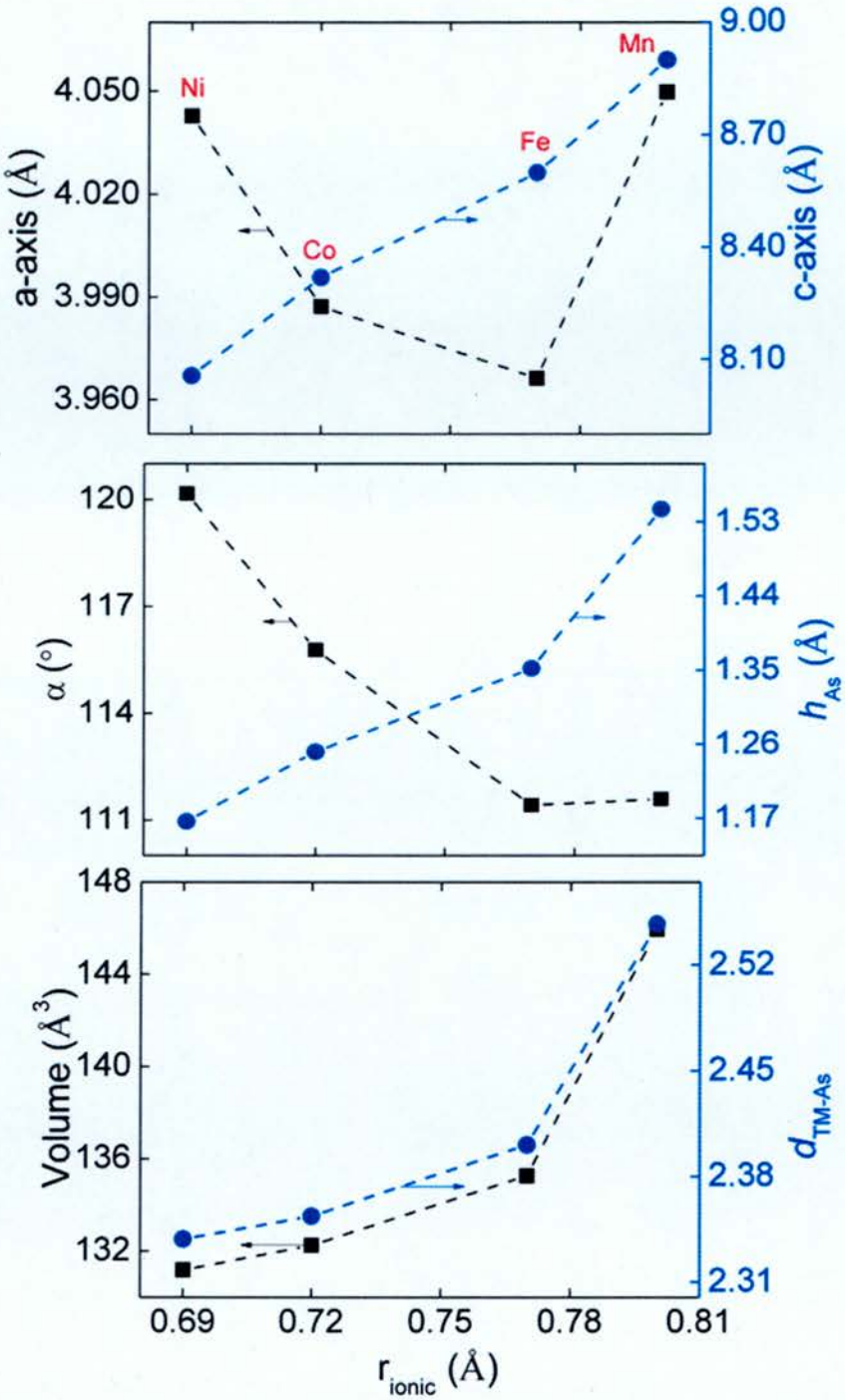

Figure 7.1: Variation in the a- and c-axis, As-*TM*-As Angle, height of the Arsenic atom, *TM*-As and Volume with the ionic radii of the transition metal for Nd*TM*AsO (*TM* = Mn, Fe, Co and Ni).

7.2 Electronic and Magnetic Properties of Nd*TM*AsO

Study of the effects of various transition metals using substitution within the Fe-As layer reveals that the electronic and magnetic properties dramatically vary with the number of 3d-electrons of *TM*.

NdMnAsO is found to be an antiferromagnetic semiconductor, while NdFeAsO is an antiferromagnet showing poor metallic behavior and NdCoAsO is a metallic ferromagnet. Furthermore, NdNiAsO is a good metal with low temperature superconducting behavior. The magnetic susceptibility for all Nd*TM*AsO materials is consistent with localized Nd^{3+} moments with $T_{N,Nd} \leq 10$ K for TM = Fe, Co, Ni and $T_{N,Nd} \leq 23$ K for TM = Mn.

Calcium doping in $Nd_{1-x}Ca_xFeAsO$ ($0 \leq x \leq 0.05$) led to suppression of the $T_{SDW} \sim 130$ K and insulating behavior. This is in agreement with other published studies on Ca doped 1111-type materials, although it is still not clear, why Ca doping did not lead to superconductivity. A reduction of the Curie constant, C, is observed upon Ca substitution due to the dilution of the antiferromagnetism in the Nd sublattice. In contrast, $NdFe_{1-x}Co_xAsO$ ($0.05 \leq x \leq 0.175$) materials are superconducting with the highest $T_c = 16.5$ K for $x = 0.118$. In NdNiAsO, heat capacity and electrical resistivity measurements suggest the possible coexistence of magnetic ordering of the Nd^{3+} moments below 1.3 K and superconductivity with $T_{c,\,\text{midpoint}} = 1.1$ K.

7.2.1 Enhancement of T_c

In general, large T_c values in the Fe-based superconductors are observed if the As–Fe–As bond angle, α, approaches a regular tetrahedron (~ 109.5°). For well-characterized cobalt-doped superconductors, the maximum observed critical temperatures ($T_{c,max}$) are plotted in Fig. 7.2a against the tetrahedral As-Fe-As angle (α). The following observations can be made: (1) $T_{c,max}$ increases as α tends toward the regular tetrahedral value. This is in agreement with the literature for indirectly doped superconductors, although there is no evidence for a maximum occurring at the ideal tetrahedral angle. (2) The 122-type materials have higher T_c's than the 1111-type for a given value of α.

This contrasts the situation for indirect doping where the largest T_c's up to 55 K are obtained for electron-doped 1111 phases such as $NdFeAsO_{1-x}F_x$, while the hole-doped 122 phases with a smaller separation between Fe_2As_2 planes are limited to 38 K for $Ba_{1-x}K_xFe_2As_2$ (both parents have $\alpha \sim 111.2°$).

As discussed above, cobalt doped samples with more distorted twofold α angle have lower T_c. This approach is not valid in Ni analogues, in which T_c increases with more distorted α (Fig. 7.2b). From simple bonding considerations, the orbital overlap between *TM* and As is optimized at the ideal tetrahedral angle ($\alpha = 109.5°$), and a lower density of states (DOS) at the Fermi level is expected. In case of the *TM* = Fe materials, this optimizes T_c, whereas in case of *TM* = Ni more distorted $TMAs_4$ tetrahedra and higher DOS at E_F appear favourable. This is consistent with an electron-phonon mediated superconducting mechanism (BCS theory) where a higher DOS at E_F is predicted to lead to higher T_c's. Similar correlation between α (towards ideal) and T_c (reduced) is observed for all known 1111 and 122-type NiAs and NiP superconductors. The maximum observed critical temperatures (T_c) for Fe- and Ni-based superconductors are plotted in Fig. 7.2 against the tetrahedral As-Fe-As angle (α).

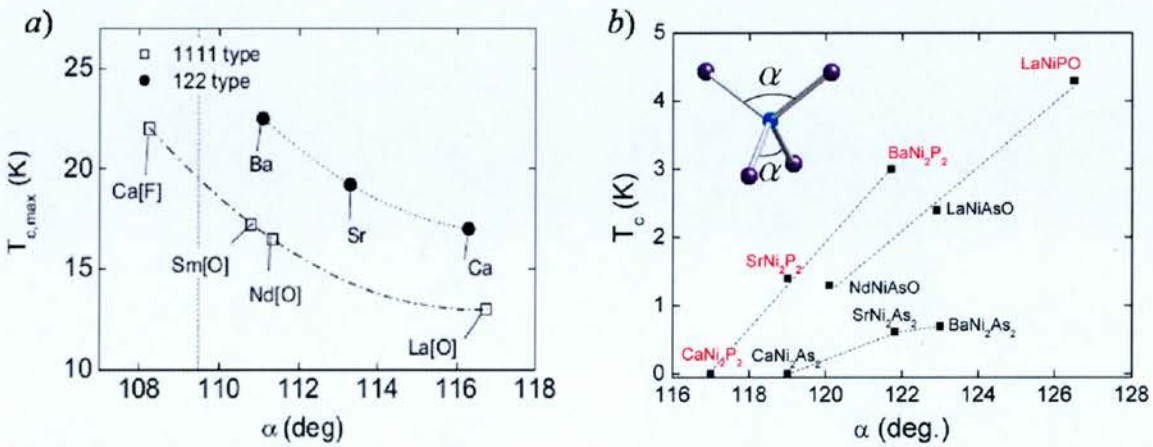

Figure 7.2: Variation in the superconducting T_c with tetrahedral As-Fe-As angle (defined in the inset) for a) Cobalt doped 122-type *Ae*Fe_2As_2 and 1111-type *RE*FeAs(O,F) and b) 122-type *Ae*Ni_2As_2 and 1111-type *RE*Ni*Pn*O (*Pn* = P and As). The lines (solid, dash) are intended as a guide for the eyes.

7.3 Magnetic Structures

The magnetic ordering in the Nd*TM*AsO (*TM* = Mn, Fe, Co and Ni) compositions was investigated using high-flux neutron powder diffraction (NPD) on ~ 2 g polycrystalline samples. The magnetic structures of Nd*TM*AsO (*TM* = Mn, Fe and Co) are shown in Fig. 7.3. For the *TM* = Mn, Fe and Co compositions, the magnetic cell is a commensurate superstructure with the magnetic propagation vector **k** = 0 for *TM* = Mn and **k** = (1, 0, 0), (1, 0, ½) for *TM* = Fe, Co. NPD reveals that FM Co moments ($T_c \leq 85$ K) order at low temperature, while the AFM Mn moments are found to be ordered up to 360 K ($T_{N,Mn} = 359$ K). Magnetic moments of the transition metal moments are comparable in NdFeAsO and NdCoAsO with value of $m_{Fe} \sim 0.30(1)$ μ_B and $m_{Co} \sim 0.26$-0.3 μ_B.

In all systems, the ordering of the Nd moments is observed at much lower temperatures with $T_N \leq 23$ K (*TM* = Mn), $T_N \sim 2$ K (*TM* = Fe) and $T_N \sim 9$ K (*TM* = Co). In NdCoAsO, the Nd spin ordering results in the antiferromagnetic coupling of the existing ferromagnetic planes. The fitted Co magnetic moment remains same and the Nd magnetic moment is $m_{Nd} \sim 1.39(1)$ μ_B in NdCoAsO.

In NdMnAsO, upon cooling, a spin-reorientation (SR) transition of the Mn moments into the *ab* plane occurs ($T_{SR} = 23$ K). This coincides with the long-range ordering of the Nd moments, which are restricted to the basal plane. The fitted Nd magnetic moment is $m_{Nd} \sim 1.94(1)$ μ_B. The magnetic propagation vector remains **k** = 0. At base temperature (1.6 K) the fitted Mn moment is $m_{ab,Mn} \sim 1.46(6)$ μ_B.

From our NPD data it is not clear whether, in the NdFeAsO material, the Fe moments are aligned along *a*- or *c*-axis, upon Nd ordering. From our data analysis, the best Rietveld fit with the lowest value of χ^2 (0.96) is achieved using the Γ_6^1 model in which the AFM ordered Fe spins are aligned along *c*-axis, whilst the AFM ordered Nd spins are aligned along *a*-axis. With this model, the total Fe magnetic moment is m = 1.30(7) μ_B and the Nd magnetic moment is $m_{Nd} \sim 1.46(6)$ μ_B. Another neutron powder diffraction experiment is planned in near future in order to describe the low temperature magnetic cell in NdFeAsO.

In NdNiAsO, none of the magnetic peaks indexes on a commensurate superstructure related to the NdNiAsO cell or any of the impurities (NiAs, Nd_2O_3) present. This suggests that the mechanism of the magnetism in NdNiAsO is different than for the other *TM* analogues.

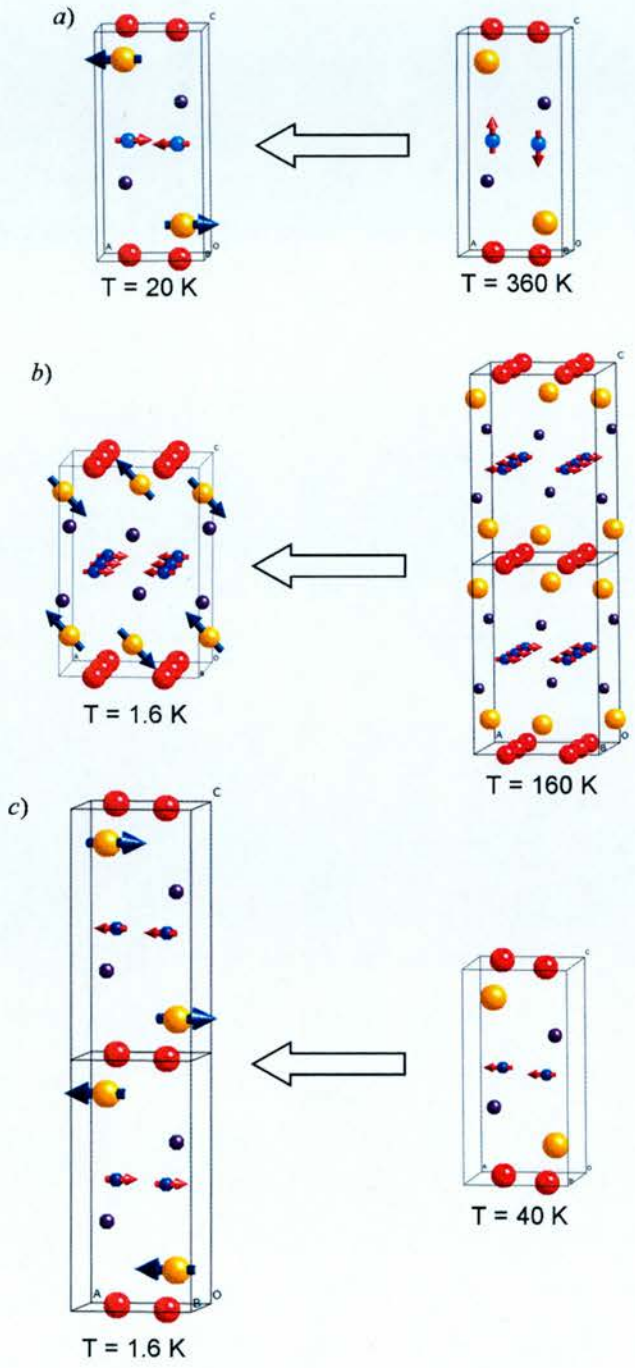

Figure 7.3: Magnetic structures of a) NdMnAsO, b)NdFeAsO and c)NdCoAsO.

Reprint of Publications

CHEMISTRY OF
MATERIALS
Article

Chem. Mater. **2009,** *21,* 2967–2972 2967
DOI:10.1021/cm9007188

Response of the Crystal Structure and Electronic Properties to Calcium Substitution in NdFeAsO

A. Marcinkova,[†] E. Suard,[‡] A. N. Fitch,[§] S. Margadonna,[†] and J. W. G. Bos*,[†]

[†]*School of Chemistry and Centre for Science at Extreme Conditions, University of Edinburgh, Edinburgh EH9 3JJ, United Kingdom,* [‡]*Institut Laue Langevin, 38042 Grenoble, France, and* [§]*European Synchrotron Radiation Facility, 39043 Grenoble, France*

Received March 13, 2009. Revised Manuscript Received April 27, 2009

Synchrotron X-ray, neutron powder diffraction, magnetic susceptibility, and electrical resistance measurements were used to investigate the $Nd_{1-x}Ca_xFeAsO$ series. The solubility of calcium is limited to $0 \leq x \leq 0.05$. Within this interval, the iron arsenide layer contracts linearly in agreement with the hole doping of anti-bonding iron 3d-orbital states at the Fermi level. Depletion of the free charge carriers results in a transition to semiconducting behaviour. The iron spin-density wave (SDW) transition temperature is reduced from 140 K ($x = 0$) to 125 K ($x = 0.025$) to 130 K ($x = 0.05$). Long-range SDW ordering is only observed in neutron diffraction concomitant with that of the rare-earth sublattice ($T_{N,Nd} \approx 2$ K), revealing that the Nd ordering enhances the ordered Fe moment in spite of the large difference in ordering temperature. The transition to semiconducting behaviour results in a dramatic change in the magnitude and field dependence of the magnetoresistance (MR), which is much reduced ($R/R_0 = 1.6$ for $x = 0$, 1.03 for $x = 0.025$, and 1.06 for $x = 0.05$ at 5 K and in 9 Tesla) and becomes more linear for $x > 0$. Finally, MR is first observed at the onset of the structural $P4/nmm \rightarrow Cmma$ transition, and increases more rapidly below T_{SDW}, providing further evidence that the structural phase transition and SDW are linked.

Introduction

The discovery[1] of high-T_c superconductivity in $LaFeAsO_{1-x}F_x$ generated enormous scientific interest and led to the rapid exploration of other iron-based superconductors. Presently, four main groups are known: 1111 type RFeAsO and AeFeAsF,[1−5] 122 type $AeFe_2As_2$,[6−8] 111 type A_xFeAs,[9−11] and 11 type $FeSe_{1-d}$,[12,13] where R = La, Ce−Nd, Sm, Gd−Dy, Ae = Ba, Sr, Ca, Eu, and A = Li, Na. The 1111 and 122 materials share many features. Perhaps the most important one is that superconductivity emerges from a magnetically ordered metallic state by charge carrier doping.[14] In the RFeAsO materials, this may be achieved by electron and hole doping, whereas the $AeFe_2As_2$ materials become superconducting upon hole doping only. There is a wide variety of chemical ways for charge carrier doping into the conducting iron arsenide layers. This includes substitutions in the electronically inert layers, such as $(R_{1-x}Sr_x)$,[15] $(Ae_{1-x}K_x)$,[7] $(O_{1-x}F_x)$[1] and (O_{1-d}),[16] but also by direct doping on the Fe site by for example Co.[17] Hydrostatic pressure has also been used to suppress the magnetic ordering and induce superconductivity.[18] Band structure calculations show that the electronic states at the Fermi level are mostly made up out of Fe 3d orbital states with a small but non-zero contribution of the pnictide-atom.[19−21] The largest contribution is from the Fe $3d_{x^2-y^2}$ orbital, which points directly towards the nearest

*Corresponding author. E-mail: j.w.g.bos@ed.ac.uk.

(1) Kamihara, Y.; Watanabe, T.; Hirano, M.; Hosono, H. *J. Am. Chem. Soc.* **2008**, *130*, 3296.
(2) Chen, G. F.; Li, Z.; Wu, D.; Li, G.; Hu, W. Z.; Dong, J.; Zheng, P.; Luo, J. L.; Wang, N. L. *Phys. Rev. Lett.* **2008**, *100*, 247002.
(3) Chen, X. H.; Wu, T.; Wu, G.; Liu, R. H.; Chen, H.; Fang, D. F. *Nature* **2008**, *453*, 761.
(4) Matsuishi, S.; Inoue, Y.; Nomura, T.; Hirano, M.; Hosono, H. *J. Phys. Soc. Jpn.* **2008**, *77*, 113709.
(5) Matsuishi, S.; Inoue, Y.; Nomura, T.; Yanagi, H.; Hirano, M.; Hosono, H. *J. Am. Chem. Soc.* **2008**, *130*, 14428.
(6) Chen, G. F.; Li, Z.; Li, G.; Hu, W. Z.; Dong, J.; Zhou, J.; Zhang, X. D.; Zheng, P.; Wang, N. L.; Luo, J. L. *Chin. Phys. Lett.* **2008**, *25*, 3403.
(7) Sasmal, K.; Lv, B.; Lorenz, B.; Guloy, A. M.; Chen, F.; Xue, Y. Y.; Chu, C. W. *Phys. Rev. Lett.* **2008**, *101*, 107007.
(8) Rotter, M.; Tegel, M.; Johrendt, D. *Phys. Rev. Lett.* **2008**, *101*, 107006.
(9) Parker, D. R.; Pitcher, M. J.; Clarke, S. J. *Chem. Commun.* **2009**, 2189.
(10) Pitcher, M. J.; Parker, D. R.; Adamson, P.; Herkelrath, S. J. C.; Boothroyd, A. T.; Ibberson, R. M.; Brunelli, M.; Clarke, S. J. *Chem. Commun.* **2008**, 5918.
(11) Tapp, J. H.; Tang, Z. J.; Lv, B.; Sasmal, K.; Lorenz, B.; Chu, P. C. W.; Guloy, A. M. *Phys. Rev. B* **2008**, *78*, 060505.
(12) Hsu, F. C.; Luo, J. Y.; Yeh, K. W.; Chen, T. K.; Huang, T. W.; Wu, P. M.; Lee, Y. C.; Huang, Y. L.; Chu, Y. Y.; Yan, D. C.; Wu, M. K. *Proc. Natl. Acad. Sci., U.S.A.* **2008**, *105*, 14262.
(13) Margadonna, S.; Takabayashi, Y.; McDonald, M. T.; Kasperkiewicz, K.; Mizuguchi, Y.; Takano, Y.; Fitch, A. N.; Suard, E.; Prassides, K. *Chem. Commun.* **2008**, 5607.
(14) Zhao, J.; Huang, Q.; de la Cruz, C.; Li, S. L.; Lynn, J. W.; Chen, Y.; Green, M. A.; Chen, G. F.; Li, G.; Li, Z.; Luo, J. L.; Wang, N. L.; Dai, P. C. *Nat. Mater.* **2008**, *7*, 953.
(15) Kasperkiewicz, K.; Bos, J. W. G.; Fitch, A. N.; Prassides, K.; Margadonna, S. *Chem. Commun.* **2009**, 707.
(16) Kito, H.; Eisakt, H.; Iyo, A. *J. Phys. Soc. Jpn.* **2008**, *77*, 063707.
(17) Sefat, A. S.; Jin, R. Y.; McGuire, M. A.; Sales, B. C.; Singh, D. J.; Mandrus, D. *Phys. Rev. Lett.* **2008**, *101*, 117004.
(18) Alireza, P. L.; Ko, Y. T. C.; Gillett, J.; Petrone, C. M.; Cole, J. M.; Lonzarich, G. G.; Sebastian, S. E. *J. Phys.: Condens. Matter* **2009**, *21*, 012208.
(19) Singh, D. J.; Du, M. H. *Phys. Rev. Lett.* **2008**, *100*, 237003.
(20) Haule, K.; Shim, J. H.; Kotliar, G. *Phys. Rev. Lett.* **2008**, *100*, 226402.
(21) Kasinathan, D.; Ormeci, A.; Koch, K.; Burkhardt, U.; Schnelle, W.; Leithe-Jasper, A.; Rosner, H. *New J. Phys.* **2009**, *11*, 025023.

Published on Web 05/18/2009

neighbour Fe atoms and is highly dispersive in the $a-b$ plane but remains flat along the c-direction. The second largest contribution is from the xz and yz orbitals.[21] The origin of the magnetic ordering in the parent material remains under debate but is commonly attributed to a spin-density wave (SDW) instability at the Fermi surface.[22] Among the new high-T_c groups, the $RFeAsO_{1-x}F_x$ materials are of particular interest as they afford the highest critical temperatures and fields up to 55 K and ~100 T.[23−25]

Here we report on the crystal and magnetic structures, the magnetic susceptibilities, and electrical resistivities of the $Nd_{1-x}Ca_xFeAsO$ series. Substitution of Ca^{2+} on the Nd^{3+} site corresponds to nominal hole doping (oxidation of iron). The NdFeAsO parent is a poor metal that shows a separate (in temperature) SDW and tetragonal (*P4/nmm*) to orthorhombic (*Cmma*) transition. These transitions occur at 140 and 160 K, respectively. The magnetic ordering is confirmed by neutron powder diffraction, μSR, NMR, and Mossbauer with an ordered iron moment of ~0.25 μ_B.[26−30] The structural transition is second order and a broadening of synchrotron X-ray diffraction reflections is observed below 160 K, while full splitting is observed below 140 K.[30,31] There are two published neutron powder diffraction studies of the Fe SDW in NdFeAsO. One finds magnetic ordering below 2 K only, which coincides with the magnetic ordering of the Nd sublattice.[32] The refined moments are $m_x = m = 0.9(1)\,\mu_B$ for Fe and $m_x = 1.22(7)\,\mu_B$, $m_z = 0.96(9)\,\mu_B$, and $m = 1.55(4)\,\mu_B$ for Nd. In this case, the magnetic cell is identical to the crystallographic one and the Fe moments align in ferromagnetic stripes with the antiparallel alignment along the longer a-axis. The other demonstrates that the iron moments remain aligned in stripes up to $T_{SDW} = 141(6)$ K ($\gg T_{N,Nd} \approx 2$ K) but with a much reduced moment ($m = 0.25(7)\,\mu_B$) and a magnetic cell that is doubled along the c-axis.[29] The 3-fold increase in the ordered Fe moment below $T_{N,Nd}$ is unexpected, as the large difference in ordering temperatures suggests that the two sublattices do not interact much. Electron doping NdFeAsO via fluorine substitution or oxygen deficiency results in superconductivity with a maximum $T_c \approx 55$ K for in $NdFeAsO_{1-x}F_x$ and $NdFeAsO_{1-d}$.[16,33,34] In addition, these materials have upper critical fields on the order of 100 Tesla.[35] The pairing mechanism in these superconductors remains unclear but is likely related to the SDW, although measurements of the phonon density of states reveal small differences between parent and superconducting compositions in $NdFeAsO_{1-x}F_x$.[36] Hole doping via chemical substitution of Sr^{2+} on the Nd-site has been reported by some of us and affords a superconducting phase with $T_c = 15$ K for $x = 0.2$ in the series $Nd_{1-x}Sr_xFeAsO$.[15] The present study is part of our investigation into the chemical stability of the 1111-type materials and the effects that different dopants have on the crystal structure and physical properties of this important class of materials. To the best of our knowledge, this is the first detailed report on the effects of Ca doping in any of the 1111 type superconductors.

Experimental Section

Polycrystalline samples of $Nd_{1-x}Ca_xFeAsO$ were prepared using standard solid-state chemistry methods. Stoichiometric amounts of NdAs, FeAs, Fe, Fe_2O_3, and CaO were mixed intimately using mortar and pestle and pressed into dense pellets. These were heated for 24 hours at 1150 °C with one intermediate regrinding. All chemicals were obtained from Sigma Aldrich with at least 99.9% purity and all sample manipulations were done inside an Ar filled glovebox. The precursors FeAs and NdAs were prepared from stoichiometric mixtures of the elements heated in evacuated quartz tubes for 2 h at 500 °C, followed by 16 h at 900 °C for NdAs and 750 °C for FeAs. Laboratory powder X-ray diffraction using a Bruker D8 Advance diffractometer (Cu $K_{\alpha 1}$) revealed the presence of a CaO impurity phase for samples with $x > 0.15$. Traces of Nd_2O_3 or NdAs were observed for some attempts but never exceed 5 mass % from Rietveld fitting and are absent in the best samples. The initial exploration of these materials was done on a 0.5 g scale. For $x = 0$ and $x = 0.05$, 2 g samples were prepared for neutron powder diffraction measurements. Room-temperature synchrotron X-ray powder diffraction patterns were collected on the ID31 instrument at the European Synchrotron Radiation Facility, Grenoble. The prepared samples were measured during two experiments; the first with $\lambda = 0.39986$ Å was done on compositions $x = 0$, 0.05, and 0.10; the second with $\lambda = 0.40030$ Å was done on $x = 0.025$, 0.05, 0.075, and 0.15. The $x = 0.05$ sample was measured in both experiments for scaling purposes. Data sets were collected between $2 \le 2\theta \le 40°$ and binned with a stepsize of 0.002°. Rietveld fitting of these data sets showed that the solubility of calcium is limited to $x = 0.05$

(22) Mazin, II; Johannes, M. D.; Boeri, L.; Koepernik, K.; Singh, D. J. *Phys. Rev. B* **2008**, *78*, 085104.
(23) Bos, J. W. G.; Penny, G. B. S.; Rodgers, J. A.; Sokolov, D. A.; Huxley, A. D.; Attfield, J. P. *Chem. Commun.* **2008**, 3634.
(24) Ren, Z. A.; Lu, W.; Yang, J.; Yi, W.; Shen, X. L.; Li, Z. C.; Che, G. C.; Dong, X. L.; Sun, L. L.; Zhou, F.; Zhao, Z. X. *Chin. Phys. Lett.* **2008**, *25*, 2215.
(25) Ren, Z. A.; Yang, J.; Lu, W.; Yi, W.; Che, G. C.; Dong, X. L.; Sun, L. L.; Zhao, Z. X. *Mater. Res. Innovations* **2008**, *12*, 105.
(26) Aczel, A. A.; Baggio-Saitovitch, E.; Budko, S. L.; Canfield, P. C.; Carlo, J. P.; Chen, G. F.; Dai, P.; Goko, T.; Hu, W. Z.; Luke, G. M.; Luo, J. L.; Ni, N.; Sanchez-Candela, D. R.; Tafti, F. F.; Wang, N. L.; Williams, T. J.; Yu, W.; Uemura, Y. J. *Phys. Rev. B* **2008**, *78*, 214503.
(27) Carlo, J. P.; Uemura, Y. J.; Goko, T.; MacDougall, G. J.; Rodriguez, J. A.; Yu, W.; Luke, G. M.; Pengcheng Dai; Shannon, N.; Miyasaka, S.; Suzuki, S.; Tajima, S.; Chen, G. F.; Hu, W. Z.; Luo, J. L.; Wang, N. L. *Phys. Rev. Lett.* **2009**, *102*, 087001.
(28) McGuire, M. A.; Hermann, R. P.; Sefat, A. S.; Sales, B. C.; Jin, R.; Mandrus, D.; Grandjean, F.; Long, G. J. *New J. Phys.* **2009**, *11*, 025011.
(29) Chen, Y.; Lynn, J. W.; Li, J.; Li, G.; Chen, G. F.; Luo, J. L.; Wang, N. L.; Dai, P. C.; dela Cruz, C.; Mook, H. A. *Phys. Rev. B* **2008**, *78*, 064515.
(30) Jeglic, P.; Bos, J.-W. G.; Zorko, A.; Brunelli, M.; Koch, K.; Rosner, H.; Margadonna, S.; Arcon, D. *Phys. Rev. B* **2009**, *79*, 094515.
(31) Fratini, M.; Caivano, R.; Puri, A.; Ricci, A.; Ren, Z. A.; Dong, X. L.; Yang, J.; Lu, W.; Zhao, Z. X.; Barba, L.; Arrighetti, G.; Polentarutti, M.; Bianconi, A. *Supercond. Sci. Technol.* **2008**, *21*, 092002.
(32) Qiu, Y.; Bao, W.; Huang, Q.; Yildirim, T.; Simmons, J. M.; Green, M. A.; Lynn, J. W.; Gasparovic, Y. C.; Li, J.; Wu, T.; Wu, G.; Chen, X. H. *Phys. Rev. Lett.* **2008**, *101*, 257002.
(33) Chen, G. F.; Li, Z.; Wu, D.; Dong, J.; Li, G.; Hu, W. Z.; Zheng, P.; Luo, J. L.; Wang, N. L. *Chin. Phys. Lett.* **2008**, *25*, 2235–2238.
(34) Ren, Z. A.; Yang, J.; Lu, W.; Yi, W.; Shen, X. L.; Li, Z. C.; Che, G. C.; Dong, X. L.; Sun, L. L.; Zhou, F.; Zhao, Z. X. *Europhys. Lett.* **2008**, *82*, 57002.
(35) Jaroszynski, J.; Hunte, F.; Balicas, L.; Jo, Y. J.; Raicevic, I.; Gurevich, A.; Larbalestier, D. C.; Balakirev, F. F.; Fang, L.; Cheng, P.; Jia, Y.; Wen, H. H. *Phys. Rev. B* **2008**, *78*, 174523.
(36) Le Tacon, M.; Krisch, M.; Bosak, A.; Bos, J. W. G.; Margadonna, S. *Phys. Rev. B* **2008**, *78*, 140505.

(by refinement of the Nd/Ca occupancies). Variable-temperature high-resolution neutron powder diffraction data were collected on the high-resolution super-D2B powder diffractometer at the Insitut Laue Langevin in Grenoble, France. Data sets were recorded at 1.6 K and 175 K for $x = 0$ and $x = 0.05$. The instrument was used without additional collimation and with a large diameter beam to maximize the number of neutrons on the sample. The neutron wavelength used was $\lambda = 1.594$ Å. Data were recorded at $5 \leq 2\theta \leq 160°$ with a stepsize of 0.05°. High-flux neutron powder diffraction experiments were performed on the D20 instrument at the ILL.[37] The instrument was set up in the highest flux mode with $\lambda = 2.42$ Å. Data sets were collected over 4 h each at 1.6, 30, and 175 K in the $5 \leq 2\theta \leq 150°$ interval using a position sensitive detector. The GSAS suite of programs and the EXPGUI graphical user interface were used for Rietveld fitting of the synchrotron X-ray and neutron powder diffraction data.[38,39] The temperature dependences of the zero field cooled magnetic susceptibilities were measured in a field of 1 Tesla using a Quantum Design Magnetic Property Measurement System. The electrical resistance and magnetoresistance were measured in a standard four-point geometry using the resistance option of a Quantum Design Physical Property Measurement System. The dimensions of the bars were approximately $2 \times 1 \times 5$ mm^3.

Results

Crystal Structure. The synchrotron diffraction data were used to follow the x-dependence of the room temperature crystal structure. Rietveld fits for the $x = 0.025$ and $x = 0.05$ samples are shown in Figure S1 in the Supporting Information, whereas the fit for the $x = 0$ pattern is reported in ref 15. Increasing the Ca^{2+} content leads to an expansion of the *ab* plane, whereas the *c*-axis initially contracts and then increases slightly for $x = 0.05$ (Table 1). This results in an initial drop in cell volume followed by a modest increase (Table 1) and is consistent with the behavior observed in the $Nd_{1-x}Sr_xFeAsO$ series.[15] In contrast to these changes, the modification of the FeAs tetrahedral layers upon doping is systematic (Figure 1): First, the Fe−As distance decreases linearly upon increasing x, as is expected for hole doping (partial oxidation of Fe^{2+} to Fe^{3+}). Secondly, the Fe−As−Fe angle increases linearly, leading to a compression of the FeAs layer. The net effect of the shortened FeAs bond and increase in Fe−As−Fe angle is a linear decrease in the FeAs layer thickness (Fig. 1). The changes to the (Nd/Ca)−O and (Nd/Ca)−As bond lengths and angles are not linear but follow an increase−decrease (or decrease−increase) pattern, and are given in Table 1.

High-resolution neutron powder diffraction was used to follow the temperature dependence of the $x = 0$ and $x = 0.05$ samples. The data sets collected at 175 K could be indexed using the tetragonal *P*4/*nmm* cell. Upon further cooling to 1.6 K, a tetragonal to orthorhombic structural transition occurs and both samples have low-temperature diffraction patterns consistent with the previously reported *Cmma* model for NdFeAsO.[31] A Rietveld fit for the $x = 0.05$ sample is given in Figure S2 in the Supporting Information. The refined lattice constants, atomic parameters, and selected bond length and angles are given

Table 1. Room Temperature Lattice Constants, Atomic Parameters, Selected Bond Lengths (Å) and Angles (deg), and Fit Statistics for the $Nd_{1-x}Ca_xFeAsO$ Series

		$x = 0$	$x = 0.025$	$x = 0.05$
a-axis (Å)		3.96594(1)	3.96773(1)	3.96805(1)
c-axis (Å)		8.59786(5)	8.58658(5)	8.58668(5)
V (Å^3)		135.233(1)	135.177(1)	135.201(1)
Nd	z	0.13888(6)	0.13935(6)	0.13894(7)
	occ	1.00	0.969(4)	0.950(5)
	U_{iso}	0.0068(2)	0.0057(2)	0.0045(2)
Ca	z		0.13935(6)	0.13894(7)
	frac		0.031(4)	0.050(5)
	U_{iso}		0.0057(2)	0.0045(2)
Fe	U_{iso}	0.0062(2)	0.0059(4)	0.0046(4)
As	z	0.6575(1)	0.6572(1)	0.6568(1)
	U_{iso}	0.0062(3)	0.0074(3)	0.0057(3)
O	U_{iso}	0.003(1)	0.016(2)	0.018(2)
Fe−As		2.4010(5)	2.3996(6)	2.3979(7)
As−Fe−As		111.36(4)	111.53(4)	111.66(5)
		108.54(2)	108.45(2)	108.39(2)
Nd−As		3.3061(5)	3.3045(6)	3.3087(7)
As−Nd−As		116.04(3)	116.18(3)	115.99(4)
Nd−O		2.3147(3)	2.3168(3)	2.3151(3)
O−Nd−O		117.89(2)	117.81(2)	117.96(2)
χ^2		2.0	2.1	2.1
wR_p (%)		15.2	18.1	18.1
R_p (%)		11.7	11.8	12.7
R_F^2 (%)		7.61	5.6	5.1

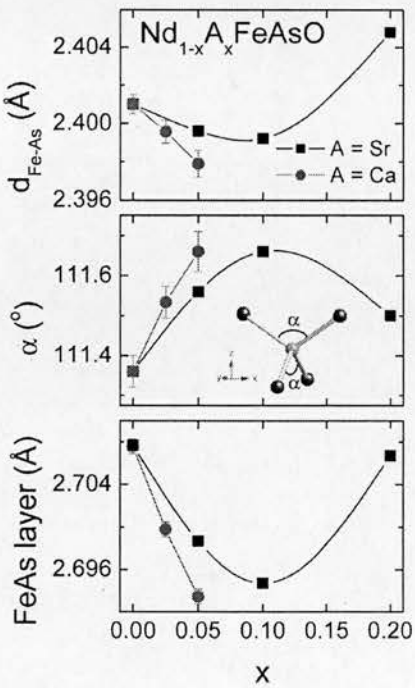

Figure 1. Doping dependence of the Fe−As bond distance, As−Fe−As tetrahedral angle, and FeAs layer thickness of the $Nd_{1-x}A_xFeAsO$ (A = Ca, Sr) series. The data for the Sr series are reproduced from our earlier work.[15]

(37) Hansen, T. C.; Henry, P. F.; Fischer, H. E.; Torregrossa, J.; Convert, P. *Meas. Sci. Technol.* **2008**, *19*, 034001.
(38) Larson, A. C.; Von Dreele, R. B. General Structure Analysis System (GSAS) ; Report LAUR 86-748; Los Alamos National Laboratory: Los Alamos, NM, 2000
(39) Toby, B. H. *J. Appl. Crystallogr.* **2001**, *34*, 210.

in Table 2. The structural transition leads to a rectangular distortion of the iron square planar sublattice (Table 2), which facilitates the long-range SDW ordering of the Fe moments.

Magnetic Susceptibilities. The inverse magnetic susceptibilities of the $Nd_{1-x}Ca_xFeAsO$ samples are shown in Figure 2 and are dominated by the (linear) paramagnetic contribution of the Nd^{3+} moments. This makes it difficult to asses the much smaller contribution of the iron moments to the magnetic susceptibility. A Curie−Weiss (CW) fit of the paramagnetic region was used to obtain an indication of the Nd^{3+} magnetism. The fitted Curie constants are given in the inset to Figure 2 as are the expected values for paramagnetic Nd^{3+} ($^4I_{9/2}$). The experimental values reveal a linear decrease in agreement with the partial replacement of magnetic Nd^{3+} with diamagnetic Ca^{2+}. However, the magnitude of the Curie constants is much larger than expected for $x = 0$ and $x = 0.025$, which may signal a significant contribution of the iron spins to the magnetic susceptibility, although the iron moments are not expected to show CW behavior. The experimental and calculated values are in good agreement for the most highly doped sample ($x = 0.05$). The Weiss temperatures are negative, indicative of antiferromagnetic interactions between Nd^{3+} spins, and are approximately −30 K for all x. We note that the CW model does not describe the magnetism in this system accurately and the results of the fits should therefore be treated with some caution.

Resistance. The temperature dependence of the resistance is shown in Figure 3. The $x = 0$ composition shows the typical drop below $T_{max} \approx 160$ K that is associated with the onset of the T→O structural transition, which is caused by the SDW transition that occurs around 140 K. The latter temperature corresponds to the maximum in dR/dT, which occurs at ~140 K for our sample. The polycrystalline nature of our samples prevent us from making quantitative statements but it is evident that upon Ca^{2+} substitution, the temperature dependence of the resistance changes from metallic to semiconducting for $x = 0.025$ and remains semiconducting for $x = 0.05$. The drop in resistance observed for $x = 0$ is almost completely suppressed in the $x = 0.025$ materials but re-appears in the $x = 0.05$ composition. In fact, for $x = 0.025$, $dR/dT < 0$ over the entire measured temperature range, indicating semiconducting behavior, whereas the maximum slope occurs at ~125 K. For $x = 0.05$, $T_{max} = 145$ K, whereas $(dR/dT)_{max} \approx 130$ K. These observations are consistent with a scenario where NdFeAsO is hole doped by substitution of Ca^{2+} leading to a depletion of free (*n*-type) charge carriers and thereby to semiconducting behaviour. This is qualitatively the same as the behaviour observed for the $Nd_{1-x}Sr_xFeAsO$ series with the distinction that Sr doping affords $x_{max} = 0.2$. At these higher doping levels, metallic conduction reappears, leading to superconductivity with $T_c = 15$ K.[15]

Magnetoresistance. The magnetoresistance of the $Nd_{1-x}Ca_xFeAsO$ samples was obtained from the measurement of R(H) curves between $-9\ T \le \mu_0 H \le 9$ T. The as-measured curves were found to be slightly asymmetric for the $x = 0$ and $x = 0.05$ samples (inset to Figure 4), and in

Table 2. Lattice Constants, Atomic Parameters and Selected Bond Lengths (Å) and Angles (deg) for $Nd_{1-x}Ca_xFeAsO$ from Variable-Temperature D2B Neutron Powder Diffraction Data

		0		0.05	
		175	1.6	175	1.6
space group		*P4/nmm*	*Cmma*	*P4/nmm*	*Cmma*
a-axis (Å)		3.96133(4)	5.6154(1)	3.96351(5)	5.6157(1)
b-axis (Å)			5.5856(1)		5.5908(1)
c-axis (Å)		8.5772(2)	8.5591(2)	8.5662(2)	8.5479(2)
V (Å^3)		134.597(3)	268.461(7)	134.570(5)	268.372(6)
Nd/Ca	z	0.1389(2)	0.1390(2)	0.1388(2)	0.1389(2)
	U_{iso}	0.0036(7)	0.0004(6)	0.0023(6)	0.0005(6)
Fe	U_{iso}	0.0076(6)	0.0062(6)	0.0079(5)	0.0061(6)
As	z	0.6582(3)	0.6587(3)	0.6574(3)	0.6578(3)
	U_{iso}	0.0078(7)	0.0059(7)	0.0072(7)	0.0043(8)
O	U_{iso}	0.0061(8)	0.0049(8)	0.0050(7)	0.0049(6)
χ^2		2.4	2.4	2.9	2.8
wR_p (%)		5.2	5.2	5.9	5.7
R_p (%)		4.1	4.1	4.6	4.5
R_F^2 (%)		4.1	4.3	4.2	4.6
Fe−As		2.401(2)	2.401(2)	2.397(2)	2.397(2)
As−Fe−As		111.2(1)	111.1(1)	111.5(1)	111.5(1)
		108.64(5)	108.45(5)	108.45(5)	108.28(5)
			108.89(5)		108.65(5)
Nd−O		2.311(1)	2.310(1)	2.311(1)	2.310(1)
Nd−As		3.298(1)	3.299(1)	3.302(1)	3.302(1)
			3.286(1)		3.292(1)
Fe−Fe		2.80108(3)	2.80771(6)	2.80263(3)	2.80785(5)
			2.79280(6)		2.79538(5)

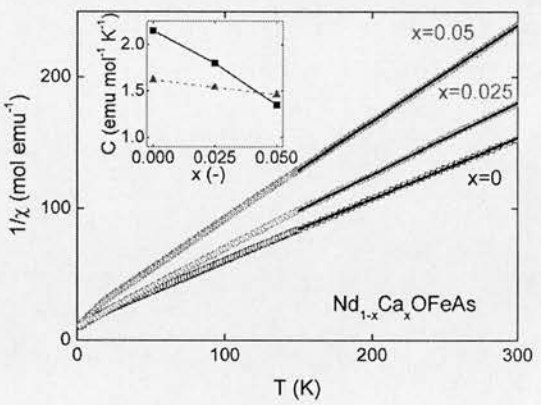

Figure 2. Inverse magnetic susceptibilities for the $Nd_{1-x}Ca_xFeAsO$ series. The inset shows a comparison between the experimental Curie constants (C) and the expected ones for Nd^{3+} ($^4I_{9/2}$).

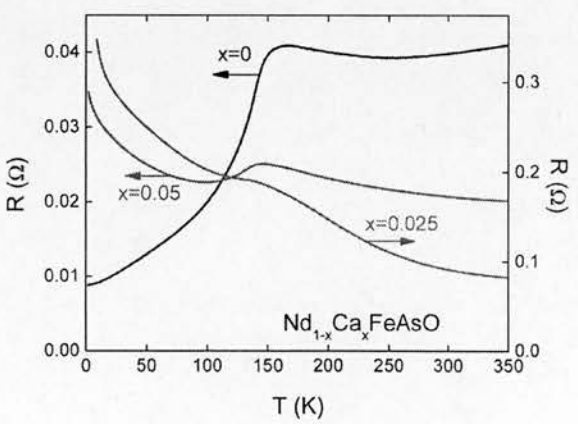

Figure 3. Temperature dependence of the electrical resistance for the $Nd_{1-x}Ca_xFeAsO$ series.

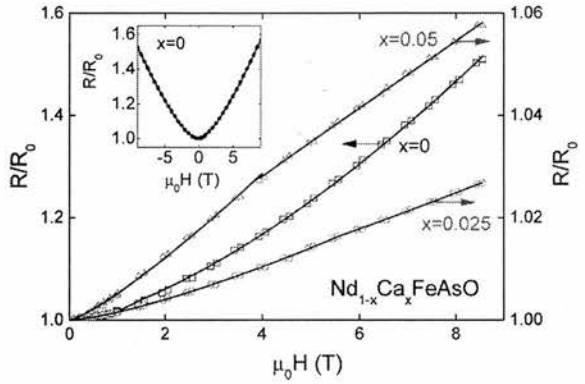

Figure 4. Magnetic field dependence of the magnetoresistance [$R/R_0 = R(H)/R(H=0)$] for the $Nd_{1-x}Ca_xFeAsO$ series at 5 K. The solid lines are power law fits to the data (see text). The inset shows the raw data collected for $x = 0$.

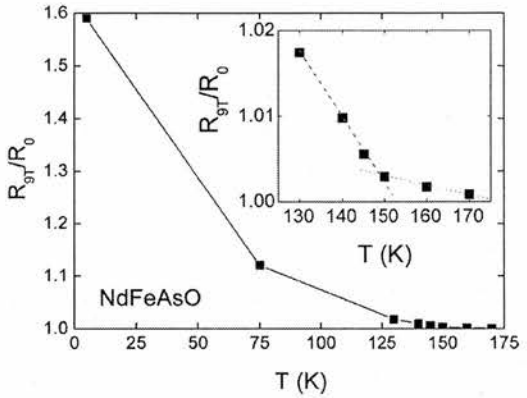

Figure 5. Temperature dependence of the magnetoresistance in 9 Tesla for NdFeAsO.

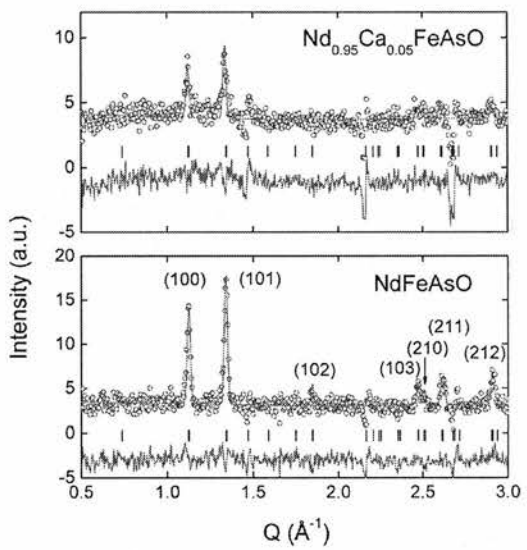

Figure 6. Rietveld fits to 2−30 K difference (magnetic contribution only) neutron diffraction patterns for $Nd_{1-x}Ca_xFeAsO$ ($x = 0$ and $x = 0.05$). The as-collected patterns are shown in Figure S3 of the Supporting Information.

the following, only the symmetric part of the MR response is given (Figure 4). The asymmetry arises from a Hall resistance due to the slight misalignment of the contact electrodes. The shape of the field dependence of the MR for the $x = 0$ sample is typical for a metallic conductor with an H^2 field dependence below $H = 1$ T. In larger applied fields, R/R_0 follows a power law with an exponent $n = 1.48$ (1). The solid lines in Figure 4 are fits. Upon Ca substitution, both the magnitude and shape of the MR change dramatically. The MR at 9 Tesla is 1.6 for $x = 0$, reduces to 1.03 for $x = 0.025$, and then increases to 1.06 for $x = 0.05$. At low fields, the MR is no longer quadratic and no longer typical of a metal. Furthermore a crossover in field dependence is visible at ~5.5 T for $x = 0.025$ and at ~4 T for $x = 0.05$ (Figure 4). For $x = 0.025$, power law fits yield $n = 1.38$ (1) for $0 \le \mu_0 H \le 5.5$ T and $n = 1.17(1)$ for $5.5 < \mu_0 H \le 8.5$ T. For $x = 0.05$, the values are n = 1.22(1) for $0 \le \mu_0 H \le 4$ T and $n = 0.96(1)$ for $4 < \mu_0 H \le 8.5$ T. These measurements reveal that the field dependence of R/R_0 becomes more linear for larger x and in larger applied magnetic fields. The temperature dependence of the 9 T MR for the $x = 0$ parent material is given in Figure 5. This reveals that the MR is largest at low temperatures and falls of with increasing temperature. In the vicinity of the SDW (~140 K) and structural transition (~160 K), two linear regions can be discerned. Small magnetoresistances are already observable upon the onset of the structural transition, whereas the MR increases more rapidly when the three-dimensional SDW ordering occurs. These observations show that the positive MR is related to the SDW ordering and provides further evidence that the structural transition and SDW are coupled. Our results are in excellent agreement with a recent single crystal study where $R/R_0 \approx 1.1$ at 75 K and 9 Tesla, revealing that the observed MR is intrinsic and not related to the polycrystalline nature of the samples.[40]

Magnetic Structure. Samples with $x = 0$ and $x = 0.05$ were studied using high-flux neutron powder diffraction. Identical counting times were used to collect data sets at 1.6, 30, and 175 K (see Figure S3 in the Supporting Information). These were carefully subtracted to separate the magnetic scattering from the structural contributions. The resulting 2−30 K difference patterns are shown in Figure 6. For $x = 0$, two strong and five weaker magnetic reflections were observed. These could all be indexed using the Cmma crystallographic cell. The intensities were fitted adequately using the combined Nd and Fe ordering model proposed by Qiu et al.[32] The refined moments are for Nd $m_x = 1.37(7)\,\mu_B$, $m_z = 1.31(8)\,\mu_B$, $m = 1.90(3)\,\mu_B$ and for Fe $m_x = 1.10(9)\,\mu_B$. Subtraction of the 175 K and 30 K patterns showed no magnetic reflections within the experimental accuracy (0.2−0.3 μ_B). For $x = 0.05$, the 2−30 K difference pattern (Figure 6) shows an identical magnetic diffraction pattern to that observed for $x = 0$. The reduction in intensities is consistent with a slightly lower ordering temperature of the Nd-sublattice resulting from the dilution of the magnetic Nd^{3+} lattice by non-magnetic Ca^{2+}. The refined moment are $m_x = 0.27(7)\,\mu_B$, $m_z = 0.42(5)\,\mu_B$, and $m = 0.50(2)\,\mu_B$ for Nd and $m_x = 0.27(5)\,\mu_B$ for Fe.

(40) Cheng, P.; Yang, H.; Jia, Y.; Fang, L.; Zhu, X. Y.; Mu, G.; Wen, H. H. *Phys. Rev. B* **2008**, *78*(13), 134508.

The 30−175 K difference pattern again showed no evidence for magnetic reflections within the experiment accuracy.

Discussion

The structures and properties of the $Nd_{1-x}Ca_xFeAsO$ series have been investigated. Synchrotron powder X-ray diffraction reveals that the $Nd_{1-x}Ca_xFeAsO$ series forms for $0 \leq x \leq 0.05$. This is substantially lower than $x_{max} = 0.20$ observed for the analogous Sr-series.[15] Both substitutions result in a formal $Fe^{(2+x)+}$ oxidation state but the sizes of the dopant cations are different. The ionic radius of Ca^{2+} is 1.12 Å, whereas that of Sr^{2+} is significantly larger at 1.26 Å. The radius for Nd^{3+} is tabulated as identical to that for Ca^{2+} (values for 8-fold coordination in oxides).[41] The structural response of the iron arsenide layer of the $Nd_{1-x}Sr_xFeAsO$ series has been included in Figure 1 to facilitate a comparison. It is evident that the magnitude of the changes in bond length, angle and layer thickness are comparable in the two series in spite of the different x_{max}. For the smaller Ca^{2+} cation a linear contraction in FeAs layer thickness is observed up to the maximum doping level $x = 0.05$, above which the structure is no longer stable. The larger Sr^{2+} cation reverses this trend, and for $x > 0.1$ the FeAs layer expands again. This expansion signals significant changes to the bonding that lead to the appearance of a superconducting state with $T_c = 15$ K for $x = 0.2$. At the moment, we cannot offer a good explanation for the difference in x_{max} between the two series.

The decrease in the FeAs layer thickness for $Nd_{1-x}Ca_xFeAsO$ is consistent with hole doping of the anti-bonding iron bands at the Fermi level. This results in a depletion of *n*-type charge carriers as evidenced by the transition from metallic to semiconducting behaviour (Fig. 3). The SDW transition remains intact and its transition temperature is reduced moderately. From $(dR/dT)_{max}$, T_{SDW} decreases from 140 K ($x = 0$) to 125 K ($x = 0.025$) and then increases to 130 K ($x = 0.05$). The presence of the SDW is confirmed by low-temperature neutron powder diffraction (Figure 6). Our results suggest a significant enhancement of the ordered Fe moment below $T_{N,Nd}$, which is surprising because of the weak coupling between the two sublattices as evidenced by the large difference between $T_{N,Nd}$ and T_{SDW}. In general, the small iron moments in the 1111 materials are not well understood, as electronic structure calculations consistently suggest that iron should have a moment of 1−2 μ_B.[22] Mazin and Johannes have suggested[42] that iron in fact has a large moment but that this appears strongly reduced because of fluctuations caused by antiphase boundaries and stacking faults along the *z*-direction. In this scenario, ordering of the Nd sublattice provides enhanced three-dimensional coherency and leads to observation of a larger Fe moment in neutron powder diffraction, consistent with our experimental results.

Magnetoresistance measurements (Fig. 5) reveal that the MR in the parent material first appears at the onset of the SDW transition (~160 K) and increases more rapidly when long range SDW ordering is fully established (below ~140 K). Ca substitution changes both the magnitude and field dependence of the MR. The MR is strongly reduced for the semiconducting samples suggesting that the concentration of free charge carriers is important. In conjunction, the field dependence of the MR changes from typical metallic to a near linear field dependence, with a transition evident near 5 Tesla for $x = 0.025$ and near 3.5 Tesla for $x = 0.05$. These measurements reveal that the MR is related to the SDW and the number of free charge carriers. The microscopic reason for the large positive MR is not well understood, which is not surprising given the debate of the nature of the SDW.[22,42] Generally, the magnitude of the MR is found to be larger in the 1111 RFeAsO parent materials than in the 122 $AeFe_2As_2$ group. The R/R_0 ratio in $BaFe_2As_2$ is ~1.1 at 5 K and 6.5 T compared to ~1.35 in NdFeAsO for the same conditions. This suggests that there might be a correlation with the ordered iron moment found from neutron powder diffraction, which is typically lower for the RFeAsO samples [0.25(7) μ_B for NdFeAsO compared to 0.87(3) μ_B for $BaFe_2As_2$],[43] or using the arguments above, that materials with stronger fluctuations (lower ordered Fe moment) have larger positive MR. It is worth pointing out that the MR shows an anomaly at the R-sublattice ordering temperature for R = Ce, Pr, and Nd, despite the absence of significant bonding between RO and FeAs layers.[28]

In conclusion: the substitution of Ca^{2+} in $Nd_{1-x}Ca_xFeAsO$ is possible for $0 \leq x \leq 0.05$ and results in a linear compression of the FeAs layer, which is consistent with a depletion of charge carriers from the anti-bonding electronic states at the Fermi level. This results in changes in the trends in resistance with temperature consistent with a transition from metallic to semiconducting behaviour as *x* increases, and is accompanied by a sharp reduction in the magnitude of the magnetoresistance, and a change to more linear field dependences with high-field transitions evident for the doped samples. The SDW transition temperatures are 140 K ($x = 0$), 125 K ($x = 0.025$) and 130 K ($x = 0.05$). Simultaneous Fe and Nd spin order is observed at 1.6 K, whereas no SDW ordering of the Fe spins could be detected at 30 K, revealing that ordering of the rare-earth sublattice strongly enhances the ordered iron moment.

Acknowledgment. J.W.G.B. acknowledges the Royal Society of Edinburgh for financial support and the EPSRC for provision of beam time at the ILL and ESRF. Andrew Huxley is acknowledged for scientific discussions.

Supporting Information Available: Rietveld fits to the room temperature synchrotron diffraction and 1.6 K neutron powder diffraction data. As-collected high-flux neutron powder diffraction patterns (PDF). This information is available free of charge via the Internet at http://pubs.acs.org.

(41) Shannon, R. D. *Acta Crystallogr., Sect. A* **1976**, *32*, 751.
(42) Mazin, II; Johannes, M. D. *Nat. Phys.* **2009**, *5*, 141.
(43) Huang, Q.; Qiu, Y.; Bao, W.; Green, M. A.; Lynn, J. W.; Gasparovic, Y. C.; Wu, T.; Wu, G.; Chen, X. H. *Phys. Rev. Lett.* **2008**, *101*, 257003.

Suppression of the superconducting transition of $R\mathrm{FeAsO}_{1-x}\mathrm{F}_x$ (R=Tb, Dy, and Ho)

Jennifer A. Rodgers,[1,2] George B. S. Penny,[1,2] Andrea Marcinkova,[1,2] Jan-Willem G. Bos,[1,2] Dmitry A. Sokolov,[1,3] Anna Kusmartseva,[1,2] Andrew D. Huxley,[1,3] and J. Paul Attfield[1,2,*]

[1]*Centre for Science at Extreme Conditions, University of Edinburgh, King's Buildings, Mayfield Road, Edinburgh EH9 3JZ, United Kingdom*

[2]*School of Chemistry, University of Edinburgh, Edinburgh EH9 3JJ, United Kingdom*

[3]*SUPA, School of Physics, University of Edinburgh, Edinburgh EH9 3JZ, United Kingdom*

(Received 31 July 2009; published 28 August 2009)

A suppression of superconductivity in the late rare-earth $R\mathrm{FeAsO}_{1-x}\mathrm{F}_x$ materials is reported. The maximum critical temperature (T_c) decreases from 51 K for R=Tb to 36 K for $\mathrm{HoFeAsO}_{0.9}\mathrm{F}_{0.1}$, which has been synthesized under 10 GPa pressure. This suppression is driven by a decrease in the Fe-As-Fe angle below an optimum value of 110.6°, as the angle decreases linearly with unit-cell volume (V) across the $R\mathrm{FeAsO}_{1-x}\mathrm{F}_x$ series. A crossover in electronic structure around this optimum geometry is evidenced by a change in sign of the compositional dT_c/dV, from negative values for previously reported large R materials to positive for $\mathrm{HoFeAsO}_{0.9}\mathrm{F}_{0.1}$.

DOI: 10.1103/PhysRevB.80.052508 PACS number(s): 74.62.Dh, 74.62.Bf, 74.70.Dd

Rare earth (R) oxypnictides RFeAsO (Ref. 1) were recently discovered to superconduct when doped, with critical temperatures surpassed only by the high-T_c cuprates. Several families of superconducting iron pnictides have subsequently been discovered.[2] These all have layered structures containing AsFeAs slabs with Fe tetrahedrally coordinated by As. The main types are the 1111 materials based on RFeAsO or MFeAsF (M=Ca,Sr,Ba), the 122 phases $M\mathrm{Fe}_2\mathrm{As}_2$, and the 111 AFeAs (A=Li,Na) family. The related binaries FeX (X=Se,Te) are also superconducting.

The electron-doped 1111 materials $R\mathrm{FeAsO}_{1-x}\mathrm{F}_x$ and $R\mathrm{FeAsO}_{1-\delta}$ materials remain prominent as they have the highest T_c's, up to 56 K, and allow lattice and doping effects to be investigated through variations in the R^{3+} cation size and the anion composition. A strong lattice effect is evident at the start of the rare-earth series, as T_c rises from 26 K for $\mathrm{LaFeAsO}_{1-x}\mathrm{F}_x$ to 43 K under pressure,[3,4] and to a near-constant maximum 50–56 K in the $R\mathrm{FeAsO}_{1-x}\mathrm{F}_x$ and $R\mathrm{FeAsO}_{1-\delta}$ series for R=Pr to Gd,[5–10] but whether lattice effects ultimately enhance or suppress superconductivity for the late R's has been unclear. The late rare-earth $R\mathrm{FeAsO}_{1-x}\mathrm{F}_x$ materials and the oxygen-deficient $R\mathrm{FeAsO}_{1-\delta}$ superconductors require high-pressure synthesis, leading to significant challenges as single phase samples are difficult to prepare, and accurate analyses of cation stoichiometries and O and F contents are difficult. To investigate the effect of the lattice for later R, we have synthesized multiple samples of $R\mathrm{FeAsO}_{0.9}\mathrm{F}_{0.1}$ (R=Tb, Dy, and Ho) under varying high-pressure conditions. Here we report superconductivity in $\mathrm{HoFeAsO}_{0.9}\mathrm{F}_{0.1}$ for which the maximum T_c of 36 K is markedly lower than in the previous R analogs. This is part of a systematic suppression of superconductivity by the smaller, late R cations. $\mathrm{HoFeAsO}_{0.9}\mathrm{F}_{0.1}$ also shows a reversal in the sign of the compositional dT_c/dV (V=unit-cell volume) compared to the early R materials, confirming that the decreasing R size has a significant effect on the bands contributing to the Fermi surface.

Polycrystalline ceramic $R\mathrm{FeAsO}_{1-x}\mathrm{F}_x$ samples (R=Tb, Dy, and Ho) were synthesized by a high-pressure method and investigated by powder x-ray diffraction, magnetization, and conductivity measurements.[11] Initial results for $R\mathrm{FeAsO}_{1-x}\mathrm{F}_x$ (R=Tb and Dy) were published elsewhere.[12] Both materials were found to be superconducting with maximum T_c's of 46 and 45 K, respectively. Little difference in superconducting properties between samples with nominal compositions of x=0.1 and 0.2 were observed, and the x=0.2 materials were generally of lower phase purity, and so the x=0.1 composition was used in subsequent syntheses. The best samples typically contain ~80% by mass of the superconducting phase with residual nonsuperconducting $R_2\mathrm{O}_3$ and RAs phases also present. The sample purity and superconducting properties are not sensitive to synthesis pressure over a range that moves to higher pressures as R decreases in size; R=Tb and Dy superconductors were respectively prepared at 7–10 and 8–12 GPa, heating at 1050–1100 °C. Repeated syntheses of $\mathrm{TbFeAsO}_{1-x}\mathrm{F}_x$ gave several samples with higher T_c's than the above value, the highest value is T_c(max)=51 K (Fig. 1). Further $\mathrm{DyFeAsO}_{1-x}\mathrm{F}_x$ samples did not show higher transitions than before, so we conclude that T_c(max) in this system is 45 K.

Tetragonal $\mathrm{HoFeAsO}_{0.9}\mathrm{F}_{0.1}$ was obtained from reactions at 10 GPa pressure and the properties of six $\mathrm{HoFeAsO}_{0.9}\mathrm{F}_{0.1}$ samples prepared under varying conditions are summarized

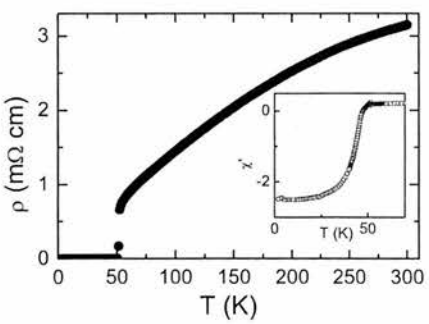

FIG. 1. Resistivity and (inset) susceptibility data for an optimum sample of $\mathrm{TbFeAsO}_{0.9}\mathrm{F}_{0.1}$, showing a sharp superconducting transition at T_c=51 K. The sample was prepared at 7 GPa and 1050 °C.

TABLE I. Synthesis conditions (all samples were synthesized at 10 GPa), refined lattice parameters and volume, T_c's, mass fractions, and superconducting volume fractions for $HoFeAsO_{1-x}F_x$ samples.

Sample	t_{synth} (hr)	T_{synth} (°C)	a (Å)	c (Å)	Vol (Å^3)	T_c (K)	Mass frac. (%)	Diamag. frac. (%)
1	2	1150	3.8246(3)	8.254(1)	120.74(3)	29.3	75	70
2	2	1100	3.8272(2)	8.2649(8)	121.06(2)	33.0	74	85
3	1	1150	3.8258(5)	8.264(2)	120.96(4)	33.2	73	76
4	3	1100	3.8282(5)	8.261(2)	121.07(5)	33.7	84	74
5	2	1100	3.8282(2)	8.2654(7)	121.13(2)	35.2	81	57
6	2	1100	3.8297(7)	8.270(2)	121.30(7)	36.2	58	46

in Table I. Crystal structure refinements and phase analysis were carried out by fitting powder x-ray diffraction data (Fig. 2).[13] Magnetization measurements demonstrate that all six $HoFeAsO_{1-x}F_x$ samples are bulk superconductors with T_c's of 29–36 K (Fig. 3). Resistivities show smooth high-temperature evolutions without apparent spin-density wave anomalies. The transitions to the zero resistance state have widths of less than 4 K.

Although all of the samples in Table I have the same starting composition, small variations in synthesis pressure and temperature result in a dispersion in x around the nominal 0.1 value for the $HoFeAsO_{1-x}F_x$ phase and corresponding variations in superconducting properties. T_c increases to a maximum value, T_c(max), at the upper solubility limit of x in $RFeAsO_{1-x}F_x$ systems,[7] and this is consistent with the observation that the superconducting phases in samples 1, 3, and 4, which are heated at high temperatures or for longer times and so are likely to have a slightly lower F content, have lower T_c's (average 32.1 K) than the other three samples, made under nominally identical "optimum" conditions, which have average T_c=34.8 K. Sample 6 shows the highest T_c=36.2 K and the lowest proportion of the $HoFeAsO_{1-x}F_x$ phase and a correspondingly low diamagnetic volume fraction. This demonstrates that the sample is at the upper limit of the superconducting composition range and so gives a realistic T_c(max) for the $HoFeAsO_{1-x}F_x$ system.

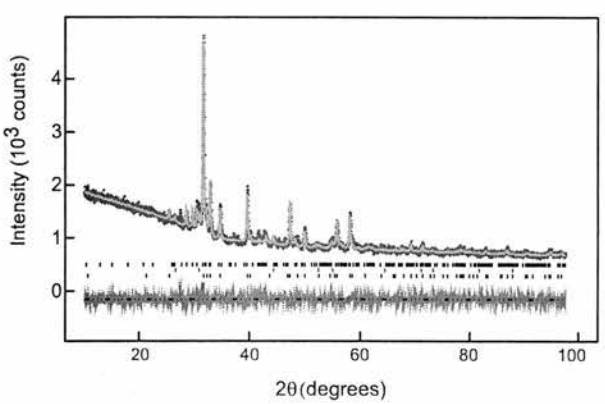

FIG. 2. Fitted x-ray diffraction profile for $HoFeAsO_{0.9}F_{0.1}$ (sample 5) at room temperature. The Bragg markers (from top to bottom) are for the minority phases, Ho_2O_3 and HoAs, and for $HoFeAsO_{0.9}F_{0.1}$.

Although the doping values x for the high-pressure $RFeAsO_{1-x}F_x$ samples are not known precisely, comparing ensembles of samples with similar phase purities made under similar conditions reveals a clear suppression of superconductivity by lattice effects for heavier R. For example, all of our $TbFeAsO_{1-x}F_x$ superconductors have higher T_c's (five $TbFeAsO_{1-x}F_x$ samples, T_c=45–51 K) than all of the $HoFeAsO_{1-x}F_x$ materials (in Table I). The T_c(max) values of 51, 45, and 36 K for $RFeAsO_{1-x}F_x$ with R=Tb, Dy, and Ho, respectively, thus represent the trend correctly.

Figure 4 shows a plot of the maximum critical temperatures, T_c(max), against unit-cell volume for many reported $RFeAsO_{1-x}F_x$ and $RFeAsO_{1-\delta}$ systems and our above materials. T_c(max) rises slowly as cell volume decreases for R =La to Pr and then shows a broad maximum, between R =Pr and Tb in the $RFeAsO_{1-x}F_x$ materials, before falling rapidly as R changes from Tb to Dy to Ho. This trend is not seen in the reported $RFeAsO_{1-x}$ superconductors, where T_c(max) remains approximately constant,[14,15] apparently because they have larger cell volumes than their $RFeAsO_{1-x}F_x$ analogs (see Fig. 4).

The size of the R^{3+} cation tunes the electronic properties through variations in the geometry of the FeAs slab. A trend between the As-Fe-As (or equivalent Fe-As-Fe) angle and T_c has been reported for the early R materials.[16] The upper panel of Fig. 4 shows representative reported values for optimal $RFeAsO_{1-x}F_x$ superconductors including our R=Tb, Dy, and Ho materials. This demonstrates that the angle decreases monotonically with R size and so does not show a universal correlation with T_c(max). The T_c(max) variation in the $RFeAsO_{1-x}F_x$ series is described by a simple $\cos(\phi - \phi_0)$ function, shown in Fig. 4, where the value of the As-

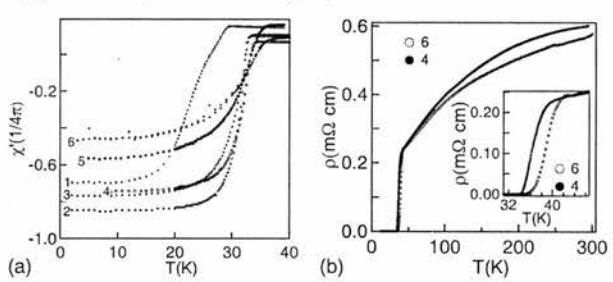

FIG. 3. Superconductivity measurements for $HoFeAs_{0.9}F_{0.1}$; (a) ac magnetic volume susceptibility for the six samples; (b) resistivities for samples 4 and 6.

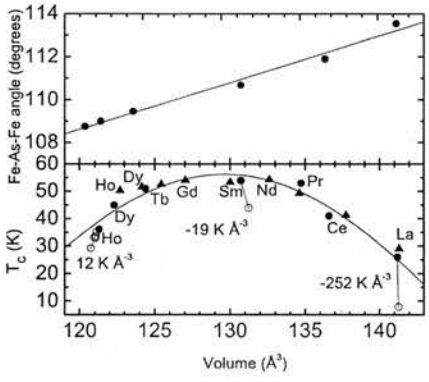

FIG. 4. Variation in Fe-As-Fe angle ϕ (upper panel) and superconducting T_c (lower panel) with unit-cell volume for different $R\mathrm{FeAsO}_{1-x}\mathrm{F}_x$ (circles) (Refs. 19, 22, 5, 7, and 12) and $R\mathrm{FeAsO}_{1-\delta}$ (triangles) (Refs. 14 and 15). $T_c(\mathrm{max})$ points are shown as filled symbols. The fit of equation $T_c(\mathrm{max})=T_c(\mathrm{max})_0\cos A(\phi-\phi_0)$ with parameters $T_c(\mathrm{max})_0=56$ K, $A=0.03$, and $\phi_0=110.6°$ is also shown. dT_c/dV values are derived from the data for suboptimally doped materials (open symbols) in the R=La (Ref. 19), Sm (Ref. 7), and Ho (this Brief Report) systems.

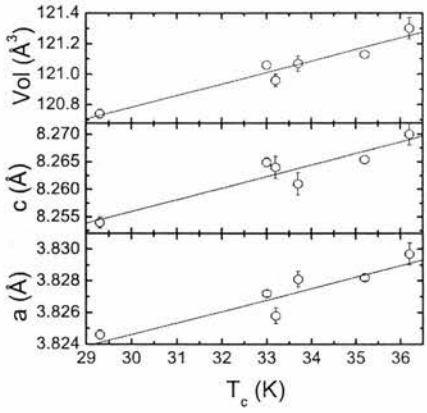

FIG. 5. Variations in T_c with the tetragonal unit-cell parameters and volume for the six $\mathrm{HoFeAsO}_{1-x}\mathrm{F}_x$ samples in Table I.

Fe-As angle corresponding to the global maximum T_c, $\phi_{\max}=110.6°$, is close to the ideal 109.5° value for a regular FeAs_4 tetrahedron. All five of the Fe $3d$ bands are partially occupied and contribute to the Fermi surface of the iron arsenide superconductors through hybridization with As $4s$ and $4p$ states.[17] Decreasing the tetrahedral angle through 109.5° marks the crossover from tetragonal compression to elongation of the FeAs_4 tetrahedra. In a crystal-field model, this reverses the splittings of the t_2 and e d-orbital sets and so a significant crossover in the real electronic structure is likely to occur near 109.5°.

Evidence for the above crossover also comes from a discovered change in the sign of the compositional dT_c/dV near optimum doping in the $R\mathrm{FeAsO}_{1-x}\mathrm{F}_x$ systems.[18] The unit-cell parameters and volume for the six $\mathrm{HoFeAsO}_{1-x}\mathrm{F}_x$ samples in Table I show a positive correlation with T_c (Fig. 5), in contrast to early R=La (Ref. 19) and Sm (Ref. 7) analogs, where lattice parameters and volume decease with increasing T_c. The T_c, V points for near-optimally doped R=La, Sm, and Ho $R\mathrm{FeAsO}_{1-x}\mathrm{F}_x$ superconductors are shown in Fig. 4 together with the derived dT_c/dV values. dT_c/dV for a single $R\mathrm{FeAsO}_{1-x}\mathrm{F}_x$ system follows the overall trend in $dT_c(\mathrm{max})/dV$ for different R's, changing from a negative value at large R=La to a small positive slope at R=Ho.

The compositional dT_c/dV for a given $R\mathrm{FeAsO}_{1-x}\mathrm{F}_x$ system reflects two competing effects of variations in the fluoride content x on the lattice volume. F^- is slightly smaller than O^{2-} so the anion substitution effect gives a negative contribution to the compositional dT_c/dV, independent of R. The concomitant effect of doping electrons into the Fe d bands tends to expand the lattice (and increase T_c), but the magnitude of this positive dT_c/dV term depends on the nature of the bands at the Fermi surface. The observed shift from negative to positive dT_c/dV as R changes from La to Ho shows that the decreasing size of the R^{3+} cation leads to significant changes in the Fermi surface, with volume-expanding (antibonding) bands more prominent for smaller R. Calculations have confirmed that the electronic structure near the Fermi level is sensitive to such small changes in the As z coordinate (equivalent to changing the Fe-As-Fe angle).[20] Small changes in the contributions of the d bands are likely to be particularly important in a multigap scenario for superconductivity, as evidenced in gap measurements of $\mathrm{TbFeAsO}_{0.9}\mathrm{F}_{0.1}$ and other iron arsenide materials.[21]

In summary, our analysis of multiple samples of $R\mathrm{FeAsO}_{1-x}\mathrm{F}_x$ (R=Tb, Dy, and Ho) superconductors demonstrates that the maximum critical temperature falls from 51 K for R=Tb to 36 K for the previously unreported Ho analog. Hence, the effect on the lattice of substituting smaller late rare earths in the $R\mathrm{FeAsO}_{1-x}\mathrm{F}_x$ lattice suppresses superconductivity. This lattice control appears to be through tuning of the interatomic angles in the FeAs layer, with the optimum angle being 110.6°, near the ideal tetrahedral value. The compositional dT_c/dV changes sign around the optimum angle evidencing significant changes in the Fermi surface. It appears difficult to increase the critical temperatures above 56 K in 1111 type iron arsenide materials through tuning lattice effects, although the possibility of higher T_c's in other structure types remains open.

We acknowledge EPSRC, the Royal Society of Edinburgh and the Leverhulme trust for support.

*Corresponding author; j.p.attfield@ed.ac.uk

[1] P. Quebe, L. J. Terbuchte, and W. Jeitschko, J. Alloys Compd. **302**, 70 (2000).

[2] J. W. Lynn and P. Dai, Physica C **469**, 469 (2009).

[3] Y. Kamihara, T. Watanabe, M. Hirano, and H. Hosono, J. Am. Chem. Soc. **130**, 3296 (2008).

[4] H. Takahashi, K. Igawa, K. Arii, Y. Kamihara, M. Hirano, and H. Hosono, Nature (London) **453**, 376 (2008).

[5] Z. A. Ren, J. Yang, W. Lu, W. Yi, G. C. Che, X. L. Dong, L. L. Sun, and Z. X. Zhao, Mater. Res. Innovations **12**, 105 (2008).

[6] Z. A. Ren, J. Yang, W. Lu, W. Yi, X. L. Shen, Z. C. Li, G. C. Che, X. L. Dong, L. L. Sun, F. Zhou, and Z. X. Zhao, EPL **82**, 57002 (2008).

[7] X. H. Chen, T. Wu, G. Wu, R. H. Liu, H. Chen, and D. F. Fang, Nature (London) **453**, 761 (2008).

[8] Z. A. Ren, W. Lu, J. Yang, W. Yi, X. L. Shen, Z. C. Li, G. C. Che, X. L. Dong, L. L. Sun, F. Zhou, and Z. X. Zhao, Chin. Phys. Lett. **25**, 2215 (2008).

[9] R. H. Liu, G. Wu, T. Wu, D. F. Fang, H. Chen, S. Y. Li, K. Liu, Y. L. Xie, X. F. Wang, R. L. Yang, L. Ding, C. He, D. L. Feng, and X. H. Chen, Phys. Rev. Lett. **101**, 087001 (2008).

[10] P. Cheng, L. Fang, H. X. Yang, X. Zhu, G. Mu, H. Luo, Z. Wang, and H. Wen, Sci. China, Ser. G **51**, 719 (2008).

[11] Samples were synthesized from stoichiometric amounts of *R*As, Fe_2O_3, FeF_2, and Fe, using a Walker multianvil module within a 1000 ton press. The products were dense, black, sintered polycrystalline pellets. Powder x-ray diffraction data were collected on a Bruker AXS D8 diffractometer using Cu $K\alpha_1$ radiation. Data were recorded at $10 \leq 2\theta \leq 100°$ with a step size of 0.007° for Rietveld analysis. ac magnetic susceptibility was measured from 3 to 50 K with a field of 0.5 Oe oscillating at 117 Hz using a Quantum Design SQUID magnetometer. Electrical resistivity was measured by a four-probe method between 1.7 and 300 K using a Quantum Design physical property measurement system and an APD cryogenics closed cycle refrigeration unit with an in-house built sample stage.

[12] J.-W. G. Bos, G. B. S. Penny, J. A. Rodgers, D. A. Sokolov, A. D. Huxley, and J. P. Attfield, Chem. Commun. **31**, 3634 (2008).

[13] $HoFeAsO_{0.9}F_{0.1}$ has a tetragonal structure (space group $P4/nmm$; results from fit shown in Fig. 2; goodness of fit $\chi^2 = 1.60$, residuals; $R_{wp}=3.94\%$, $R_p=3.02\%$; cell parameters $a = 3.8282(2)$ Å, $c=8.2654(7)$ Å; atom positions $[x,y,z]$ and isotropic temperature (U) factors; Ho $[\frac{1}{4},\frac{1}{4},0.1454(4)]$, 0.044(2) Å^2; As $[\frac{1}{4},\frac{1}{4},0.6659(5)]$, 0.029(2) Å^2; Fe $(\frac{3}{4},\frac{1}{4},\frac{1}{2})$, 0.014(2) Å^2; O,F $(\frac{3}{4},\frac{1}{4},0)$, 0.26(2) Å^2). The secondary Ho_2O_3 phase is in a high-pressure *B*-type rare-earth oxide modification, space group $C2/m$, $a=13.841(2)$ Å, $b=3.4984(5)$ Å, $c = 8.608(1)$ Å, $\beta=100.08(1)°$.

[14] K. Miyazawa, K. Kihou, P. M. Shirage, C. H. Lee, H. Kito, H. Eisaki, and A. Iyo, J. Phys. Soc. Jpn. **78**, 034712 (2009).

[15] J. Yang, X. L. Shen, W. Lu, W. Yi, Z. C. Li, Z. A. Ren, G. C. Che, X. L. Dong, L. L. Sun, F. Zhou, and Z. X. Zhao, New J. Phys. **11**, 025005 (2009).

[16] J. Zhao, Q. Huang, C. de la Cruz, S. Li, J. W. Lynn, Y. Chen, M. A. Green, G. F. Chen, G. Li, Z. Li, J. L. Luo, N. L. Wang, and P. Dai, Nature Mater. **7**, 953 (2008).

[17] D. J. Singh and M.-H. Du, Phys. Rev. Lett. **100**, 237003 (2008).

[18] The compositional dT_c/dV quantifies the changes in T_c and unit-cell volume V due to variations in doping level x at constant (atmospheric) pressure, and is complementary to the pressure-induced dT_c/dV at constant x. Both derivatives are negative for $LaFeAsO_{1-x}F_x$, and we thus predict a positive pressure-induced dT_c/dV (pressure suppression of superconductivity) for $HoFeAsO_{1-x}F_x$.

[19] Q. Huang, J. Zhao, J. W. Lynn, G. F. Chen, J. L. Luo, N. L. Wang, and P. Dai, Phys. Rev. B **78**, 054529 (2008).

[20] S. Lebègue, Z. P. Yin, and W. E. Pickett, New J. Phys. **11**, 025004 (2009).

[21] K. A. Yates, K. Morrison, J. A. Rodgers, G. B. S. Penny, J. W. G. Bos, J. P. Attfield, and L. F. Cohen, New J. Phys. **11**, 025015 (2009).

[22] G. F. Chen, Z. Li, D. Wu, G. Li, W. Z. Hu, J. Dong, P. Zheng, J. L. Luo, and N. L. Wang, Phys. Rev. Lett. **100**, 247002 (2008).

Superconductivity in $NdFe_{1-x}Co_xAsO$ ($0.05<x<0.20$) and rare-earth magnetic ordering in NdCoAsO

Andrea Marcinkova,[1] David A. M. Grist,[1] Irene Margiolaki,[2] Thomas C. Hansen,[3] Serena Margadonna,[1] and Jan-Willem G. Bos[1,4]

[1]*School of Chemistry and Centre for Science at Extreme Conditions, University of Edinburgh, Edinburgh EH9 3JJ, United Kingdom*

[2]*European Synchrotron Radiation Facility, 39043 Grenoble, France*

[3]*Institute Laue Langevin, 38042 Grenoble, France*

[4]*Department of Chemistry–EPS, Heriot-Watt University, Edinburgh EH14 4AS, United Kingdom*

(Received 11 September 2009; revised manuscript received 22 December 2009; published 19 February 2010)

The phase diagram of $NdFe_{1-x}Co_xAsO$ for low cobalt substitution consists of a superconducting dome ($0.05<x<0.20$) with a maximum critical temperature of 16.5(2) K for $x=0.12$. The $x=1$ end member, NdCoAsO, is an itinerant ferromagnet ($T_C=85$ K) with an ordered moment of 0.30(1) μ_B at 15 K. Below $T_N=9$ K, Nd spin ordering results in the antiferromagnetic coupling of the existing ferromagnetic planes. Rietveld analysis reveals that the electronically important twofold tetrahedral angle increases from 111.4° to 115.7° in this series. Underdoped samples with $x=0.046(2)$ and $x=0.065(2)$ show distortions to the orthorhombic *Cmma* structure at 72(2) and 64(2) K, respectively. The temperature dependences of the critical fields $H_{c2}(T)$ near T_c are linear with almost identical slopes of 2.3(1) T K^{-1} for $x=0.065(2)$, $x=0.118(2)$, and $x=0.172(2)$. The estimated critical field $H_{c2}(0)$ and correlation length for optimally doped samples are 26(1) T and 36(1) Å. A comparison of the maximum reported critical temperatures of well-characterized cobalt-doped 122- and 1111-type superconductors is presented.

DOI: 10.1103/PhysRevB.81.064511 PACS number(s): 74.70.−b, 74.25.Dw

I. INTRODUCTION

The 2008 discovery[1] of high-T_c superconductivity based on iron arsenide layers has generated enormous interest (Refs. 2 and 3 and references therein). Presently, the most widely investigated systems are the 1111-type *R*FeAsO (*R* =La, rare-earth) and 122-type $AEFe_2As_2$ (*AE*=alkaline earth) superconductors. Both contain square planar Fe layers, with Fe tetrahedrally coordinated by As, which are kept apart by either *R*O layers or *AE* ions. The 1111-type superconductors were the first to be discovered and hold the current record for critical temperatures and fields (up to 55 K and of the order of 100 T), while single crystals of the 122's (T_c up to 38 K) are readily available making detailed physical property studies possible. Like the cuprates, the iron arsenides have an antiferromagnetic (AF) parent. In contrast to the cuprates, the parent materials are metallic and not Mott insulators. The magnetism is therefore not due to superexchange but to Fermi surface nesting in the two-dimensional band structure, which results in a spin-density wave (SDW) state.[4,5] The parent materials are rendered superconducting (SC) via chemical doping[2,3] or in some cases application of hydrostatic pressure.[6] Both electron- and hole-doped superconductors exist.[2,3] Most temperature-composition phase diagrams show a dome-shaped SC region and suggest the coexistence of magnetic order and superconductivity for underdoped samples.[7–11] An exception is the phase diagram of $LaFeAsO_{1-x}F_x$ where a discontinuous transition into the superconducting state is reported.[12] In the cuprate high-T_c superconductors, chemical substitutions on the copper site are detrimental to superconductivity. By contrast in the iron arsenides, direct substitution on the Fe site with a variety of transition metals is known to induce superconductivity. This was first reported for 1111-type $LaFe_{1-x}Co_xAsO$ with a maximum critical temperature of 13–14 K.[13] Other well-characterized cobalt-doped superconductors include 122-type $AE(Fe_{1-x}Co_x)_2As_2$ (*AE*=Ba, Sr, and Ca),[14–16] 1111-type $SmFe_{1-x}Co_xAsO$,[17] and 1111-type $CaFe_{1-x}Co_xAsF$.[18] The highest reported T_c for cobalt doping is 22 K and is found for $Ba(Fe_{1-x}Co_x)_2As_2$ and $CaFe_{1-x}Co_xAsF$. The twofold tetrahedral As-Fe-As angle (α) is an important electronic parameter with higher T_c's found as α tends to the ideal cubic value (109.5°).[8,19] Most forms of chemical doping result in a reduction in α and values closer to 109.5°. For example, indirect electron doping of NdFeAsO ($\alpha=111.4°$) via F substitution or O deficiency reduces α by ~0.4° and ~1° for optimally doped samples.[19,20] This is also true for hole-doped 122 systems such as $Ba_{1-x}K_xFe_2As_2$ where $\alpha=109.5°$ for samples with $T_c=38$ K ($x=0.4$) compared to $\alpha=111.2°$ for the parent material.[21] In contrast, our results show that α increases with cobalt substitution (~1° for $x=0.12$), which is expected to have an unfavorable effect and reduce T_c from what is possible for a given nominal doping level (x). This effect is common to all cobalt-doped superconductors but does not seem to have been explicitly pointed out in the literature.

The fully substituted $x=1$ samples are also of considerable interest. LaCoAsO is an itinerant ferromagnet[13,22] with an anomalous magnetization similar to MnSi and $Fe_xCo_{1-x}Si$.[23] $BaCo_2As_2$ is not ferromagnetic (FM) but is in close proximity to a FM quantum critical point.[24] The presence of Nd in the current $x=1$ composition offers the prospect of studying the interplay between rare-earth and transition-metal magnetism. In the case of the *R*FeAsO parent materials this has generated much interest and a variety of combined *R* and Fe magnetic structures have been reported.[25,26] In all cases, T_N of the *R* sublattice is much lower than T_{SDW} (~140 K) for the Fe magnetic order, and the weak *R*-Fe interaction is not considered crucial in explaining the higher T_c's observed for magnetic *R* ions.[20,25]

In this paper, the temperature-composition phase diagram for $NdFe_{1-x}Co_xAsO$ ($0 \leq x \leq 1$) is reported from a combination of synchrotron x-ray, neutron powder-diffraction, magnetic susceptibility, and electrical resistivity measurements. These measurements reveal a SC dome extending from $0.05 < x < 0.20$ with maximum $T_c = 16.5(2)$ K and $H_{c2}(0) = 26(1)$ T for $x = 0.12$. NdCoAsO is an itinerant ferromagnet ($T_C = 85$ K) that shows a transition to long-range AF order ($T_N = 9$ K) upon ordering of the rare-earth spins. This work follows on from our earlier investigations into the effects of electron (via F substitution)[20,27] and hole doping (via Ca and Sr substitution)[28,29] of the parent material NdFeAsO.

II. EXPERIMENTAL

Polycrystalline samples of the $NdFe_{1-x}Co_xAsO$ ($x_{nominal} = 0$, 0.05, 0.075, 0.10, 0.125, 0.15, 0.175, 0.20, 0.25, 0.50, and 1) were prepared using standard solid-state chemistry methods. Stoichiometric mixtures of NdAs, Fe_2O_3, Fe, Co_3O_4, and Co powders of at least 99.9% purity were mixed using mortar and pestle and pressed into pellets. The pellets were vacuum sealed into quartz tubes and heated for 48 h at 1150 °C for $0 \leq x_{nominal} \leq 0.25$ and at 1050 °C for $x_{nominal} = 0.5$ and $x_{nominal} = 1$. The reactions were initially done on a 0.5 g scale. Larger 2 g samples of $x_{nominal} = 0.075$, 0.125, 0.175, and 1 were prepared for neutron powder diffraction. The starting material NdAs was prepared by heating stoichiometric mixtures of Nd and As pieces at 850 °C for 2 × 12 h with an intermediate shaking of the sealed tube. Initial phase analysis was done using laboratory powder x-ray diffraction on a Bruker D8 AXS diffractometer with a Cu $K_{\alpha 1}$ radiation source. Zero field cooled (ZFC) and field cooled (FC) dc magnetic susceptibilities were measured using a Quantum Design Magnetic Property Measurement System (MPMS). The applied magnetic field (H) for the superconductivity tests was 20 Oe. The temperature dependence of the susceptibility of the $x_{nominal} = 1$ sample was measured in $H = 10$ kOe. The temperature and field dependences of the electrical resistivity were measured using the resistance option of a Quantum Design Physical Property Measurement System (PPMS). The resistivities were measured using the four point contact method on bars of approximately 1 × 1 × 5 mm^3. Sintered samples tend to degrade into powder when not kept in a closed container. This does not affect the crystallinity or the diamagnetic response but prevented us from obtaining resistivity measurements for some of the reported samples. High-resolution synchrotron powder-diffraction measurements were done on the ID31 beamline at the European Synchrotron Radiation Facility in Grenoble. The x-ray wavelength used was 0.3994 Å and data were binned with a 0.02° step size between $0 \leq 2\theta \leq 35°$. The samples were contained in 0.5 mm diameter silica capillaries. Room-temperature patterns were collected for all prepared samples while selected samples ($x_{nominal} = 0.05, 0.075, 0.125, 1$) were studied as a function of temperature using shorter scans. Room-temperature neutron powder-diffraction patterns for $x_{nominal} = 0.075$, 0.125, 0.175, and 1 were collected on the D20 beamline[30] at the Institute Laue Langevin in Grenoble. The instrument was used in the high-flux setting with and $\lambda = 1.304$ Å (42° take-off angle, Cu monochromator). The samples were contained in 6 mm diameter vanadium cans and cooled in a standard orange cryostat. Variable temperature data were collected between 1.7 and 100 K for NdCoAsO at wavelength $\lambda = 2.419$ Å (42° take-off angle, pyrolytic graphite monochromator). Data were collected between $10 \leq 2\theta \leq 140°$ and binned with a 0.1° step size. Rietveld analysis of the collected powder-diffraction data was done using the GSAS suite of programs.[31] A pseudo-Voigt function using Stephens anisotropic peak broadening was used to describe the peak shape for the synchrotron x-ray diffraction data.[32]

III. STRUCTURE AND PROPERTIES OF NdCoAsO ($x = 1$)

The temperature dependence of the crystal structure of NdCoAsO was followed between room temperature (RT) and 5 K using synchrotron x-ray powder diffraction. No structural transitions were observed and the structure was described using the $P4/nmm$ structural model reported by Quebe *et al.*[33] The RT lattice constants, atomic parameters, selected bond lengths, and fit statistics are summarized in Table I. The refined lattice constants and fractional coordinates at 5 K are as follows: $a = 3.97940(1)$ Å, $c = 8.29849(3)$ Å, $z_{Nd} = 0.14264(4)$, and $z_{As} = 0.65071(7)$ [$\chi^2 = 4.1$, $wR_p = 9.5\%$, $R_p = 6.2\%$, and $R_F^2 = 2.4\%$]. The Co-As bond distance contracts moderately from 2.3546(3) Å at RT to 2.3501(3) Å at 5 K, while the tetrahedral angle remains almost constant with RT and 5 K values of 115.70(3)° and 115.69(4)°, respectively.

The dc magnetic susceptibility is shown in Fig. 1(a) and reveals a FM divergence of the susceptibility with $T_c = 85$ K followed by a transition to an AF state at $T_N = 9$ K. The Curie temperature was determined from the local maximum in $d\chi/dT$, while the Néel temperature was taken when $d\chi/dT$ changes sign [Fig. 1(a)]. Zero field cooled and field cooled curves collected in 1 T do not show any thermal hysteresis. The high-temperature susceptibility does not follow the Curie-Weiss law. To further investigate the magnetic properties, $M(H)$ isotherms were collected at 1.7, 50, and 100 K. These data are shown in the inset of Fig. 1(b). The main panel shows the derived Arrott plots, M^2 versus H/M, that were used to determine the nature of the magnetic ground state.[34] Extrapolation of the linear high-field behavior for a ferromagnet yields a negative H/M-axis intersect, while the same extrapolation for AF and paramagnetic (PM) states intersect the H/M axis at a positive value. At 1.7 and 100 K, the Arrott plots clearly indicate the absence of ferromagnetism and are consistent with antiferromagnetism and paramagnetism, respectively. At 50 K, the Arrott plot indicates a FM ground state. The isothermal $M(H)$ measurements are therefore consistent with a PM to FM to AF sequence of ordering transitions upon cooling from RT. No magnetic hysteresis is evident from the measurement at 50 K indicating that NdCoAsO is an extremely soft ferromagnet without any sizable remnant magnetization.

The temperature dependence of the electrical resistivity of NdCoAsO is typical of that of a good metal [RRR = 25; Fig. 1(a)]. The magnetic ordering transitions do not result in large

TABLE I. Lattice constants, refined atomic parameters, selected bond distances and angles, and fit statistics for the combined Rietveld fits to synchrotron x-ray and neutron powder-diffraction data for selected $NdFe_{1-x}Co_xAsO$ compositions. Space group $P4/nmm$; Nd on $2c(1/4,1/4,z)$; Fe/Co on $2b(3/4,1/4,1/2)$; As on $2c(1/4,1/4,z)$; O on $2a(1/4,3/4,0)$.

$x_{nominal}$		0.075	0.125	0.175	1.00
a axis (Å)		3.96754(1)	3.96711(3)	3.96759(4)	3.98724(1)
c axis (Å)		8.58069(5)	8.5611(1)	8.5462(1)	8.31835(4)
Volume (Å^3)		135.072(1)	134.734(1)	134.532(1)	132.246(1)
Nd	U_{iso} (Å^2)	0.0041(1)	0.0046(1)	0.0049(1)	0.0060(1)
	z	0.13911(3)	0.13962(4)	0.14004(6)	0.14221(5)
	Occ.	1.00	1.00	1.00	1.00
Fe/Co	U_{iso} (Å^2)	0.0049(1)	0.0050(2)	0.0049(3)	0.0066(2)
	Fe-occ.	0.918(4)	0.886(6)	0.827(8)	0
	Co-occ.	0.076(4)	0.123(6)	0.180(8)	0.996(2)
	Tot-occ.	0.994(5)	1.009(8)	1.007(11)	0.996(2)
As	U_{iso} (Å^2)	0.0057(1)	0.0057(1)	0.0060(2)	0.0059(1)
	z	0.65681(5)	0.65577(8)	0.6549(1)	0.65066(8)
	Occ.	1.011(2)	1.024(3)	1.019(3)	1.003(2)
O	U_{iso} (Å^2)	0.0047(3)	0.0048(4)	0.0029(6)	0.0036(3)
	Occ.	0.978(4)	0.962(6)	0.980(8)	1.000(4)
$x_{Rietveld}$		0.076(4)	0.122(6)	0.178(8)	0.996(2)
d(Fe/Co-As) (Å)		2.3970(3)	2.3902(4)	2.3850(5)	2.3546(3)
∠As-(Fe/Co)-As (deg)		111.70(2)	112.17(3)	112.56(4)	115.70(3)
∠As-(Fe/Co)-As (deg)		108.37(1)	108.14(1)	107.95(2)	106.45(1)
χ^2		3.1	3.2	5.2	3.1
NPD	wR_p	3.6	3.6	3.3	3.0
	R_p	2.5	2.5	2.4	2.3
	R_F^2	2.9	2.5	2.8	3.0
XRD	wR_p	7.9	8.7	12.9	10.1
	R_p	5.4	6.2	8.7	6.8
	R_F^2	2.5	2.7	7.8	3.5
NdAs (wt%)		1.4(1)	6.3(1)	3.4(1)	8.6(1)
CoAs (wt%)					7.3(3)
Nd_2O_3 (wt%)		1.1(1)	3.4(1)	2.3(1)	

anomalies in $R(T)$ but are evident in dR/dT, which shows a maximum at ~85 K and a minimum at ~9 K [Fig. 1(a)]. The slope remains positive throughout revealing that the sample is metallic over the entire temperature range.

The magnetic ordering in NdCoAsO was further investigated using high-flux neutron powder diffraction on a 2 g polycrystalline sample. Patterns were collected for 2 h each at 1.7, 15, 40, 70, and 100 K. At 1.7 K, long-range AF order was confirmed by the presence of magnetic Bragg reflections that were not present in the 5 K synchrotron powder-diffraction pattern. These reflections were all indexed on a tetragonal cell doubled along the crystallographic c direction ($a_m=a_N$, $c_m=2c_N$, where the subscript m denotes magnetic and N the nuclear cell). The indexing of the most prominent magnetic reflections is given in Fig. 1(c). Upon heating to 15 K, the AF reflections disappear in agreement with the magnetic susceptibility data. Careful subtraction of the 100 and 15 K data revealed weak magnetic contributions to the nuclear (001) and (002) Bragg reflections. Similar FM intensities were also evident in the 40 K pattern but at 70 K there is no evidence for magnetic Bragg diffraction. This apparent disagreement with susceptibility data is most likely due to the small ordered FM cobalt moment close to T_C. The possible FM and AF magnetic structures were analyzed using

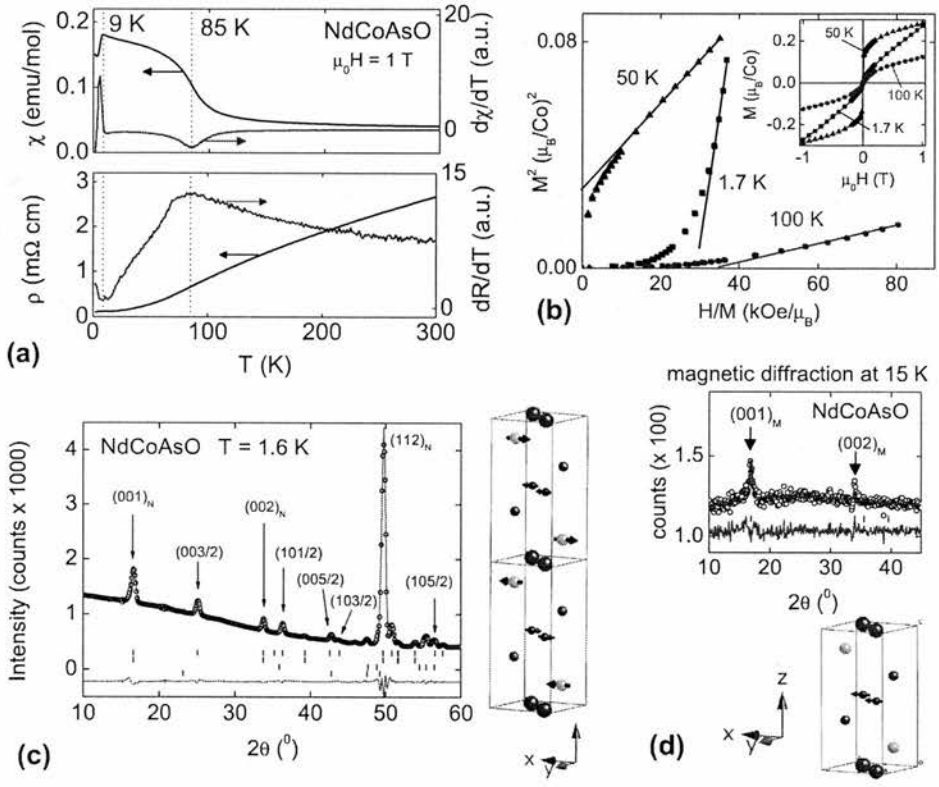

FIG. 1. (Color online) This figure summarizes the measurements on NdCoAsO. Panel (a) shows the temperature dependence of the ZFC magnetic susceptibility (χ) and electrical resistivity (ρ) and their temperature derivatives. Panel (b) shows Arrott plots derived from the isothermal $M(H)$ measurements (shown in the inset). Panel (c) shows the Rietveld fits to the 1.7 K neutron powder-diffraction data (fit statistics: wR_p=3.5%, R_p=2.3%, and R_F^2=8.4%) and a representation of the magnetic structure at that temperature. The tick marks are from top to bottom: magnetic phase, NdCoAsO, CoAs, and NdAs. Panel (d) shows the Rietveld fit to the 15–100 K difference neutron powder-diffraction pattern and a schematic representation of the fitted ferromagnetic magnetic structure.

representational analysis. These calculations were performed using version 2K of the program SARAH representational analysis.[35] In both the FM (**k**=0) and AF [**k**=(0 0 1/2)] states all 16 symmetry elements of the $P4/nmm$ space group leave the magnetic propagation vector (**k**) invariant or transform it into an equivalent vector and thus constitute the small group $G_{\mathbf{k}}$. In the FM state, the decomposition of the magnetic representation Γ_{Mag} in terms of the irreducible representations (IRs) of $G_{\mathbf{k}}$ for the Co site is $1\Gamma_3^1+1\Gamma_6^1+1\Gamma_9^2+1\Gamma_{10}^2$. The representations used are after Kovalev[36] and the character table is given in Table I (supplementary material).[37] The resulting basis vectors for the two independent cobalt atoms are given in Table II. The allowed models correspond to an easy-axis ferromagnet (Γ_3^1), an easy-plane ferromagnet (Γ_9^2), and two checkerboard antiferromagnets with moments along the c direction (Γ_6^1) or in the basal plane (Γ_{10}^2), respectively. The solutions with moments in the basal plane are no longer tetragonal and therefore independent m_x and m_y components are allowed.[38] The absence of a measurable lattice distortion, however, prevents their unique determination. In the AF state the decomposition is $\Gamma_{\mathrm{Mag}}=1\Gamma_2^1+1\Gamma_7^1+1\Gamma_9^2+1\Gamma_{10}^2$ and $\Gamma_{\mathrm{Mag}}=1\Gamma_2^1+1\Gamma_3^1+1\Gamma_9^2+1\Gamma_{10}^2$ for the Co and Nd

TABLE II. Basis vectors $[m_x,m_y,m_z]$ for the space group $P4/nmm$ with **k**=0 and **k**=(0 0 1/2). Co1: (1/4, 3/4, 1/2); Co2: (3/4, 1/4, 1/2); Nd1: (1/4, 1/4, 0.14); Nd2: (3/4, 3/4, 0.86); coordinates in crystallographic cell.

	k=0				**k**=(0 0 1/2)		
	Γ_3^1	Γ_6^1	Γ_9^2	Γ_{10}^2	Γ_2^1	Γ_9^2	Γ_{10}^2
Co1	$[0\ 0\ m_z]$	$[0\ 0\ m_z]$	$[m_x\ m_y\ 0]$	$[m_x\ m_y\ 0]$	$[0\ 0\ m_z]$	$[m_x\ m_y\ 0]$	$[m_x\ m_y\ 0]$
Co2	$[0\ 0\ m_z]$	$[0\ 0\ -m_z]$	$[m_x\ m_y\ 0]$	$[-m_x\ -m_y\ 0]$	$[0\ 0\ m_z]$	$[-m_x\ -m_y\ 0]$	$[m_x\ m_y\ 0]$
Nd1					$[0\ 0\ m_z]$	$[m_x\ m_y\ 0]$	$[m_x\ m_y\ 0]$
Nd2					$[0\ 0\ m_z]$	$[-m_x\ -m_y\ 0]$	$[m_x\ m_y\ 0]$

sites, respectively. In the case of a second-order phase transition, Landau theory states that only a single IR becomes critical. This leaves the Γ_2^1, Γ_9^2, and Γ_{10}^2 symmetries for combined Nd and Co ordering. The unit cell contains two independent Co and two independent Nd sites with basis vectors as given in Table II. The Γ_2^1 and Γ_{10}^2 solutions have FM Co and FM Nd planes (coupled AF) with moments constrained along the c direction and in the basal plane, respectively. The Γ_9^2 solution has AF Co planes and FM Nd planes (coupled AF). The presence of only magnetic (00l) reflections in the FM state reveals that the ordered moment is constrained to the basal plane and that the Γ_9^2 solution is the correct one. Rietveld fitting gives an ordered moment of 0.30(1) μ_B at 15 K and 0.26(1) μ_B at 40 K. A representation of the magnetic structure is shown in Fig. 1(d). Attempts to fit the magnetic intensities to any of the other three models in Table II were not successful. Subtraction of the 15 and 1.7 K data showed that the FM contribution to the (00l) reflections has disappeared at base temperature. Trial Rietveld refinements quickly established that the Γ_2^1 and Γ_9^2 models do not give good fits to the observed magnetic intensities. The Γ_{10}^2 solution in contrast yields an excellent fit to the data. In this model, adjacent FM Nd layers couple AF, and the FM Co layer at $z=1/4$ couples AF with the FM Co layer at $z=3/4$, and adjacent Co and Nd moments are antiparallel. All moments are constrained to the basal plane and Rietveld fitting gives $m_{Co}=0.26(6)$ μ_B and $m_{Nd}=1.39(4)$ μ_B at 1.7 K. The final Rietveld fit and a schematic representation of the magnetic structure are given in Fig. 1(c).

IV. STRUCTURE AND PROPERTIES OF $NdFe_{1-x}Co_xAsO$ $(0<x<1)$

Inspection of the synchrotron x-ray powder-diffraction patterns revealed that all prepared samples have the tetragonal $P4/nmm$ structure at RT. The lattice constants were obtained from Rietveld fits and revealed that the crystallographic c/a ratio varies linearly with x over the entire composition range $(0\leq x\leq 1)$ as shown in Fig. 2. The solid circles are selected samples where the composition has been confirmed from combined Rietveld fits to synchrotron x-ray and neutron powder-diffraction data. The linear dependence suggests that the c/a ratio can be used as an experimental measure of the composition. For most compositions, the agreement between the nominal and calculated (c/a-derived) compositions is within 1–3 esd's (Table III). For some samples (e.g., $x_{nominal}=0.10$) a larger deviation is found, which signals the formation of impurities that change the stoichiometry of the main phase. Use of the calculated compositions results in a smoother x dependence of the refined lattice constants, bond lengths, and bond angles. In addition, it discriminates between samples with the same nominal composition but different SC transition temperatures and vice versa (Table III). For these reasons, the compositions (x) used in this paper are the ones calculated from the c/a ratio unless stated otherwise. The x dependences of the lattice constants are shown in Fig. 2. The a axis is almost constant at low doping levels, in agreement with other cobalt-doped superconductors,[17,39] and increases moderately for $x>0.25$.

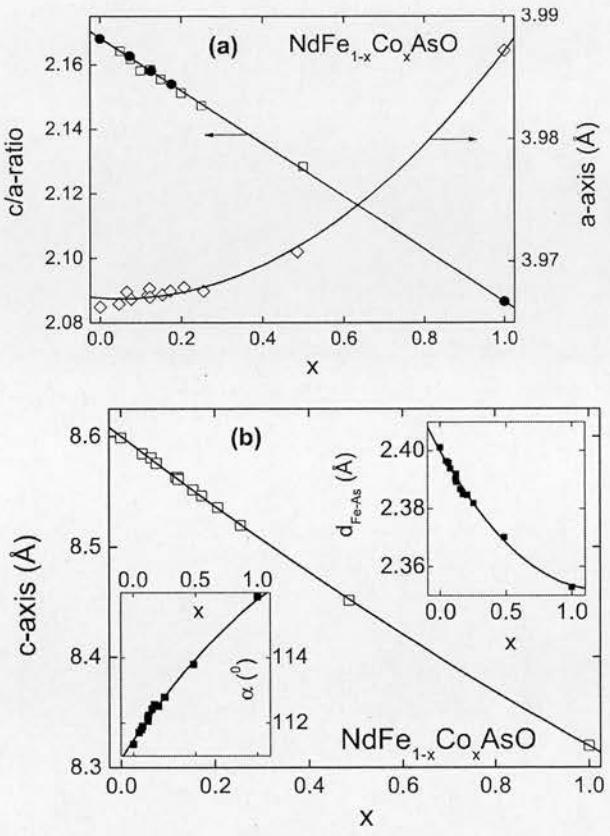

FIG. 2. (a) Left axis: crystallographic c/a ratio versus $x_{nominal}$ for $NdFe_{1-x}Co_xAsO$. The fitted line is $c/a=-0.0814(5)x+2.167\,99(4)$. Right axis: the a axis versus the composition derived from the c/a ratio (x). (b) Crystallographic c axis plotted versus x. The insets show the x dependence of the Fe-As bond distance and the tetrahedral As-Fe-As angle (α, defined in the inset of Fig. 9) for the $NdFe_{1-x}Co_xAsO$ series. The solid lines are guides for the eyes.

In contrast, the c axis contracts rapidly. The (Fe/Co)-As bond lengths show a gradual contraction from 2.40 Å for $x=0$ to 2.35 Å for $x=1$, while the tetrahedral angle increases from 111.4° ($x=0$) to 115.7° [$x=1$; inset of Fig. 2(b)].

In order to independently confirm the composition of selected samples, a combined Rietveld analysis of room-temperature synchrotron x-ray and neutron powder-diffraction data was undertaken. This allows the simultaneous refinement of the total transition-metal site occupancy and the iron to cobalt ratio. The total occupancy is effectively obtained from fitting the x-ray data as there is no significant scattering contrast between Fe and Co, while the difference in neutron scattering length [Fe: 9.45 fm, Co: 2.49 fm] allows for the determination of the Co/Fe ratio. Four compositions were studied: $x_{nominal}=0.075$, 0.125, 0.175, and 1, while the $x=0$ composition has been previously reported.[29] In these refinements, the lattice constants were kept at the synchrotron x-ray values and the neutron wavelength [$\lambda=1.3010(2)$ Å] was refined to fit the neutron-diffraction data. The fit to the $x_{nominal}=0.125$ x-ray and neutron powder-diffraction data is shown in Fig. 3. The other fits are given in Fig. 1 (supplementary material). The results of

TABLE III. Crystallographic c/a ratios, compositions from the c/a ratio (x), compositions from Rietveld fits (x_{Rietveld}), and critical temperatures from the onset of diamagnetism and resistive transition midpoint for the $NdFe_{1-x}Co_xAsO$ series.

x_{nominal}	c/a	x [a]	x_{Rietveld}	T_c, χ_{onset} (K)	T_c, R_{mid} (K)
0	2.16799(4)	0			
0.05	2.16420(4)	0.047(2)		<1.8	<1.8
0.075 (NPD)	2.16272(4)	0.065(2)	0.076(4)	12.8(2)	9.2(2)
0.075	2.16180(4)	0.076(2)		15.0(2)	
0.10	2.15808(4)	0.122(2)		16.7(2)	16.2(2)
0.125	2.15840(4)	0.118(2)		16.5(2)	16.0(2)
0.125 (NPD)	2.15802(4)	0.123(2)	0.122(6)	16.6(2)	
0.15	2.15546(4)	0.154(2)		15.1(2)	
0.175 (NPD)	2.15398(4)	0.172(2)	0.178(8)	13.4(2)	12.6(2)
0.2	2.15121(4)	0.206(2)		<1.8	<1.8
0.25	2.14726(4)	0.255(2)		<1.8	<1.8
0.50	2.12845(4)	0.486(2)			
1	2.08657(4)	1	0.996(2)		

[a] $c/a=-0.0814(5)x+2.167\,99(4)$.

the combined Rietveld fits are summarized in Table I. They reveal that the total occupancy of the transition-metal site is unity in all cases and that the refined Fe and Co fractions are within a single estimated standard deviation of the nominal values. This result is robust as trials with randomly picked Fe and Co fractions always recovered the result shown in Table I. The refinement of the other site occupancies indicates slightly larger than full occupancies on the As site and slightly reduced O-site occupancies (Table I). It is not clear if these are significant but we note that in a simple ionic model with As^{3-} and O^{2-} the charge doping effects cancel out. In addition, oxygen deficient 1111-type samples, such as $NdFeAsO_{1-d}$, have only been prepared using high-pressure high-temperature synthesis routes suggesting that ambient pressure routes do not normally lead to oxygen deficiencies.[40]

Variable temperature synchrotron x-ray diffraction was used to follow the $P4/nmm$ (T) to $Cmma$ (O) transition associated with the AF ordering that occurs in 1111-type parent materials. In case of NdFeAsO ($x=0$), a broad transition with initial broadening of Bragg reflections at ~160 K followed by a full splitting at ~140 K has been reported.[20,41] The latter temperature corresponds to the onset of long-range AF order of the Fe spins.[42] For $NdFe_{1-x}Co_xAsO$ [$x=0.047(2)$, $x=0.065(2)$, and $x=0.123(2)$], data were collected on heating from 4 K. At low temperatures a broadening of reflections with Miller indexes $h\neq 0$ and $k\neq 0$, consistent with the well established $T\rightarrow O$ transition, was evident (Fig. 2; supplementary material). However, no peak splitting occurs down to the lowest measured temperatures. Structural refinements using the orthorhombic $Cmma$ model showed a clear divergence of the a and b axes for $x=0.047(2)$ and $x=0.065(2)$, respectively. In contrast, refinements for $x=0.122(2)$ showed no evidence for a structural distortion as Rietveld fits with the $P4/nmm$ and $Cmma$ structural models gave the same residuals and almost identical a and b axes. The slight broadening evident for $x=0.122(2)$ in Fig. 2 (supplementary material) can therefore not be attributed to the $T\rightarrow O$ transition. The temperature dependence of the lattice constants is shown in Fig. 4, where the orthorhombic cell constants (a_O, b_O) have been divided by $\sqrt{2}$. The lattice constants above the $T\rightarrow O$ transition were obtained from fits to the $P4/nmm$ structural model. The transition temperatures were taken from the onset temperature of orthorhombic strain, $s=(a_O-b_O)/(a_O+b_O)$, and are 72(2) K [$x=0.047(2)$] and 64(2) K [$x=0.065(2)$], respectively (Fig. 4). The low field ZFC susceptibilities for the $NdFe_{1-x}Co_xAsO$ solid solution series are given in Fig. 5. Superconducting transitions are observed for samples with $0.065(2)\leq x\leq 0.172(2)$. The transition temperatures were taken from the diamagnetic onset temperature and are summarized in Table III. This reveals almost identical values of 16.5(2) K for optimally doped samples near $x=0.12$ [$x=0.118(2)$, $x=0.122(2)$, and $x=0.123(2)$]. The diamagnetic shielding fractions vary from 30%–70% of $4\pi\chi$ for samples with $x=0.12$ and are lower on the underdoped and overdoped sides as are the critical temperatures. The SC transitions were confirmed by electrical resistance measurements. The normalized resistances $R/R_{300\text{ K}}$ are given in Fig. 6. The 300 K resistivities fall between 5 mΩ cm for $x=0$ and 2 mΩ cm for $x=1$. The normal state resistance for $x=0$ shows the familiar drop below $T\sim 160$ K with the maximum slope dR/dT at 140 K. These temperatures correspond to the onset of the $T\rightarrow O$ transition and AF order, respectively.[20] Samples with $x>0.2$ have metallic temperature dependences indicating a transition to more conventional metallic behavior on the overdoped side. On the underdoped side, increasing x suppresses the SDW transition and no large anomaly in $R(T)$ is evident for any of the SC samples. At low temperatures SC transitions are evident. The transition temperatures were taken from the 50% of normal state resistance values ($0.5R_N$) and are listed in Table III. The obtained values are in good agreement with the values from the magnetic susceptibility measurements. The widths of the resistive transitions were determined by taking the difference

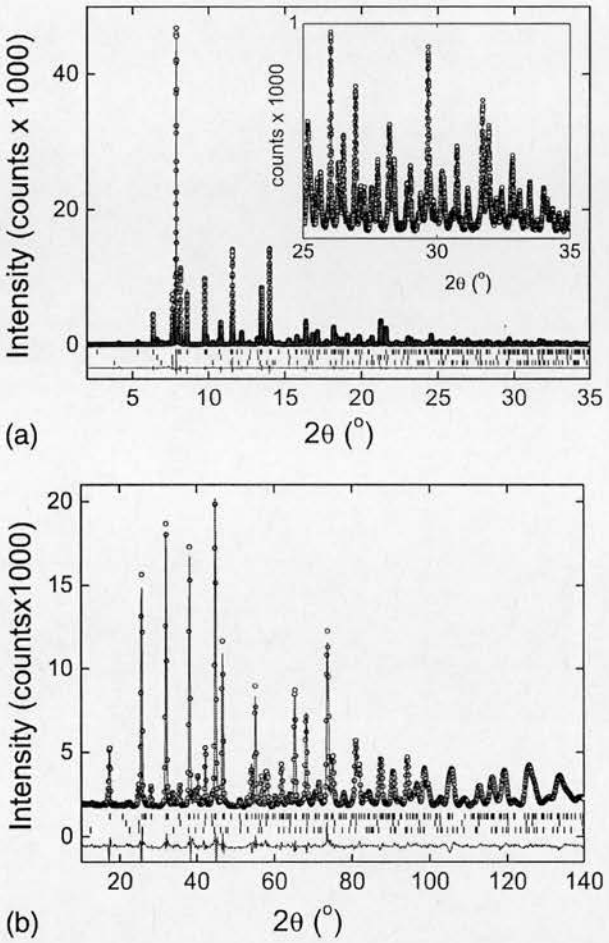

FIG. 3. (Color online) Combined Rietveld fit to room-temperature synchrotron x-ray (a) and neutron powder-diffraction data (b) for a sample with $x_{nominal}=0.125$. Observed data are indicated by open circles, the fit by the (solid) red line, and the difference curve (solid green line) is shown at the bottom. Bragg positions are indicated by vertical markers. The bottom markers correspond to NdAs and Nd_2O_3 impurities (Table I).

between $0.9R_N$ and $0.1R_N$ and are ~2 K wide for the optimally doped samples ($x=0.12$), ~5 K for $x=0.065(2)$, and ~3 K for $x=0.0172(2)$. This is comparable to other polycrystalline 1111-type cobalt-doped superconductors including $LaFe_{1-x}Co_xAsO$ (Refs. 13 and 17) and $SmFe_{1-x}Co_xAsO$ (Ref. 17), and polycrystalline samples of $Ba(Fe_{1-x}Co_x)_2As_2$.[9] The field dependence of $R(T)$ in the vicinity of the SC transition was studied up to 9 T for samples with $x=0.065(2)$, $x=0.118(2)$, and $x=0.172(2)$. The results are shown in the left panels of Fig. 7 and reveal a significant suppression of T_c with applied magnetic field. The upper critical fields were determined at the temperatures of the 10%, 50%, and 90% reduction in the normal state resistance. The results are plotted in the right-hand side panels of Fig. 7. In all samples, an initial rapid reduction in small applied fields $\mu_0 H < 0.5$ T is evident. This is followed by an approximately linear decrease for $\mu_0 H > 1$ T, which shows no sign of saturation. The slopes are dependent on the used resistance criterion signaling a broadening of the transition in applied magnetic fields. This is characteristic for type-II superconductors and was also observed in the $LaFe_{1-x}Co_xAsO$ series.[13] Using the $0.5R_N$ criterion, almost identical slopes of −2.5(1) T K^{-1} [$x=0.065(2)$], −2.3(1) T K^{-1} [$x=0.118(2)$], and −2.3(1) T K^{-1} [$x=0.172(2)$] were obtained from linear fits between $1 \le \mu_0 H \le 9$ T. The linear dependence of $H_{c2}(T)$ near T_c suggests that the Werthamer-Helfand-

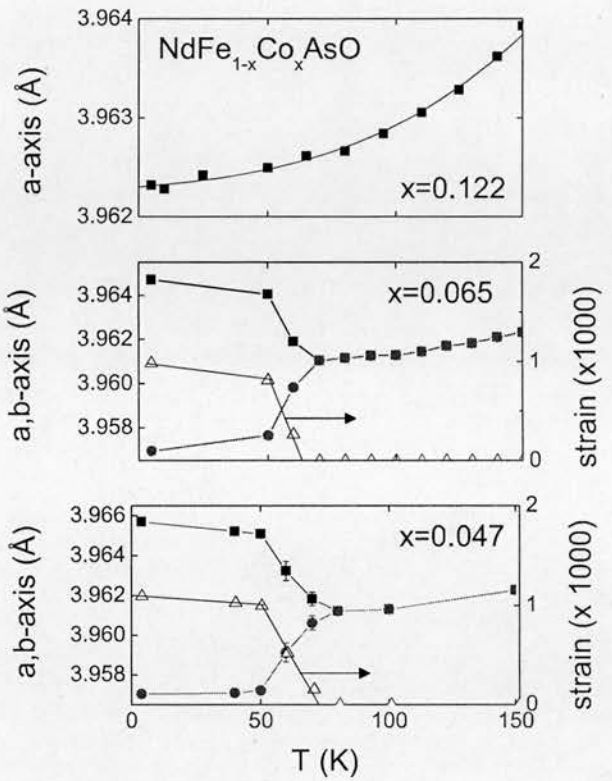

FIG. 4. (Color online) Temperature dependence of the crystallographic basal plane lattice constants and orthorhombic strain for selected low-x $NdFe_{1-x}Co_xAsO$ compositions.

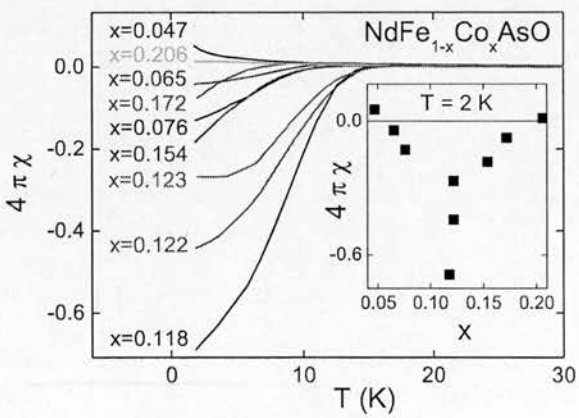

FIG. 5. (Color online) Temperature dependence of the low field magnetic susceptibilities for $NdFe_{1-x}Co_xAsO$. The inset shows x dependence of the diamagnetic fraction at 2 K.

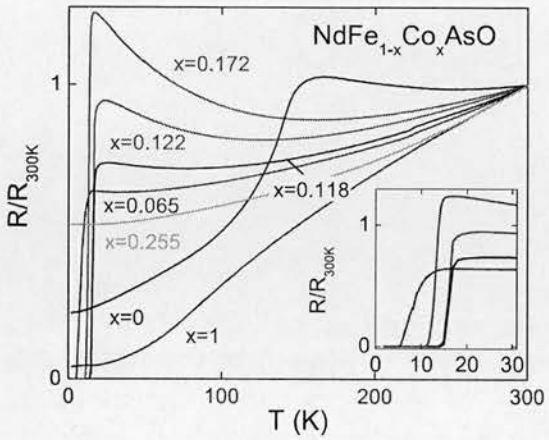

FIG. 6. (Color online) Temperature dependence of the normalized electrical resistance ($R/R_{300\ K}$) for $NdFe_{1-x}Co_xAsO$. The inset illustrates the superconducting transitions.

Hohenberg model, which predicts $H_{c2}(0)=0.69\ T_c[dH_{c2}/dT]$, can be used to estimate the upper critical field at zero temperature.[43] This yields the following estimates: $H_{c2}(0)=14(1)$ T for $x=0.065(2)$, $H_{c2}(0)=26(1)$ T for $x=0.118(2)$, and $H_{c2}(0)=21(1)$ T for $x=0.172(2)$. The SC coherence length (ξ) is given by $\xi^2(0)=\Phi_0/2\pi H_{c2}(0)$, where $\Phi_0=2.07\times10^{-7}$ Oe cm^2, yielding a coherence length of 36(1) Å for $x=0.118(2)$.

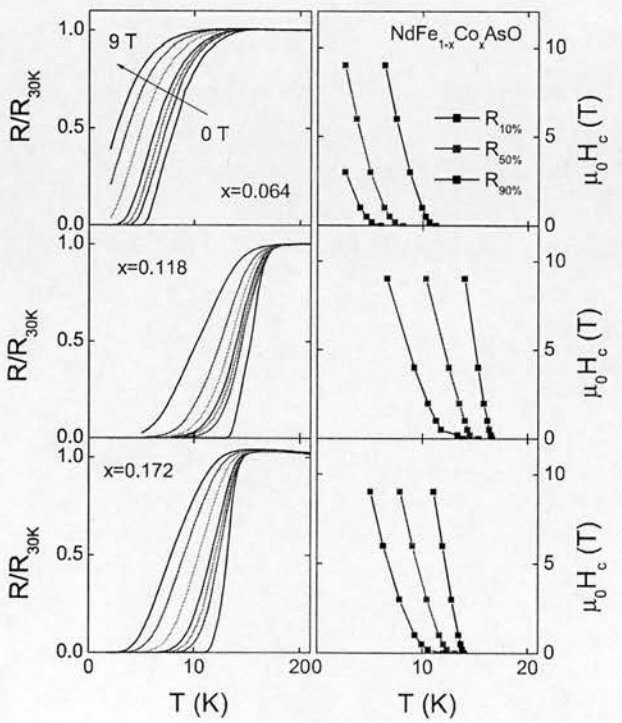

FIG. 7. (Color online) Temperature and field dependences of the electrical resistance for selected $NdFe_{1-x}Co_xAsO$ compositions. $H_{c2}(T)$ derived from 10% ($0.1R_N$), 50% ($0.5R_N$), and 90% ($0.9R_N$) resistance drops are shown on the right-hand side.

V. DISCUSSION

Like the isostructural *R*FeAsO high-T_c parent materials NdCoAsO exhibits significant interplay between the rare-earth and transition-metal sublattices. Below 85 K, NdCoAsO is an itinerant FM with a small ordered cobalt moment of 0.3 μ_B constrained to the *ab* plane. This is analogous to LaCoAsO, which has a Curie temperature of ~60 K and a moment of 0.5 μ_B,[13,22] and consistent with calculations for LaCoAsO that reveal a spin-polarized band structure with a small ordered moment.[22] Our Arrott plots suggest a linear dependence of M^2 on H/M in large fields typical of weak itinerant ferromagnets such as $ZrZn_2$ but different to the "anomalous" M^4 dependence reported for LaCoAsO.[23] More extensive measurements are needed to investigate this. Below 9 K, Nd spin ordering transforms NdCoAsO to an AF metal. Both the FM and AF transitions are evident in the temperature derivative of the resistance but do not result in large anomalies as observed for *R*FeAsO. In the *R*FeAsO materials the Fe spins order in a striped pattern with a small ordered moment of ~0.4 μ_B for all *R* from spectroscopic methods such as Mossbauer and μSR.[25] Neutron powder diffraction, in contrast, suggests a wider spread of 0.3–0.8 μ_B,[26] which Maeter *et al.* have attributed to an induced magnetization on the *R* sublattice below T_{SDW} that contributes to the "Fe" magnetic Bragg reflections.[25] It is not clear from our measurements whether this is important but the almost constant Co moment between 1.7 and 40 K (~0.3 μ_B) suggests that there is no significant induced "Nd contribution." The spectroscopic measurements also suggest that the *R* spin ordering does not have any effect on the magnitude of the Fe moment, while for neutron powder diffraction increases have been reported, in particular, for *R*=Nd.[42,44] In the current case, the available evidence points toward an unchanged Co moment. However, we note that in symmetry unrestricted refinements (i.e., by allowing canting out of the basal plane) it is possible to obtain solutions with $m_{Co}=0.9(2)$ μ_B but these are characterized by large correlations and large estimated standard deviations. Trial refinements with noncollinear *R* ordering analogous to that reported for CeFeAsO (Ref. 8) did not give satisfactory fits to the data. The fitted Nd moment is 1.39(4) μ_B, which is comparable to the value for NdFeAsO [1.55(4) μ_B].[29,44]

The lattice constants, bond distances, and angles for $NdFe_{1-x}Co_xAsO$ change gradually, signaling the formation of a solid solution, as confirmed by Rietveld refinement of the Fe/Co occupancies of selected samples against neutron and synchrotron x-ray data. Furthermore, the structural analysis reveals that the c/a ratio can be used as an experimental measure of the composition [Fig. 2(a)]. This is valid because the combined x-ray and neutron refinements presented in Table I confirm that the only significant compositional change throughout the series is the Fe/Co ratio. The twofold As-Fe-As tetrahedral angle (α, defined in Fig. 9) increases with x. This is in contrast to most other forms of chemical doping and may in part explain why cobalt doping has not yielded the high T_c's observed in other electron-doped superconductors, such as $NdFeAsO_{1-x}F_x$ and $NdFeAsO_{1-d}$, despite having the same nominal amount of doping. The chemical disorder introduced by mixing Fe/Co on the same crystallo-

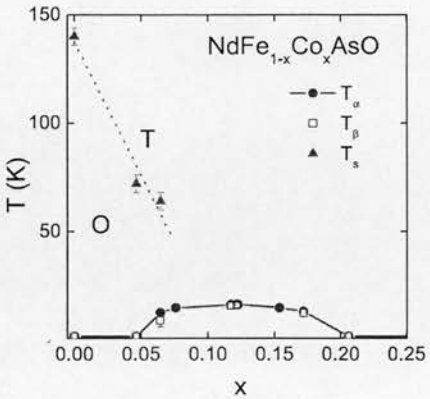

FIG. 8. (Color online) Temperature-composition phase diagram for $NdFe_{1-x}Co_xAsO$ showing the suppression of the structural $T \rightarrow O$ phase transition with increasing Co concentration and the superconducting dome. The data points for the $T \rightarrow O$ structural transition (T_s) were obtained from synchrotron x-ray powder diffraction, while the superconducting T_c values were obtained from the diamagnetic onset temperatures (T_α; red circles) and midpoint resistances (T_β; black squares). Error bars indicate 10% and 90% of the resistive transition. The green dotted line is a linear fit to the T_s data.

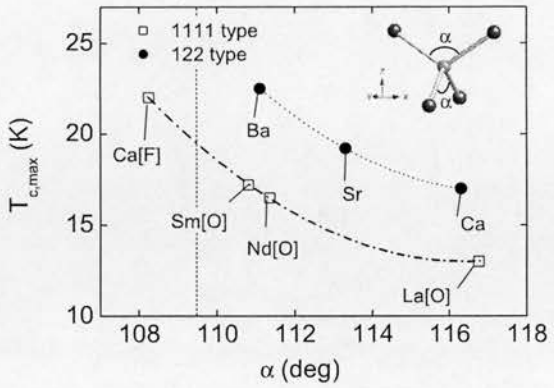

FIG. 9. (Color online) Variation in the superconducting T_c with tetrahedral As-Fe-As angle (defined in the inset) for well-characterized 122-type $AE(Fe_{1-x}Co_x)_2As_2$ (solid circles) and 1111-type $RFe_{1-x}Co_xAsO$ and $AEFe_{1-x}Co_xAsF$ (open squares) superconductors. The line is intended as a guide for the eyes. Data were taken from the following references: Ca[F] (Ref. 18), La[O] (Refs. 13 and 17), Sm[O] (Ref. 17), Ca (Ref. 15), Sr (Ref. 16), and Ba (Ref. 39).

graphic site is also expected to have a detrimental effect on the maximum attainable T_c's. The variable temperature synchrotron diffraction study reveals subtle structural distortions consistent with the well established $T \rightarrow O$ structural transition upon cooling for samples with $x=0.046(2)$ and $x=0.065(2)$. This confirms that replacement of Fe with Co suppresses the $T \rightarrow O$ transition and the associated SDW.

The phase diagram for low cobalt substitutions is presented in Fig. 8 and reveals the presence of a SC dome with limiting compositions $0.05 < x < 0.20$. The maximum critical temperature is 16.5(2) K for $x=0.12$. The underdoped samples ($x \leq 0.075$) have the orthorhombic *Cmma* structure. The presence of a "dome" and possible overlap between magnetic and SC regions is consistent with results published for other 1111- and 122-type cobalt-doped superconductors although the existence of phase coexistence is still under debate.[9,17,18,45] The critical field, $H_{c2}(T)$, increases by approximately 2.3(1) T K^{-1} for the three measured compositions upon cooling below T_c. This is smaller than for "indirect" (not Fe-site) electron-doped superconductors, such as $NdFeAsO_{1-x}F_x$, where values of 4–5 T K^{-1} have been observed.[46] However, similar values are reported for other cobalt-doped superconductors[13,39] suggesting that the superconductivity in these materials is less robust against applied magnetic fields.

Finally, the maximum observed critical temperatures ($T_{c,max}$) for well-characterized cobalt-doped superconductors are plotted in Fig. 9 against the tetrahedral As-Fe-As angle (α). The angles used are for the parent materials as α is not commonly reported for doped compositions. However, this does not affect the reported trends significantly as the increase in α upon cobalt doping is expected to be similar in all materials. The following observations can be made: (1) $T_{c,max}$ increases as α tends toward the cubic value. This is in agreement with the literature for indirectly doped superconductors,[8,19,47] although there is no evidence for a maximum occurring at the ideal tetrahedral angle. (2) The 122-type materials have higher T_c's than the 1111-type for a given value of α. This contrasts the situation for indirect doping where the largest T_c's up to 55 K are obtained for electron-doped 1111 phases such as $NdFeAsO_{1-x}F_x$, while the hole-doped 122 phases with a smaller separation between Fe_2As_2 planes are limited to 38 K for $Ba_{1-x}K_xFe_2As_2$ (both parents have $\alpha \sim 111.2°$). This suggests that were it possible to electron dope the 122 superconductors via chemical substitutions on the *AE* site higher T_c's than 55 K may be achieved.

To summarize, we have investigated the structures and properties of the $NdFe_{1-x}Co_xAsO$ series ($0 \leq x \leq 1$). For low cobalt doping, the phase diagram contains a superconducting dome ($0.05 < x < 0.20$, maximum $T_c = 16.5(2)$ K for $x=0.12$). Samples with $x \leq 0.075$ have the orthorhombic *Cmma* structure at low temperatures. NdCoAsO is an itinerant ferromagnet ($T_C = 85$ K) with a small cobalt moment (0.3 μ_B) that shows a transition to an antiferromagnetic state at $T_N = 9$ K.

Noted added in proof. Recently, we became aware of a preprint article on NdCoAsO by McGuire *et al.*[48] that supports the results presented here.

ACKNOWLEDGMENTS

J.W.G.B. acknowledges the Royal Society of Edinburgh for financial support and the EPSRC-GB for the provision of beam time at the ILL and ESRF.

[1] Y. Kamihara, T. Watanabe, M. Hirano, and H. Hosono, J. Am. Chem. Soc. **130**, 3296 (2008).

[2] K. Ishida, Y. Nakai, and H. Hosono, J. Phys. Soc. Jpn. **78**, 062001 (2009).

[3] M. V. Sadovskii, Phys. Usp. **51**, 1201 (2008).

[4] D. J. Singh and M. H. Du, Phys. Rev. Lett. **100**, 237003 (2008).

[5] I. I. Mazin, D. J. Singh, M. D. Johannes, and M. H. Du, Phys. Rev. Lett. **101**, 057003 (2008).

[6] C. W. Chu and B. Lorenz, Physica C **469**, 385 (2009).

[7] A. J. Drew, C. Niedermayer, P. J. Baker, F. L. Pratt, S. J. Blundell, T. Lancaster, R. H. Liu, G. Wu, X. H. Chen, I. Watanabe, V. K. Malik, A. Dubroka, M. Rossle, K. W. Kim, C. Baines, and C. Bernhard, Nature Mater. **8**, 310 (2009).

[8] J. Zhao, Q. Huang, C. de la Cruz, S. L. Li, J. W. Lynn, Y. Chen, M. A. Green, G. F. Chen, G. Li, Z. Li, J. L. Luo, N. L. Wang, and P. C. Dai, Nature Mater. **7**, 953 (2008).

[9] J. H. Chu, J. G. Analytis, C. Kucharczyk, and I. R. Fisher, Phys. Rev. B **79**, 014506 (2009).

[10] X. F. Wang, T. Wu, G. Wu, R. H. Liu, H. Chen, Y. L. Xie, and X. H. Chen, New J. Phys. **11**, 045003 (2009).

[11] H. Chen, Y. Ren, Y. Qiu, W. Bao, R. H. Liu, G. Wu, T. Wu, Y. L. Xie, X. F. Wang, Q. Huang, and X. H. Chen, Europhys. Lett. **85**, 17006 (2009).

[12] H. Luetkens, H. H. Klauss, M. Kraken, F. J. Litterst, T. Dellmann, R. Klingeler, C. Hess, R. Khasanov, A. Amato, C. Baines, M. Kosmala, O. J. Schumann, M. Braden, J. Hamann-Borrero, N. Leps, A. Kondrat, G. Behr, J. Werner, and B. Buchner, Nature Mater. **8**, 305 (2009).

[13] A. S. Sefat, A. Huq, M. A. McGuire, R. Y. Jin, B. C. Sales, D. Mandrus, L. M. D. Cranswick, P. W. Stephens, and K. H. Stone, Phys. Rev. B **78**, 104505 (2008).

[14] A. S. Sefat, R. Y. Jin, M. A. McGuire, B. C. Sales, D. J. Singh, and D. Mandrus, Phys. Rev. Lett. **101**, 117004 (2008).

[15] N. Kumar, R. Nagalakshmi, R. Kulkarni, P. L. Paulose, A. K. Nigam, S. K. Dhar, and A. Thamizhavel, Phys. Rev. B **79**, 012504 (2009).

[16] A. Leithe-Jasper, W. Schnelle, C. Geibel, and H. Rosner, Phys. Rev. Lett. **101**, 207004 (2008).

[17] C. Wang, Y. K. Li, Z. W. Zhu, S. Jiang, X. Lin, Y. K. Luo, S. Chi, L. J. Li, Z. Ren, M. He, H. Chen, Y. T. Wang, Q. Tao, G. H. Cao, and Z. A. Xu, Phys. Rev. B **79**, 054521 (2009).

[18] S. Matsuishi, Y. Inoue, T. Nomura, H. Yanagi, M. Hirano, and H. Hosono, J. Am. Chem. Soc. **130**, 14428 (2008).

[19] C. H. Lee, A. Iyo, H. Eisaki, H. Kito, M. T. Fernandez-Diaz, T. Ito, K. Kihou, H. Matsuhata, M. Braden, and K. Yamada, J. Phys. Soc. Jpn. **77**, 083704 (2008).

[20] P. Jeglic, J. W. G. Bos, A. Zorko, M. Brunelli, K. Koch, H. Rosner, S. Margadonna, and D. Arcon, Phys. Rev. B **79**, 094515 (2009).

[21] M. Rotter, M. Pangerl, M. Tegel, and D. Johrendt, Angew. Chem., Int. Ed. **47**, 7949 (2008).

[22] H. Yanagi, R. Kawamura, T. Kamiya, Y. Kamihara, M. Hirano, T. Nakamura, H. Osawa, and H. Hosono, Phys. Rev. B **77**, 224431 (2008).

[23] H. Ohta and K. Yoshimura, Phys. Rev. B **79**, 184407 (2009).

[24] A. S. Sefat, D. J. Singh, R. Jin, M. A. McGuire, B. C. Sales, and D. Mandrus, Phys. Rev. B **79**, 024512 (2009).

[25] H. Maeter, H. Luetkens, Y. G. Pashkevich, A. Kwadrin, R. Khasanov, A. Amato, A. A. Gusev, K. V. Lamonova, D. A. Chervinskii, R. Klingeler, C. Hess, G. Behr, B. Buchner, and H. H. Klauss, Phys. Rev. B **80**, 094524 (2009).

[26] J. W. Lynn and P. C. Dai, Physica C **469**, 469 (2009).

[27] M. Le Tacon, M. Krisch, A. Bosak, J. W. G. Bos, and S. Margadonna, Phys. Rev. B **78**, 140505 (2008).

[28] K. Kasperkiewicz, J. W. G. Bos, A. N. Fitch, K. Prassides, and S. Margadonna, Chem. Commun. **2009**, 707.

[29] A. Marcinkova, E. Suard, A. N. Fitch, S. Margadonna, and J. W. G. Bos, Chem. Mater. **21**, 2967 (2009).

[30] T. C. Hansen, P. F. Henry, H. E. Fischer, J. Torregrossa, and P. Convert, Meas. Sci. Technol. **19**, 034001 (2008).

[31] A. C. Larson and R. B. Von Dreele, Los Alamos National Laboratory LAUR Report No. 86, 2000 (unpublished).

[32] P. W. Stephens, J. Appl. Crystallogr. **32**, 281 (1999).

[33] P. Quebe, L. J. Terbuchte, and W. Jeitschko, J. Alloys Compd. **302**, 70 (2000).

[34] A. Arrott, Phys. Rev. **108**, 1394 (1957).

[35] A. S. Wills, Physica B **276-278**, 680 (2000).

[36] O. V. Kovalev, *Representations of the Crystallographic Space Groups* (Gordon and Breach Science Publishers, Switzerland, 1993).

[37] See supplementary material at http://link.aps.org/supplemental/10.1103/PhysRevB.81.064511 for the Character Table of the small group Gk, room temperature synchrotron x-ray and neutron diffraction Rietveld profiles for $x=0.075$, $x=0.175$, and $x=100$, and tetragonal to orthorhombic peak broadening observed in synchrotron x-ray powder diffraction for underdoped $NdFe_{1-x}Co_xAsO$ samples.

[38] A. Authier, *International Tables for Crystallography, Volume D* (Kluwer Academic Publishers, Dordrecht, 2003).

[39] N. Ni, M. E. Tillman, J. Q. Yan, A. Kracher, S. T. Hannahs, S. L. Bud'ko, and P. C. Canfield, Phys. Rev. B **78**, 214515 (2008).

[40] K. Miyazawa, K. Kihou, P. M. Shirage, C. H. Lee, H. Kito, H. Eisaki, and A. Iyo, J. Phys. Soc. Jpn. **78**, 034712 (2009).

[41] M. Fratini, R. Caivano, A. Puri, A. Ricci, Z. A. Ren, X. L. Dong, J. Yang, W. Lu, Z. X. Zhao, L. Barba, G. Arrighetti, M. Polentarutti, and A. Bianconi, Supercond. Sci. Technol. **21**, 092002 (2008).

[42] Y. Chen, J. W. Lynn, J. Li, G. Li, G. F. Chen, J. L. Luo, N. L. Wang, P. C. Dai, C. de la Cruz, and H. A. Mook, Phys. Rev. B **78**, 064515 (2008).

[43] N. R. Werthamer, E. Helfand, and P. C. Hohenberg, Phys. Rev. **147**, 295 (1966).

[44] Y. Qiu, W. Bao, Q. Huang, T. Yildirim, J. M. Simmons, M. A. Green, J. W. Lynn, Y. C. Gasparovic, J. Li, T. Wu, G. Wu, and X. H. Chen, Phys. Rev. Lett. **101**, 257002 (2008).

[45] C. Lester, J. H. Chu, J. G. Analytis, S. C. Capelli, A. S. Erickson, C. L. Condron, M. F. Toney, I. R. Fisher, and S. M. Hayden, Phys. Rev. B **79**, 144523 (2009).

[46] J. Jaroszynski, F. Hunte, L. Balicas, Y. J. Jo, I. Raicevic, A. Gurevich, D. C. Larbalestier, F. F. Balakirev, L. Fang, P. Cheng, Y. Jia, and H. H. Wen, Phys. Rev. B **78**, 174523 (2008).

[47] J. A. Rodgers, G. B. S. Penny, A. Marcinkova, J.-W. G. Bos, D. A. Sokolov, A. Kusmartseva, A. D. Huxley, and J. P. Attfield, Phys. Rev. B **80**, 052508 (2009).

[48] M. A. McGuire *et al.*, arXiv:0912.4237, Phys. Rev. B (to be published).

Nd-induced Mn spin-reorientation transition in NdMnAsO

A. Marcinkova,[1,2] T. C. Hansen,[3] C. Curfs,[4] S. Margadonna,[1,2] and J. -W. G. Bos[5,*]
[1]*School of Chemistry, University of Edinburgh, Edinburgh EH9 3JJ, United Kingdom*
[2]*Centre for Science at Extreme Conditions, University of Edinburgh, King's Buildings, Mayfield Road, Edinburgh EH9 3JZ, United Kingdom*
[3]*Institut Laue Langevin, 38042 Grenoble, France*
[4]*European Synchrotron Radiation Facility, 39043 Grenoble, France*
[5]*Department of Chemistry-EPS, Heriot-Watt University, Edinburgh EH14 4AS, United Kingdom*
(Received 16 July 2010; revised manuscript received 15 September 2010; published 29 November 2010)

A combination of synchrotron x-ray, neutron powder-diffraction, magnetization, heat-capacity, and electrical-resistivity measurements reveals that NdMnAsO is an antiferromagnetic semiconductor with large Neel temperature [T_N=359(2) K]. At room temperature the magnetic propagation vector $\mathbf{k}$=0 and the Mn moments are directed along the crystallographic c axis [m_{Mn}=2.41(6) μ_B]. Upon cooling a spin-reorientation (SR) transition of the Mn moments into the ab plane occurs (T_{SR}=23 K). This coincides with the long-range ordering of the Nd moments, which are restricted to the basal plane. The magnetic propagation vector remains $\mathbf{k}$=0. At base temperature (1.6 K) the fitted moments are $m_{ab,Mn}$=3.72(1) μ_B and $m_{ab,Nd}$=1.94(1) μ_B. The electrical resistivity is characterized by a broad maximum at 250 K, below which it has a metallic temperature dependence but semiconducting magnitude ($\rho_{250\ K}$=50 Ω cm, residual resistivity ratio=2), and a slight upturn at the SR transition.

DOI: 10.1103/PhysRevB.82.174438 PACS number(s): 75.25.−j, 75.30.Kz, 75.50.Ee

I. INTRODUCTION

The discovery[1] of high-temperature superconductivity in $LaFeAsO_{1-x}F_x$ has generated enormous interest and led to the rapid exploration of materials with similar structures. High-T_c superconductivity has since been found in 1111-type RFeAsO and AeFeAsF (R=rare earth and Ae=alkaline earth), 122-type $AeFe_2As_2$, 111-type A_xFeAs (A=Li,Na) and 11-type $FeSe_{1-d}$-based materials that all have square planar Fe layers with tetrahedral As (Se) coordination.[2,3] The 1111-type materials have the highest superconducting temperatures (up to 55 K).[4,5] It is now well established that the superconductivity in these materials occurs at the expense of an itinerant antiferromagnetic (AF) spin-density wave,[6–8] and is induced either by chemical doping or application of hydrostatic pressure. It is therefore of much interest to study the interplay between composition, structure, magnetism, and superconductivity in these but also in other non-Fe-based materials. For instance, the reported Ni analogs are conventional superconductors with <4 K transition temperatures without any evidence for the importance of magnetism in the pairing mechanism.[9–11] The isostructural Co materials are ferromagnetic (FM) metals or on the boundary of ferromagnetism.[12–15] The Mn analogs in contrast are not metallic but semiconducting and are antiferromagnetic.[16–19] This pronounced difference has been attributed to a much stronger hybridization between Mn 3d and pnictogen p states, which leads to an electronic structure that is not derived from the Fe-Ni materials.[18] The best characterized example is $BaMn_2As_2$, which has a G-type magnetic structure with moments aligned along the c axis [3.88(4) μ_B at 10 K] and a Neel temperature of 625(1) K.[19] Heat capacity and electrical resistivity reveal a Sommerfeld coefficient close to zero, a metallic temperature dependence between 100–400 K and a room-temperature (RT) resistivity of 165 mΩ cm.[17,18] Among the 1111-type materials, LaMnPO has been characterized in some detail.[16] It has a similar magnetic structure to $BaMn_2As_2$ but with a parallel alignment of the nearest-neighbor (NN) Mn moments along the c axis. Resistivity measurements on polycrystalline samples revealed Arrhenius-type semiconducting behavior between 200–300 K with a RT value of 2 kΩ cm.

The 1111-type materials offer the possibility to investigate the interplay between rare-earth (R) and transition-metal (TM) magnetism in this important class of materials. So far most of the experimental evidence points to a rather weak interaction between R and TM sublattices. For instance, the increase in T_c on going from La to the later R in the RFeAsO-based superconductors has been attributed to a structural effect rather than a strong 4f-3d hybridization.[20–22] One noteworthy exception is CeFePO, where the absence of low-temperature superconductivity is related to a strong hybridization resulting in heavy-fermion behavior.[23] In case of the Fe and Co RTMAsO materials, the most common effect of magnetic R ordering is a change in sign of the magnetic coupling between adjacent TM planes, while the in-plane ordering remains intact.[3,14,15,20] For example, for NdCoAsO, the coupling between adjacent Co planes changes from FM to AF upon ordering of the Nd moments without affecting the in-plane order.

Here, we report on the crystal and magnetic structure, and physical properties of NdMnAsO using synchrotron x-ray, neutron powder-diffraction, magnetization, and electrical-resistance measurements. Analysis of the neutron-diffraction data reveals a spin-reorientation (SR) transition of the Mn moments from parallel to the c axis into the basal plane upon ordering of the Nd moments. This demonstrates that a magnetic R sublattice can change the orientation of the transition-metal moments and is not limited to altering the spin-orientation between unchanged planes.

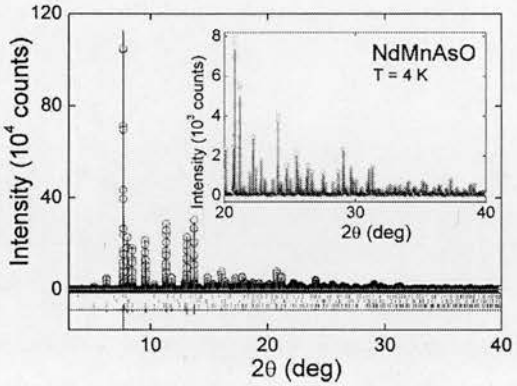

FIG. 1. (Color online) Rietveld fit to 4 K synchrotron x-ray powder-diffraction data for NdMnAsO. Observed data are indicated by open circles, the fit by the solid line, and the difference curve is shown at the bottom. The Bragg markers are for NdMnAsO (top), MnAs (middle), and Nd_2O_3 (bottom).

II. EXPERIMENTAL

Polycrystalline NdMnAsO (2 g) was prepared using solid-state chemistry methods and used for all measurements. A stoichiometric mixture of NdAs and MnO (Sigma Aldrich, 99.999%) was homogenized using mortar and pestle, pressed into pellets and heated for 24 h at 1100 °C inside an evacuated quartz tube. NdAs was prepared from a 1:1 ratio of Nd (Sigma Aldrich, 99.99%) and As (Sigma Aldrich, 99.9%), which was heated for 2 h at 500 °C in an evacuated quartz tube, immediately followed by 16 h at 900 °C. Initial phase analysis was done using laboratory powder x-ray diffraction on a Bruker D8 AXS diffractometer with a Cu $K_{\alpha 1}$ radiation source. High-resolution synchrotron x-ray powder-diffraction measurements were done on the ID31 beam line at the European Synchrotron Radiation Facility in Grenoble, France. The x-ray wavelength used was 0.3998 Å, the sample was contained in a 0.5 mm diameter borosilicate glass capillary, and data were collected between 4–250 K. The real and anomalous x-ray dispersion coefficients were calculated using the program FPRIME and a linear-absorption correction $\mu R = 1.5$ was used.[24] The neutron powder-diffraction experiments were done on the D20 beamline at the Institute Laue Langevin in Grenoble, France.[25] The instrument was used in the high-flux setting with $\lambda = 2.41$ Å. The sample was contained in a 6 mm diameter cylindrical vanadium can. Between 1.6–30 K, 30 min data sets were collected at fixed temperature. From 30–300 K, 5 min data sets were collected on a ramp of 1.25 K/min. A linear-absorption correction $\mu R = 0.3$ was applied. Rietveld analysis of the powder-diffraction data was done using the GSAS/EXPGUI suite of programs.[26,27] The zero-field-cooled (ZFC) magnetic susceptibility was measured using a Quantum Design magnetic property measurement system (MPMS). The temperature and field dependences of the electrical resistivity were measured using the resistance option of a Quantum Design physical property measurement system (PPMS). Heat-capacity data were collected using the heat-capacity option of the PPMS. A sintered platelet of about 9 mg was used, the sample coupling constant was always larger than 98%.

TABLE I. Refined lattice constants, atomic parameters, selected bond lengths (Å) and angles (deg), and fit statistics for NdMnAsO from Rietveld fits against synchrotron x-ray powder-diffraction data. Nd: $2c(\frac{1}{4},\frac{1}{4},z)$; Mn: $2b(\frac{3}{4},\frac{1}{4},\frac{1}{2})$; As: $2c(\frac{1}{4},\frac{1}{4},z)$; O: $2a(\frac{3}{4},\frac{1}{4},0)$. Impurities: 1.5(1) wt % Nd_2O_3, 1.0(1) wt % MnAs.

T (K)	4	100	250
SG	*P4/nmm*	*P4/nmm*	*P4/nmm*
a axis (Å)	4.04446(1)	4.04503(1)	4.04979(5)
c axis (Å)	8.87383(2)	8.88258(2)	8.89935(2)
Volume (Å^3)	145.16	145.34	145.97
Nd U_{iso} (Å^2)	0.0010(1)	0.0025(1)	0.0053(1)
z	0.12991(5)	0.12992(4)	0.12976(4)
Frac	1.00	1.00	1.00
Mn U_{iso} (Å^2)	0.0017(1)	0.0039(2)	0.0073(2)
Frac	1.00	1.00	1.00
As U_{iso} (Å^2)	0.0013(1)	0.0044(2)	0.0071(2)
z	0.6737(1)	0.6736(1)	0.6736(1)
Frac	1.00	1.00	1.00
O U_{iso} (Å^2)	0.0041(1)	0.0046(1)	0.009(1)
Frac	1.00	1.00	1.00
d(Nd-O) (Å)	2.3277(2)	2.3286(2)	2.3308(2)
∠Nd-O-Nd (deg) $2x$	120.63(2)	120.58(2)	120.63(2)
∠Nd-O-Nd (deg) $4x$	104.22(2)	104.22(2)	104.21(2)
d(Mn-As) (Å)	2.5456(5)	2.5424(4)	2.5468(4)
∠As-Mn-As (deg) $2x$	111.65(2)	111.54(1)	111.59(2)
∠As-Mn-As (deg) $4x$	105.20(3)	105.41(2)	105.32(2)
d(Mn-Mn) (Å)	2.85983(1)	2.86027(1)	2.86364(1)
χ^2	5.1	4.7	5.1
wR_p	12.8	14.1	15.0
R_p	8.3	9.6	9.6
R_F^2	4.3	5.5	5.1

III. RESULTS

Rietveld analysis of the synchrotron x-ray powder-diffraction data confirms the tetragonal ZrCuSiAs structure reported by Nientiedt *et al.*[28] down to 4 K. The fit to the 4 K data set is given in Fig. 1, and a summary of the fitted parameters and selected bond distances and angles at 4, 100, and 250 K are given in Table I. Upon cooling the lattice contracts gradually along the a (0.1%) and c axes (0.3%) and no large anomalies are observed (Fig. 2). The c/a ratio does evidence a change in trend at T_{SR} signaling a weak coupling between the lattice and magnetic order. The Mn-As bond distance [2.5468(4) Å] and twofold As-Mn-As tetrahedral angle [111.59(2)°] do not change significantly with temperature. The "anomalous" nature of the Mn material is illustrated by its unit-cell volume (146 Å^3), which is much larger than expected based on a simple extrapolation of the values for NdFeAsO (135 Å^3) and NdCoAsO (132 Å^3).[14,29] Refinement of the atomic site occupancies confirmed the nominal composition. The temperature dependence of the magnetic susceptibility (χ) evidences local moment magnetism (Fig. 3) with two transitions visible at 23 and 4 K. From the neutron powder-diffraction experiment (below) it is known

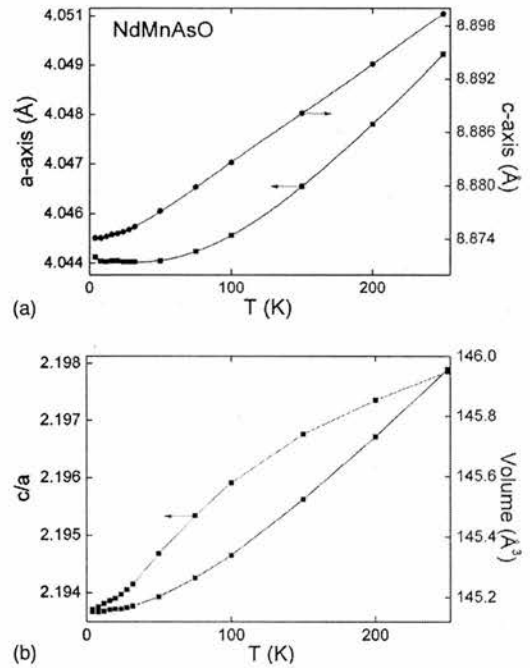

FIG. 2. (Color online) (a) Temperature dependence of the crystallographic a and c axes for NdMnAsO. (b) Temperature dependence of the unit-cell volume and the c/a ratio for NdMnAsO.

that $T_{N,Mn}=359(2)$ K, while the transition at 23 K corresponds to the long-range AF ordering of the Nd moments, and a concomitant SR of the Mn moments. The presence of Nd and Mn moments makes interpretation of the $\chi(T)$ data difficult. In particular, the data in Fig. 3 cannot be modeled using a single Curie-Weiss term, $\chi(T)=C/(T-\theta_W)$, unless $\chi_{Mn}(T)$ is negligible. To obtain an indication of the relative importance of the Nd and Mn contributions, $1/\chi$ was fitted to a single Curie-Weiss term between 125–300 K. This yields $C=2.39(2)$ emu K^{-1} mol^{-1} and $\theta_W=-43.1(8)$ K. The fitted Curie constant is larger than expected for $^4I_{9/2}$ Nd^{3+} [$C=1.6$ emu K^{-1} mol^{-1}], which suggests that both Nd and Mn

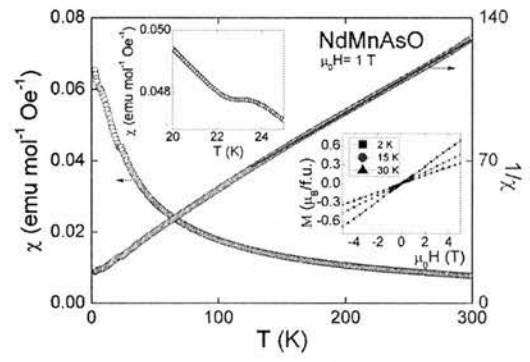

FIG. 3. (Color online) Temperature dependence of the ZFC magnetic (χ) and inverse magnetic ($1/\chi$) susceptibilities for NdMnAsO. The solid line is a fit to the Curie-Weiss law. The insets show the field dependence of the magnetization at 2, 15, and 30 K, and a closeup of $\chi(T)$ at the Nd ordering transition.

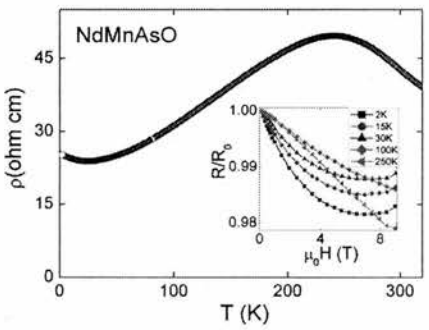

FIG. 4. (Color online) Temperature dependence of the electrical resistivity for NdMnAsO. The inset shows the field dependence of the normalized resistivity R/R_0 at 2, 15, 30, 100, and 250 K.

contribute to $\chi(T)$ in this temperature interval. This is supported by the neutron-diffraction results which reveal that the Mn moments are not saturated down to 50 K. The transition at 4 K corresponds to the saturation of the ordered Nd moments, and cannot be attributed to magnetic impurities (Table I) as Nd_2O_3 does not order down to at least 1.8 K, and MnAs is FM with a Curie temperature above RT. The linear field dependence of the magnetization (inset to Fig. 3) is in agreement with a complete AF (2 and 15 K) or AF plus paramagnetic ground state (30 K).

The temperature and field dependences of the electrical resistivity are summarized in Fig. 4. The magnitude of the resistivity falls between 25 and 50 Ω cm, which places NdMnAsO in the semiconducting regime. The temperature dependence is characterized by a broad hump at 250 K, above which semiconducting behavior is found, while below a metallic temperature dependence is evident. At T_{SR} the resistivity shows a moderate upturn, which may be due to increased spin scattering. This type of temperature dependence is typical of a degenerate semiconductor and was also observed in $BaMn_2As_2$ single crystals.[17] However, in the current case, the magnitude of the resistivity is one to two orders of magnitude larger, which may be related the presence of insulating Nd_2O_2 blocks and to the polycrystalline nature of the samples. Measurements on single crystals are needed to probe the intrinsic transport properties of this material. The magnetoresistance (MR) was obtained from the symmetric part of $R(H)$ curves measured between $-9\leq\mu_0H\leq 9$ T. This was done to eliminate spurious Hall-effect contributions due to misalignment of the contact electrodes. At low temperatures (<30 K), the field dependence shows a rapid drop followed by a saturation at the 1–2 % level. At higher temperatures, the field dependence is linear with a similar MR of 2% in 9 T observed at 250 K.

The temperature dependence of the heat capacity (C) in applied magnetic fields of 0 and 9 T is given in Fig. 5. This confirms the presence of a phase transition at 23 K, while there is no evidence for a transition at 4 K. In zero field, the transition appears second order with a clear maximum at 23 K. Application of a magnetic field broadens the transition, and moves the maximum to lower temperatures, in agreement with the observed antiferromagnetic ordering. We note that even in zero applied magnetic field the transition appears

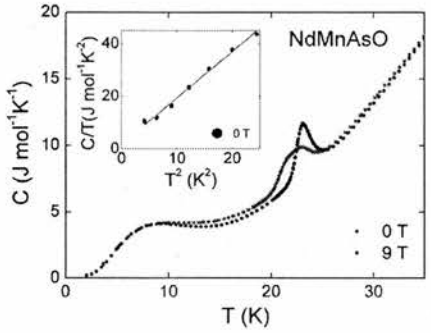

FIG. 5. (Color online) Temperature dependence of the heat capacity (C) in applied magnetic fields of 0 and 9 T. The inset shows a linear fit to C/T versus T^2 at low temperatures.

somewhat broad, which is consistent with the neutron data that reveals a Mn-spin reorientation occurring in a narrow temperature interval. A linear fit to C/T versus T^2 at low temperatures (inset to Fig. 5) yields a Sommerfeld coefficient close to zero [$\gamma=1.2(7)$ J mol^{-1} K^{-2}], which is in agreement with the observed semiconducting behavior.

Comparison of the x-ray and neutron data revealed magnetic contributions to the nuclear (102) and (103) reflections, and completely magnetic (100) and (101) reflections in the neutron-diffraction patterns from 300–25 K [Fig. 5(a)]. Below 25 K, a magnetic contribution to the (002) reflection develops and there is a clear change in the relative intensities of the other magnetic reflections [Fig. 5(b)]. In all cases, the magnetic reflections are indexed on the nuclear cell and the magnetic propagation vector $\mathbf{k}=0$ at all measured temperatures. Magnetic representational analysis was used to derive the symmetry allowed magnetic structures. These calculations were done using version 2 K of the SARAH representational analysis program,[30] and confirm that all symmetry elements of the $P4/nmm$ space group (SG) leave the magnetic propagation vector ($\mathbf{k}=0$) invariant, and thus constitute the small group $G_{\mathbf{k}}$. The decomposition of the magnetic representation (Γ_{Mag}) into the irreducible representations (IRs) of $G_{\mathbf{k}}$ is $\Gamma_3^1+\Gamma_6^1+\Gamma_9^2+\Gamma_{10}^2$ for the Mn sites and $\Gamma_2^1+\Gamma_3^1+\Gamma_9^2+\Gamma_{10}^2$ for the Nd sites. The representations used are after Kovalev,[31] and the character table can be found in Ref. 14. The symmetry allowed basis vectors are given in Table II. Inspection of this table reveals that there are two FM (Γ_3^1 and Γ_9^2) and three AF solutions (Γ_2^2, Γ_6^1, and Γ_{10}^2). The two FM models are not in agreement with the observed data and can therefore be discarded. The AF models differ in the easy magnetization direction, which is either along the c axis or in the basal plane. We note that according to Landau theory, only a single IR becomes critical in a second-order phase transition, and as a starting point only models corresponding to a single IR were tested. Between 300–25 K, the magnetic intensities were best fitted using the Γ_6^1 model with the Mn moments aligned along the c direction. (The R_{wp} values for the tested models are given in Table II.) The Rietveld fit and a graphic representation of the model are given in Fig. 6(a). Trial refinements using a "forbidden" linear combination of the Γ_6^1 and Γ_2^1 models did not fit the data well ($R_{wp}=7.7\%$), and there is no evidence from our data for ordering of the Nd moments above 25 K. For $T<20$ K, the magnetic intensities were fitted well using the Γ_{10}^2 model with ordered Mn and Nd moments (Table II), which are both constrained to the basal plane [Fig. 6(b)]. The ordered moments at 1.6 K are 3.72(1) μ_B for Mn and 1.941(1) μ_B for Nd. Rietveld refinements using models with an out-of-plane component on the Nd and/or the Mn sublattice did not result in an improvement, and were generally unstable. Finally, a small intermediate temperature interval ($20\leq T<25$ K) was identified in which the magnetic intensities were fitted using several trial models. At 21.7(2) K, the Γ_6^1 and the Γ_{10}^2 models are indiscernible ($R_{wp}=5.3\%$), while models with Mn(m_{ab},m_c) and Nd(m_{ab}) or only Mn(m_{ab},m_c) yielded an improved fit ($R_{wp}=5.1\%$). This suggests that there is an intermediate phase with a Mn moment rotation angle (ϕ) in between 0°–90° with respect to the c axis. However, the comparable fits also demonstrate that this phase exists only in a narrow temperature interval, which is in agreement with the heat-capacity and magnetic-susceptibility data. The temperature dependence of the ordered moments [using the model with Mn(m_{ab},m_z) and Nd(m_{ab}) between $20<T<25$ K] are given in Fig. 6(c). The fitted ϕ values are 12(10)° at 23.6(2) K, 29(5)° at 21.7(2) K, and 80(9)° at 19.9(2) K. This suggests that the SR temperature interval is <3 K. The temperature evolution of the ordered Nd moment is of some interest: an initial rapid increase to about 0.9 μ_B consistent with a second-order phase transition is observed but is followed by a gradual increase in moment to a maximum value of 1.9 μ_B at 4 K, which corresponds to the second transition observed in the magnetic susceptibility. There is no evidence for a phase transition to a different magnetic structure at 4 K as the statistics above and below are comparable, and no sig-

TABLE II. Basis vectors [m_x,m_y,m_z] for space group $P4/nmm$ with $\mathbf{k}=0$ and R_{wp} values for fits against the 1.6 and 30 K data sets. Mn1: (0.75, 0.25, 0.5), Mn2: (0.25, 0.75, 0.5), Nd1: (0.25, 0.25, 0.139), and Nd2: (0.75, 0.75, 0.861).

	Γ_2^1	Γ_3^1	Γ_6^1	Γ_9^2	Γ_{10}^2
Mn1		[0 0 m_z]	[0 0 m_z]	[m_x m_y 0]	[m_x m_y 0]
Mn2		[0 0 m_z]	[0 0 $-m_z$]	[m_x m_y 0]	[$-m_x$ $-m_y$ 0]
Nd1	[0 0 m_z]	[0 0 m_z]		[m_x m_y 0]	[m_x m_y 0]
Nd2	[0 0 $-m_z$]	[0 0 m_z]		[m_x m_y 0]	[$-m_x$ $-m_y$ 0]
R_{wp}, 30 K (%)	Unstable		5.1		16.3
R_{wp}, 1.6 K (%)	10.5		9.3		5.4

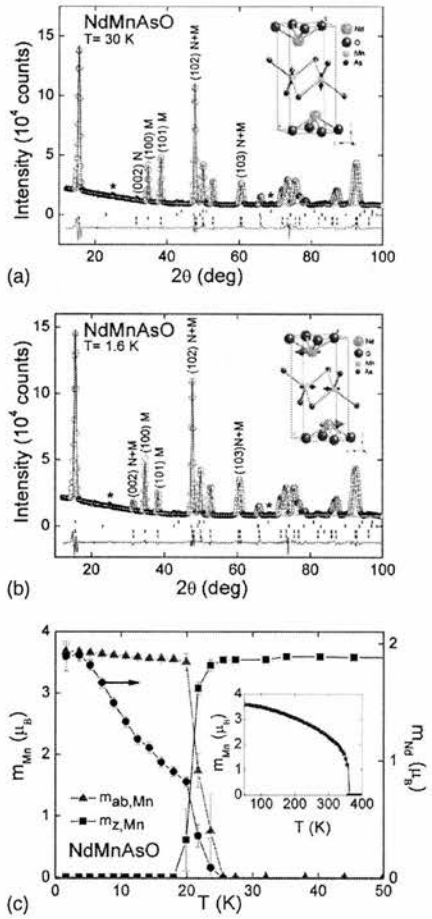

FIG. 6. (Color online) Rietveld fits to (a) 30 K and (b) 1.6 K neutron powder-diffraction data for NdMnAsO. The observed data are indicated by open circles, the fit by the solid line, and the difference curve is shown at the bottom. From top to bottom: Bragg markers are for NdMnAsO, the magnetic phase, Nd_2O_3 [2.0(2) wt %] and MnAs [1.0(2) wt %]. (30 K: R_{wp}=5.1%, R_p =3.2%, and R_F^2=3.4%, 1.6 K: R_{wp}=5.5%, R_p=3.5%, and R_F^2 =5.1%). The insets to (a) and (b) show graphic representations of the fitted magnetic structures. The temperature evolution of the fitted Nd and Mn moments between 1.6 and 50 K is given in (c). The inset shows the temperature evolution of the ordered Mn moment between 50–300 K. The solid line is a fit to $m=m_0(1-T/T_N)^\beta$ (see text). The unidentified reflections denoted by the asterisks do not change intensity between1.6 and 400 K.

nificant changes in magnetic intensities are observed. The temperature evolution of the ordered Mn moment above 50 K is shown in the inset to Fig. 6(c). A fit to $m=m_0(1-T/T_N)^\beta$ yields m_0=3.85(2) μ_B K, T_N=359(2) K, and β =0.27(1).

IV. DISCUSSION

The magnetic and electronic properties of NdMnAsO are of much interest, in particular, in comparison with the isostructural Fe, Co, and Ni materials, which are all itinerant

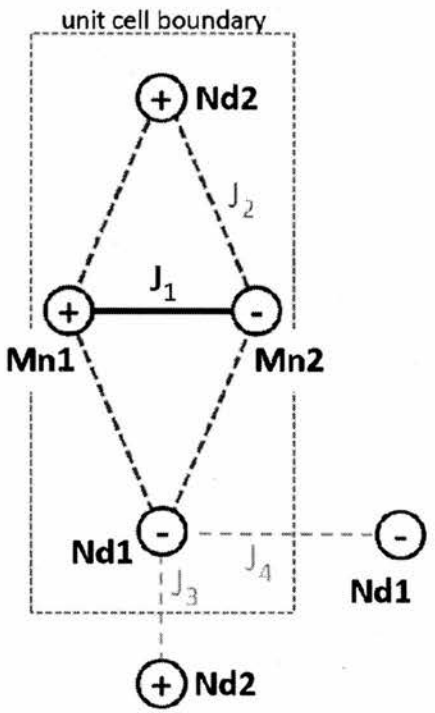

FIG. 7. (Color online) Schematic representation of the main magnetic interactions for NdMnAsO. Within the unit cell, the Nd and Mn ions lie on a diamond-shaped plane. The AF NN interactions (J_1) between Mn ions are all satisfied, leading to G-type magnetic ordering. The symmetric Heisenberg-exchange interaction (J_2) between the Nd and Mn sublattice is frustrated, leaving antisymmetric (Dzyaloshinsky-Moriya) exchange as the strongest magnetic interaction, and a postulated perpendicular orientation of the ordered Mn and Nd moments. Within the Nd-O_2-Nd block the J_3 pathway is antiferromagnetic while J_4 is ferromagnetic. Magnetic interactions between the As-Mn_2-As (Nd-O_2-Nd) blocks are expected to be much weaker due to the large separation between the blocks. The relative orientations of the ordered magnetic moments within each sublattice at 1.6 K are denoted by the +/− signs. The labeling of the atoms corresponds to that used in Table II.

systems. From a structural point of view the most pronounced difference is the unit-cell volume (or the MnAs bond distance), which is much larger than expected based on a simple extrapolation of the itinerant systems. This signals significant differences in bonding, which is confirmed by the local moment magnetism and semiconducting behavior observed in the title material. The main novel result comes from the neutron powder-diffraction study that reveals a significant coupling between the Nd and Mn magnetic sublattices, which results in a spin reorientation of the Mn moments. This type of transition has not been observed in any of the itinerant 1111-type systems, although it has been postulated for PrFeAsO.[20] The analysis of the neutron powder-diffraction data demonstrates that the SR of the Mn moments occurs in a narrow temperature interval (<3 K), and proceeds via an intermediate phase with a Mn rotation angle between 0°–90° with respect to the c axis. This interpretation is in agreement with a recent preprint on PrMnSbO that

reveals an identical SR transition occurring over a much wider (~10 K) temperature interval.[32] The narrow SR transition for NdMnAsO is consistent with the magnetic-susceptibility and heat-capacity measurements that evidence a second-order phase transition at T_{SR}. The probable cause of the SR is the competing single-ion anisotropy of Nd and Mn as observed in the RFeO$_3$ perovskites,[33–35] and the high-T_c parent materials R_2CuO$_4$,[36] which have all been accounted for using a phenomenological description involving competing single-ion anisotropies. In the current case, the Mn^{2+} ion (free ion values: $S=5/2$, orbital angular momentum $L=0$) prefers to orient its moment along the c axis, while the Nd^{3+} moment (free ion values: $S=3/2$ and $L=6$) lies in the basal plane. Since the single-ion anisotropy of Nd^{3+} dominates that of Mn^{2+} ($L=0$) a SR transition of the Mn moments can occur as soon as an ordered moment develops on the Nd sublattice. The preferred basal plane orientation for the Nd moments is supported by calculations of the crystalline electric field splitting of the $4f$ states.[36] The development of a small magnetization on the Nd sublattice [Fig. 6(c)], followed by an almost linear increase to the saturation value has also been observed in a recent single-crystal study on NdFeAsO,[37] and it may be that this is a general feature of these materials. Further theoretical analysis is needed to explain this unexpected behavior, and to elucidate the magnetic coupling between the Nd and *TM* sublattices. At RT only the Mn sublattice is magnetically ordered and has a NN AF checkerboard alignment in the basal plane [Fig. 6(a)]. The coupling between Mn planes is FM, and the ordered moment is aligned along the c axis. The in-plane checkerboard arrangement suggests that next-nearest-neighbor (NNN) interactions are negligible. This is in contrast to NdFeAsO, where in a localized model strong NNN interactions are needed to stabilize the observed spin-stripe ordering.[38] Within the insulating Nd-O_2-Nd blocks the magnetic order is characterized by AF coupled FM planes [Fig. 6(b)]. An identical arrangement occurs for NdCoAsO that also remains tetragonal to the lowest measured temperatures.[14,15] In contrast, the *Cmma* ($\sqrt{2}a\times\sqrt{2}a\times c$) superstructure for NdFeAsO ($\mathbf{k}=0$) allows for a different type of ordering with AF-coupled AF Nd planes.[38] To further analyze the observed SR a schematic representation of the main magnetic interactions in NdMnAsO is presented in Fig. 7. Within the unit cell, the magnetic ions form a diamond shape with Nd at the top and bottom corners. As discussed, the AF NN Mn-Mn interaction J_1 (through-space distance $d=2.86$ Å) is dominant and leads to the observed checkerboard magnetic ordering. Within the AF Nd-O_2-Nd blocks there are two main interactions: J_3 which cuts across the block (Nd1-Nd2, $d=3.68$ Å), and J_4 which is along the block (Ndn-Ndn, $n=1,2$, $d=4.04$ Å). Based on the Nd-O-Nd bond angles (Table I) and the Kanamori-Goodenough rules for superexchange both are expected to be AF, although only J_3 is in the experimental structure. The interaction between the Nd and Mn sublattices proceeds via four identical paths ($J_2, d=3.86$ Å), which leads to a frustrated arrangement of symmetric Heisenberg-exchange interactions between local moments. This leaves the weaker antisymmetric (Dzyaloshinsky-Moriya) exchange as the strongest magnetic interaction, and a postulated perpendicular orientation of the ordered Mn and Nd moments. Unfortunately, due to the tetragonal symmetry this cannot be verified experimentally. Finally, the Neel temperature [359(2) K] is much reduced compared to the 625 K reported for $BaMn_2As_2$.[19] In addition, the critical exponent [$\beta=0.27(1)$] is lower than reported for $BaMn_2As_2$ [$\beta=0.35(2)$], which is close to the expected value for a three-dimensional Heisenberg magnet ($\beta=0.367$).[19] These observations point to a reduced magnetic coupling and more two-dimensional behavior in this 1111-type material compared to the 122's, which is plausible given the larger distance between the Mn layers. The extrapolated ordered moment at 0 K is 3.85(2) μ_B, which is identical to the value reported for $BaMn_2As_2$ [3.88(4) μ_B at 10 K].[19] To conclude, NdMnAsO is a local moment semiconductor that exhibits a Mn spin-reorientation transition from aligned along the c direction into the basal plane upon ordering of the Nd moments.

Note added in proof. Recently, we became aware of a manuscript on NdMnAsO by Emery *et al.*[39] that supports the RT magnetic structure reported here.

ACKNOWLEDGMENT

STFC-GB is acknowledged for the provision of beam time at the ILL and ESRF.

*j.w.g.bos@hw.ac.uk

[1] Y. Kamihara, T. Watanabe, M. Hirano, and H. Hosono, J. Am. Chem. Soc. **130**, 3296 (2008).

[2] K. Ishida, Y. Nakai, and H. Hosono, J. Phys. Soc. Jpn. **78**, 062001 (2009).

[3] M. D. Lumsden and A. D. Christianson, J. Phys.: Condens. Matter **22**, 203203 (2010).

[4] C. H. Lee, A. Iyo, H. Eisaki, H. Kito, M. T. Fernandez-Diaz, T. Ito, K. Kihou, H. Matsuhata, M. Braden, and K. Yamada, J. Phys. Soc. Jpn. **77**, 083704 (2008).

[5] J. A. Rodgers, G. B. S. Penny, A. Marcinkova, J.-W.G. Bos, D. A. Sokolov, A. Kusmartseva, A. D. Huxley, and J. P. Attfield, Phys. Rev. B **80**, 052508 (2009).

[6] C. de la Cruz, Q. Huang, J. W. Lynn, J. Y. Li, W. Ratcliff, J. L. Zarestky, H. A. Mook, G. F. Chen, J. L. Luo, N. L. Wang, and P. C. Dai, Nature (London) **453**, 899 (2008).

[7] A. J. Drew, C. Niedermayer, P. J. Baker, F. L. Pratt, S. J. Blundell, T. Lancaster, R. H. Liu, G. Wu, X. H. Chen, I. Watanabe, V. K. Malik, A. Dubroka, M. Rossle, K. W. Kim, C. Baines, and C. Bernhard, Nature Mater. **8**, 310 (2009).

[8] H. Luetkens, H. H. Klauss, M. Kraken, F. J. Litterst, T. Dellmann, R. Klingeler, C. Hess, R. Khasanov, A. Amato, C. Baines, M. Kosmala, O. J. Schumann, M. Braden, J. Hamann-Borrero, N. Leps, A. Kondrat, G. Behr, J. Werner, and B. Buchner, Nature Mater. **8**, 305 (2009).

[9] A. Subedi and D. J. Singh, Phys. Rev. B **78**, 132511 (2008).

[10] F. Ronning, E. D. Bauer, T. Park, N. Kurita, T. Klimczuk, R. Movshovich, A. S. Sefat, D. Mandrus, and J. D. Thompson, Physica C **469**, 396 (2009).
[11] L. Boeri, O. V. Dolgov, and A. A. Golubov, Physica C **469**, 628 (2009).
[12] A. S. Sefat, D. J. Singh, R. Jin, M. A. McGuire, B. C. Sales, and D. Mandrus, Phys. Rev. B **79**, 024512 (2009).
[13] H. Yanagi, R. Kawamura, T. Kamiya, Y. Kamihara, M. Hirano, T. Nakamura, H. Osawa, and H. Hosono, Phys. Rev. B **77**, 224431 (2008).
[14] A. Marcinkova, D. A. M. Grist, I. Margiolaki, T. C. Hansen, S. Margadonna, and J.-W.G. Bos, Phys. Rev. B **81**, 064511 (2010).
[15] M. A. McGuire, D. J. Gout, V. O. Garlea, A. S. Sefat, B. C. Sales, and D. Mandrus, Phys. Rev. B **81**, 104405 (2010).
[16] H. Yanagi, T. Watanabe, K. Kodama, S. Iikubo, S. Shamoto, T. Kamiya, M. Hirano, and H. Hosono, J. Appl. Phys. **105**, 093916 (2009).
[17] Y. Singh, A. Ellern, and D. C. Johnston, Phys. Rev. B **79**, 094519 (2009).
[18] J. M. An, A. S. Sefat, D. J. Singh, and M. H. Du, Phys. Rev. B **79**, 075120 (2009).
[19] Y. Singh, M. A. Green, Q. Huang, A. Kreyssig, R. J. McQueeney, D. C. Johnston, and A. I. Goldman, Phys. Rev. B **80**, 100403 (2009).
[20] H. Maeter, H. Luetkens, Y. G. Pashkevich, A. Kwadrin, R. Khasanov, A. Amato, A. A. Gusev, K. V. Lamonova, D. A. Chervinskii, R. Klingeler, C. Hess, G. Behr, B. Buchner, and H. H. Klauss, Phys. Rev. B **80**, 094524 (2009).
[21] M. A. McGuire, R. P. Hermann, A. S. Sefat, B. C. Sales, R. Y. Jin, D. Mandrus, F. Grandjean, and G. J. Long, New J. Phys. **11**, 025011 (2009).
[22] P. Jeglič, J.-W. G. Bos, A. Zorko, M. Brunelli, K. Koch, H. Rosner, S. Margadonna, and D. Arčon, Phys. Rev. B **79**, 094515 (2009).
[23] M. G. Holder, A. Jesche, P. Lombardo, R. Hayn, D. V. Vyalikh, S. Danzenbacher, K. Kummer, C. Krellner, C. Geibel, Y. Kucherenko, T. K. Kim, R. Follath, S. L. Molodtsov, and C. Laubschat, Phys. Rev. Lett. **104**, 096402 (2010).
[24] R. B. von Dreele, Program FPRIME for Windows 1.0 for calculating real and anomalous x-ray dispersion coefficients, 1994.
[25] T. C. Hansen, P. F. Henry, H. E. Fischer, J. Torregrossa, and P. Convert, Meas. Sci. Technol. **19**, 034001 (2008).
[26] A. C. Larson and R. B. Von Dreele, Los Alamos National Laboratory Report No. LAUR 86, 2000 (unpublished).
[27] B. H. Toby, J. Appl. Crystallogr. **34**, 210 (2001).
[28] A. T. Nientiedt, W. Jeitschko, P. G. Pollmeier, and M. Brylak, Z. Naturforsch., B: Chem. Sci. **52**, 560 (1997).
[29] A. Marcinkova, E. Suard, A. N. Fitch, S. Margadonna, and J.-W.G. Bos, Chem. Mater. **21**, 2967 (2009).
[30] A. S. Wills, Physica B **276-278**, 680 (2000).
[31] O. V. Kovalev, *Representations of the Crystallographic Space Groups* (Gordon and Breach Science, Switzerland, 1993).
[32] S. A. J. Kimber, A. H. Hill, Y. Z. Zhang, H. O. Jeschke, R. Valenti, C. Ritter, I. Schellenberg, W. Hermes, R. Pottgen, and D. N. Argyriou, Phys. Rev. B **82**, 100412(R) (2010).
[33] Y. B. Bazaliy, L. T. Tsymbal, G. N. Kakazei, A. I. Izotov, and P. E. Wigen, Phys. Rev. B **69**, 104429 (2004).
[34] H. Horner and C. M. Varma, Phys. Rev. Lett. **20**, 845 (1968).
[35] Y. B. Bazaliy, L. T. Tsymbal, G. N. Kakazei, and P. E. Wigen, J. Appl. Phys. **95**, 6622 (2004).
[36] R. Sachidanandam, T. Yildirim, A. B. Harris, A. Aharony, and O. Entin-Wohlman, Phys. Rev. B **56**, 260 (1997).
[37] W. Tian, W. Ratcliff, M. G. Kim, J. Q. Yan, P. A. Kienzle, Q. Huang, B. Jensen, K. W. Dennis, R. W. McCallum, T. A. Lograsso, R. J. McQueeney, A. Goldman, J. Lynn, and A. I. Kreyssig, Phys. Rev. B **82**, 060514(R) (2010).
[38] Y. Qiu, W. Bao, Q. Huang, T. Yildirim, J. M. Simmons, M. A. Green, J. W. Lynn, Y. C. Gasparovic, J. Li, T. Wu, G. Wu, and X. H. Chen, Phys. Rev. Lett. **101**, 257002 (2008).
[39] N. Emery, E. J. Wildman, J. M. S. Skakle, G. Giriat, R. I. Smith, and A. C. McLaughlin, Chem. Comm. **46**, 6777 (2010).